sciendo

acta mechanica et automatica, vol.17 no.1 (2023)

CONTENTS

ABSTRACTS

Zbyszko Klockiewicz, Grzegorz Ślaski
Comparison of Vehicle Suspension Dynamic Responses for Simplified and Advanced Adjustable Damper Models with Friction, Hysteresis and Actuation Delay for Different Comfort-Oriented Control Strategies

Throughout the years, many control strategies for adjustable dampers have been proposed, designed to boost the performance characteristics of a vehicle. Comfort control strategies such as Skyhook (SH), acceleration-driven damping or power-driven damping have been tested many times using simulation models of vehicles. Those tests, however, were carried out using simplified damper models – linear or simple bilinear with symmetric characteristics. This article presents the results of examination of the influence of using more complex damper models, with friction, hysteresis and time delay of state switching implemented, on the chosen dynamic responses of a suspension system for excitations in the typical exploitation frequency range. The results of the test are compared with those found in the literature and with the results of simulations performed with a simplified version of the advanced model used. The main conclusion is that friction and hysteresis add extra force to the already existing damping force, acting like a damping increase for all analysed control strategies. The actuation delays limit the effectiveness in a sense of comfort increasing to only some frequencies. The research shows the importance of including the proposed modules in testing for both adjustable and passive dampers.

Piotr Odyjas, Jędrzej Więckowski, Damian Pietrusiak, Przemysław Moczko
Challenges in the Design of New Centrifugal Fan with Variable Impeller Geometry

This article presents a description of design work for newly created centrifugal fans. This was done based on the example of an innovative solution that uses a change in impeller geometry. In the described solution, this is achieved by shortening and lengthening the impeller blades. The development of a technical solution with such properties requires a change of approach in the design process compared with classic solutions. Therefore, the following text describes this process from the concept stage to demonstrator tests. The principle of operation of such a solution is presented and the assumptions made based on analytical calculations are also described. The text also shows a 3D model of the centrifugal fan with variable impeller geometry, made with the help of computer aided design (CAD) tools. In the further part, numerical calculations were made on its basis. The finite element method (FEM) calculation made it possible to verify the structural strength of the project and its modal properties as well as to verify flow parameters, thanks to the use of computational fluid dynamics (CFD) calculations. The next step describes the procedure for testing centrifugal fans with variable rotor geometry, which is different from that of fans without this feature. The next part presents the results of research from the tests carried out.

Bartosz Wieczorek, Łukasz Warguła, Mateusz Kukla
Influence of a Hybrid Manual–Electric Wheelchair Propulsion System on the User's Muscular Effort

Self-propelled wheelchairs favour the rehabilitation process, forcing the user to be physically active. Unfortunately, in most cases, the manual propulsion is not adapted to the individual needs and physical capabilities of the user. This paper presents the results of operational tests of a wheelchair equipped with a hybrid propulsion system in which the muscle strength generated by the user is assisted by two independent electric motors. The research aimed to investigate the influence of the applied control algorithm and the assistance factor (W) on the value of the muscular effort (MA) while propelling the wheelchair with the use of push rims. A modified ARmedical AR-405 wheelchair equipped with two MagicPie 5 electric motors built into the wheelchair's hubs with a power of 500 W was used in this research. The tests were carried out on a wheelchair test bench simulating the moment of resistance within the range of 8–11 Nm. Surface electromyography was employed for the measurement of MA, specifically, a four-channel Noraxon Mini DTS apparatus. The research was carried out on five patients from the group of C50 anthropometric dimensions. The effort was measured for four muscles: deltoid–anterior part, deltoid–posteriori part, and triceps brachii and extensor carpi radialis longus. The effectiveness of the hybrid propulsion system was observed based on the extensor carpi radialis longus muscle. In this case, for the standard wheelchair, the MA ranged from 93% to 123%. In contrast, for a wheelchair equipped with the hybrid propulsion system, at W = 70%, the MA was within the range of 43%–75%.

Mária Michalková, Ivana Pobočíková,
Time Series Analysis of Fossil Fuels Consumption in Slovakia by ARIMA Model

According to the Green Deal, the carbon neutrality of the European Union (EU) should be reached partly by the transition from fossil fuels to alternative renewable sources. However, fossil fuels still play an essential role in energy production, and are widely used in the world with no alternative to be completely replaced with, so far. In recent years, we have observed the rapidly growing prices of commodities such as oil or gas. The analysis of past fossil fuels consumption might contribute

significantly to the responsible formulation of the energy policy of each country, reflected in policies of related organisations and the industrial sector. Over the years, a number of papers have been published on modelling production and consumption of fossil and renewable energy sources on the level of national economics, industrial sectors and households, exploiting and comparing a variety of approaches. In this paper, we model the consumption of fossil fuels (gas and coal) in Slovakia based on the annual data during the years 1965–2020. To our knowledge, no such model, which analyses historical data and provides forecasts for future consumption of gas and coal, respectively, in Slovakia, is currently available in the literature. For building the model, we have used the Box–Jenkins methodology. Because of the presence of trend in the data, we have considered the autoregressive integrated moving average (ARIMA (p,d,q)) model. By fitting models with various combinations of parameters p, d, q, the best fitting model has been chosen based on the value of Akaike's information criterion. According to this, the model for coal consumption is ARIMA(0, 2, 1) and for gas consumption it is ARIMA(2, 2, 2).

Pavol Šťastniak, Michal Rakár, Jakub Tížek
Design of a Height-Adjustable Boarding System for a New Double-Deck Railway Vehicle

This paper deals with a solution for faster and safer boarding and leaving of passengers at railway station platforms from 150 mm to 550 mm higher than the head of the rail. This conception is based on the requirements of railway infrastructure administrators, transporters and also manufacturers of passenger rolling stock. This device is designed for the new double-deck railway vehicle for suburban and regional transport, which fulfils legislative and normative requirements that are specified for the selected area of vehicle construction and operational features. Selected parts of the construction were verified through a series of simulation analyses. This article also includes a study that deals with optimization of the boarding area considering designed changes in the construction of the floor and a draft for modification of the vertical clearance of the boarding entrance area in a rough construction of the vehicle.

Jacek Jackiewicz
A Flywheel-Based Regenerative Braking System for Railway Vehicles

Regenerative braking is a technique that employs electric motors to convert the dynamic mechanical energy from the motor's spinning rotor and any attached loads into electricity. However, such a type of regenerative braking can only slow but not stop the vehicle because there is too little energy to excite the motor acting as a generator at low speeds. Therefore, this paper presents a unique flywheel-based regenerative braking system for railway vehicles. This system is supposed to meet high safety and comfort expectations in all operating conditions. The braking action control of this system should allow braking of empty or loaded vehicles according to load, the anti-blockage braking action of wheels and prevent wheel-slide during braking or wheel slip during acceleration. The new regenerative braking system under development, like any kinetic energy recovery system, requires the application of continuously variable transmission. The essence of the new solution is to design and build this type of variable transmission using only one planetary gear controlled through the powertrain control module for an electric motor cooperating concurrently. This paper describes complete modelling and simulation realisation on a closed-loop servomotor drive, which cooperates with the variable transmission of the regenerative braking system based on the Scilab/Xcos environment.

Ján Dižo, Miroslav Blatnický, Paweł Droździel, Rafał Melnik, Jacek Caban, Adam Kafrik
Investigation of Driving Stability of a Vehicle-Trailer Combination Depending on the Load's Position within the Trailer

Passenger cars are a means of transportation used widely for various purposes. The category that a vehicle belongs to is largely responsible for determining its size and storage capacity. There are situations when the capacity of a passenger vehicle is not sufficient. On the one hand, this insufficient capacity is related to a paucity in the space needed for stowing luggage. It is possible to mount a rooftop cargo carrier or a roof basket on the roof of a vehicle. If a vehicle is equipped with a towbar, a towbar cargo carrier can be used for improving its space capacity. These accessories, however, offer limited additional space, and the maximal load is determined by the maximal payload of the concerned vehicle. If, on the other hand, there is a requirement for transporting a load with a mass or dimensions that are greater than what could be supported using these accessories, then, provided the vehicle is equipped with a towbar, a trailer represents an elegant solution for such demanding requirements. A standard flat trailer allows the transportation of goods of various characters, such as goods on pallets, bulk material, etc. However, the towing of a trailer changes the distribution of the loads, together with changes of loads of individual axes of the vehicle–trailer axles. The distribution of the loads is one of the key factors affecting the driving properties of a vehicle–trailer combination in terms of driving stability, which is mainly a function of the distribution of the load on the trailer. This research introduces a study into how the distribution of the load on a trailer influences the driving stability of a vehicle–trailer combination. The research activities are based on simulation computations performed in a commercial multibody software. While the results presented in the article are reached for a particular vehicle–trailer combination as well as for a particular set of driving conditions, the applicability of the findings can also be extended more generally to the impact that the load distributions corresponding to various vehicle–trailer combinations have on the related parameters and other driving properties.

Dariusz Kurpisz, Maciej Obst, Tadeusz Szymczak, Radosław Wilde
Analytical Approach for Vehicle Body Structures Behaviour under Crash at Aspects of Overloading and Crumple Zone Length

Road safety problem is still topical, especially since the number of vehicles and the volume of traffic are increasing. It is possible to increase the safety of road users through systemic changes in many areas related to transport. The deformation of the vehicle body during an accident has an impact on the loads acting on the passengers. Vehicle body deformation depends on complex parameters, and knowledge of these parameters is essential for designing crumple zones and the accident reconstruction process. Knowledge of the mechanical parameters of the vehicle structure during deformation is also a reference to passenger injury indicators assessment. This paper reports results from the analytical approach for determining the protection level of personal vehicles. The proposed conception is based on the results from the static stiffness characteristic of the Ford Taurus, which gives the possibility of phenomenological and simple body crumple analytical description at a speed equal to 10 km/h, 40 km/h, 56 km/h and 60 km/h, which is an original part of the work. The approach enables us to describe the vehicle crash by focusing on variations of deformation in time, stiffness, vehicle collision time (duration), deceleration and dynamic crash force. Basing on the body stiffness data of the personal vehicle, the length of the deformation zone in the front of the car and the maximum values of force at the crash for a speed of 60 km/h are presented. Results obtained by the authors show that is possible to estimate the overloading level during the crash time of a vehicle based on the stiffness characteristic of the car body. The proposed methodology can be developed and the advantage of the presented procedure is an uncomplicated useful tool for solving complex problems of a vehicle crash.

Paweł Bałon, Bartłomiej Kiełbasa, Łukasz Kowalski, Robert Smusz
Thermal Performance of the Thermal Storage Energy With Phase Change Material

Values of energy supply and demand vary within the same timeframe and are not equal. Consequently, to minimise the amount of energy wasted, there is a need to use various types of energy storing systems. Recently, one can observe a trend in which phase change materials (PCM) have gained popularity as materials that can store an excess of heat energy. In this research, the authors analysed paraffin wax (cheese wax)'s capability as a PCM energy storing material for a low temperature energy-storage device. Due to the relatively low thermal conductivity of wax, the authors also analysed open-cell ceramic Al2O3/SiC composite foams' (in which the PCM was dispersed) influence on heat exchange process. Thermal analysis on paraffin wax was performed, determining its specific heat in liquid and solid state, latent heat (LH) of melting, melting temperature and thermal conductivity. Thermal tests were also performed on thermal energy container (with built-in PCM and ceramic foams) for transient heat transfer. Heat transfer coefficient and value of accumulated energy amount were determined.

Piotr Rybak, Zdzisław Hryciów, Bogusław Michałowski, Andrzej Wiśniewski
Assessment of the Impact of Wear and Tear of Rubber Elements in Tracked Mechanism on the Dynamic Loads of High-Speed Tracked Vehicles

The operation of high-speed tracked vehicles takes place in difficult terrain conditions. Hence, to obtain a high operational relia-bility, the design or modernisation process must be precise and should consider even the slightest details. The article presents issues related to the problem of formulating vehicle models using partial models of flexible elements used in tracked mechanisms. Changes occurring in the shape and properties of elements such as track pads and roadwheel bandages as a consequence of operating conditions are presented. These changes are reflected in the presented elastic–damping characteristics of components of the crawler mechanism. Numerical studies have shown that deterioration of chassis suspension components after a significant mileage may increase dynamic loads (forces) acting on the running gear. Increased forces in the running gear naturally result in increased stresses in the road surface on which the vehicle is travelling, which can pose a danger (or excessive wear and tear) to road infrastructure components such as culverts, bridges and viaducts. In the literature, model tests of objects are carried out on models that represent new vehicles, and the characteristics of the adopted elements correspond to elements not affected by the process and operating conditions. Its influence should not be ignored in the design, testing and running of a special vehicle. The tracked mechanism, as running gear, is designed for special high-speed vehicles for off-road and off-road driving. Its design ensures high off-road traversability. The dynamic loads originating from off-road driving are superimposed on those generated by the engine, drive train and interaction of the tracks with the roadwheels, sprocket, idler and supporting tracks return rollers.

Robert Baran, Krzysztof Michalczyk, Mariusz Warzecha
Experimental Analysis of Transverse Stiffness Distribution of Helical Compression Springs

This paper presents the results of an experimental analysis of the distribution of transverse stiffness of cylindrical compression helical springs with selected values of geometric parameters. The influence of the number of active coils and the design of the end coils on the transverse stiffness distribution was investigated. Experimental tests were carried out for 18 sets of spring samples that differed in the number of active coils, end-coil design and spring index, and three measurements were taken per sample, at two values of static axial deflection. The transverse stiffnesses in the radial directions were tested at every 30° angle. A total of 1,296 measurements were taken, from which the transverse stiffness distributions were determined. It was shown

that depending on the direction of deflection, the differences between the highest and lowest value of transverse stiffness of a given spring can exceed 25%. The experimental results were compared with the results of the formulas for transverse stiffness available in the literature. It was shown that in the case of springs with a small number of active coils, discrepancies between the average transverse stiffness of a given spring and the transverse stiffness calculated based on literature relations can reach several tens of percent. Analysis of the results of the tests carried out allowed conclusions to be drawn, making it possible to estimate the suitability of a given computational model for determining the transverse stiffness of a spring with given geometrical parameters.

Yuriy Pyr'yev, Andrzej Penkul, Leszek Cybula
Research of Dynamic Processes in an Anvil During a Collision with a Sample

The paper concerns modelling the dynamics of the contact system of the tested sample with an elastic half-space (anvil) during their collision. The original elements in the paper include the proposed general approach to solving the problem of contact dynamics. The presented approach consists in determining the force of impact on the sample during the collision and the joint solution of the problem for the tested sample and the problem for an elastic semi-space under the conditions of the assumptions of Hertz's theory. The resulting interaction forces allow the determination of displacements and stresses.

Bouchmel Mliki, Rached Miri, Ridha Djebali, Mohamed A. Abbassi
CuO–Water MHD Mixed Convection Analysis and Entropy Generation Minimization in Double-Lid–Driven U-Shaped Enclosure with Discrete Heating

The present study explores magnetic nanoliquid mixed convection in a double lid–driven U-shaped enclosure with discrete heating using the lattice Boltzmann method (LBM) numerical method. The nanoliquid thermal conductivity and viscosity are calculated using the Maxwell and Brinkman models respectively. Nanoliquid magnetohydrodynamics (MHD) and mixed convection are analyzed and entropy generation minimisation has been studied. The presented results for isotherms, stream isolines and entropy generation describe the interaction between the various physical phenomena inherent to the problem including the buoyancy, magnetic and shear forces. The operating parameters' ranges are: Reynolds number ($\mathrm{Re}: 1-100$), Hartman number ($\mathrm{Ha}: 0-80$), magnetic field inclination (γ: $0°-90°$), nanoparticles volume fraction (ϕ: $0-0.04$) and inclination angle (α: $0°-90°$). It was found that the $\mathrm{N_{um}}$ and the total entropy generation augment by increasing Re, ϕ: and γ. conversely, an opposite effect was obtained by increasing Ha and α. The optimum magnetic field and cavity inclination angles to maximum heat transfer are $\gamma = 90°$ and $\alpha = 0$.

Andrew Omame, Fiazud Din Zaman
Solution of the Modified Time Fractional Coupled Burgers Equations Using the Laplace Adomian Decomposition Method

In this work, a coupled system of time-fractional modified Burgers' equations is considered. Three different fractional operators: Caputo, Caputo-Fabrizio and Atangana-Baleanu operators are implemented for the equations. Also, two different scenarios are examined for each fractional operator: when the initial conditions are $u(x, y, 0) = \sin(xy)$, $v(x, y, 0) = \sin(xy)$, and when they are $u(x, y, 0) = e^{\{-kxy\}}$, $v(x, y, 0) = e^{\{-kxy\}}$, where k, α are some positive constants. With the aid of computable Adomian polynomials, the solutions are obtained using Laplace Adomian decomposition method (LADM). The method does not need linearization, weak nonlinearity assumptions or perturbation theory. Simulations are also presented to support theoretical results, and the behaviour of the solutions under the three different fractional operators compared.

Patryk Różyło
Failure Analysis of Beam Composite Elements Subjected to Three-Point Bending using Advanced Numerical Damage Models

This paper deals with the experimental and numerical analysis of three-point bending phenomenon on beam composite profiles. Flat rectangular test specimens made of carbon–epoxy composite, characterised by symmetric [0/90/0/90]s laminate ply lay-up, were used in this study. Experimental testing was carried out with a COMETECH universal testing machine, using special three-point bending heads. In addition, macroscopic evaluation was performed experimentally using a KEYENCE Digital Microscope with a mobile head recording real-time images. Parallel to the experimental studies, numerical simulations were performed using the finite element method in ABAQUS software. The application of the above-mentioned interdisciplinary research techniques allowed for a thorough analysis of the phenomenon of failure of the composite material subjected to bending. The obtained research results provided a better understanding of the failure mechanism of the composite material.

DOI 10.2478/ama-2023-0001

acta mechanica et automatica, vol.17 no.1 (2023)
Special Issue "Machine Modeling and Simulations 2022"

COMPARISON OF VEHICLE SUSPENSION DYNAMIC RESPONSES FOR SIMPLIFIED AND ADVANCED ADJUSTABLE DAMPER MODELS WITH FRICTION, HYSTERESIS AND ACTUATION DELAY FOR DIFFERENT COMFORT-ORIENTED CONTROL STRATEGIES

Zbyszko KLOCKIEWICZ*, Grzegorz ŚLASKI*

*Faculty of Mechanical Engineering, Institute of Machine Design, Poznan University of Technology,
ul. Piotrowo 3, 61-138, Poznan, Poland

zbyszko.klockiewicz@put.poznan.pl, grzegorz.slaski@put.poznan.pl

received 1 July 2022, revised 10 August 2022, accepted 11 August 2022

Abstract: Throughout the years, many control strategies for adjustable dampers have been proposed, designed to boost the performance characteristics of a vehicle. Comfort control strategies such as Skyhook (SH), acceleration-driven damping or power-driven damping have been tested many times using simulation models of vehicles. Those tests, however, were carried out using simplified damper models – linear or simple bilinear with symmetric characteristics. This article presents the results of examination of the influence of using more complex damper models, with friction, hysteresis and time delay of state switching implemented, on the chosen dynamic responses of a suspension system for excitations in the typical exploitation frequency range. The results of the test are compared with those found in the literature and with the results of simulations performed with a simplified version of the advanced model used. The main conclusion is that friction and hysteresis add extra force to the already existing damping force, acting like a damping increase for all analysed control strategies. The actuation delays limit the effectiveness in a sense of comfort increasing to only some frequencies. The research shows the importance of including the proposed modules in testing for both adjustable and passive dampers.

Key words: vehicle vertical dynamics, damper model, friction, hysteresis, comfort-oriented control strategies, Skyhook, ADD, PDD

1. INTRODUCTION

The basic task of a suspension system is to ensure safe interactions between vehicle wheels and the road surface while providing satisfactory ride comfort and working in a designed motion range. Oftentimes, satisfying all those needs at once proves impossible [1] as different parameters of suspension elements have different optimal values for safety and comfort. Also, the use of a damper in a typical configuration between sprung and unsprung masses in some situations helps dampen vibrations, while in others, it induces them. The need to change the way in which a damper works in different situations led to the creation of adaptive or semiactive suspension systems. They allow for changing some parameters or switching the damping force during one cycle of vibration. The idea is not new – the patent for adjustable hydraulic shock absorbers was granted in 1957 [2], while control strategies for computer models of vehicles were studied as far back as 1973 [3]. The first widely used control was the comfort-oriented Skyhook (SH) strategy [4], which since then was implemented numerous times in simulations and real-life applications [5–7]. Since then, many more control strategies have been proposed [8], including safety-oriented Groundhook [9], acceleration-driven damper (ADD) [10, 11, 12] and power-driven damper (PDD) [11, 13].

The ADD control strategy minimises the vertical body acceleration (comfort objective) when no road preview is available. Unlike the SH control, the ADD control suppressed the resonance and amplitude in the middle- and high-frequency bands [12]. This strategy uses the same sensors as the SH algorithms and a simple two-state controllable damper.

The PDD control strategy provides results comparable with those of the ADD control strategy, avoiding, at the same time, the chattering effects of the damping control valve [11].

Although much research in that field is conducted purely on theoretical, simplified vehicle models, the real-life implementation of said strategies, while not unseen [14], remains rare. The simplified suspension models use simplified models of damping forces, often utilising the linear damping coefficient [11]. More advanced models include nonlinear characteristics and/or asymmetrical characteristics. In some cases, dry friction is added, while taking damping force hysteresis into account is rare. The same is true for properties connected with damping force adjustment, especially the delay time between the control signal and damping characteristic change.

The authors decided to research into the influence of every additional feature of the damper model on the effectiveness of the damping control strategy in comparison to the model used as the reference model. The subject of research was transfer functions of a quarter car model with different damper models (with internal friction, hysteresis and activation delay implemented) tested with the use of a chirp signal within a frequency range of 0.01–25 Hz.

The present study aims to test the amount of difference in chosen dynamic responses when using a more advanced damper model in simulations, with internal friction, hysteresis and activation delay implemented. Simulations using models with such

DOI 10.2478/ama-2023-0001

features have been carried out before [15, 16]; however, the aim of these models was different from that attempted in this study.

2. RESEARCH METHOD

The current research used computer simulations of a vertical dynamics model of a quarter car implemented in MATLAB/Simulink software. In this research, a set of modified quarter car models with different damper models were used for the different cases of advanced shock absorber models, as presented in Tab. 1.

Tab. 1. Shared features of a quarter car model used in research

Case no.	Nonlinear characteristic	Friction	Hysteresis	Delay
1	✓	-	-	-
2	✓	✓	-	-
3	✓	-	✓	-
4	✓	-	-	✓
5	✓	✓	✓	✓

Case number 1 was chosen as the easiest way to model real damper characteristics as static characteristics. Case numbers 2–5 were also tested in two variants – once without any of the control strategies and once with one of the three tested strategies – SH, ADD or PDD. Other parameters of a suspension were shared between all versions of a model – linear stiffness characteristics of a tire and suspension (Tab. 2).

Tab. 2. Shared features of a quarter car model used in research

Parameter	Unsprung mass	Sprung mass	Tire stiffness	Tire damping	Suspension stiffness
Unit	(kg)	(kg)	(kN/m)	(Ns/m)	(kN/m)
Value	50	400	200	350	30

The tested models were subjected to excitation, enabling the calculation of dynamic responses of suspension in the form of transfer functions between excitation and responses important to the evaluation of the suspension dynamic performance:

– suspension deflection for the evaluation of the necessary rattle space,
– sprung mass acceleration and sprung mass displacement for evaluation of ride comfort, and
– cumulative tire force for the evaluation of safety potential.

The excitation used was a vertical sinusoidal displacement with a constant amplitude of 3 mm, which had variable frequency starting from 0.0001 Hz up to 40 Hz (Fig. 1). The frequency increases were as follows:

1. from 0.0001 to 1 in 100 s – 0.0099 Hz/s,
2. from 1 Hz to 3 Hz in 60 s – 0.0333 Hz/s,
3. from 3 Hz to 10 Hz in 100 s – 0.07 Hz/s and
4. from 10 Hz to 40 Hz in 80 s – 0.375 Hz/s.

Important frequencies when analysing suspension dynamics cover a range from 0.5 Hz to 25 Hz. The frequency values change in a nonlinear fashion in order to allow more cycles in a lower range to occur, which in turn gives better results when calculating transfer functions. Frequencies, both below 0.5 Hz and above 25 Hz, were added to the simulation in order to further stabilise results of the *tfestimate* MATLAB function used to estimate the transfer function of suspension.

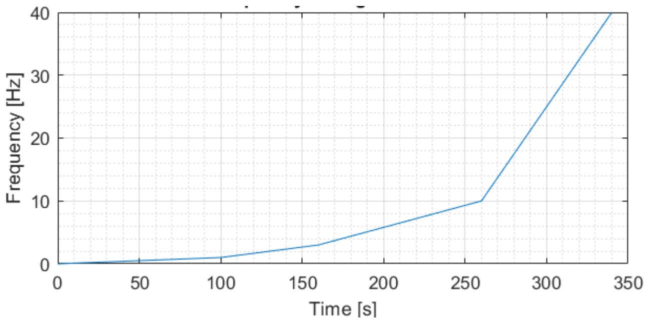

Fig. 1. Changes of the frequency of the input signal over simulation time

2.1. Advanced adjustable damper model

The damper model for all cases, in addition to case no. 1 (labelled as 'linear'), had a nonlinear, asymmetric characteristic, which was identified after empirical testing of damping forces for different levels of control current and averaging these forces to get static characteristics [1], as presented in Fig. 1.

To simplify modelling of the influence of control current on a damping force characteristics, the medium static damping characteristics, between the lowest and the highest, were used as a base characteristic and multiplied by a specific number dependent on the control current and whether the damper was compressed or extended (Fig. 2), resulting in a force that is within the range defined by maximum nonlinear and minimum nonlinear characteristics on the graph. This allowed to model damping forces due to control strategies changing only control current as the input.

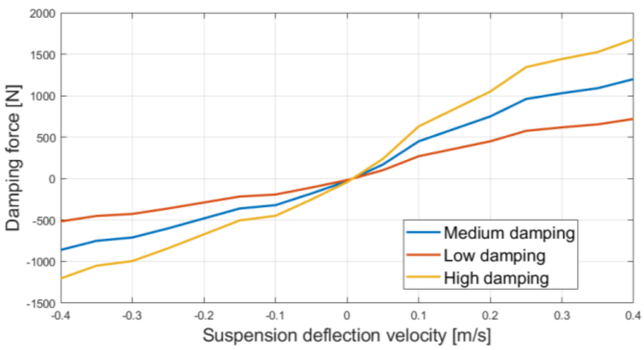

Fig. 2. Damper model static characteristics

All the versions of a damper model, in addition to case no. 1,included a model of an adjustable damper with hysteresis, friction and actuation delay modelled (switched off individually for particular tests). The implementation of this model, based on the study mentioned in Ref [17], was described in the study mentioned in Ref [16] and is shown in Fig. 3.

A total of three main modules to model the total damper force were applied:

DOI 10.2478/ama-2023-0001

– static damping force,
– hysteresis force, and
– friction force.

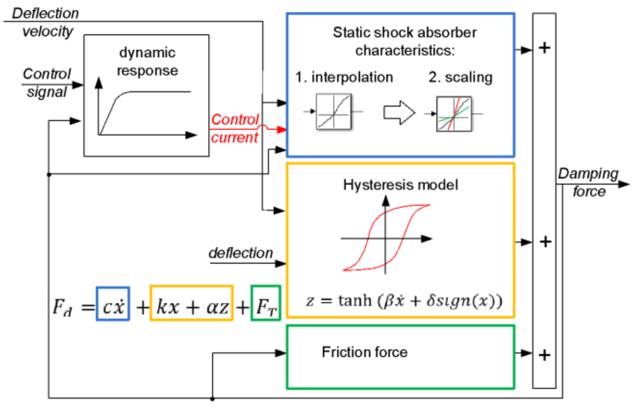

Fig. 3. Damper model diagram

The module generating the biggest forces in the damper model is the static damping characteristics module, which is modelling damping force as a function of deflection speed, differing for the compression and rebound, and also on the control current if it is electrically adjusted damper. For linear and symmetrical characteristics, its damping force can be modelled by simple equations (it was applied for a linear damper for case number 1):

$$F_d = c\dot{x} \tag{1}$$

where c is the damping coefficient and $\dot{x}$ is the damper compression/extension velocity.

In cases of nonlinear and asymmetrical characteristics (in case numbers 2–6), nonlinear equations or interpolation of experimental characteristics can be used. Implementing a damper model in a MATLAB/Simulink software via the lookup table block can be used for the interpolation of the damping force value.

For the adjustable damper, the interpolation is also necessary for the value of damping force in relation to the control current. It too can be carried out with a lookup table block (two-dimensional) for the three-dimensional shock absorber characteristics. In case of a linear relation between control current and damping forces, the medium damping F_{dS_m} static characteristic can be used, and the coefficient to increase or decrease damping force according to the value of valve coil current and state of damper work – compression or rebound:

$$F_{dS\_I} = F_{dS\_m} \cdot K_I \tag{2}$$

where $F_{d\_S\_I}$ is the interpolated value of damping force from static characteristics for given current, F_{dS_m} is the middle static characteristics damping force (for the middle value of valve coil current), and K_I is the coefficient to increase or decrease damping force according to the value of valve coil current and state of damper work – compression or rebound. For modelled shock absorber, formulas for calculating K_I values according to the current value I_c (0.6 $\leq I_c \leq$1.6 [A]) were determined for compression and rebound, respectively, as follows:

$$\mathrm{K_{IC}} = -0.55\mathrm{I_c} + 1.59 \text{ and } \mathrm{K_{IR}} = -0.71\mathrm{I_c} + 1.74 \tag{3}$$

The Simulink implementation of implementation of Eqs (2) and (3) is presented in Fig. 4.

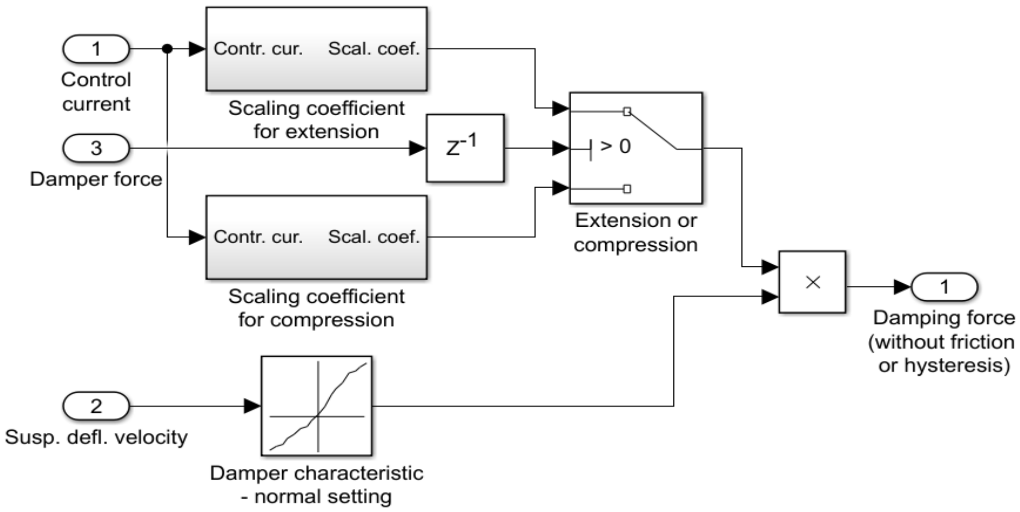

Fig. 4 Damping force calculation subsystem

The damper hysteresis module is important for high damping forces and high velocities. A simple model based on the work mentioned in Ref [6] is proposed to model the hysteretic force–velocity characteristic of the damper. This model is given by the following formulas:

$$F_h = kx + \alpha z \tag{4}$$

$$z = F_0 \cdot tanh\left(\beta\dot{x} + \delta sign(x)\right) \tag{5}$$

where *k* is the stiffness coefficient which is responsible for the hysteresis opening found from the vicinity of zero velocity; a large value of *k* corresponds to the hysteresis opening of the ends; *z* is the hysteretic variable given by the hyperbolic tangent function; β is the scale factor of the damper velocity defining the hysteretic slope, and the large value of β gives a step hysteretic slope; δ is the factor determining the width of the hysteresis through the term δsign(*x*), a wide hysteresis resulting from a large value of δ; and α is the scale factor of the hysteresis that determines the height of the hysteresis, and its value depends on the control current.

On the base of an analysis of the dynamic characteristic of tested shock absorber, a formula for the relation between the scale factor α and valve coil current I_C was developed:

$$\alpha = \alpha_0 \cdot (-2.15 I_C + 4.45) \quad (6)$$

where α_0 is the scale factor α of the hysteresis for middle static characteristics damping force.

The hysteresis force value was dependent on both the suspension deflection and its velocity, as well as on the control current value and a number of empirically obtained parameters [19].

The internal friction module is modelling force F_T, and it consists of two elements – the value of kinetic friction force and a signum function due to the model friction force with the opposite sign to the damping force.

The module modelling response time of a shock absorber is based on the model presented in the study mentioned in Refs [7, 8] and consists of two blocks modelling the delay for the damping force increase:

– dead time T_0,
– time delay with a time constant T_Z.

Considering that the time response of tested shock absorbers depends on the stroke direction and the valve operating state, including switching direction (from soft to hard, or vice versa), the four different time delays with use of different values of T_0 and T_Z are calculated in the model and is used according to compression/rebound movement and switching direction. For tested shock absorber, these values were determined to be the same for compression and rebound directions; for switching from soft to hard, they were T_0=4 ms and i T_Z=5 ms, and for switching from hard to soft, T_0=2 ms and i T_Z=3 ms.

This shows that the transfer functions obtained and analysed in the research will not be the same as those in the simpler model, for example, [11]. However, their general course of variability should remain the same with slight changes. The aim of the research designed and presented in this article was to check the qualitative and quantitative influence of taking into account friction, hysteresis and delay time on the transfer function obtained for some comfort-oriented semiactive control strategies for suspension damping.

Lastly, the friction force calculation depended on the suspension deflection velocity; if it was greater than a given threshold, then the friction force had a value equal to defined kinematic friction (35 N), and if it was smaller, then the kinematic friction value was multiplied by a ratio of current suspension deflection velocity to the threshold value (Fig. 1).

$$F_f = \begin{cases} 35 \; if \; v_{defl} > 0.1 \; m/s \\ 35 \cdot \frac{v_{defl}}{0.1} \; if \; v_{defl} < 0.1 \; m/s \end{cases} \; [N] \quad (7)$$

All the versions of a model that had a control strategy implemented also had a delay module, which caused the current change to occur over a given amount of time. The three modules – friction, hysteresis and delay – could be turned on or off to test their impact on the model behaviour.

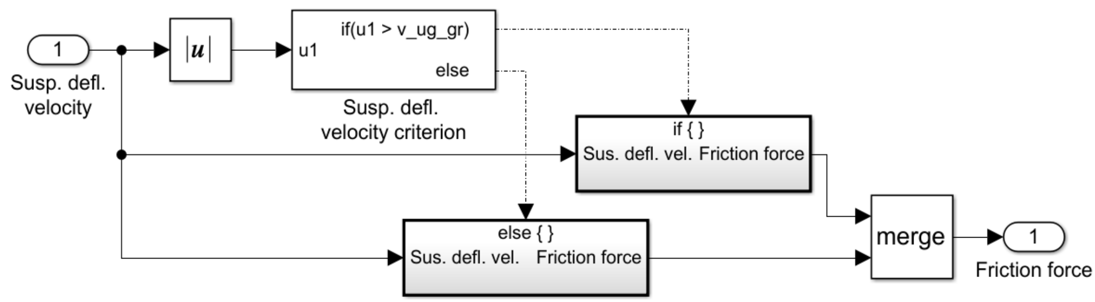

Fig. 5. Friction force calculation subsystem

As stated previously, there were a few versions of a quarter car model; two static versions, one was set to maximum damping force and one with minimum force; and three versions that had different control strategies implemented. The strategies were SH, ADD and PDD. For reference, there were also simplified versions for each of these, which did not have hysteresis, friction or delays, as well as a version with a fully linear characteristic, which was used to determine the influence of previously mentioned modules in the most basic damper model. These three control strategies can be found in many studies, for example, studies given in Refs [6, 7, 11, 19].

3. TESTING AND SIMULATION RESULT ANALYSIS METHODOLOGY

In the cases analysed, a quarter car model was used containing a nonlinear damper model with controllable friction and hysteresis modules, which could be turned on or off. In addition to the damper module, the rest of the model was linear, with the parameters of the model presented in Tab. 2. For each variant, the same excitation was applied – a changing frequency sine wave of amplitude 3 mm, with the course of frequency variability shown in Fig.1.

The influence of implementing friction, hysteresis or both the factors simultaneously was analysed for three indicators – suspension deflections, cumulative force between the tire and the road surface, and sprung mass accelerations for passive dampers and semiactive dampers controlled with different strategies. Analysed indicators allow for the suspension performance evaluation in terms of ride comfort, ride safety and kinematic limitations caused by the finite work range of the suspension.

Because these indicators are not defined by a single value, but rather as a function of frequency, the tool chosen for the analysis was the transfer functions between the given indicator and kinematic excitation.

These functions were calculated using the response signals (deflection, cumulative tire force and sprung mass acceleration) obtained during simulations, as would be performed for a real-life experiments. The transfer functions between these responses and kinematic excitation were then calculated in MATLAB using the *tfestimate* function for the nonlinear, passive model without friction, hysteresis and actuation delay modules, which served as a reference to which results for other variants were then compared to. The reason why these functions were not calculated based on the element characteristics was the nonlinear characteristic of control strategies. The resulting transfer functions were then plotted as graphs, showing their magnitude as the function of frequency, with the range of frequencies from 0.5 Hz to 25 Hz being investigated.

The results for the relative values between a given case and the reference model were represented as bar charts to show the values for four chosen frequencies – near first resonant frequency (ca. 1 Hz), 3 Hz, second resonant frequency (around 10 Hz) and maximum tested frequency 25 Hz.

4. RESULTS

4.1. Influence of friction, hysteresis and actuation delay on the SH strategy

The first tested control strategy that was the SH strategy. The friction and hysteresis affect the work of a damper, as if the damping force increased the, causing the magnitudes for road excitation to suspension deflection transfer function to decrease (Fig. 6).

For transfer functions between road excitation and both cumulative tire force and sprung mass acceleration, friction and hysteresis caused minor changes in the magnitude - dropping by at most 5 % in comparison to reference model. The increase is slightly more significant, especially in the range of 3 to 4 Hz, where friction causes a 10% increase, and the hysteresis contributes to a 20% increase. These values drop significantly, being on par with the reference model for cumulative tire force, while for sprung mass acceleration, after decreasing to around 102%–104% of reference value in the range of 9–10 Hz, it increases again to a maximum tested frequency of 25 Hz. A delay of 30 ms did not have much of an impact on a lower frequency response, as expected. With the growing frequency, its influence increases, which could be observed for sprung mass accelerations and cumulative tire force with the relative increase in magnitude of frequencies in the range of 1.5 Hz to 6 Hz. For suspension deflections, the changes become apparent around 4 Hz value, when relative magnitude starts dropping quickly, reaching 75% for 10 Hz. For higher frequencies it starts going back up, reaching 102% for 25 Hz. The drop in value is visible for other analysed values as well, along with the increase in relative magnitude for values over 10 Hz. Because of the nature of excitation, which is periodical, researchers theorise this behaviour is caused by the fact that the delayed response first starts to act in counterphase to the intended changes, but after reaching a certain threshold, the change from a previous cycle starts to coincide with the next excitation cycle, making the strategy work better. This is supported by a test, in which a 60-ms delay was added, and the results between 30 ms and 60 ms were plotted; it was noticed that for 60 ms, the analogous changes were happening for lower frequencies. The effects of friction, hysteresis and delay combined added up to the total effect in the model with all three being active.

Tab. 3 and Fig. 7 present absolute and relative values of transfer functions of suspension deflection for damper model with the SH control strategy. Frequency ranges chosen for analysis included characteristic frequency bands, such as first and second resonant frequencies or maximal tested frequency.

This way of result presentation was also chosen for the rest of results to minimise number of charts in the article and for easier interpretation of the obtained results.

For the SH control strategy, suspension deflections were mostly influenced by hysteresis for sprung mass resonant frequency and delay in actuation for unsprung mass resonant frequency. Friction had a less impact on transfer function values overall. It can also be noted that all three factors combined caused a larger difference in the transfer function value than the sum of their individual influences. Fig. 8 presents transfer functions between road excitation and cumulative tire force. Tab. 4 and Fig. 9 present absolute and relative values of these transfer functions for the damper model with the SH control strategy.

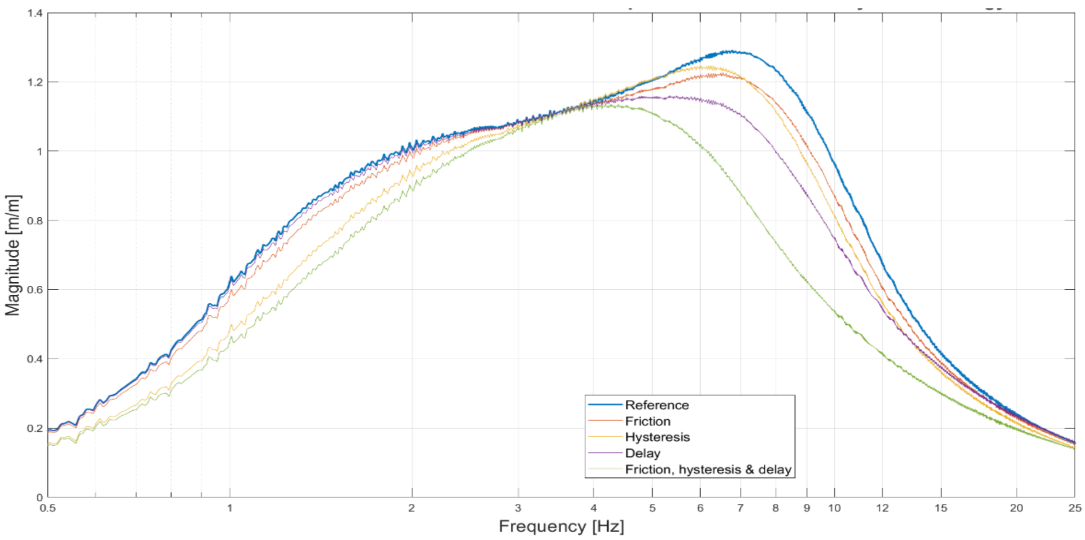

Fig. 6. Transfer functions between kinematic excitation and suspension deflection for the SH (SkyHook) control strategy for advanced and simple damper models. SH, SkyHook

DOI 10.2478/ama-2023-0001

Tab. 3. Absolute values of transfer functions from road excitation to suspension deflection (m/m) for SH, SkyHook

	1st resonant freq. –1 Hz	–3 Hz	2nd resonant freq. –10 Hz	Max. tested freq. 25 Hz
Reference	0.82	1.08	1.15	0.18
Friction	0.77	1.08	1.01	0.18
Hysteresis	0.65	1.07	0.96	0.16
Delay 60 ms	0.8	1.08	0.87	0.19
Fric. + Hyst. + Delay 60 ms	0.6	1.06	0.63	0.16

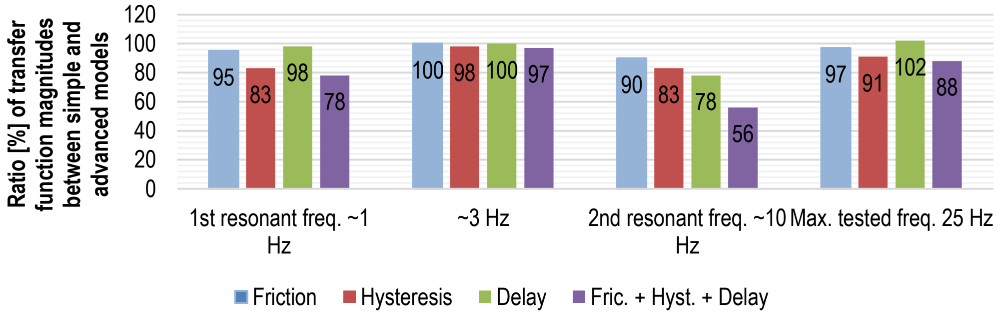

Fig. 7. Relative values of transfer functions from road excitation to suspension deflection of advanced and simple damper models for SH control strategy. SH, SkyHook

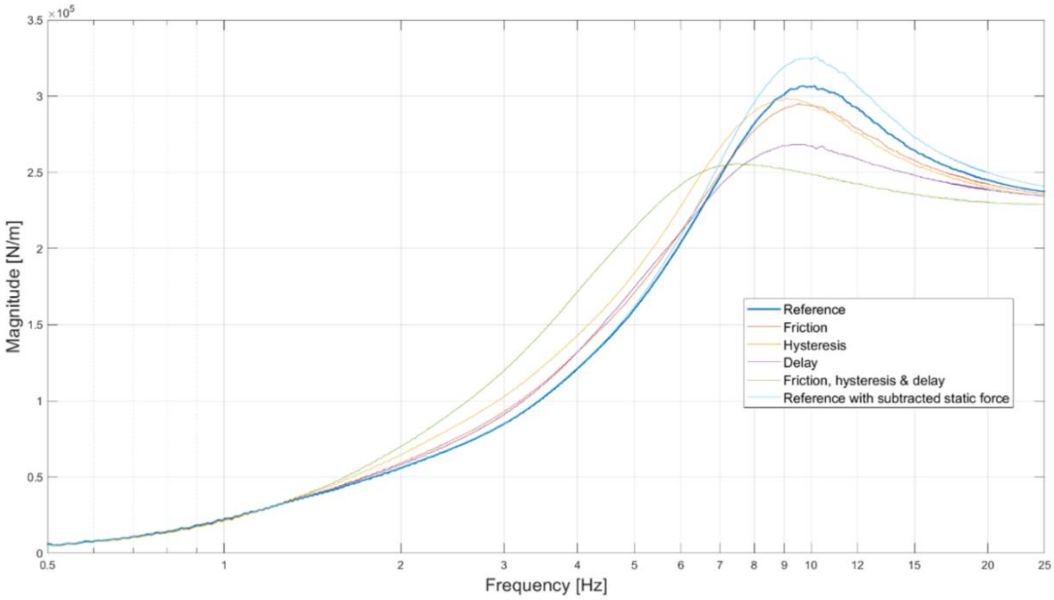

Fig. 8. Transfer functions between kinematic excitation and cumulative tire force for SH control strategy. SH, SkyHook

Tab. 4. Absolute values of transfer functions from road excitation to cumulative tire force (N*10^5/m) for SH, SkyHook

	1st resonant freq. –1 Hz	–3 Hz	2nd resonant freq. –10 Hz	Max. tested freq. 25 Hz
Reference	0.36	0.82	3.05	2.39
Friction	0.37	0.90	2.85	2.38
Hysteresis	0.37	1.03	2.98	2.37
Delay 60 ms	0.37	0.88	2.65	2.37
Fric. + Hyst. + Delay 60 ms	0.37	1.20	2.53	2.30

sciendo
DOI 10.2478/ama-2023-0001
acta mechanica et automatica, vol.17 no.1 (2023)
Special Issue "Machine Modeling and Simulations 2022"

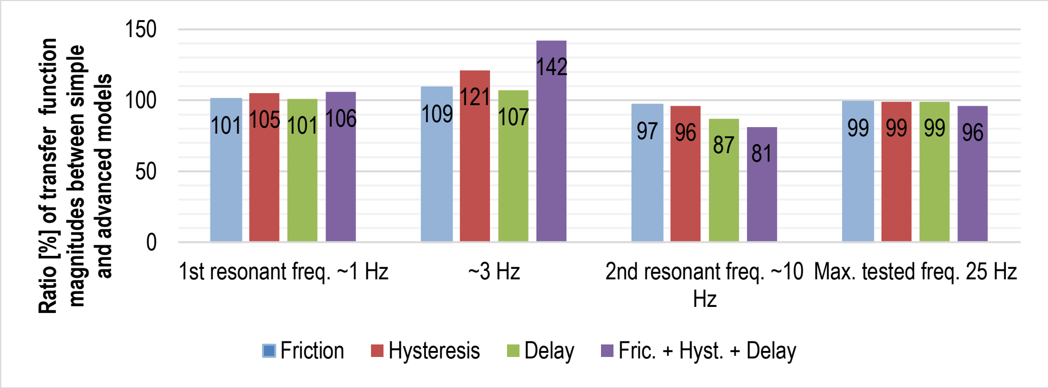

Fig. 9. Relative values of transfer function magnitudes from excitations to tire force cumulative for the SH control strategy and different shock absorber models. SH, SkyHook

Cumulative tire forces for the SH strategy were mostly influenced by hysteresis for 3 Hz and delay for 10 Hz. The highest changes, in general, were seen for the 3 Hz range, where implementation of all three advanced options in the damper model caused the transfer function value to increase by over 40% compared with the reference model; apart from that, for other frequencies, the change was no larger than 13%.

Fig. 10 presents transfer functions between road excitation and sprung mass accelerations, and Tab. 5 and Fig. 11 present absolute and relative values of transfer functions of sprung mass accelerations for the damper model using the SH control strategy. The influence on sprung mass accelerations of all three factors for both resonant frequencies was small, reaching 6% at most; however, it could be much more clearly seen for 3 Hz and 25 Hz. As could be expected, the higher the frequency, more the delay in actuation, contributing to over 30% higher transfer function values.

The influence on sprung mass accelerations of all three factors for both resonant frequencies was small, reaching 6% at most; however, it could be much more clearly seen for 3 Hz and 25 Hz. As could be expected, the higher the frequency, the more delay in actuation of shock absorber valves, contributing to over 30% higher transfer function values.

The increase in magnitudes of transfer functions between road excitation and cumulative tire force and between sprung mass acceleration is significant in the range of 3–4 Hz, where friction causes a 10% increase and hysteresis contributes to a 20% increase. These values drop significantly being on par with the reference model for cumulative tire force, while sprung mass acceleration after decreasing to around 102%–104% of the reference value in the range of 9–10 Hz, they increased again up to a maximum tested frequency of 25 Hz.

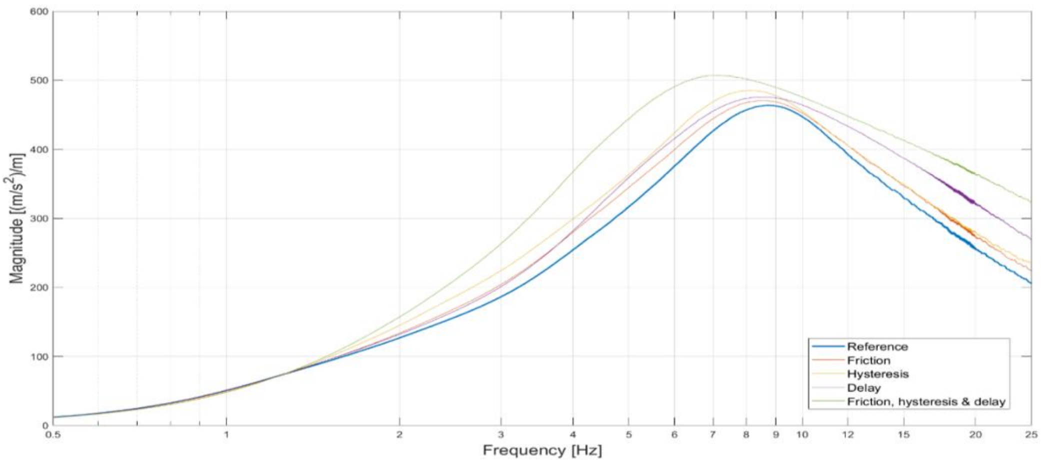

Fig. 10 Transfer functions from kinematic excitation to sprung mass acceleration for the SH control strategy. SH, SkyHook

Tab. 5. Absolute values of transfer functions from road excitation to sprung mass acceleration the for SH control strategy for different damper models

Values in $(m/m/s^2)$	1st resonant freq. –1 Hz	–3 Hz	2nd resonant freq. –10 Hz	Max. tested freq. 25 Hz
Reference	90	190	460	205
Friction	90	205	465	225
Hysteresis	90	230	475	235
Delay 60 ms	90	200	470	270
Fric. + Hyst. + Delay 60 ms	90	265	485	325

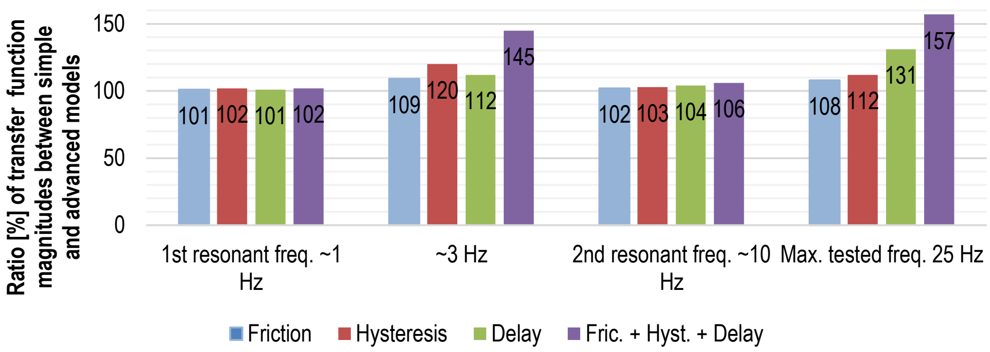

Fig. 11. Relative values of transfer function magnitudes from excitations to sprung mass accelerations for the SH control strategy for different shock absorber models. SH, SkyHook

A delay of 30 ms did not have much of an impact on lower frequency response, as expected. With the growing frequency, its influence increased, which could be observed for sprung mass accelerations and cumulative tire force as the relative increase in magnitude for frequencies in the range of 1.5–6 Hz. For suspension deflections, the changes caused by delay became apparent around 4 Hz value, when relative magnitude started dropping quickly, reaching 75% for 10 Hz, after which frequency it started going back up, reaching 102% for 25 Hz. The drop in value is visible for other analysed values as well, along with the rise in relative magnitude for values over 10 Hz. Because of the nature of excitation, which is periodical, researchers theorise this behaviour is caused by the fact that the delayed response first starts to act in counterphase to the intended changes, but after reaching a certain threshold, the change from a previous cycle starts to coincide with the next excitation cycle, making the strategy work better. This is supported by a test, in which a 60-ms delay was added and the results between 30 ms and 60 ms were plotted; it was noticed that for 60 ms, the analogous changes occurred for lower frequencies. The effects of friction, hysteresis and delay combined once again added up to the total effect in the model, with all three being active.

4.2. Influence of friction, hysteresis and actuation delay on ADD strategy

The second analysed strategy was ADD, and similar patterns emerge when analysing the transfer functions (Fig. 12), with slightly different values.

Tab. 6. and Figs. 12 and 13 present absolute and relative values of transfer functions of suspension deflection for the damper model using the ADD control strategy. In general, the influence of friction and hysteresis was comparable with that of the SH strategy, with the exception of hysteresis having a greater impact on low frequency behaviour, increasing the relative values. Delay, in general, has less impact on the all analysed transfer functions; however, interestingly, it causes a slight increase (3%–4%) in the relative value near the first resonant frequency across the board and also for the second resonant frequency (2%–3%) in case of sprung mass acceleration and cumulative tire force. For suspension deflection, the relative magnitude is lowered by the same amount of around 3%.

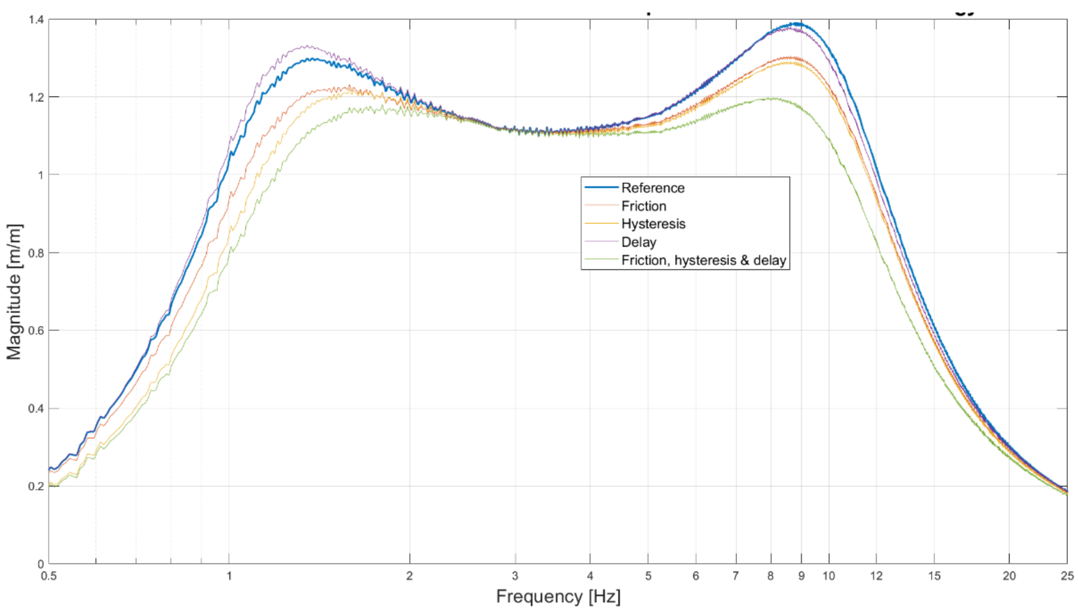

Fig. 12. Transfer functions between kinematic excitation and suspension deflection for the ADD control strategy. ADD, acceleration-driven damper

Tab. 6. Absolute values of transfer functions from road excitation to suspension deflection (m/m) for the ADD control strategy for different damper models

	1st resonant freq. –1 Hz	–3 Hz	2nd resonant freq. –10 Hz	Max. tested freq. 25 Hz
Reference	1.28	1.13	1.39	0.19
Friction	1.22	1.13	1.29	0.19
Hysteresis	1.21	1.13	1.27	0.19
Delay 60 ms	1.33	1.13	1.35	0.19
Fric. + Hyst. + Delay 60 ms	1.15	1.13	1.16	0.18

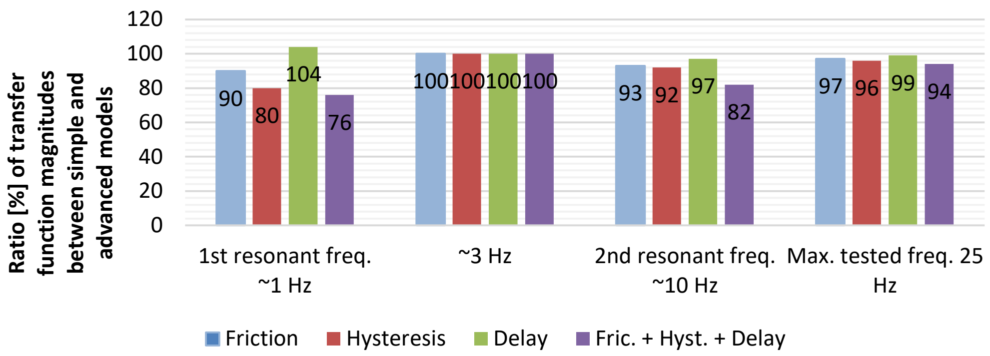

Fig. 13. Relative values of transfer function magnitudes from excitations to suspension deflections for the ADD control strategy for different shock absorber models. ADD, acceleration-driven damper

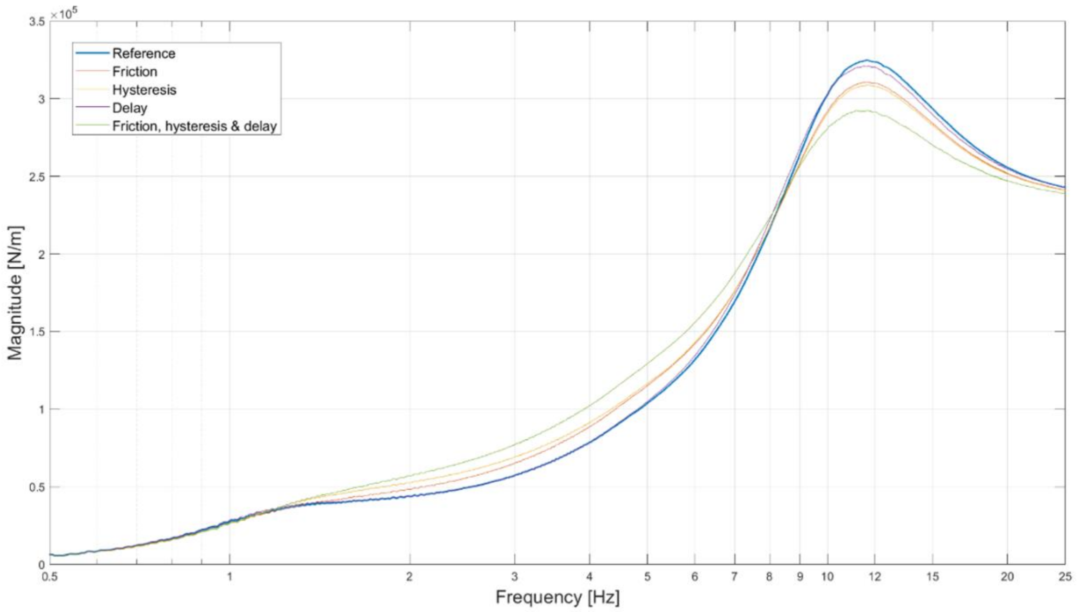

Fig. 14. Transfer functions between kinematic excitation and cumulative tire force for the ADD control strategy. ADD, acceleration-driven damper

Tab. 7. Absolute values of transfer functions between road excitation and cumulative tire force (N*10^5/m) for ADD

	1st resonant freq. –1 Hz	–3 Hz	2nd resonant freq. –10 Hz	Max. tested freq. 25 Hz
Reference	0.37	0.57	3.25	2.43
Friction	0.36	0.67	3.10	2.42
Hysteresis	0.36	0.71	3.09	2.42
Delay 60 ms	0.0.40	0.57	3.22	2.43
Fric. + Hyst. + Delay 60 ms	0.35	0.78	2.90	2.41

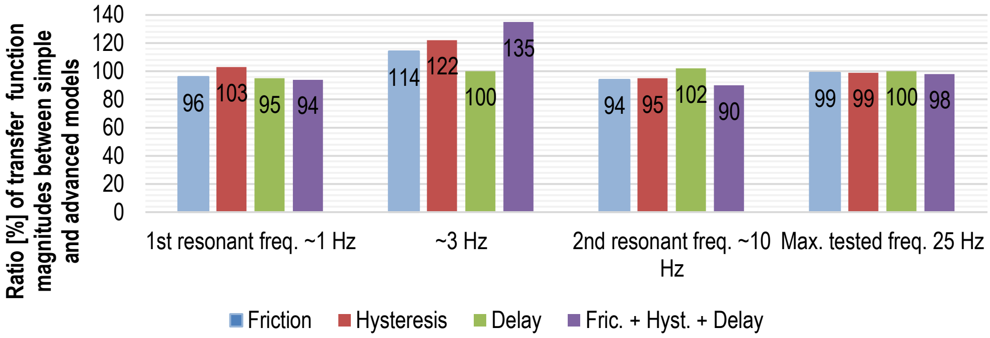

Fig. 15. Relative values of transfer function magnitudes from excitations to cumulative tire force for the ADD control strategy for different shock absorber models. ADD, acceleration-driven damper

The ADD control strategy in case of suspension deflections is less influenced by the addition of damper model elements like friction, hysteresis and especially actuation delay than by the SH control strategy. Friction and hysteresis affect the model behaviour to almost an identical degree, which does not exceed 10%.

Tab. 7 and Fig. 14 present absolute and relative (Fig. 15) values of transfer functions of cumulative tire force for various damper models with the ADD control strategy.

In terms of cumulative tire force, the influence of hysteresis and friction can be seen more clearly, especially for the 3 Hz range. The transfer function values there are around 15% to 20% higher, when these two model elements are added. The actuation delay still does not produce a meaningful change in transfer function values.

Tab. 8 and Fig. 16 present absolute and relative (Fig. 17) values of transfer functions of sprung mass accelerations for the damper model with the ADD control strategy.

Sprung mass accelerations are mostly influenced by hysteresis, followed by friction. Delay once again almost does not influence the results. The highest impact is seen for 3 Hz and 25 Hz as was also the case for the SH control strategy.

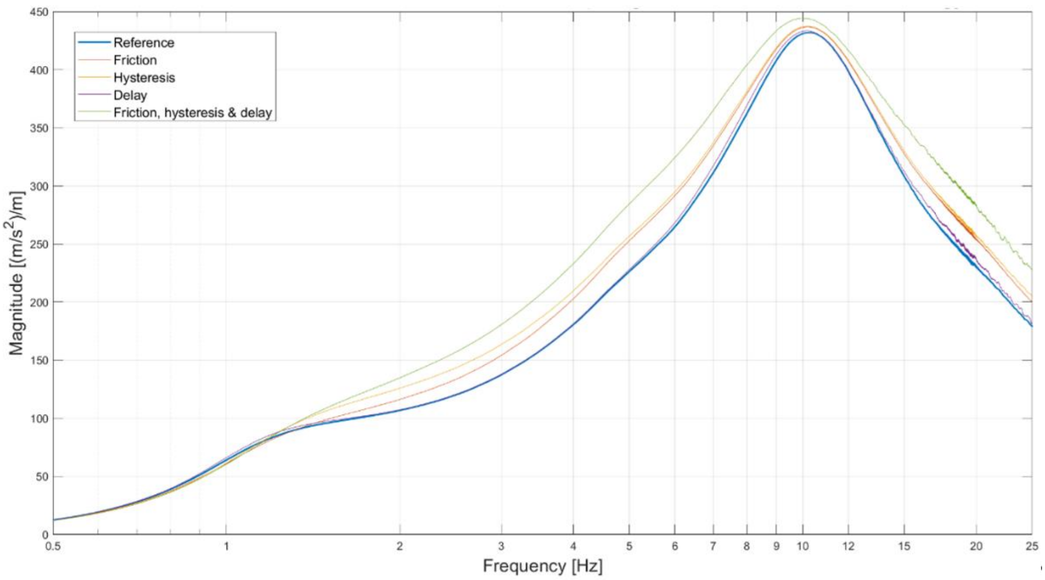

Fig. 16. Transfer functions between kinematic excitation and sprung mass acceleration for the ADD control strategy. ADD, acceleration-driven damper

Tab. 8. Absolute values of transfer functions between road excitation and sprung mass acceleration ([m/s^2]/m) for ADD

	1st resonant freq. –1 Hz	–3 Hz	2nd resonant freq. –10 Hz	Max. tested freq. 25 Hz
Reference	65	135	430	182
Friction	63	155	438	200
Hysteresis	63	168	438	203
Delay 60 ms	66	135	431	185
Fric. + Hyst. + Delay 60 ms	63	180	442	230

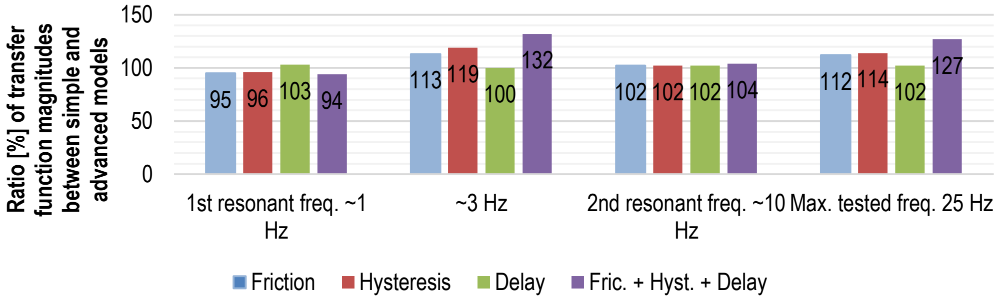

Fig. 17. Relative values of sprung mass accelerations for ADD. ADD, acceleration-driven damper

In general, in a case of the ADD strategy, the influence of friction and hysteresis was comparable with that in the SH strategy, with the exception of hysteresis having a greater impact on low frequency behaviour, increasing the relative values. Delay, in general, has less impact on the all analysed transfer functions; however, interestingly, it causes a slight increase (3%–4%) in the relative value near the first resonant frequency across the board and also for the second resonant frequency (2%–3%) in case of sprung mass acceleration and cumulative tire force. For suspension deflection, the relative magnitude is lowered by the same amount of around 3%.

4.3. Influence of friction, hysteresis and actuation delay the PDD strategy

The last tested control strategy was the PDD strategy. The overall impact of friction and hysteresis on the behaviour of the model was similar to that of the ADD strategy, with hysteresis having relative gain slightly lower by around 12% to 14% points for the first and second resonant frequencies, respectively, for suspension deflection – Tab. 9. Cumulative tire force and sprung mass acceleration functions also have slightly lower relative gains for most frequencies, except for the 3–4 Hz range, where the relative gain is actually higher by around 10% points. Delay functions a bit differently; it has almost no impact on any of the dynamic responses. The cumulative effects of all three are as previously – mostly a sum of individual influences.

The effects of the PDD strategy are similar to those of ADD, with the difference being that in case of PDD, the influence is on average 5%–10% higher for hysteresis, while friction and delay do not change much. The greatest effects are seen for both resonant frequencies.

Tab. 10 and Figs. 20 and 21 present absolute and relative values of transfer functions of cumulative tire force for the damper model with the PDD control strategy.

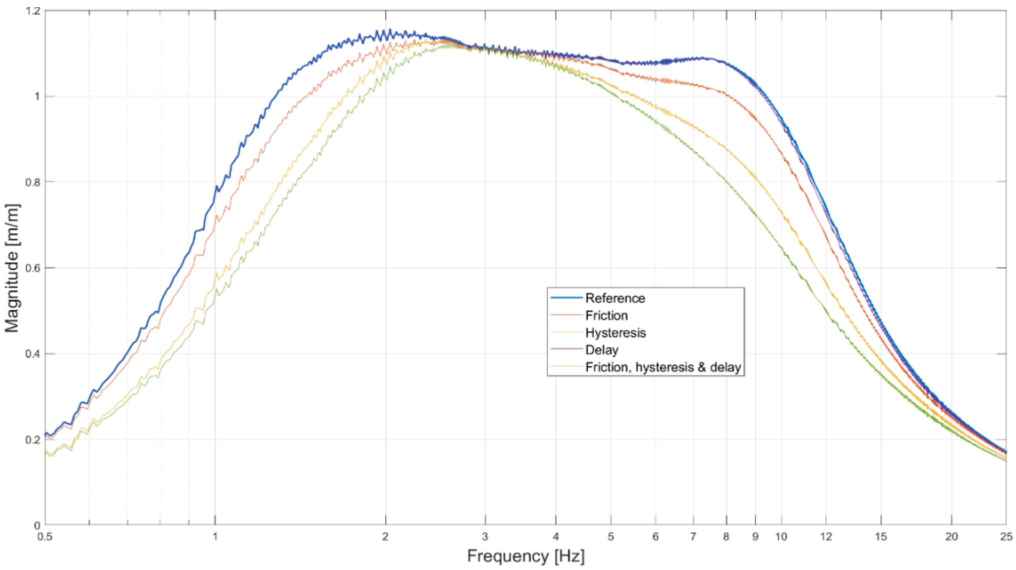

Fig. 18. Transfer functions between kinematic excitation and suspension deflection for the PDD control strategy. PDD, power-driven damper

Tab. 9. Absolute values of transfer functions between road excitation and suspension deflection (m/m) for PDD

	1st resonant freq. –1 Hz	–3 Hz	2nd resonant freq. –10 Hz	Max. tested freq. 25 Hz
Reference	0.78	1.12	1.08	0.17
Friction	0.72	1.12	1.01	0.17
Hysteresis	0.58	1.12	0.88	0.16
Delay 60 ms	0.78	1.12	1.08	0.17
Fric. + Hyst. + Delay 60 ms	0.53	1.12	0.72	0.15

DOI 10.2478/ama-2023-0001

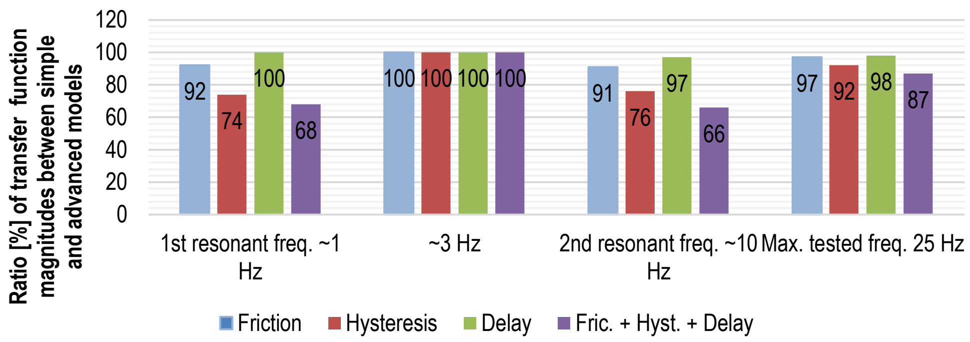

Fig. 19 Relative values of suspension deflections for PDD. PDD, power-driven damper

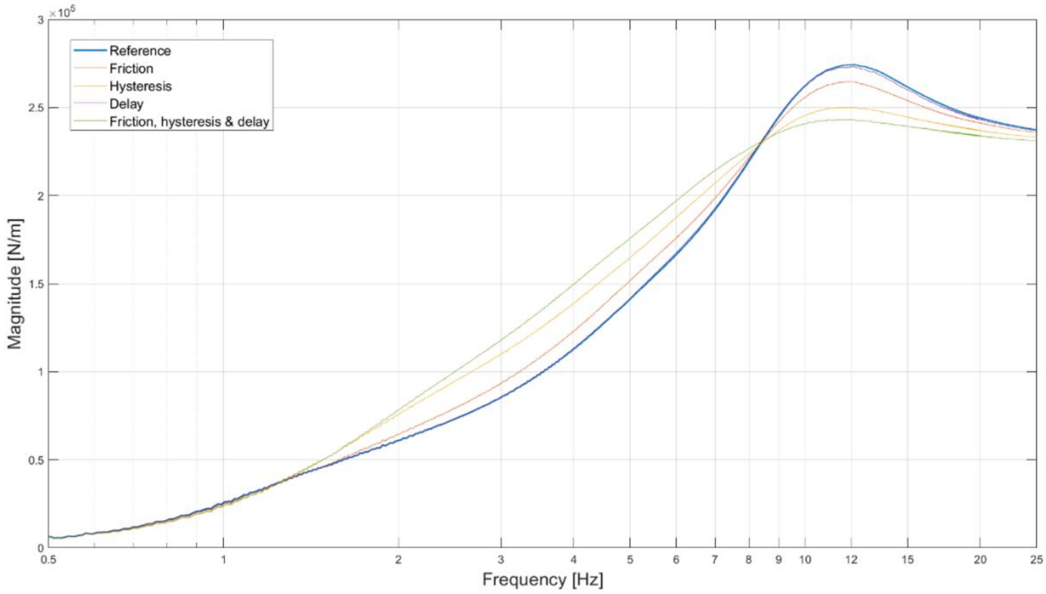

Fig. 20. Transfer functions between kinematic excitation and cumulative tire force for the PDD control strategy. PDD, power-driven damper

Tab. 10. Absolute values of transfer functions between road excitation and cumulative tire force (N*10^5/m) for PDD

	1st resonant freq. –1 Hz	–3 Hz	2nd resonant freq. –10 Hz	Max. tested freq. 25 Hz
Reference	0.42	0.81	2.68	2.34
Friction	0.42	0.91	2.57	2.34
Hysteresis	0.46	1.12	2.50	2.31
Delay 60 ms	0.42	0.81	2.65	2.35
Fric. + Hyst. + Delay 60 ms	0.46	1.20	2.40	2.29

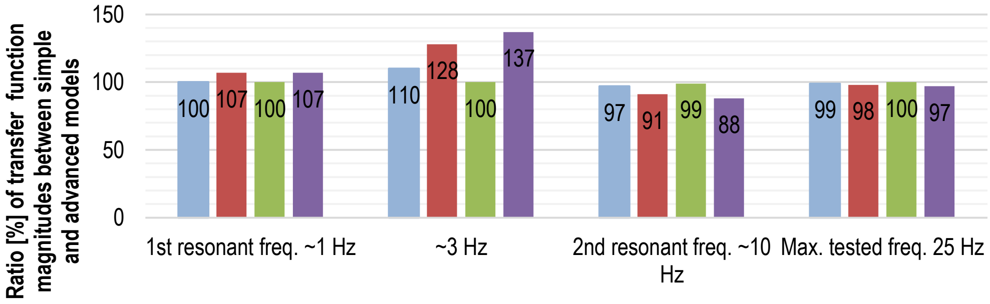

Fig. 21. Relative values of cumulative tire force for PDD. PDD, power-driven damper

Similarly to suspension deflection, the effects on cumulative tire strength are comparable for PDD and ADD strategies. The highest influence is caused by hysteresis, especially for low (1–3 Hz) frequencies, while friction and delay almost do not play a role when it comes to changing transfer function values.

Tab. 11 and Fig. 7 present absolute and relative (Fig. 23) values of transfer functions of sprung mass accelerations for the damper model with the PDD control strategy.

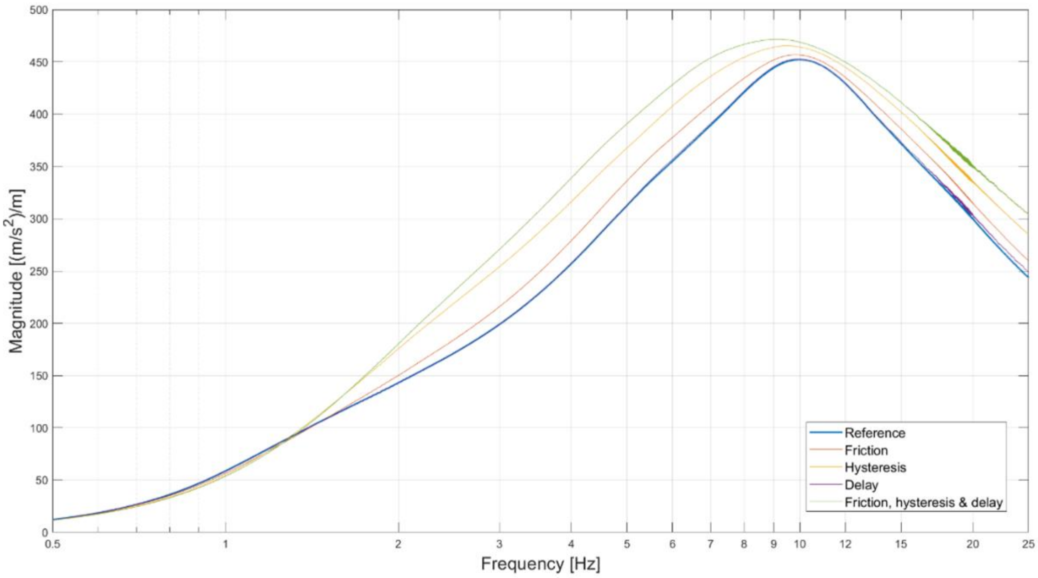

Fig. 22 Transfer functions between kinematic excitation and sprung mass acceleration for the PDD control strategy. PDD, power-driven damper

Tab. 11. Absolute values of transfer functions between road excitation and sprung mass acceleration ([m/s^2]/m) for PDD

	1st resonant freq. –1 Hz	–3 Hz	2nd resonant freq. –10 Hz	Max. tested freq. 25 Hz
Reference	60	200	450	248
Friction	58	215	452	260
Hysteresis	57	254	465	285
Delay 60 ms	60	200	442	250
Fric. + Hyst. + Delay 60 ms	56	270	470	305

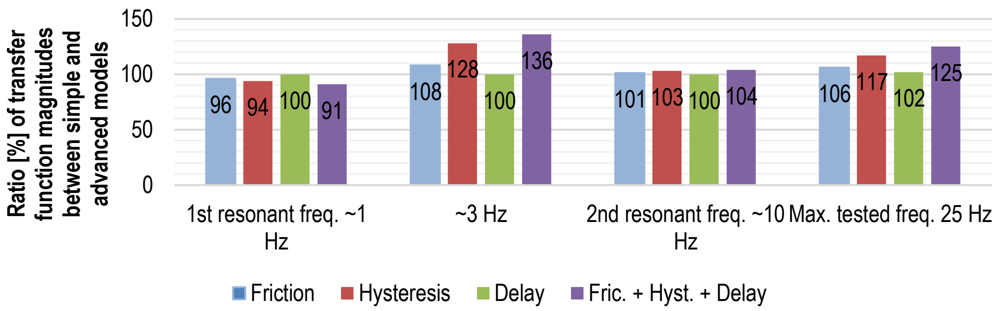

Fig. 23. Relative values of sprung mass accelerations for PDD. PDD, power-driven damper

Sprung mass accelerations are slightly less affected by the advanced damper model elements for the PDD strategy than those for ADD, but the highest influences can yet again be found for 3 Hz and 25 Hz. Hysteresis plays the largest role in transfer function values.

The overall impact of friction and hysteresis on the behaviour of the model controlled by the PDD strategy was similar to that of an ADD strategy, with hysteresis having relative gain slightly lower by around 12%–14% points for the first and second resonant frequencies, respectively, for suspension deflection. Cumulative tire force and sprung mass acceleration functions also have slightly lower relative gains for most frequencies, except for the 3–4 Hz range, where the relative gain is actually higher by around 10% points. Delay functions a bit differently; it has almost no impact on any of the dynamic responses. The cumulative effects of all three are as previously – mostly a sum of individual influences.

5. CONCLUSIONS

In case of simulation testing of the advanced nonlinear model of suspension (stiffness and damping suspension forces controlled by nonlinear strategies), transfer functions have to be calculated using response signals (deflection, cumulative tire force and sprung mass acceleration) obtained during simulations, as would be performed for real-life experiments. After preparing simulated signals in the form of time histories, frequency response evaluation can be made using the quotient of estimator of cross-power spectral density of kinematic excitation signals and suspension responses signals and estimator of power spectral density of kinematic excitation signals. This method can be implemented with the use of ready-to-use software functions used to estimate transfer functions, for example, MATLAB *tfestimate*, which was proved in the present research.

The obtained results allow for formulating the following conclusions about the influence of friction and hysteresis on transfer functions for suspension controlled with various control strategies:

SH: Friction and hysteresis increase the damping force, causing the magnitudes for road excitation to suspension deflection transfer function to decrease. It has a similar effect on transfer functions between road excitation and cumulative tire force, as well as sprung mass acceleration, albeit to a lesser degree.

The decrease in the transfer function of suspension deflection for only friction added is smaller for the range of 1 Hz (5%) than for the 10 Hz range (10%). Friction and hysteresis decrease transfer function magnitude, respectively, about 22% and 44%. In the range of frequencies between sprung mass and unsprang mass resonance (between 1 Hz and 10 Hz) and over unsprung mass resonance (about 25 Hz), the influence of friction and hysteresis is smaller – 3% and 12,% respectively.

The transfer function for tire forces was mostly influenced by hysteresis (for 3 Hz) and delay (for 10 Hz). The greatest increase in the transfer function was seen for the 3 Hz range, where implementation of all models friction, hysteresis and delay increased this function value by about 40% compared with the reference model; apart from that, for other frequencies, the change was no larger than 13%.

Actuation delay makes a little difference for low frequencies, but this influence starts growing once 1 Hz frequency is achieved, peaking around 3 Hz, when it starts to drop again. In addition to changing transfer function values, delay also seems to shift unsprung mass resonant frequency to lower by around 1 Hz.

ADD: The same effects of adding friction and hysteresis to the damper model as in SH case can be observed; they act as if damping force increased. Delay contribution, while acting in the same manner for unsprung mass resonant frequency, actually causes the model to behave like damping force was lower for the sprung mass resonant frequency. In general, compared with other modules, delay plays a much smaller role in the ADD control strategy, contributing to at most 5% change for resonant frequencies for either of analysed dynamic responses. Friction, while mostly having a similar extent of influence on transfer functions, reaches 10% of change in the value for sprung mass resonant frequency in the suspension deflection transfer function. The highest impact on all transfer functions is caused by hysteresis, exceeding 20% in case of tire force.

PDD: Delay has almost no effect on the transfer functions for responses in the PDD control strategy. The effects of friction and hysteresis once again mimic the increase in damping force. Also, similar to the ADD control strategy, hysteresis seems to play a much greater role for all analysed dynamic responses, with even higher relative changes – up to 30% for cumulative tire forces.

The main conclusion is that friction and hysteresis add extra force to the already existing damping force, thus acting as if its value increased for all analysed control strategies. Hysteresis seems to have higher impact than friction for all strategies, reaching up to a 30% relative change (PDD tire force), while friction reaches at most 14% (ADD, also tire force). SH and ADD strategies seem to be mildly affected by implementation of actuation delay, while the PDD strategy remains practically unchanged until 15 Hz, where slight changes (no more than 2% relative value) can be observed for some of the transfer functions. Its importance can potentially be higher, if the actuation delay is $>$60 ms.

The research shows the importance of including proposed modules in testing for both adjustable and passive dampers. The combined effects of all three modules often exceed a 40% relative value change, which might lead to greatly overestimated gains from implying such theoretically beneficial control strategies. The inclusion of friction and hysteresis in the equations defining the strategies, to offset their real-life effects on stiffening suspension, might yield positive results. As for the effects of actuation delay, its influence might be diminished by developing forward scanning sensors, which could prepare suspension for upcoming excitations in advance.

REFERENCES

1. Els PS, Theron NJ, Uys PE, Thoresson MJ. The ride comfort vs. handling compromise for off-road vehicles. J. Terramechanics, 2007;44(4):303–317.
2. Sturari C, Adjustable shock absorber, US2780321A, 1957.
3. Yue C. Control law designs for active suspensions in automotive vehicles, 1988.
4. Crosby MJ, Karnopp DC. The Active Damper—A New Concept for Shock and Vibration Control. Shock Vib. Bull. 1973;43:119–133
5. Emura J, Kakizaki S, Yamaoka F, Nakamura M. Development of the Semi-Active Suspension System Based on the Sky-Hook Damper Theory. J. Passeng. CARS. 1994;103:1110–1119.
6. Hong KS, Sohn HC, Hedrick JK. Modified Skyhook Control of Semi-Active Suspensions: A New Model, Gain Scheduling. and Hardware-in-the-Loop Tuning. J. Dyn. Syst. Meas. Control, 2002;124(1): 158–167.
7. Savaresi SM, Spelta C. Mixed Sky-Hook and ADD: Approaching the Filtering Limits of a Semi-Active Suspension. J. Dyn. Syst. Meas. Control. 2007;129(4):382–392
8. Ślaski G. Studium projektowania zawieszeń samochodowych o zmiennym tłumieniu. Poznań: Wydawnictwo Politechniki Poznańskiej, 2012.
9. Valášek M, Novák M, Šika Z, Vaculín O. Extended ground-hook – New concept of semi-active control of truck's suspension. Veh. Syst. Dyn. 1997;27(5-6):289–303.
10. Savaresi SM, Silani E, Bittanti S. Acceleration-Driven-Damper (ADD): An Optimal Control Algorithm For Comfort-Oriented Semiactive Suspensions. J. Dyn. Syst. Meas. Control. 2005;127(2):218–229
11. Savaresi SM, Poussot-Vassal C, Spelta C, Sename O, Dugard L. Semi-Active Suspension Control Design for Vehicles. 2010.
12. Morselli R, Zanasi R. Control of port Hamiltonian systems by dissipative devices and its application to improve the semi-active suspension behavior'. Mechatronics. 2008;18(7):364–369.
13. Gao H, Li Z, Sun W. Energy-Driven-Damper (EDD): Comfort-Oriented Semiactive Suspensions Optimized From an Energy Perspective. IEEE Trans. Control Syst. Technol. 2020;28(5): 2069–2076.
14. Dąbrowski K. Algorytmizacja adaptacyjnego sterowania tłumieniem zawieszenia samochodu dla uwzględnienia zmienności warunków eksploatacji. 2018.
15. Koo JH, Goncalves FD, Ahmadian M. A comprehensive analysis of the response time of MR dampers. Smart Mater. Struct., 2006;15(2).

DOI 10.2478/ama-2023-0001 acta mechanica et automatica, vol.17 no.1 (2023)
Special Issue "Machine Modeling and Simulations 2022"

16. Krauze P, Kasprzyk J. Driving safety improved with control of magnetorheological dampers in vehicle suspension. Appl. Sci. 2020;10(24):1–29
17. Kwok NM, Ha QP, Nguyen TH, Li J, Samali B. A novel hysteretic model for magnetorheological fluid dampers and parameter identification using particle swarm optimization. Sensor and Actuators, 2006;A 132:441-451.
18. Klockiewicz Z, Ślaski G, Dąbrowski K. Simulation investigation of individual bumps recognition possibilities for damping control and possible suspension performance improvements. 2020 12th Int. Sci. Conf. Automot. SAFETY, Automot. Saf. 2020.
19. Galanti F. Modelling, Simulation, and Control for a Skyhook suspension. 2013.

Zbyszko Klockiewicz: https://orcid.org/0000-0003-4353-550X

Grzegorz Ślaski: https://orcid.org/0000-0002-6011-6625

DOI 10.2478/ama-2023-0002

CHALLENGES IN THE DESIGN OF A NEW CENTRIFUGAL FAN WITH VARIABLE IMPELLER GEOMETRY

Piotr ODYJAS*, Jędrzej WIĘCKOWSKI*, Damian PIETRUSIAK*, Przemyslaw MOCZKO*

*Faculty of Mechanical Engineering, Department of Machine Design and Research, Wroclaw University of Science and Technology, ul. Łukasiewicza 7/9, 50-371 Wrocław, Poland

piotr.odyjas@pwr.edu.pl, jedrzej.wieckowski@pwr.edi.pl, damian.pietrusiak@pwr.edu.pl, przemyslaw.moczko@pwr.edu.pl

received 1 July 2022, revised 27 September 2022, accepted 4 October 2022

Abstract: This article presents a description of design work for newly created centrifugal fans. This was done based on the example of an innovative solution that uses a change in impeller geometry. In the described solution, this is achieved by shortening and lengthening the impeller blades. The development of a technical solution with such properties requires a change of approach in the design process compared with classic solutions. Therefore, the following text describes this process from the concept stage to demonstrator tests. The principle of operation of such a solution is presented and the assumptions made based on analytical calculations are also described. The text also shows a 3D model of the centrifugal fan with variable impeller geometry, made with the help of computer aided design (CAD) tools. In the further part, numerical calculations were made on its basis. The finite element method (FEM) calculation made it possible to verify the structural strength of the project and its modal properties as well as to verify flow parameters, thanks to the use of computational fluid dynamics (CFD) calculations. The next step describes the procedure for testing centrifugal fans with variable rotor geometry, which is different from that of fans without this feature. The next part presents the results of research from the tests carried out.

Key words: centrifugal fan, adjustable fan blade, efficiency, field tests

1. INTRODUCTION

The current trend to use more and more efficient machines and environmentally friendly ones push for the development of numerous technological devices. A similar situation applies to rotary machines, which include, among others, fans. The principle of operation and construction of fans has not undergone significant changes for years. Truly, fans made of light or artificial metals are currently appearing on the market, but the principle of their work is still the same.

The problem of fans operating in changing conditions seems to be still a challenging task for fan users and designers. Basically, the fan is applied to installation according to one, nominal working point in which the fan should have the best possible efficiency. Unfortunately in many cases, the fan is used in installations where changes in the flow parameters take place in time. In such cases, it is expected to ensure that fan can be operated still with relatively high efficiency. Generally, there are two main solutions applied in the case of centrifugal fans that need to be regulated. These are regulated by a change of the rotational velocity with the use of frequency inverter and radial vane inlet control (RVIC) system, where the change of the fan characteristic occurs due to a swirl formed in the fan inlet duct. The first solution generally ensures the best efficiency of the fan with the regulation in a wide range [1–6].

Other solutions that were proposed within years are less efficient or more demanding from the point of view of difficulties in their design or manufacturing. In the first group, there are such solutions as fan regulation with the use of throttling devices (especially in outlet ducts) and fan regulation with the use of a variable geometry system. These are the mainly used two control systems. The first one is the regulation by change of the blade width, which causes a shift of the fan pressure curve in direction of lower (narrower impeller width) or higher (wider impeller width) flow rate values. The second solution is based on the change of the trailing edge angle of the blade. It is realised by rotation of the movable blade end in upward or downward directions. Definitely, as shown by currently gathered knowledge, the first solution is much less efficient than the second one [1–9].

In contrast to both mentioned solutions with regulation method via variable geometry, we proposed a completely new idea of centrifugal fan regulation [10]. This solution is based on the fact that the change in the blade length causes a change in the amount of energy inverted within the impeller. The lengthening or shortening of the blade length also causes a change in the impeller outlet diameter D2 and a change of the velocity triangle on the trailing edge. It leads to a change in the flow parameters and the characteristics of the centrifugal fan. This simple idea is presented in Fig. 1.

In this article, we describe the designing process of this new fan from its conception to manufacturing and testing of the prototype. This work widens knowledge about regulation methods, their drawbacks and possible application.

2. ANALYTICAL CALCULATIONS

In the first step, analytical calculations have been used to design the geometry of the basic fan. This basic geometry was then used to find the geometry of the fan with the variable geometry. The variability of the basic blade trailing edge diameter D2, as well as blade length *l*, has been assumed as ±10% of deviations from their basic values. On this basis, the design and calculation of the steering mechanism for the adjustment of the blade during movement or standstill were made. In this case, computational methods from the theory of the construction of machines and mechanisms were used. The following subsections present the results of each step of the calculation.

2.1. Evaluation of the basic geometry of the centrifugal fan

In the first stages of the project, it was assumed that the designed centrifugal fan at its basic operating point had a total pressure rise of $\Delta pt = 2500$ Pa and volumetric flow rate V = 2.78 m^3/s, with the nominal rotational speed $n = 1500$ rpm. On this basis, the preliminary geometry of the new fan has been designed with the use of analytical methods described in the literature [3–6]. As a result, following geometrical data of the impeller have been defined (Fig. 1):

- inlet bore diameter D0 = 384.5 mm;
- blade inlet diameter D1 = D0;
- blade outer diameter D2 = 810 mm;
- diameter of disc and cover of the impeller D22 = 820 mm;
- the width of the blade on the diameter D1: b1 = 172 mm;
- the width of the blade on the diameter D2: b2 = 123 mm;
- blade leading edge angle: ®1 = 24°;
- trailing edge angle: ®2 = 29°;
- number of blades: $z = 12$.

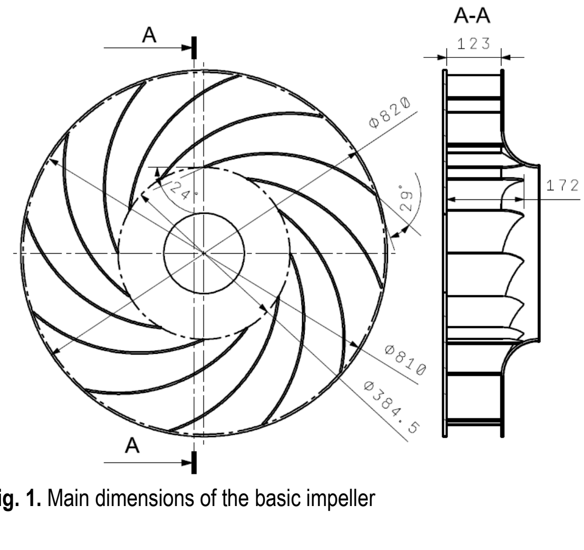

Fig. 1. Main dimensions of the basic impeller

The length of the blade *l* in the basic impeller is equal to 410.33 mm. Assuming that the change of the D2 diameter in the newly designed fan should be in the range of ±10%, it means that the minimal D2min diameter is equal to 729 mm and the maximal D2max diameter is equal to 891 mm. Then, resultant blade lengths in minimal and maximal positions will be $l_{min} = 369.30$ mm and $l_{max} = 451.36$ mm, respectively. The geometry of the impeller with a blade in minimal, basic (middle) and maximal positions is shown in Figs 2–4. Apart from the calculations of the impeller, dimensions of the volute casing have been defined. The geometrical model of this casing is shown in Fig. 5. The fan inlet diameter is 450 mm and the outlet hole from the volute is 355 mm x 450 mm. The width of the volute casing is equal to 355 mm.

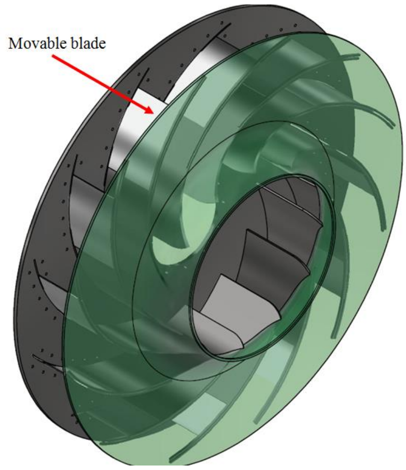

Fig. 2. Geometrical model of the centrifugal fan impeller with the movable blade in the basic (middle) position

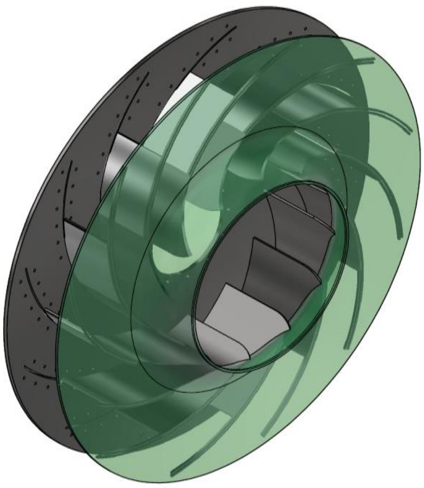

Fig. 3. Geometrical model of the centrifugal fan impeller with the movable blade in minimal position

Fig. 4. Geometrical model of the centrifugal fan impeller with the movable blade in maximal position

DOI 10.2478/ama-2023-0002

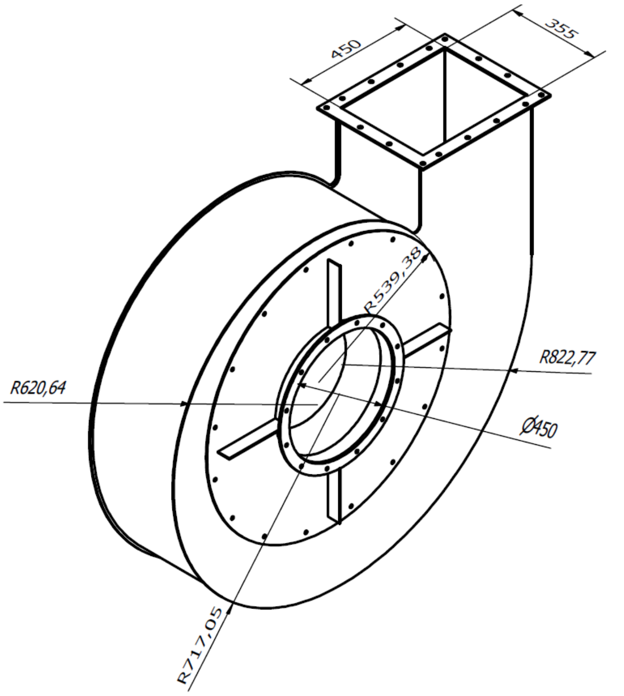

Fig. 5. Geometrical model of the designed centrifugal fan volute casing with main dimensions

2.2. Calculations and description of the steering mechanism

The calculations of the forces acting on the main elements of the steering system were carried out based on the relevant literature [11, 12]. First, the maximum forces acting on the blade supports (pos. 5 and 6, Fig. 6) were calculated, derived from the centrifugal force related to the mass of the movable part of the blade (pos. 2, Fig. 6). The mechanism in the final version is shown in Figs 6 and 7. The translation of the movable blade (pos. 2, Fig. 6) is executed, along rails (pos. 5 and 6, Fig. 6), by the tie rod (pos. 3, Fig. 6). The movement of the strand is possible as a result of the rotary motion of the steering disc (item 4, Fig. 6). The movement of the steering disk is relative to the rotating shaft and hub of the fan. The control disc is rotated (in relation to the shaft) by the link (item 8, Fig. 7), the movement of which is generated by the positive coupling of the link with the adjusting drum (item 9, Fig. 7). The positive connection of the link with the drum is realised through the slots of the helical track, which in fact enables the axial movement of the drum along the shaft to be changed to the angular movement of the link. The axial movement of the drum is ensured by a screw drive independent of the fan drive system. The position of the fan blades can be controlled during operation and at a standstill position of the fan. The designed solution of the moving blade system has special handles for each blade (pos. 7, Fig. 6). This handle is also a slider on 2D rails (pos. 6, Fig. 6).

The performed FEM calculations allowed for precise shaping of the blade made of an aluminum alloy with a thickness of 2 mm. The shape of the blade in the final solution is shown in Fig. 8. Its weight is equal to 213 g. Based on this mass, the forces acting on the tie rod and other elements were calculated, assuming that the friction coefficient between the sliding elements was relatively high and amounted to 0.5. Finally, the axial force that must be applied on the drum to move the blade from the maximum position was calculated and it is 12 kN.

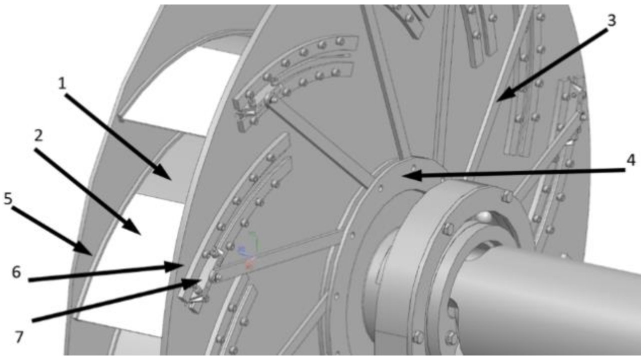

Fig. 6. Impeller geometry with tie rods mechanism—parts mounted to the impeller

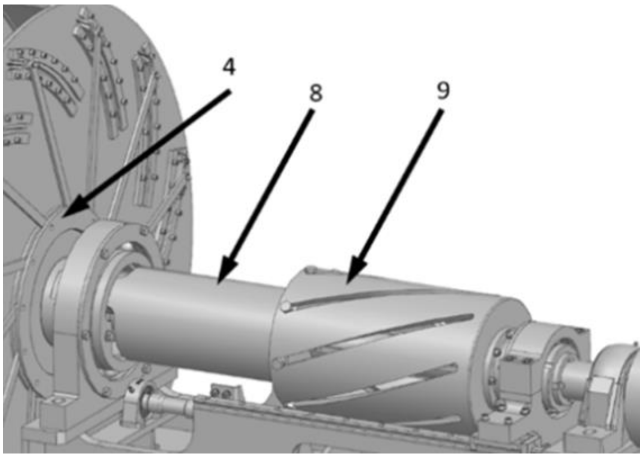

Fig. 7. Impeller geometry with tie rods mechanism—parts mounted on the drive shaft

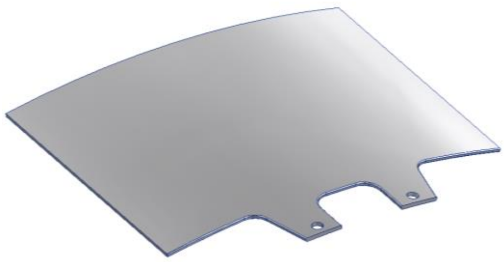

Fig. 8. Final form of the geometrical shape of the movable blade

3. NUMERICAL CALCULATIONS

CAD tools are currently one of the most popular solutions for designing process support. They allow for the integration of work on the shape of the developed solution with strength calculations. In the case of technical devices responsible for the transport of liquids and gases, flow calculations are also important. They are also currently being made with a CAD tool. The following subsections present the effects of individual verification stages of the project.

3.1. Geometrical model

Based on the preliminary choice of the geometry type and dimensions, with further calculations of the mechanism done, the

3D geometrical model of the fan was prepared. The whole model of the designed fan is shown in Fig. 9. In Figs 5–8, the model of the volute casing, impeller with adjusting mechanism and the final shape of the movable blade are shown. This model was used to check if there are any collisions between moving parts in the model to prevent serious problems after manufacturing the fan. The main parts of the fan that are subject to high inertia forces (rotating parts) and resultant forces in the mechanism have been optimised with the use of FE analysis. A simplified model of the impeller was also used for preliminary CFD calculations to calculate fan performance curves. It was needed to estimate the range of operation of the newly designed fan.

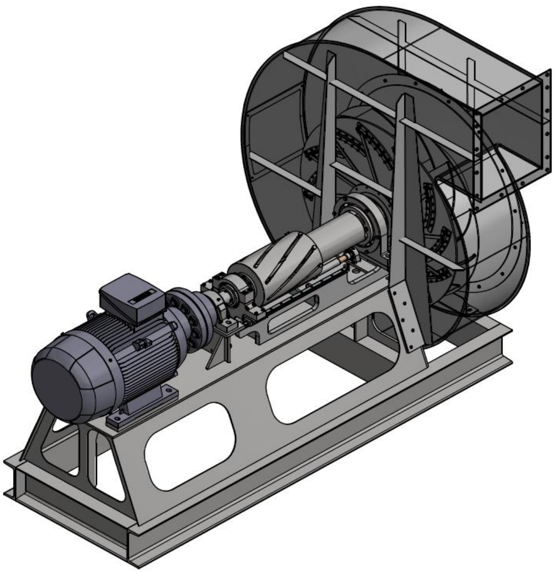

Fig. 9. 3-D geometrical model of the whole fan designed during the project

Ultimately, based on the geometrical mode and results of numerical simulations, technical drawings of the fan have been prepared to enable manufacturing of the fan prototype with a new regulation method.

3.2. FEM simulations

Based on this step, the calculation of the most vulnerable components of the fan with the use of FE analysis has been carried out. The main intention was to check if any of these components are sufficiently resistant to loads acting during fan and mechanism operation. These components were any rotating parts (impeller parts and others from adjusting mechanism) and other components of the fan that were subject to load. Due to the quite complicated mechanism of adjusting the position of the movable blades, the calculations to ascertain the strength were carried out independently for the individual components of the fan. The loads acting on these elements were determined based on analytical calculations, taking into account the kinematics of the system and the maximum operational loads (rotational speed). This approach is used to limit the size of the analysis by limiting the size of numerical models, while correctly refining the finite element mesh. In the case of modal analysis, FEM calculations were carried out for the entire fan rotor assembly to correctly identify the frequency and mode of natural vibrations. On the other hand, the bolted connections used in the fan were carried out analytically.

In case when the strength of fan components was not sufficient, the geometry of that component has been optimised. If modifications of the geometry did not succeed, more rigid materials have been chosen for such components. That was especially visible in the case of the blade, adjusting drum and connector.

In the first step, with the use of the geometrical model, the discrete model of the calculated components has been prepared according to the best practices [13–15]. These were mostly solid models to ensure a more detailed assessment. After that proper boundary conditions have been applied and an enabled numerical simulation was run. Exemplary mesh generated on the calculated component are shown in Figs 10–12. In the case of the adjusting drum, the mesh size was about 3 mm, and the numbers of TETRA6 elements and nodes in the model were equal to 377,629 and 215,431, respectively. In the case of the connector mixed with TETRA6 and HEXA20, the mesh was used. The basic size of the element was 4 mm with local refinement to 2 mm, and the total number of elements and nodes in the model was equal to 122,840 and 216,324, respectively. In the case of the movable blade with holder and tie rod, basic mixed TETRA6 and HEXA20 mesh was used. The basic size of elements was 3 mm with local refinement to 0.5 mm. The total number of elements and nodes, in this case, was equal to 128,957 and 221,964, respectively. The results of the calculation of these components are shown in Figs 13–15. The input basic material adopted for the structural elements of the fan (impeller, shaft, blade control mechanism) was steel S355 with the yield point Re = 355 MPa. Analytical calculations of the system loads showed that the mass of the moving part of the blade has a significant influence on the stress effort of the control system components. Therefore, it was assumed that the movable blade of the impeller would be made of a lightweight material, an aluminium alloy.

Based on the strength calculations, the above assumptions were verified. In the case of the adjusting drum, the local high stress was found with a maximum value of 330 MPa. This gave a safety factor of $x = 1.08$, which was considered too low. On this basis, it was found that these elements should be made of steel with a higher yield point and higher safety factors. In the case of the movable blade, the local maximum stress concentrations were obtained at the level of 298 MPa. The target material was the alloy EN AW-7075-T6 with a yield strength of Re-500 MPa, which gave the safety factor $x = 1.68$.

Fig. 10. Mesh generated on the geometrical model of the adjusting drum

DOI 10.2478/ama-2023-0002

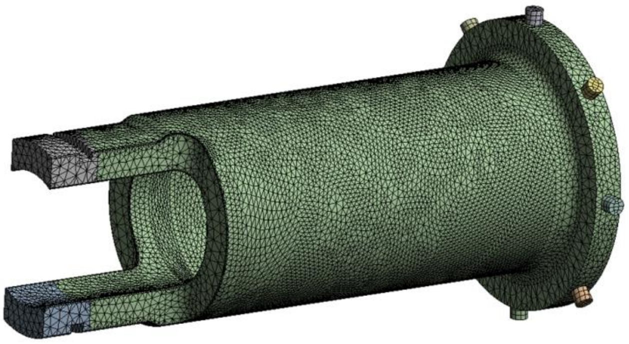

Fig. 11. Mesh generated on the geometrical model of the connector

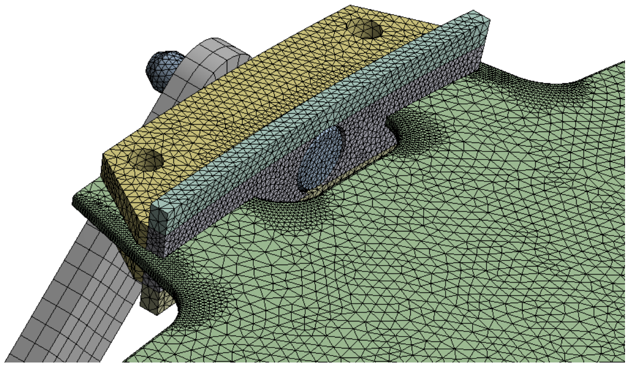

Fig. 12. Mesh generated on the geometrical model of one of the most critical assemblies in the model (movable blade connected with holder and tie rod)

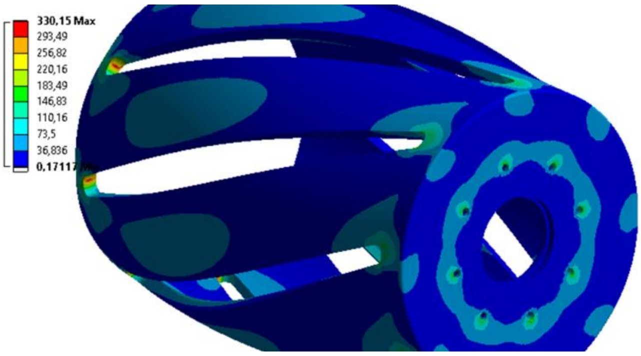

Fig. 13. Von-Mises stress distribution (in MPa) along the adjusting drum

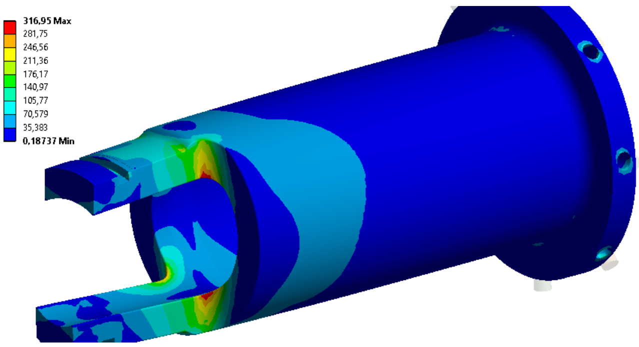

Fig. 14. Von-Mises stress distribution (in MPa) along the connector

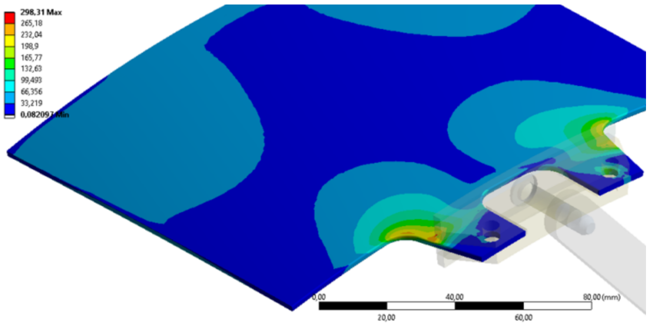

Fig. 15. Von-Mises stress distribution (in MPa) along the movable blade

3.3. CFD simulations

Numerical analysis with the use of CFD flow measurement has been realised in the early stage of the fan design process. The goal of this analysis was to preliminary evaluate fan performance curves in at least a few different positions of the movable blade. It was realised for the minimal, maximal and basic (middle) positions of the blade. In the first step, a geometrical model of the fan with the impeller in three positions was prepared. Geometrical models were simplified and in each case, the blade was without division for the fixed and movable parts. What is more, the impeller shroud and impeller hub were cut to the blade's trailing edge. The flow domain was divided into three parts: inlet zone, impeller rotating zone and outlet zone (fan volute casing zone). The calculation was carried out with the use of the 'frozen rotor approach', where terms representing the effect of the centrifugal force during impeller rotation with a rotational speed equal to $n = 1500$ rpm are taken into consideration within the impeller zone. Each domain was meshed with the use of a structural grid and the total number of elements was about five million, depending on the blade position and impeller size (grid generated in case of blade middle position is shown in Figs 16–18). To use proper turbulence model, boundary layer with first cell y+ value about 30 was created [22–24]. It means that the first cell thickness in the case of each domain was as follows:

– inlet: 0.86 mm,
– impeller: 0.63 mm,
– volute: 0.86 mm.

The growth ratio of the cells in the direction normal to the wall was in the range of 1.2–1.25.

To get the whole set of fan performance curves, each model was calculated in at least five different working points. The CFD calculations were run using a turbulence two equations model k-ω (SST), following the best practices for CFD calculation of turbomachinery equipment [25–29]. The inlet boundary condition was defined as the velocity inlet to the required volumetric flow rate. The outlet boundary condition was chosen as a pressure outlet with specified static pressure equal to 0. Additionally, turbulence intensity in the inlet and outlet sections has been chosen as 5% with the proper value of hydraulic diameter. Since maximal pressure rise was estimated at about 3500 Pa, each simulation was run as incompressible flow. The density of air in the model was defined as 1.2 kg/m³, following the standard requirements.

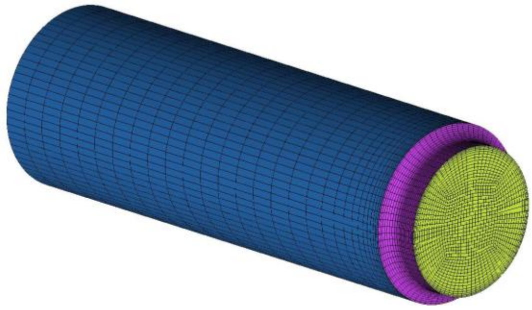

Fig. 16. CFD mesh generated on the fan inlet duct

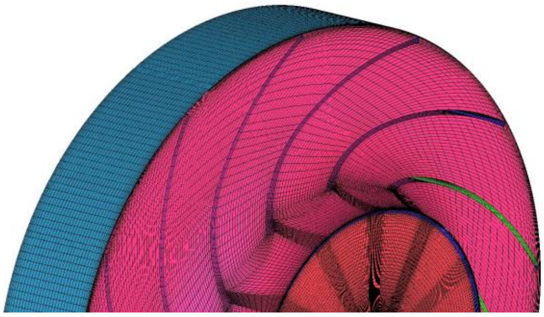

Fig. 17. CFD mesh generated on the impeller with the blade in middle position

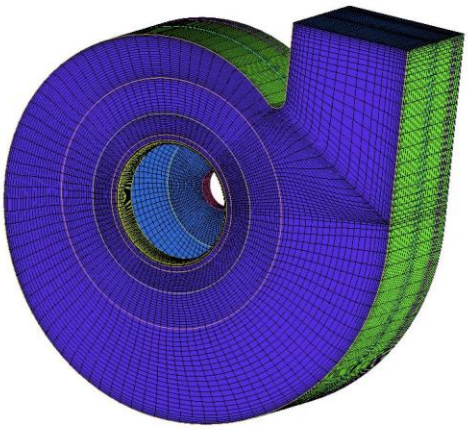

Fig. 18. CFD mesh generated on the volute casing

Any simulations were conducted until the most important flow parameters pressure and flow rate converged. As a result, a set of fan performance curves has been received (Fig. 19). These are the total pressure rise curve, shaft efficiency curve and shaft power curve in the function of volumetric flow rate. It must be underlined that each simulation was conducted with a simplified model of the fan with the movable blade. The movable and fixed blades were connected and the whole blade was only shortened or lengthened in case of minimal or maximal positions of the movable blade. This was because of the preliminary stage of the project. The main purpose of this simulation was to estimate the fan output in the expected operating range. This made it possible to define what to expect in the scope of regulation and, second, to define the energy requirements. On this basis, an appropriate electric motor was selected. At this early stage of the project, full validation of the simulations performed could not be performed due to the inability to perform tests on the prototype. However, during the simulations, the best experience during the preparation of the CFD fan model was maintained, and all the rules related to, for example, the quality and type of the mesh of the elements used were adhered to. The results of experimental tests on the prototype carried out in the final stage of the works, confirmed the results obtained from CFD simulation tests.

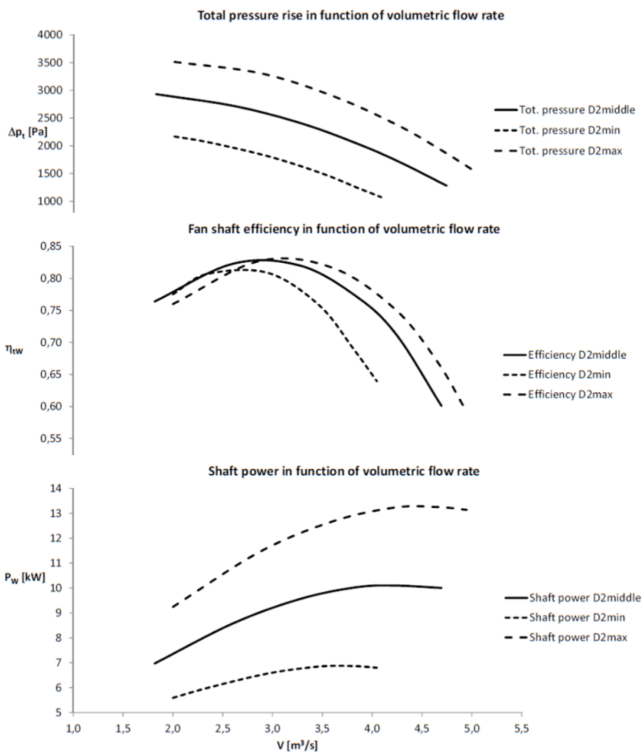

Fig. 19. Fan performance curves of the designed fan in minimal, basic (middle) and maximal movable blade positions get from CFD simulations

3.4. Modal analysis

Modal analysis is a very important step during the designing of the new rotating machinery components. During the fan operation, there are two main excitation frequencies to be considered in the dynamic safety analysis. The first frequency is the result of the rotation velocity and in the case of rotation with rotational speed 1500 rpm is equal to f_{rot} = 25 Hz. The second frequency is blade passing frequency and is equal to f_{BPF} = 300 Hz in the case of the designed fan since it is equipped with 12 blades. Modal analysis with the use of numerical techniques (FE analysis) should be performed before manufacturing the fan. Such an approach gives a chance to prevent high vibration levels and noise emissions during fan operation. Thanks to this, the higher durability of the most important rotating component as well as the bearing can be achieved [3, 4, 17–21].

In the case of a designed fan, which can be operated in different configurations of the movable blade and can also be adjusted with the use of a frequency inverter, the modal analysis can be used as a tool to find the most dangerous ranges of frequencies. Then these values can be used to prepare guidelines for the user to prevent the operation of the fan within these ranges. The designed fan needs to be verified with the blade at least in a few different blade positions between maximal and

DOI 10.2478/ama-2023-0002

minimal ones. What is more, modal analysis of a single component seems to be not a sufficient source of information about the behaviour of such a component when it works in connection with others. Because of that, a simulation of the main rotating components with the blade in minimal, maximal and middle (basic) positions has been conducted. Existing contacts between connected elements have been simplified and replaced by rigid or beam elements to ensure interaction between these components. The geometrical mixed surface and solid model of the components calculated during modal analysis are shown in Fig. 20. There is an impeller with a movable blade in a maximal position. Based on this model, a solid-shell discrete model has been prepared. What is more, the shaft was simplified and modelled with the use of a beam element. The discrete model is shown in Fig. 21. All simulations were carried out with a pre-stressed model (loads due to rotational movement with a speed of 1500 rpm and gravity forces). As a result, natural frequencies and mode shapes have been identified. These results are summarised in Table 1 and the exemplary mode shapes are shown in Figs 22–29. Beyond normal mode shapes of the impeller (torsion and bending modes), there are also visible shapes connected with the steering mechanism, especially with the tie rod since they are vulnerable to vibration because of their small bending stiffness. Many of the natural frequencies (about 300 Hz) are close to the blade passing frequency in case of impeller movement with a rotational speed of 1500 rpm. Mostly these shapes are bending of the tie rod, but not only.

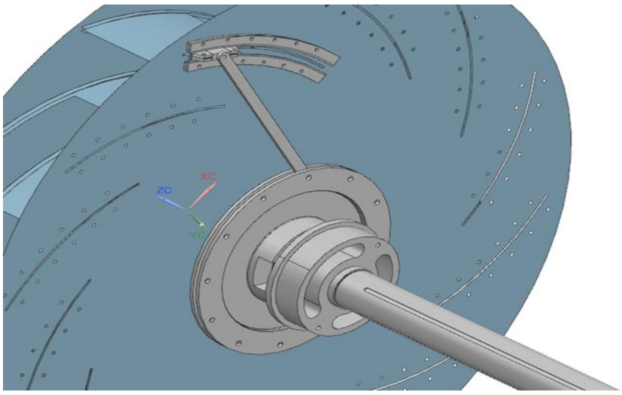

Fig. 20. Geometrical model of the impeller with adjusting mechanism and shaft with the blade in the maximal position

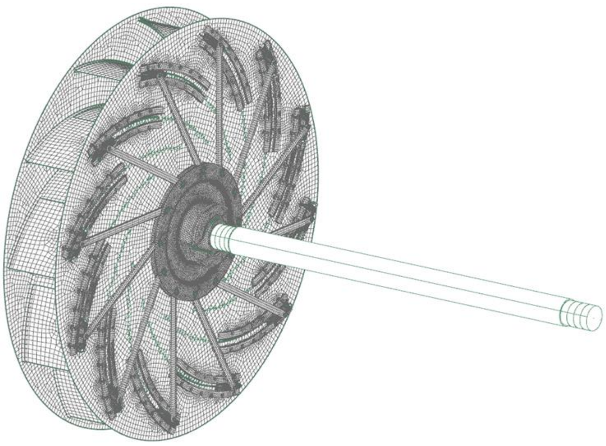

Fig. 21. Discrete model of the impeller with adjusting mechanism and shaft

Tab. 1. The results of the modal analysis of the impeller with the most important components of the regulation mechanism with the blade in minimal, maximal and basic (middle) positions

No of consecutive natural frequencies	Natural frequency with respect to the position of the movable blade (Hz)		
	Minimal	Basic (middle)	Maximal
1	29.78	29.72	29.7
2	40.88	40.42	40.7
3	40.89	40.43	40.71
4	80.45	79.82	80.41
5	218.64	246.53	258.62
6	219.16	246.71	258.74
7	243.56	256.36	261.28
8	247.46	256.79	261.45
9	247.98	282.54	288.41
10	268.59	299.45	301.85
11	268.89	300.62	302.39
12	272.22	301.01	306.46
13	273.02	301.17	308.41
14	287.98	301.33	308.44
15	293.28	305.89	309.8
16	293.54	306.05	309.98
17	306.63	307.6	312.53
18	307.57	307.62	312.55
19	307.71	308.96	313.68
20	308.13	308.98	313.79
21	308.40	309.32	314.17
22	309.97	326.3	358.85
23	309.99	326.78	359.18
24	310.75	330.89	413.46
25	310.76	333.42	413.73

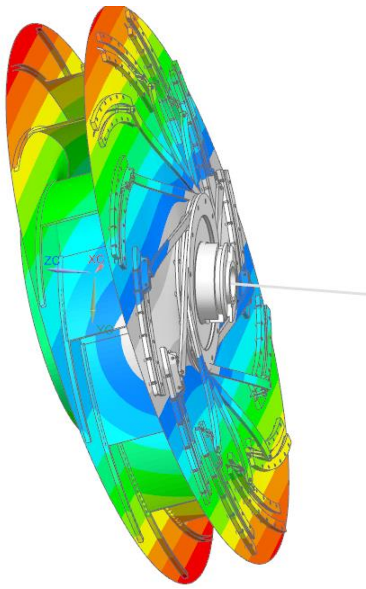

Fig. 22. Exemplary mode shape of the impeller with the blade in minimal position (2nd bending mode shape, natural frequency 40.88 Hz)

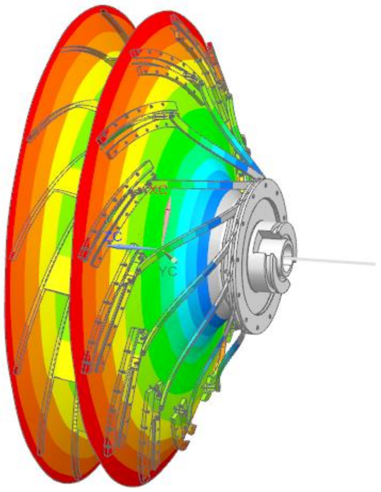

Fig. 23. Exemplary mode shape of the impeller with the blade in minimal position (4th bending mode shape, natural frequency 80.45 Hz)

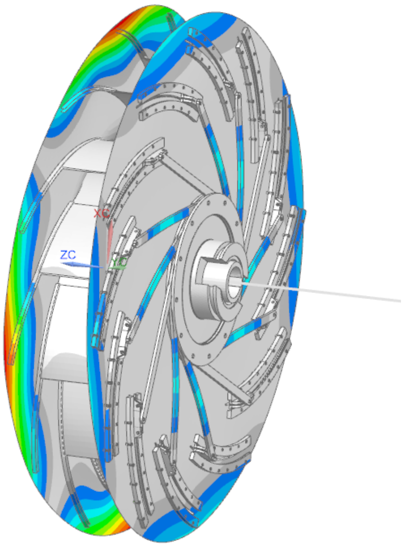

Fig. 24. Exemplary mode shape of the impeller with the blade in minimal position (15th bending mode shape, natural frequency 293.28 Hz)

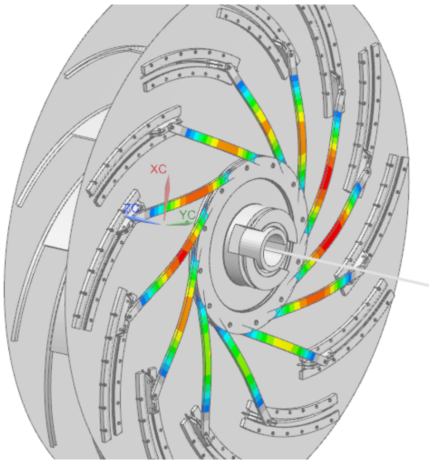

Fig. 25. Exemplary mode shape of the impeller with the blade in minimal position (17th bending mode shape, natural frequency 306.63 Hz)

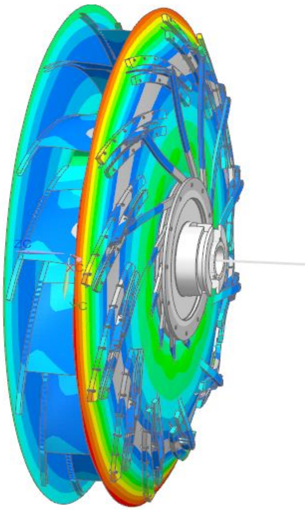

Fig. 26. Exemplary mode shape of the impeller with the blade in basic (middle) position (9th bending mode shape, natural frequency 282.54 Hz)

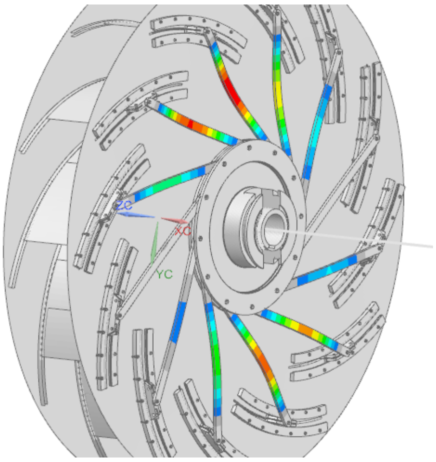

Fig. 27. Exemplary mode shape of the impeller with the blade in basic (middle) position (11th bending mode shape, natural frequency 300.62 Hz)

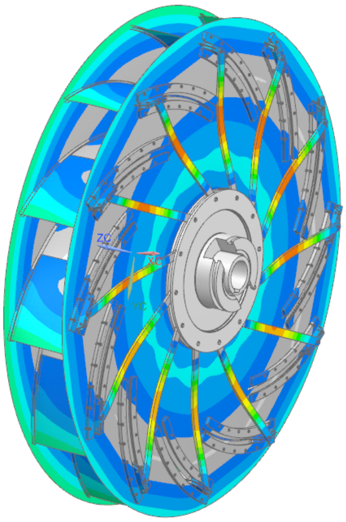

Fig. 28. Exemplary mode shape of the impeller with the blade in maximal position (9th bending mode shape, natural frequency 288.41 Hz)

DOI 10.2478/ama-2023-0002

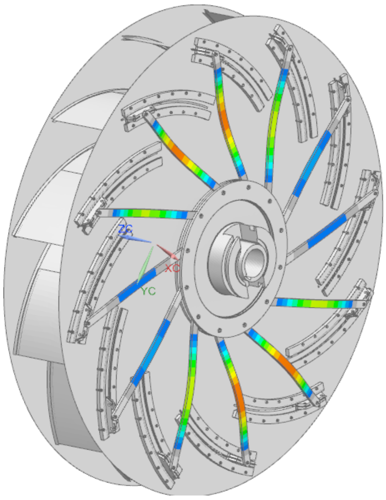

Fig. 29. Exemplary mode shape of the impeller with the blade in maximal position (10th bending mode shape, natural frequency 301.85 Hz)

4. FINAL PROJECT

The end result after the analytical and numerical calculations is the preparation of technical documentation of the prototype. Then, on this basis, its production is commissioned for further testing. Figs 30 and 31 show the developed centrifugal fan with variable impeller geometry. The change occurs by shortening and lengthening the moving part of the blade (pos. 1). This movement is carried out by using a specially designed mechanism (pos. 2), which changes the translational movement into a rotational movement.

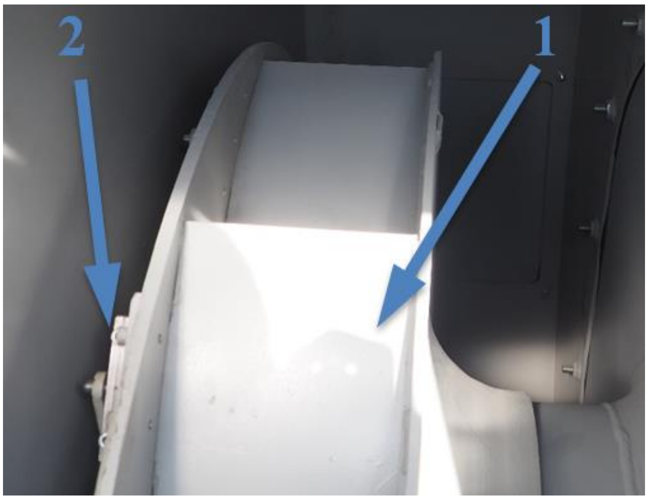

Fig. 30. Prototype of the centrifugal fan impeller with adjusting mechanism

The developed form of the finished solution allows you to change the geometry during the operation of the fan. This is possible because of the forcing mechanism (pos. 2). It has been designed to allow free rotation of the fan shaft inside the mechanism. Without this feature, it would be impossible to shorten and lengthen the blade during operation. At this stage of the project, it was necessary to verify the correctness of the work of the entire mechanism regulating the geometry of the impeller. This is a necessary step before proceeding with the field tests, which are described in the next section. The finished demonstrator is shown in Fig. 32.

Fig. 31. Steering mechanism forcing a change in rotor geometry on the prototype impeller

Fig. 32. Prototype of the centrifugal fan with variable impeller geometry

5. FIELD TEST

Test on the real object was aimed at verification of the performance and vibration level of the prototype fan. In the following subsections, the results of these measurements are summarised.

5.1. Fan performance testing

Fan performance curves measured during testing on standardised airways are used to evaluate the real capabilities of the fan. For example, based on these curves, the fan selection process is into the expected application.

A test stand to measure fan performance curves has been prepared following suitable standards [30]. It was a standard test method with an inlet-side test duct [30]. The whole stand during

sciendo
DOI 10.2478/ama-2023-0002
acta mechanica et automatica, vol.17 no.1 (2023)
Special Issue "Machine Modeling and Simulations 2022"

measurements is shown in Fig. 33. The fact that between minimal and maximal movable blade positions, there is an infinite number of possible blade positions, measurements have been conducted only in five different positions. These are minimal, maximal and three others with an interval equal to 25% of the whole blade path. These positions have been named as pos. 0% (minimal), pos. 25% and pos. 50% (basic-middle), pos. 75% and pos. 100% (maximal). To get the data that required to draw fan performance curves according to the required standard, measurements were conducted in five different working points for each blade position. It was realised by throttling of the fan in the inlet duct. The received results showed as fan performance curves are presented in Fig. 34. These are curves of total pressure rise, shaft efficiency and shaft power in function of volumetric flow rate. The received results show that the newly designed fan has a wider range of operation with efficiency >60%. The range of the pressure regulation in the case of constant volume flow rate is about 30%, When we consider regulation along exemplary resistance curve shown in Fig. 34, fan conventional regulation range is equal to 0.145 [1, 2]. The minimal efficiency in this case is for the lowest blade position and it is about 65%. The highest efficiency is for 75% opening of the movable blade (pos. 75%) and it is about 81%.

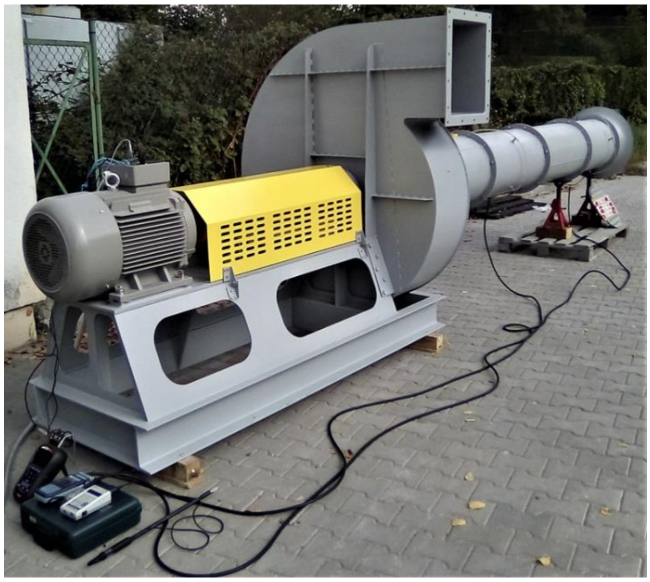

Fig. 33. Standardised airway system during measurements of the prototype fan

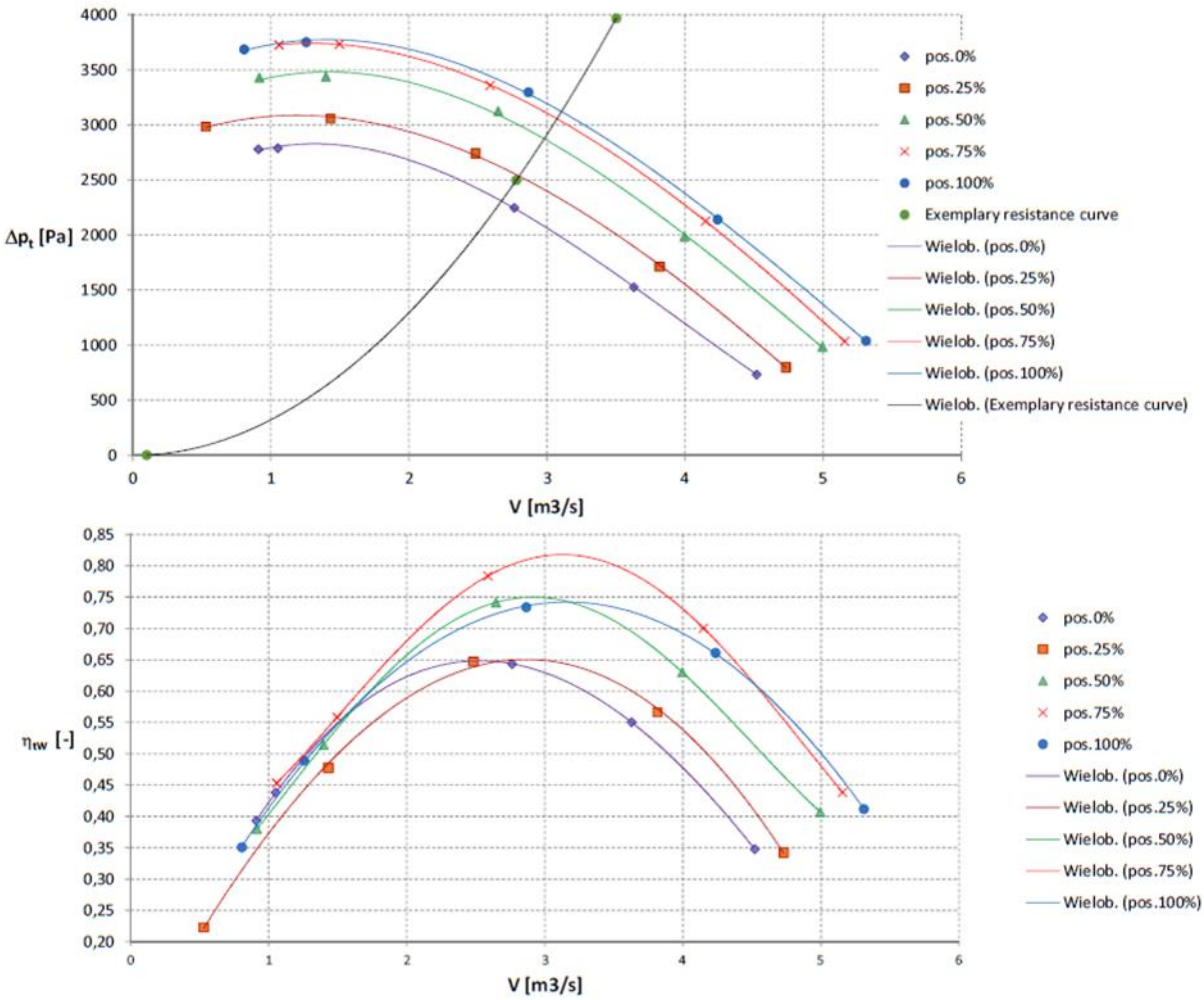

DOI 10.2478/ama-2023-0002

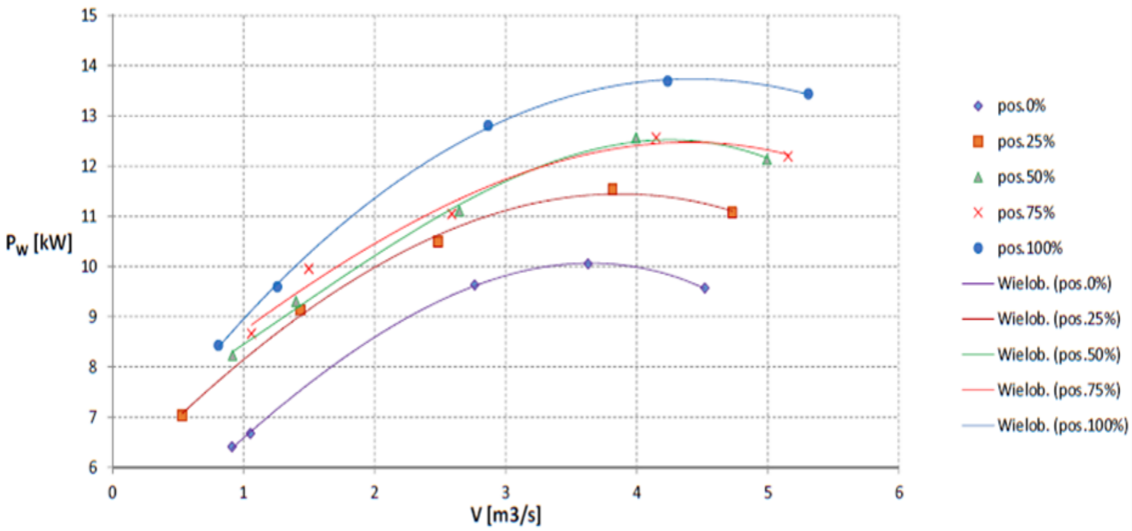

Fig. 34. Fan performance curves of the designed fan measured with the use of standardised airways. These are curves measured in 5 different positions between minimal and maximal with an interval of 25%

5.2. Vibration testing

The vibration tests were taken during regular operation with 1500 rpm.

The reference of the rotating unit rotational velocity was measured by the tachometer (laser sensor) on channel 1 (C1). The accelerometers were placed on the fixed bearing along the shaft axis (channel 2 – C2), on the fixed bearing radial horizontal direction (channel 3 – C3), on the fixed bearing radial vertical direction (channel 4 – C4), on the fan housing back wall (channel 5 – C5) and the fan housing side/cylindrical wall (channel 6 – C6). The placement of the sensor is presented in Fig. 35. The acceleration spectra are presented in Fig. 36. The vibration energy represented by the RMS factor is listed in Table 2.

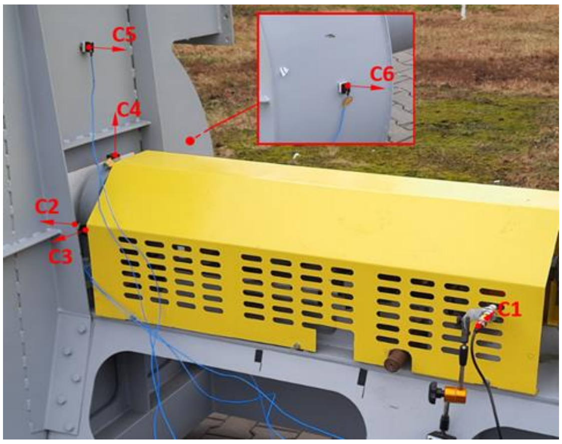

Fig. 35. Placement of the sensors during vibrations tests

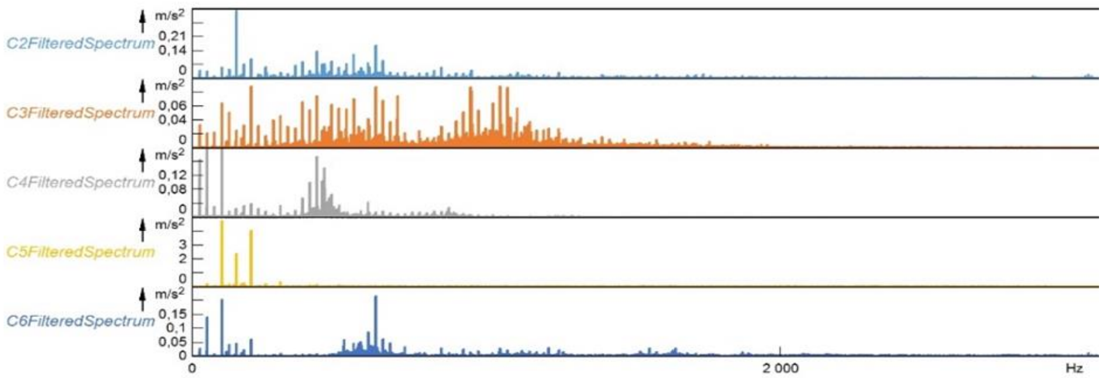

Fig. 36. Vibrations spectra

Tab. 2. Energy of the vibrations

C2	C3	C4	C5	C6
0.49	0.48	0.39	4.95	0.58

One can observe that the harmonics of the rotational velocity (25 Hz) are clearly visible at all measurement channels. As identified in the numerical modal analysis and analytical calculations, the two main ranges of possible resonances are placed at 25 Hz and 300 Hz. The analysis of the measured spectra does not provide any evidence of resonance trouble. Vibrations of the tie rods (Fig. 30) look to have the local character, as presented in the modal analysis results, and do not transfer to the bearings and casing. However, that does not exclude possible increased wear of the tie rods and connected components in future operations.

The frequency spectrum level and the RMS value of channel 5 exceed several times the average level, but one has to keep in mind that the placement of the sensor is at the backwall casing plate of low stiffness in this particular direction.

In general, the values presented in Table 2 are satisfactory from the point of view of the requirements for industrial fans.

6. CONCLUSIONS

Summarising the above sections, the development of a fan with variable impeller geometry requires to perform two additional tasks, compared with the classic solution. The first is to design a mechanism responsible for changing the geometry. In classic solutions, this process is not needed because the geometry of the fan cannot be changed. The second step requires more calculations to verify the project. This is due to the need to verify the strength, flow and dynamic properties of different positions of the variable geometry system. In the presented solution, the test results show that thanks to this type of control of the parameters of the radial fan, it will be able to operate with about 60% greater change in total pressure increase and a 40% increase in the flow rate, and with efficiency >60% while maintaining a constant rotational speed of the rotor. Such parameters were obtained by assuming that the length of the movable part of the blade is about 30% of the length of the fixed part. Therefore, it has been shown that it is possible to significantly and effectively change the operating characteristics of the radial fan without changing the rotational speed.

The results show the great potential of such a solution. In many cases, it is possible to replace the control method by using a frequency converter, i.e., a variable rotational speed, for the proposed method of blade length control. This lowers the construction costs of fans, especially those with a higher power, where the cost of the inverter is significant. In addition, efficiency losses that occur during inverter operation are also eliminated.

REFERENCES

1. Kuczewski S. Wentylatory. Warszawa: WNT, 1978.
2. Kuczewski S. Wentylatory promieniowe. Warszawa: WNT, 1966.
3. Fortuna S. Wentylatory: podstawy teoretyczne, zagadnienia konstrukcyjno-eksploatacyjne i zastosowanie Kraków: TECHWENT, 1999.
4. Bommes L, Fricke J, Grundmann R. Ventilatoren, 2. Auflage. Essen: Vulkan-Verlag, 2002.
5. Mode F. Ventilatoranlagen: Theorie, Berechnung, Anwendung. Berlin New York: Walter de Gruyter, 1972.
6. Bohl W. Ventilatoren. Würzburg: Vogel-Buchverlag, 1983.
7. Joźwik K, Papierski A, Sobczak K, Obidowski D, Kryłowicza W, Marciniak E, Wróbel G, Marciniak A, Wróblewski P, Kobierska A, Frączczak Ł, Podsędkowski L. Radial fan controlled with impeller movable blades – CFD investigations. Transactions of the Insitute of Fluid Flow Machinery. 2016; 131: 17-40.
8. Radwański J, Laskowski W, Lewkowicz J, Podsętkowski A. Wentylator promieniowy z końcowymi częściami łopatek wirnika nastawnymi w czasie ruchu. Polish home patent no. 52456, 1967 . (Urząd Patentowy PRL)
9. Bukowski A. Cichosza! Optymalizacja wentylatorów sposobem na ograniczenie hałasu i kosztów. Polski Przemysł, 2013.
10. Chmielarz W, Moczko P, Odyjas P, Rusiański E, Więckowski J, Wróblewski A. Wirnik wentylatora promieniowego. Polish home patent no. 234339, 2020. (Urząd Patentowy RP)
11. Miller S. Teoria maszyn i mechanizmów: analiza układow kinematycznych. Wrocław: Oficyna Wydawnicza Politechniki Wrocławskiej, 1996
12. Gronowicz A, Miller S, Twaróg W Teoria maszyn i mechanizmów: zestaw problemów analizy i projektowania. Wrocław: Oficyna Wydawnicza Politechniki Wrocławskiej, 2000
13. Zienkiewicz O C, Taylor R L, Zhu J Z. The Finite Element Method – Its Basis and Fundamentals. 6th edition. ELSEVIER, 2005.
14. Zienkiewicz O C, Taylor R L. The Finite Element Method for Solid and Structure Mechanics. 6th edition. ELSEVIER, 2005.
15. Rusiński E, Czmochowski J, Smolnicki T. Zaawansowana metoda elementów skończonych w konstrukcjach nośnych. Wrocław: Oficyna Wydawnicza Politechniki Wrocławskiej, 2000.
16. Rusiński E, Moczko P, Odyjas P, Pietrusiak D. Investigation of vibrations of a main centrifugal fanused in mine ventilation. Archives of Civil and Mechanical Engineering. 2014; 14: 569–579.
17. Cory W T W. Fans&Ventilation – A Practical Guide. Elsevier, 2005.
18. Czmochowski J, Moczko P, Odyjas P, Pietrusiak D. Test of Rotary Machines Vibrations in Steady and Unsteady States on the Basis of Large Diameter Centrifugal Fans. Eksploatacja I Niezawodność – Mainten ance and Reliability. 2014; 16(2): 211-216.
19. Uhl T. Komputerowo wspomagana identyfikacja modeli konstrukcji mechanicznych. Warszawa: WNT, 1997.
20. Randall R B. Vibration-based Condition Monitoring. A John Wiley and Sons, Ltd, 2011.
21. Rusiński E, Moczko P, Odyjas P, Więckowski J. The numerical and experimental vibrations analysis of WLS series fans designed for the use in underground mines. Proc. Int. Conf. Computer Aided Engineering (Polanica Zdrój) Lecture Notes in Mechanical Engineering (Springer). 2017; 489–504
22. ANSYS FLUENT 12.0 – Tutorial Guide (Ansys Inc.)
23. ANSYS FLUENT 12.0 – User's Guide (Ansys Inc.)
24. ANSYS Fluent Theory Guide (Ansys Inc.)
25. Cheah K W, Lee T S, Winoto S, Zhao Z M. Numerical Flow Simulation in a Centrifugal Pump at Design and Off-Design Conditions. International Journal of Rotating Machinery. 2007.
26. Engin T. Study of tip clearance effects in centrifugal fans with unshrouded impellers using computational fluid dynamics. Proceedings of the Institution of Mechanical Engineers, Part A: Journal of Power and Energy. 2006; 2220(6): 599-610.
27. Chunxi L, Ling W S, Yakui J. The performance of a centrifugal fan with enlarged impeller. Energy Conversopn and Managment, 2011; 52(8-9): 2902-2910.
28. Zawislak M. Zastosowanie numerycznej mechaniki płynów w celu poprawy sprawności przemysłowego systemu wentylacyjnego na bazie wentylatora FAWENT WP-80. Transp. Przemysłowy i Masz. Rob. 2014.
29. Ng W K, Damodaran M. Computational Flow Modeling for Optimizing Industrial Fan Performance Characteristics. Proc. Int. Conf. European Conference on Computational Fluid Dynamics ECCOMAS CFD (Egmond aan Zee, The Netherlands). 2006.
30. EN ISO 5801:2008 Industrial fans. Performance testing using standardized airways

Piotr Odyjas: https://orcid.org/0000-0002-3166-1720

Jędrzej Więckowski: https://orcid.org/0000-0002-5722-3833

Damian Pietrusiak: https://orcid.org/0000-0001-6792-9568

Przemysław Moczko: https://orcid.org/0000-0002-3819-1303

DOI 10.2478/ama-2023-0003

INFLUENCE OF A HYBRID MANUAL–ELECTRIC WHEELCHAIR PROPULSION SYSTEM ON THE USER'S MUSCULAR EFFORT

Bartosz WIECZOREK*, Łukasz WARGUŁA*, Mateusz KUKLA*

*Faculty of Mechanical Engineering, Institute of Machine Design, Poznań University of Technology,
ul. Piotrowo 3, 60-965 Poznań, Poland

bartosz.wieczorek@put.poznan.pl, lukasz.wargula@put.poznan.pl, mateusz.kukla@put.poznan.pl

received 28 June 2022, revised 19 October 2022, accepted 23 October 2022

Abstract: Self-propelled wheelchairs favour the rehabilitation process, forcing the user to be physically active. Unfortunately, in most cases, the manual propulsion is not adapted to the individual needs and physical capabilities of the user. This paper presents the results of operational tests of a wheelchair equipped with a hybrid propulsion system in which the muscle strength generated by the user is assisted by two independent electric motors. The research aimed to investigate the influence of the applied control algorithm and the assistance factor (W) on the value of the muscular effort (MA) while propelling the wheelchair with the use of push rims. A modified ARmedical AR-405 wheelchair equipped with two MagicPie 5 electric motors built into the wheelchair's hubs with a power of 500 W was used in this research. The tests were carried out on a wheelchair test bench simulating the moment of resistance within the range of 8–11 Nm. Surface electromyography was employed for the measurement of MA, specifically, a four-channel Noraxon Mini DTS apparatus. The research was carried out on five patients from the group of C50 anthropometric dimensions. The effort was measured for four muscles: deltoid–anterior part, deltoid–posteriori part, and triceps brachii and extensor carpi radialis longus. The effectiveness of the hybrid propulsion system was observed based on the extensor carpi radialis longus muscle. In this case, for the standard wheelchair, the MA ranged from 93% to 123%. In contrast, for a wheelchair equipped with the hybrid propulsion system, at W = 70%, the MA was within the range of 43%–75%.

Key words: assistive technology, wheelchair, electromyogram (EMG), electric propulsion, control

1. INTRODUCTION

The wheelchair is the basic device enabling the movement of people with physical disabilities. Over the years, wheelchairs have developed in many directions, increasing their functionality through the ability to overcome obstacles (stairs [1,2], thresholds [3], hills [4]) or improving basic functions such as locomotion. The locomotive function of the wheelchair is strongly dependent on its structure and was developed towards reducing weight and size [5], strengthening the frame [6] and adjusting the motion control function depending on the person's disability [7]. Structural improvement increasing the safety of movement [8,9] and systems facilitating manual propulsion of a wheelchair (e.g. through the use of gears) are also subject to research and analysis [10]. However, the main development trend is the use of electric propulsion systems [11,12]. Among the many disadvantages of wheelchairs powered solely by electric motors (greater weight [13], like the control learning problems [14–16], and difficulties in transporting electric wheelchairs in public means of transport [17], the greatest disadvantage is the reduction of the user's motor activity. This leads to a limitation of physical rehabilitation, which in turn may predispose the user to multiple long-term health problems [13]. Therefore, more work is currently being devoted to designing hybrid drive systems. When it comes to wheelchairs, a parallel hybrid drive (manual–electric) is the most advantageous [18]. In the literature, these solutions are also described as assistive technology solutions [19]. The main task of these systems is to assist the movement of people with physical disabilities, and not to completely exclude their physical activity.

Wheelchairs equipped with assistive technology solutions can assist the wheelchair users' effort by adding tractive torque of a specific value transferred by electric motors to the wheelchair's drive wheels. This value can be defined by the user [18,20,21], or set by the control algorithms based on signals from additional sensors, for example, gyroscopic systems recognising slopes [18,20]. Although solutions enabling the setting of the wheelchair drive assistance level are presented in works by Cooper et al. 2002, Oh and Hori 2013, Oh et al. 2014, no studies have shown the effect of these settings on the muscular effort parameters.

Assistive technologies make it possible to reduce the force required to generate by the operator of a machine or device, and are used and popular in many different areas of life. Examples of such systems are the steering assist system [22–24] and the brake pedal control system [25–27] in motor vehicles, electric bicycle drive systems [28–30] or rehabilitation support devices [31]. Too low value of the supporting force may hinder or prevent the performance of tasks, and in extreme cases lead to overloading the operator's musculoskeletal system. On the other hand, too great a value of supporting force may also be problematic, leading to a loss of control precision or the ability to assess the operation of the system whose control process is being carried out. Excessive support in muscle-driven propulsion systems can also overload the operator's musculoskeletal system. This paper presents the influence of the propelling force assistance factor W settings on the muscular effort of the upper limbs of the wheelchair user. In

DOI 10.2478/ama-2023-0003
acta mechanica et automatica, vol.17 no.1 (2023)
Special Issue "Machine Modeling and Simulations 2022"

the work, the propelling force assistance factor defined the value of the maximum flow rate of electric current supplied to the electric motors installed in the wheelchair's wheels. The test was carried out for various wheelchair movement resistances, thus mapping various conditions of use, such as driving uphill or driving on unpaved surfaces.

2. METHODS AND MATERIALS

2.1. Researched patients

Five men took part in the tests (Tab. 1) and they were categorised according to height, weight, age, maximum push force of the upper limb and wheelchair experience. To ensure comparability between patients, their dimensions reflected the 50th percentile of anthropometric dimensions according to the European standard NEN-EN 979. In order to ensure that people with a similar physical condition were selected for the study, participants in the same age range and having a similar value of the force generated by the upper limb were selected. The measurement method for the push force was formalised in terms of methodology. A special stand was used on which the user, in a seated position, pushed a handle connected to a strain gauge towards his knee (Fig. 1). The evaluation of the participants' experience was based on a five-point scale. This assessment was performed by the examined patients, taking into account the time of using the wheelchair, the variety of places of its use and the general confidence in moving in a wheelchair. Each patient was familiarised with the test procedure and had to fill out a consent form to participate in the research. The authors decided to conduct the research on patients without physical disabilities due to the use of prototype propulsion system solutions in difficult terrain conditions. The research and experimental protocols have been positively evaluated by the Bioethical Commission at the Karol Marcinkowski Medical University in Poznań Poland, Resolution No. 513/21 of 24 June 2020, under the guidance of Prof. M. Krawczyński for the research team led by M. Kukla. The authors obtained written consent of the researched person for publication of the research test performed with their participation. The data were presented in such a way as to ensure complete anonymity. The measurement method and data acquisition were carried out following the directives of the Bioethics Commission at the Karol Marcinkowski Medical University in Poznań Poland, which are in line with the guidelines of the Helsinki Declarations.

Tab. 1. Comparison of anthropometric features and the level of experience in wheelchair operation of the test subjects. Mean values determined with the 95% confidence interval (p = 0.05)

	Height	Weight	Age	Push force	Experience
	cm	*kg*	*Years*	*N*	*[-]*
Subject 1	183	90	32	364	●●●●●
Subject 2	179	88	33	322	●●●●●
Subject 3	175	110	31	298	●●●●○
Subject 4	178	96	30	309	●●●○○
Subject 5	171	93	33	306	●●●○○
average	176 ± 3	86 ± 9	33 ± 2	302 ± 23	–

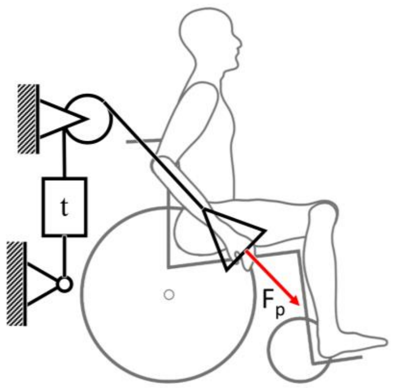

Fig. 1. Schematic illustration of the push force measurement system, where t is strain gauge force sensor and Fp is push force

2.2. The tested wheelchair

The tests were carried out using an ARMedical AR-405 wheelchair equipped with a prototype hybrid propulsion system module (parallel manual–electric hybrid) (Fig. 2) (Patent in the Patent Office of the Republic of Poland, no. exclusive rights PL 239350, 2021) and a conventional version of the AR-405 wheelchair.

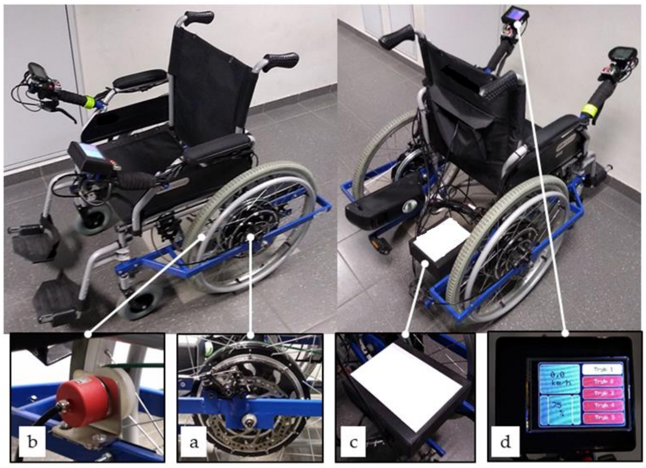

Fig. 2. The tested AR-405 wheelchair is equipped with a hybrid propulsion module. a – power of 500 W installed in the drive wheel hubs; b – incremental encoders; c – proprietary control system with a gyroscope; d – touch screen controller

The modified wheelchair was equipped with two BLDC MagicPie 5 motors by Golden Motor, with a power of 500 W installed in the drive wheel hubs (a), as well as incremental encoders (b), a proprietary control system with a gyroscope (c) and a touch screen controller (d). The screen was used to select the assistance mode and the value of the assistance gain factor W. The wheelchair control system was based on a 32-bit STM32F407 microcontroller operating at a frequency of 100 MHz. The main task of the control system was to control the rotational speed of the two BLDC motors connected with the wheel rims. The speed was measured by two incremental encoders connected to the digital inputs configured in counter mode. The signal generated by the encoder was counted in quadrature, which increased the accuracy of the measurement and allowed to determine the direc-

 DOI 10.2478/ama-2023-0003

tion of rotation. The speed value was determined with a base of 30 ms, using an independent counter.

The heart of the hybrid propulsion system was the algorithm reducing the resistance to movement of the wheelchair resulting from changing operating conditions. To move the wheelchair, a driving torque M_N (1) was generated, being the sum of the electric motor torque M_{SE} and muscular strength M_M. The M_M was only part of the total driving torque required to overcome the resistance to motion:

$$M_N = M_{SE} + M_M \quad (1)$$

In the adopted resistance to motion reduction algorithm, the driving torque generated by the incorporated electric motors results from the value of the constant assistance controlled using the assistance factor *K* and the slope angle (Fig. 3).

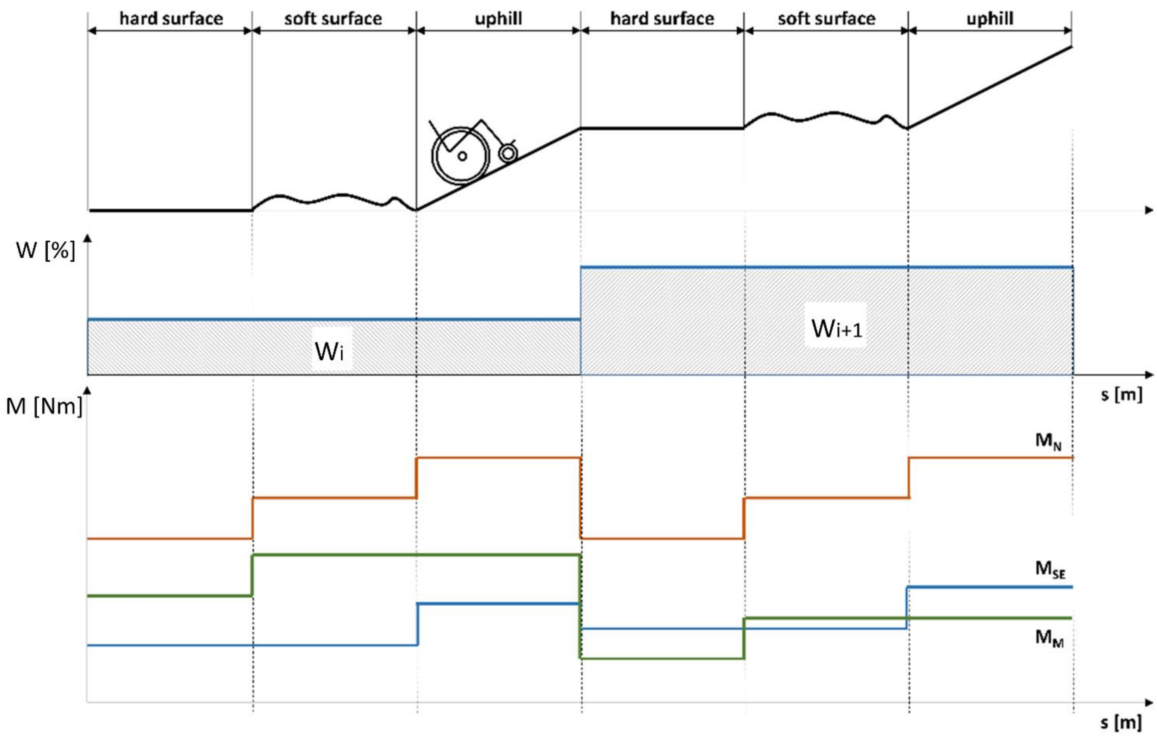

Fig. 3. Schematic diagram of the driving torque MN, muscle strength moment MM, and torque of the electric motor MSE, depending on the assistance factor w and the terrain conditions

In this mode, the system itself adjusts the reduction of resistance resulting from the slope of the terrain, whereas the user determines the level of reduction of resistance resulting from the type of the surface. The resistance reduction mode does not allow the wheelchair to be propelled solely by electric motors. To induce movement of the wheelchair in this mode, it is required to supply muscular force to the push rings of the wheelchair.

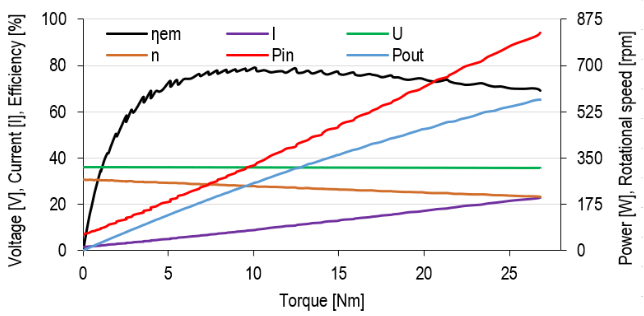

Fig. 4. Characteristics of the MagicPie 3 system by Golden Motor; based on the manufacturer's data; η_{em} is the efficiency of electric motor, n is rotational speed, I is electric current, P_{in} is input power, P_{out} is output power and U is voltage

According to the above algorithm, the share of torque provided by muscles depends on the assist factor *W* set by the user. The user can set the *W* factor in a range from 0% to 100%, where 0% meant no electric motor was involved in propelling the wheelchair. The value of assistance factor *W* was used to determine the value of the electric motors' control current. The control current was calculated based on the equation taking into account experimentally determined correction factors (2). It should be noted that the formula for the control voltage *u* was determined experimentally and allowed to calculate the value of the voltage in the range from 0 V to 3 V. In this equation, the variable is the angle of inclination of the wheelchair α and the assistance factor *W*. In this system, the driving torque of the engine (Fig. 4) is proportional to the value of the control signal *u*.

$$u = \alpha \cdot c + r_3 \cdot W + \delta, \quad (2)$$

where *u* is the signal sent to the BLDC motor controller, *α* is the wheelchair angle [°], c is the angle coefficient (0.0075), r_3 is the gain coefficient in mode 3 (0.0016), *W* is the assistance factor [%] and *δ* is the offset (1.102) [V].

2.3. Research methodology

The tests were carried out on the proprietary dynamometer for wheelchairs [32] which was used to simulate the resistance of movement of the wheelchair and its angle of inclination. During one measurement test, the participants performed 30 driving phases for 9 different configurations of the tested wheelchair. Participants performed driving phases to adjust their speed of propulsion to the pace set by the metronome at a rate of 45 beats per minute (BPM). Muscle activity (*MA*) performed during such propulsion phases was recorded by the myoMOTION software and then transformed and statistically processed.

The MA measurement that allowed to estimate the effort of the muscular system of the upper limb was performed using a Noraxon miniDTS surface electromyography apparatus, equipped with four measurement channels. The analysis and recording of the MA signal were performed with the supplied Noraxon MR3 software. The muscular effort analysis (*MA*) concerned four muscles that are involved in propelling the wheelchair: deltoid muscle anterior MA_1 and posteriori MA_2, triceps brachii MA_3 and extensor carpi radialis longus MA_4. These muscles were selected because, as shown in previous studies, they show the greatest activity when propelling a wheelchair [33].

Additionally, to determine the effort of the entire upper limb MA_{arm}, the measured effort of all measured muscles was averaged as [3]

$$MA_{arm} = \frac{\sum_{i=0}^{n} MA_i}{n} \cdot 100\%, \tag{3}$$

where MA_{arm} is the effort of the entire upper limb, MA_i is the muscular effort of the *i*-th measured muscle of the upper limb and *n* is the number of muscles measured on the upper limb.

Before starting the measurement of *MA*, each patient underwent a normalisation procedure following the guidelines of the electromyogram (EMG) apparatus manufacturer. Round electrodes covered with gel (20 mm in diameter) were used for the tests. They were placed in the central part of the examined muscle heads. The measurements were made at a frequency of 1,500 Hz. The research procedure assumed the performance of a normalisation procedure for each patient to check the value of the maximum voluntary contraction (MVC_{max}) of the examined muscles during the static test [33]. This procedure was performed 1 h before the actual *MVC* test. The purpose of the procedure was to determine the reference value (MVC_{max}) necessary for further calculations.

The measured EMG signals were rectified and then smoothed using RMS algorithms with a window width of 150 ms. The *MVC* test was then performed. This post-processing method utilises a reference value to normalise subsequent EMG data series [4]. The output is displayed as a percentage of the *MVC* value, which can be used to establish a common ground when comparing data between repetitions and individual patients:

$$MA = \frac{MVC}{MVC_{max}} \cdot 100\%, \tag{4}$$

where *MA* is the muscle effort, *MVC* is measured during the measurement test and MVC_{max} is the maximum voluntary contraction measured during the normalisation procedure.

The test procedure assumed that the participant would perform five pushes with his right hand at a frequency of 30 BPM. The entire test procedure was performed on a wheelchair dynamometer on which the resistance to motion was simulated. During the test, three values of the torque (*m*) mimicking the moment of the resistance force M_R were simulated: 8.14 Nm, 9.67 Nm and 11.19 Nm.

3. RESULTS

The research was performed on a group of five participants representing the same group of anthropometric dimensions. Each of the participants had the same four muscles tested, for which the average muscle effort is presented in Tab. 2. Muscle effort of the entire upper limb is also included in these tables. The estimation of the entire upper limb muscle effort MA_{arm} was a compilation of the average values of the muscular effort of all four measured muscles. To determine MA_{arm}, the confidence interval p = 0.05 was calculated using the *t*-Student test for the significance level.

To compare the results obtained for the wheelchair with the results obtained for the conventional wheelchair, the tests of the same muscles for the wheelchair were repeated for the wheelchair with a conventional manual propulsion system – also included in Tab. 2.

Tab. 2. Average results of MA from five participants for the tested values of the assistance factor W and the moment of resistance to movement m , where: MA_1 – MA of deltoid – anterior part, MA_2 – MA of deltoid – posterior part, MA_3 – MA of triceps brachii, MA_4 – MA of extensor carpi radialis longus, MA_{arm} – muscular effort of entire limb averaged over the measurement of four muscles. The value of MA_{arm} was determined with the confidence interval for the probability level p = 0.05 (MA, muscle activity)

W	m	MA_1	MA_2	MA_3	MA_4	MA_{arm}
-	*[Nm]*	[%]	[%]	[%]	[%]	[%]
0%	8.14	66	126	86	59	84 ± 14
	9.67	94	164	109	87	113 ± 16
	11.19	78	205	126	106	129 ± 26
25%	8.14	47	132	82	53	78 ± 18
	9.67	73	161	100	80	104 ± 19
	11.19	78	199	118	101	124 ± 25
30%	8.14	54	120	80	49	75 ± 15
	9.67	77	151	94	81	101 ± 16
	11.19	70	177	112	96	114 ± 21
40%	8.14	51	129	91	47	79 ± 18
	9.67	81	157	88	72	100 ± 18
	11.19	76	169	108	93	111 ± 19
50%	8.14	48	130	84	53	79 ± 18
	9.67	92	155	82	66	99 ± 18
	11.19	85	166	102	89	110 ± 18
60%	8.14	51	127	92	59	82 ± 16
	9.67	70	141	82	64	89 ± 16
	11.19	81	151	95	83	102 ± 15

DOI 10.2478/ama-2023-0003

70%	8.14	42	151	90	62	86 ± 22
	9.67	66	147	88	60	90 ± 19
	11.19	78	122	87	82	92 ± 10
75%	8.14	50	129	87	66	83 ± 16
	9.67	67	141	96	72	94 ±16
	11.19	71	147	93	89	100 ± 15
Standard	8.14	66	135	53	92	87 ± 16
	9.67	90	140	83	113	107 ± 18
	11.19	83	143	87	127	110 ± 20

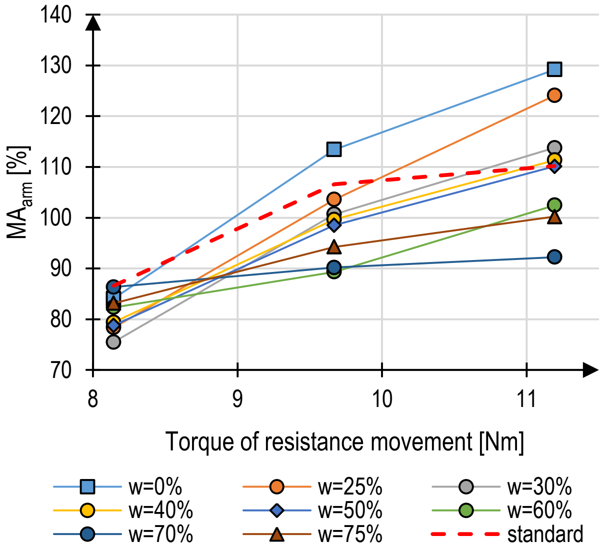

Fig. 5. Diagram showing the entire upper limb muscle effort MA_{arm} as a function of the resistance to motion moments for different values of the assistance factor W. Effort while driving a conventional wheelchair is marked as standard in the diagram

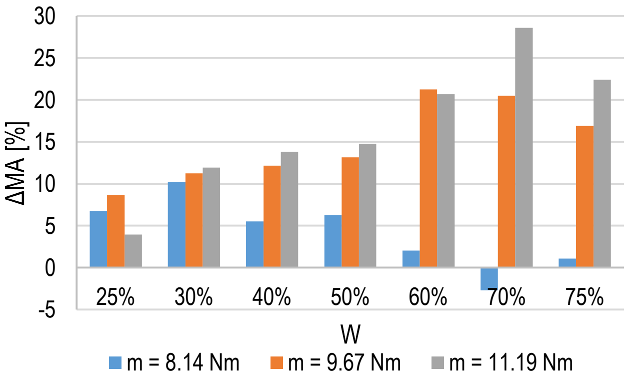

Fig. 6. Diagram of the percentage difference in muscle effort ΔMA depending on the value of the assistance factor W for the three values of the moment of resistance to motion m.
MA, muscle activity

In analysing the effort of the upper limb, it was found that the value of the assistance factor *W* affects the muscular effort (Fig. 5). Based on the observed data, it was noticed that the greatest value of the assistance factor did not always translate into the greatest reduction in the effort of the upper limb MA_{arm}.

The above observation is confirmed by the analysis of the percentage difference in the entire hand muscle effort Δ*MA* depending on the assistance factor *W* setting (Fig. 6). Based on this analysis, it is clear that for each of the three tested moments of resistance *m*, there is a different value of the assistance factor *W* that is the most effective in reducing muscle effort. For the moment of resistance to motion *m* = 8.14 Nm, corresponding to driving on a paved smooth surface, it was found that the greatest reduction in muscle effort was obtained for the assistance factor *W* = 30%, whereas for the moment of resistance to motion *m* = 11.19 Nm, it was found that the greatest reduction in muscle effort was obtained for the assistance factor *W* = 70%.

4. DISCUSSION

Driving a wheelchair with a hybrid propulsion system requires the user to re-learn how to use the wheelchair and to feel its kinematics. According to Torkia et al. [34] in 2014, problems with the control of manually propelled wheelchairs are divided into four types and are related to moving in open space, manoeuvring in confined spaces, difficulties for novice users, and barriers and circumstances that are unpredictable and specific under certain conditions. The basic ones include manoeuvring in a confined space, driving through narrow doors, obstacles (thresholds, stairs, etc.), moving in crowds and weather difficulties (strong wind, rain, snow). The problems with using manual, electric and hybrid wheelchairs are similar. However, it is the wheelchairs with additional assisting propulsion systems that require the user to learn and feel the reaction of controls, also mentioned by other researchers [35].

In the research conducted, the limit value of the assisting torque is also noticed. It can be pointed out that too high a value of the assisting torque hinders the process of controlling the wheelchair, by increasing the muscular activity, which does not result mainly from driving, but from braking the wheels of the wheelchair in order to maintain the trajectory of movement. In the case of propulsion assistance solutions, the main task of the system is to provide additional drive torque to the wheels, as in bicycles equipped with such systems. However, in bicycles, it is easier to install and use such system [36] than in wheelchairs, since the propelling force in wheelchairs is transmitted to two wheels, and the direction of travel depends on their speed (or to be more precise, on the difference in their speed). Hence, the wheelchair user must have the ability to brake the individual wheels. Research has shown that too high a value of assistive propelling force may increase the muscle effort instead of reducing it. This phenomenon is also confirmed by the muscular activity of a different group of muscles than the group used during the pushing phase. An inaptly configured and operated hybrid manual–electric propulsion system will cause jerking of the upper limbs holding the push rims. This will have an adverse effect on the muscular system, as proved by the above analysis (Fig. 6). The phenomenon was precisely demonstrated when riding a wheelchair loaded with a small moment of resistance to motion (*m* = 8.14 Nm). In this particular case, after exceeding the value of the assistance factor *W*, a decrease in the reduction of muscle effort in the upper limb was observed. Moreover, for the highest values of the *W* factor, amounting to 70% and 75%, the high value hin-

sciendo
DOI 10.2478/ama-2023-0003

ders the wheelchair riding, increasing the effort of the entire upper limb.

The above results are confirmed by the analysis of the extensor carpi radialis longus muscle responsible for holding the hand on the push rims and stabilising the wrist while pushing. The analysis of the value of the muscle effort MA_4 (Fig. 7) has confirmed that the effective value of the *W* factor depends on the value of the moment of resistance that the user must overcome to move the wheelchair. It should be noted that as the moment of resistance decreases, the accuracy of the factor *W* calibration should be increased before using a wheelchair with a hybrid propulsion system.

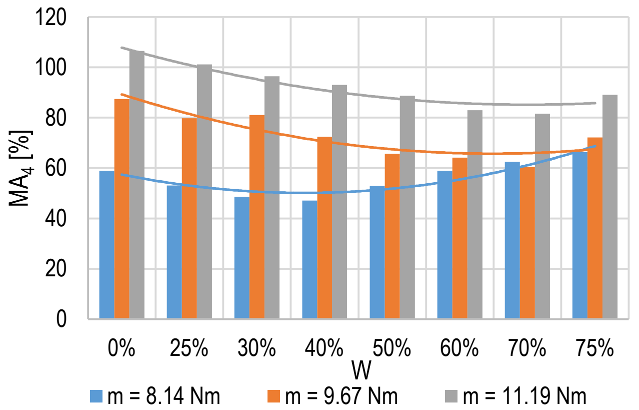

Fig. 7. Muscle Activity MA_4 diagram for the extensor carpi radialis longus musclea as a function of the assistance factor W for different values of the resistance torque m. MA, muscle activity

Since the performed analysis of a single extensor carpi radialis longus muscle coincides with the conclusions from the analysis of the muscle strength of the entire upper limb, it is possible to perform the electromyographic examination of this muscle as a non-invasive and individual calibration method of the propulsion system and the correct selection of the assistance factor *W* value depending on the area where the wheelchair is used. The values of the moments of resistance selected in the study have been estimated experimentally [35] and correspond to the resistance to motion occurring when riding a wheelchair on an even hard surface inside a building (*m* = 8.14 Nm), on pavements in an urban area contaminated with loose sand (*m* = 9.67 Nm) and approaching a paved hill with a slope of 4° (*m* = 11.1 Nm). The research fits into the modern trend of designing machines and devices using the analysis of EMG signals of the upper limb muscles, and the recorded values of this signal are similar to the results obtained by other researchers [37–39].

The conducted research has shown that the increase in the assistance factor *W* is not always reflected in the reduction of the muscle effort. In some cases, too high a value of the coefficient *W* will cause disturbances in the free movement of the arm driving the wheelchair. In the case of the tests carried out, this phenomenon was observed as the pulling movement of the grasping hand along with the hand rim in order to perform another driving phase. On the basis of the above observations, it was found that the value of the assistance coefficient *W* must be adjusted by the wheelchair user individually, depending on his physical abilities and the place of use of the wheelchair. Based on this observation, a design guideline was formulated. Namely, in the case of wheelchair propulsion systems with a manual–electric hybrid drive, it is imperative to enable the user ability to independently adjust the degree of assistance of the drive system by an electric motor.

5. CONCLUSION

Hybrid propulsion systems are currently one of the most important directions of wheelchair development. The selection of the drive torque value assisting the manual propelling of the wheelchair is a problem that includes multiple variables. As a part of the works performed, it was established that the most advantageous value of assistance factor for a man with a healthy musculoskeletal system above the waist up (refers to people with motor disabilities caused by an accident, lumbar section spinal cord injury [L1–L5] or sacral vertebrae section spinal cord injury [S1–S5] section) is within the range of 30 ± 10% when riding on a level and hard surface. When riding in conditions of increased load, for example, loose sand, the most advantageous value of assistance is 60 ± 10%, whereas when greater resistance occurs, for example, when climbing a ramp with a slope of 4°, the value is 70 ± 10%. The beneficial value of the assistance is considered to be the one that causes the least MA during movement. It has also been noticed that too high a value of the assisting propulsion torque causes problems with the control of the wheelchair movement and increases MA. This increased MA concerns a larger group of muscles in the upper limb than in the case of the conventional manual propulsion, which may indicate the need to put more force in the wheelchair riding control, which is carried out by pushing, but also braking the wheels. The presented results apply to people with disabilities who do not have problems with muscular dystrophy. In the future, the research can be extended to a larger group of users with different anthropometric dimensions (C5 and C95).

Considering the dependencies observed in the study, further research directions can be set out to automate the selection of the assistance factor W. In further works, the use of sensors determining the angle of the terrain inclination should be considered. Additionally, it would be advantageous to associate the continuous measurement of MA in the hand with the control of the value of the support factor.

REFERENCES

1. Hinderer M, Friedrich P, Wolf B. An autonomous stair-climbing wheelchair. Robot Auton Syst. 2017;94:219–25.
2. Sasaki K, Eguchi Y, Suzuki K. Stair-climbing wheelchair with lever propulsion control of rotary legs. Adv Robot. 2020;34(12):802–13.
3. Favey C, Farcy R, Donnez J, Villanueva J, Zogaghi A. Development of a New Negative Obstacle Sensor for Augmented Electric Wheelchair. Sensors. 2021;21(19):6341.
4. Wu BF, Chen YS, Huang CW, Chang PJ. An Uphill Safety Controller With Deep Learning-Based Ramp Detection for Intelligent Wheelchairs. IEEE Access. 2018;6:28356–71.
5. Nonaka M, Kashiwazaki H, Ura S, Nagamori M, Uchiyama H, Shionoya A. Evaluation of Driving Performance of Two Types of Competitive Wheelchairs for Badminton Made of Two Different Metallic Materials. Proceedings. 2020;49(1):161.
6. New design and development of a manual wheelchair for India. Disability and Rehabilitation. 2018 29(11): 56–78
7. Quaglia G, Bonisoli E, Cavallone P. The Design of a New Manual Wheelchair for Sport. Machines. czerwiec 2019;7(2):31.

DOI 10.2478/ama-2023-0003

8. Rozendaal LA, Veeger HEJ, van der Woude LHV. The push force pattern in manual wheelchair propulsion as a balance between cost and effect. J Biomech. 1 luty 2003;36(2):239–47.
9. Lee J, Jeong W, Han J, Kim T, Oh S. Barrier-Free Wheelchair with a Mechanical Transmission. Appl Sci. styczeń 2021;11(11):5280.
10. Madanhire I, Gwizo T, Mbohwa C. Design Improvement of Off-road Rough Uneven Rural Terrain Wheelchair. :14.
11. Sivakanthan S, Castagno J, Candiotti JL, Zhou J, Sundaram SA, Atkins EM, i in. Automated Curb Recognition and Negotiation for Robotic Wheelchairs. Sensors. 2021;21(23):7810.
12. Maule L, Luchetti A, Zanetti M, Tomasin P, Pertile M, Tavernini M, i in. RoboEye, an Efficient, Reliable and Safe Semi-Autonomous Gaze Driven Wheelchair for Domestic Use. Technologies. 2021;9(1):16.
13. van der Woude LHV, de Groot S, Janssen TWJ. Manual wheelchairs: Research and innovation in rehabilitation, sports, daily life and health. Med Eng Phys. 2006;28(9):905–15.
14. Yang YS, Koontz AM, Hsiao YH, Pan CT, Chang JJ. Assessment of Wheelchair Propulsion Performance in an Immersive Virtual Reality Simulator. Int J Environ Res Public Health. 2021;18(15):8016.
15. Guillon B, Van-Hecke G, Iddir J, Pellegrini N, Beghoul N, Vaugier I, i in. Evaluation of 3 Pushrim-Activated Power-Assisted Wheelchairs in Patients With Spinal Cord Injury. Arch Phys Med Rehabil. 2015;96(5):894–904.
16. Kloosterman MGM, Eising H, Schaake L, Buurke JH, Rietman JS. Comparison of shoulder load during power-assisted and purely hand-rim wheelchair propulsion. Clin Biomech. 2012;27(5):428–35.
17. Antonelli MG, Alleva S, Beomonte Zobel P, Durante F, Raparelli T. Powered off-road wheelchair for the transportation of tetraplegics along mountain trails. Disabil Rehabil Assist Technol. 2019;14(2):172–81.
18. Wieczorek B, Warguła Ł, Rybarczyk D. Impact of a Hybrid Assisted Wheelchair Propulsion System on Motion Kinematics during Climbing up a Slope. Appl Sci. 2020;10(3):1025.
19. Shionoya A, Kenmotsu Y. Development of New Wheel-Chair for Sports Competition. Proceedings. 2018;2(6):257.
20. Oh S, Kong K, Hori Y. Operation state observation and condition recognition for the control of power-assisted wheelchair. Mechatronics. 2014;24(8):1101–11.
21. Oh S, Hori Y. Disturbance Attenuation Control for Power-Assist Wheelchair Operation on Slopes. IEEE Trans Control Syst Technol. 2014;22(3):828–37.
22. Hu C, Qin Y, Cao H, Song X, Jiang K, Rath JJ, i in. Lane keeping of autonomous vehicles based on differential steering with adaptive multivariable super-twisting control. Mech Syst Signal Process. 2019;125:330–46.
23. Nazaruddin, Adhitya M, Sumarsono DA, Siregar R, Heryana G. Review of electric power steering type column steering with booster motor and future research for EV-Bus. AIP Conf Proc. 2020;2227(1):020016.
24. Wang J, Wang X, Luo Z, Assadian F. Active Disturbance Rejection Control of Differential Drive Assist Steering for Electric Vehicles. Energies. 2020;13(10):2647.
25. Kupiec J, Kupiec A. Dokładność oceny przez diagnostę siły nacisku na pedał hamulca. Autobusy Tech Eksploat Syst Transp. 2019; 20(12): 65-83.
26. Ślaski G, Pikosz H. Badania drogowe zapotrzebowania energii w celu realizacji skrętu kół samochodu osobowego. Czas Tech Mech. 2012;(R. 109, z. 3–M):57–69.
27. Borawski A, Szpica D, Mieczkowski G, Borawska E, Awad MM, Shalaby RM, i in. Theoretical Analysis of the Motorcycle Front Brake Heating Process during High Initial Speed Emergency Braking. J Appl Comput Mech. 2020;6(Special Issue):1431–7.
28. McLoughlin IV, Narendra IK, Koh LH, Nguyen QH, Seshadri B, Zeng W, i in. Campus Mobility for the Future: The Electric Bicycle. J Transp Technol. 2012;02(01):1.
29. Arango I, Lopez C, Ceren A. Improving the Autonomy of a Mid-Drive Motor Electric Bicycle Based on System Efficiency Maps and Its Performance. World Electr Veh J. 2021;12(2):59.
30. Johansen PR, Patterson D, O'Keefe C, Swenson J. The use of an axial flux permanent magnet in-wheel direct drive in an electric bicycle. Renew Energy. 2001;22(1):151–7.
31. Giesko T, Zbrowski A, Mizak W. Model mechatronicznego systemu do wspomagania rehabilitacji ruchowej. Probl Eksploat. 2012;(2): 67–78.
32. Wieczorek B, Warguła Ł. Problems of dynamometer construction for wheelchairs and simulation of push motion. MATEC Web Conf. 2019;254:01006.
33. Kukla M, Wieczorek B, Warguła Ł. Development of methods for performing the maximum voluntary contraction (MVC) test. MATEC Web Conf. 2018;157:05015.
34. Torkia C, Reid D, Korner-Bitensky N, Kairy D, Rushton PW, Demers L, i in. Power wheelchair driving challenges in the community: a users' perspective. Disabil Rehabil Assist Technol. 2015;10(3): 211–5.
35. Langner M, Sanders D. Controlling wheelchair direction on slopes. J Assist Technol. 2008;2(2):32–41.
36. Salmeron-Manzano E, Manzano-Agugliaro F. The Electric Bicycle: Worldwide Research Trends. Energies. 2018;11(7):1894.
37. Warguła Ł, Marciniak A. The Symmetry of the Muscle Tension Signal in the Upper Limbs When Propelling a Wheelchair and Innovative Control Systems for Propulsion System Gear Ratio or Propulsion Torque: A Pilot Study. Symmetry. 2022;14(5):1002.
38. Lafta HA, Guppy R, Whatling G, Holt C. Impact of rear wheel axle position on upper limb kinematics and electromyography during manual wheelchair use. Int Biomech. 2018;5(1):17–29.
39. Ohashi S, Shionoya A, Harada K, Nagamori M, Uchiyama H. Posture Estimation Using Surface Electromyography during Wheelchair Hand-Rim Operations. Sensors. 2022;22(9):3296.

Funding: This research is a part of the project: "Innovative Drive Systems for Wheelchairs – Design, Prototype, Research", number: "Rzeczy są dla ludzi/0004/2020", financed by the National Centre for Research and Development, https://www.gov.pl/web/ncbr

Bartosz Wieczorek: https://orcid.org/0000-0003-0808-298X

Łukasz Warguła: https://orcid.org/0000-0002-3120-778X

Mateusz Kukla: https://orcid.org/0000-0003-3456-3824

DOI 10.2478/ama-2023-0004

acta mechanica et automatica, vol.17 no.1 (2023)
Special Issue "Machine Modeling and Simulations 2022"

TIME SERIES ANALYSIS OF FOSSIL FUELS CONSUMPTION IN SLOVAKIA BY ARIMA MODEL

Mária MICHALKOVÁ*, Ivana POBOČÍKOVÁ*

*Faculty of Mechanical Engineering, Department of Applied Mathematics, University of Žilina,
Univerzitná 8215/1, 010 26 Žilina, Slovakia

maria.michalkova@fstroj.uniza.sk, ivana.pobocikova@fstroj.uniza.sk

received 28 June 2022, revised 23 October 2022, accepted 24 October 2022

Abstract: According to the Green Deal, the carbon neutrality of the European Union (EU) should be reached partly by the transition from fossil fuels to alternative renewable sources. However, fossil fuels still play an essential role in energy production, and are widely used in the world with no alternative to be completely replaced with, so far. In recent years, we have observed the rapidly growing prices of commodities such as oil or gas. The analysis of past fossil fuels consumption might contribute significantly to the responsible formulation of the energy policy of each country, reflected in policies of related organisations and the industrial sector. Over the years, a number of papers have been published on modelling production and consumption of fossil and renewable energy sources on the level of national economics, industrial sectors and households, exploiting and comparing a variety of approaches. In this paper, we model the consumption of fossil fuels (gas and coal) in Slovakia based on the annual data during the years 1965–2020. To our knowledge, no such model, which analyses historical data and provides forecasts for future consumption of gas and coal, respectively, in Slovakia, is currently available in the literature. For building the model, we have used the Box–Jenkins methodology. Because of the presence of trend in the data, we have considered the autoregressive integrated moving average (ARIMA (p,d,q)) model. By fitting models with various combinations of parameters p, d, q, the best fitting model has been chosen based on the value of Akaike's information criterion. According to this, the model for coal consumption is ARIMA(0, 2, 1) and for gas consumption it is ARIMA(2, 2, 2).

Key words: ARIMA model, coal, gas, consumption, Slovakia, prediction

1. INTRODUCTION

Passing the Green Deal in 2019, the European Union (EU) committed to turn Europe into the first climate-neutral continent. According to this, each EU member has set itself goals to be achieved by 2030. Slovakia has aimed towards the following goals:

- to reduce greenhouse gas emissions by −20% until 2030 compared with 2005;
- to increase the share of energy from renewable sources in gross final consumption of energy to 19.2%;
- to increase the energy efficiency by energy savings that will lead to 15.7 [Mtoe] for primary energy consumption and 10.3 [Mtoe] for final energy consumption [1, 2].

Fulfilling these targets requires a reconsideration of the national strategy for energies. Fossil fuels are still an important part of the Slovak energy mix with a share of nearly 28% [3]. With respect to the EU targets, the use of coal should end entirely by 2030. Due to reduction of coal use, there has been an obvious switch from coal to gas in electricity production recently. In 2019, the volume of electricity produced in gas-fired power plants increased by about 11% in Europe, whereas the production of coal-fired power plants decreased by 24% [4]. In addition to power generation, thermal coal is used for operations, such as cement production and industrial and household heat applications, where alternatives are also being sought. Despite gas being considered the "greener" among fossil fuels, such status is only temporary, and in the future, part of the gas consumption will be replaced with renewable sources (see, for example, Jandačka et al. [5] and Nandimandalam et al. [6]).

In this paper, we model and forecast coal and gas consumption, respectively, in Slovakia by applying autoregressive integrated moving average (ARIMA) models. The ARIMA model is commonly used for modelling production and/or consumption of fuels. Dritsaki et al. [7] built the ARIMA model to forecast oil consumption in Greece. The time series covering the period 1960–2020 was modelled by the ARIMA(1,1,1) model and the forecasts for years 2021–2023 were calculated. Ozturk and Ozturk [8] forecast consumption of coal, oil, natural gas, renewable energy sources as well as of total energy, respectively, by modelling the historical data with the ARIMA models. Based on the predictions until the year 2040, they estimated the rate of increase to be between 4% and 5% for all the sources except that of the renewable energy sources, which have been expected to increase by about 1.6%. Akpinar and Yumusak [9] predicted a year-ahead demand for natural gas for household and low consumption consumers in Turkey. They applied three models – time series decomposition, ARIMA model and Holt–Winters exponential smoothing – for monthly consumption between the years 2011 and 2014. Among these considered models, the ARIMA model performed the best. Chaturvedi et al. [10] discussed and compared the performances of three models – the seasonal ARIMA (SARIMA) model, the Long Short-Term Memory Recurrent Neural Network (LSTM RNN) model, the Facebook (Fb) Prophet model and the Indian Central

DOI 10.2478/ama-2023-0004

Energy Authority (CEA) model as a reference model – for fitting the monthly total and peak energy demand in India.

Recently, the ARIMA models have been combined with other methods for creating hybrid models in order to obtain more precise results. It is common to incorporate the artificial neural network to model the non-linearity in the data, as the ARIMA model is able to describe only the linear relationship between the inputs and the output. Manowska et al. [11] forecast the natural gas consumption in Poland using the ARIMA–LSTM hybrid model. The residuals of the ARIMA model were further modelled by the LSTM neural network taking historical consumption and prices of energy resources, that is, crude oil, natural gas and thermal coal, as predictors of the model. Using this approach, the authors achieved the average percentage error of 2%. Based on the model, the predictions of natural gas consumption in Poland up to the year 2040 were constructed. Wang [12] predicted per capita coal consumption in China using the ARIMA-BP combined model. Proceeding from the hybrid model that combines the ARIMA model and the back-propagation neural network and simply sums these two models' results, Wang improved the model accuracy by obtaining the predictions via multiple linear regression with the linear fitting of the ARIMA model and the non-linear fitting of the BP model as independent variables and the consumption as the dependent variable. The energy demand in China and India were forecast by Wang et al. [13], applying the rolling metabolic grey (MGM) model, the rolling metabolic grey – ARIMA (MGM-ARIMA) model and the non-linear metabolic grey (NMGM) model. Here, the MGM-ARIMA model combined the grey model and the ARIMA model in a different way as in the hybrid ARIMA artificial neural network models, mentioned previously. The ARIMA model was used to model the MGM model's residuals to minimise their volatility. According to the comparison of three considered models, the MGM-ARIMA model fitted the energy demand of India as the best one, and the energy demand of China as the second best, outperformed by the NMGM model. South Africa's energy consumption was analysed and predicted by Ma and Wang [14]. They considered the ARIMA model, the nonlinear grey model (NGM) and the nonlinear grey – ARIMA model. Achieving the value of the mean average percentage error less than 3%, all three models made highly reliable predictions.

The number of papers providing the prediction models regarding the energy sector in Slovakia is scarce. Recently, Pavlicko et al. [15] forecast the electricity consumption in Slovakia by applying and comparing two approaches – grey models and multi-layer feed-forward back-propagation network. They also proposed a new model combining both approaches. Based on this model, the authors obtained more accurate maximum hourly electricity consumption per day forecasts, compared with the official load predictions. Brabec et al. [16] presented a non-linear mixed effect model that was able to predict the daily consumption of natural gas for an individual consumer. This model was applied on daily-recorded consumptions of 62 larger commercial entities in Slovakia and its performance was compared with performances of the ARIMAX and ARX model, respectively. Hošovský et al. [17] modelled the daily gas consumption considering three particular types of buildings, each in a different town in Slovakia. In the paper, they compared the performance of reg(S)ARMA (the regression model with ARMA-modelled time series error terms) with regWANN (the regression wavelet neural network) model and the SARMA model as a reference model. However, as far as we have found out, no prediction model of gas or coal consumption for Slovakia as a country has been published. To fill this gap, we propose such models applying the Box–Jenkins methodology. These models can serve as reference models and the bases for further research.

This paper is organised as follows: In Section 2, the time series used for study are characterised and their descriptive statistics are given. In Section 3, we provide the methodology for building ARIMA models. In Section 4, the results of modelling process for coal and gas time series, respectively, are summarised. In addition, the forecasts for the next 10 years are made. The last section "Discussion and Conclusions" summarises and interprets the obtained results, and provides the proposals for future research. All the calculations in the paper were conducted using MATLAB software, version R2020b.

2. CHARACTERISTICS OF DATA

Data modelled in the paper represent annual values of consumption of fossil fuels in Slovakia. Namely, we analyse gas and coal consumption, respectively. The records cover the period of years 1965–2020, that is, the data count 56 observations for each commodity. The gas data are given in milliards of cubic metres; the coal data are given in exajoules. The data are obtained from the literature [18].

The descriptive statistics of datasets are summarised in Tab. 1. The value of skewness of the coal data close to zero implies that the consumptions in the considered years are distributed almost symmetrically around the mean. On the other hand, the negative value of skewness for the gas consumption shows that higher consumptions dominate. The kurtosis values in both cases are greater than 1, indicating too peaked (leptokurtic) distributions.

Tab. 1. The descriptive statistics for coal and gas dataset, respectively

Statistic	Coal [EJ]	Gas [10^9 m^3]
Minimum	0.08296	0.29853
Maximum	0.35881	7.17380
Mean	0.23709	4.28430
Variance	0.00572	3.78942
Skewness	−0.03980	−0.48146
Kurtosis	1.79441	2.17448
Lower quantile	0.17385	2.89133
Median	0.24985	4.63595
Upper quantile	0.29202	5.91770

The presence of outliers, which indicate anomalies in the data, is checked by the boxplot. As shown in Fig. 1, there are no outliers in the respective datasets of the commodities.

3. METHODOLOGY

In general, the process of modelling and analysing the time series contains several steps, namely:

- graphical analysis of data, identification of components;
- selection of the model, estimation of parameters;
- checking the adequacy of the model in relation to the data;
- forecast of future values.

DOI 10.2478/ama-2023-0004

3.1. Pre-analysis of data

The first step in modelling the time series is its visualisation that enables us to identify the presence of particular components.

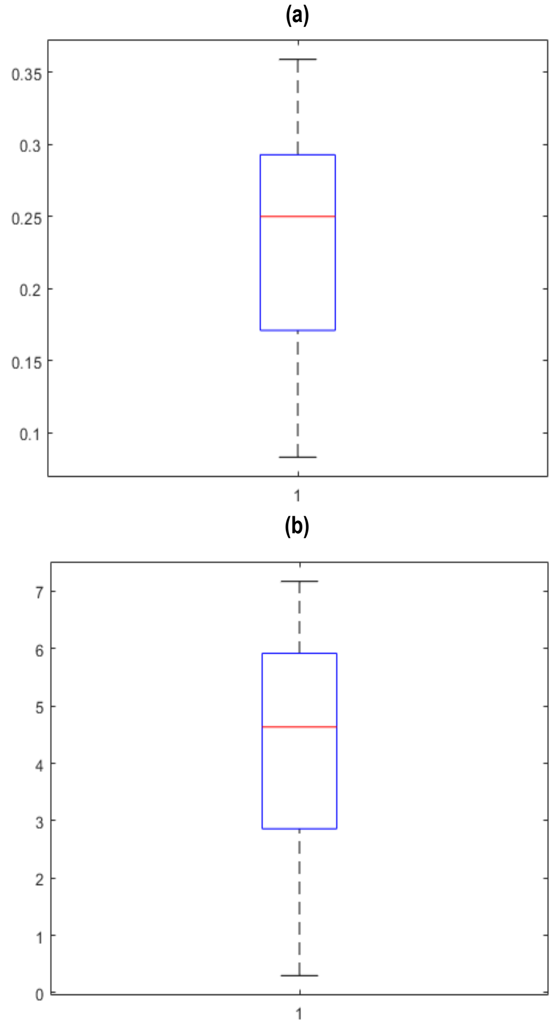

Fig. 1. Boxplot of dataset (a) coal and (b) gas

Generally, the time series includes the following components:
- trend;
- seasonal;
- cyclic;
- residual.

A trend occurs in the data when there can be observed a long-term change in the mean either as an increase, or as a decrease. However, there are cases when the trend is not monotonic. Seasonality is represented by fluctuations with a fixed frequency. These fluctuations are related to the seasonal aspects, such as a season of the year, a day in the week, etc. Similar to seasonality, cycle is also represented by altering the increase and the decrease in the data. Contrary to the seasonal component, these fluctuations do not have a fixed frequency. Usually, they are explained as a consequence of business cycles in economics. The residual component represents random changes in the data. Time series of residuals should be a white noise.

A stationary time series does not have a predictable pattern in the long-term. Therefore, the time series with trend or seasonality is not stationary. The verification of the presence of these components in the series can be done by testing the series for stationarity. There exist several stationarity tests. In this paper, we have selected the unit root tests, namely the augmented Dickey–Fuller (ADF) test and the Kwiatkowski–Phillips–Schmidt–Shin (KPSS) test. The ADF test tests the null hypothesis H_0: there is a unit root in an autoregressive AR model (the data series is not stationary) against the alternative that the data series is stationary. The KPSS test works in a reverse manner to the ADF test since it tests the null hypothesis H_0: there is no unit root in an AR model (the data series is stationary) against the alternative that there is a unit root in an AR model, thus the data series is not stationary.

The results of these two tests should be interpreted as follows:
- the time series is stationary when H_0 in the ADF test is rejected and H_0 in the KPSS test cannot be rejected;
- the time series is non-stationary when H_0 in the ADF test cannot be rejected and H_0 in the KPSS test is rejected [19, 20].

The non-stationarity in the time series is eliminated by differencing.

3.2. ARIMA model

The ARIMA models are based on regression models built on the observations themselves and on the residual component of the time series. The ARIMA(p,d,q) model is given as follows:

$$y_t'=c+\alpha_1 y_{t-1}'+\alpha_2 y_{t-2}'+\ldots+\alpha_p y_{t-p}'+\theta_1\varepsilon_{t-1}+\theta_2\varepsilon_{t-2}+\ldots+ \\ +\theta_q\varepsilon_{t-q}+\varepsilon_t \quad (1)$$

where y_t' is the differenced series, c is constant, $\alpha_1,\ldots,\alpha_p$ are the coefficients of AR(p) process, $y_{t-1}',\ldots,y_{t-p}'$ are lagged values of the differenced series, $\theta_1,\ldots,\theta_q$ are coefficients of the MA(q) process and $\varepsilon_t,\ldots,\varepsilon_{t-q}$ are independent identically distributed error terms with zero mean.

The parameters of the ARIMA(p,d,q) model are as follows:
- p is the order of the autoregressive part (the AR process);
- d is the degree of differencing involved;
- q is the order of the moving average part (MA process) [21].

The degree of differencing depends on the stationarity/non-stationarity of the time series. A stationary time series has $d=0$. The values of parameter $d>2$ seldom occur. The order of the AR and the MA processes, respectively, can be estimated from the correlogram – a plot of autocorrelation coefficients (ACF), and from a plot of partial ACF (PACF). The estimates of the ACF are given as follows [20]:

$$r_k=\frac{\sum_{t=k+1}^{n}(y_t-\bar{y}).(y_{t-k}-\bar{y})}{\sum_{t=k+1}^{n}(y_t-\bar{y})^2},\ k=0,1,\ldots,n-1 \quad (2)$$

where y_t are the observations, $\bar{y}$ is the average of the observations; and the estimates of the PACF are given as follows [20]:

$$r_{11}=r_1, \\ r_{kk}=\frac{r_k-\sum_{j=1}^{k-1}(r_{k-1,j}\cdot r_{k-j})}{1-\sum_{j=1}^{k-1}(r_{k-1,j}.r_j)},\ k>1, \quad (3) \\ r_{k,j}=r_{k-1,j}-r_{kk}.r_{k-1,k-j},\ j=1,2,\ldots k-1.$$

The methodology for estimating the parameters of the ARIMA model from its ACF and PACF can be found in the literature [20].

DOI 10.2478/ama-2023-0004

However, such estimation of the parameter orders is subjective; therefore, it is more convenient to use it as a supporting information.

In this paper, several ARIMA models with different combinations of parameters are fitted to the time series. The coefficients of each model are found as maximum likelihood estimates. The best fitting model is chosen according to the smallest value of Akaike's information criterion (AIC) [21]

$$\text{AIC}= -2\log(L)+2(p+q+k+1), \quad (4)$$

where $\log(L)$ denotes the maximised value of log likelihood function, p, q are the parameters of ARIMA model, $k = 1$ if constant $c \neq 0$ and $k = 0$ if $c = 0$.

3.3. Verification of the ARIMA model

When the model is selected and the coefficients are estimated, we need to verify the model by checking whether the residuals, given as

$$e_t=y_t - \hat{y_t}, \quad (5)$$

are a white noise. Here $\hat{y_t}$ are the modelled values. A sequence of random variables ε_t is said to be a white noise under these conditions:

- the mean is zero, $E(\varepsilon_t)=0$;
- the variance is constant, $D(\varepsilon_t)=\sigma^2$;
- random variables are not correlated,

$$cov(\varepsilon_t, \varepsilon_{t-k})=cov(\varepsilon_t, \varepsilon_{t+k}).$$

Furthermore, if the random variables ε_t are drawn from the standard normal distribution ($\varepsilon_t \sim N(0, \sigma^2)$), they are called Gaussian white noise.

The absence of correlation among the residuals is tested by the Ljung–Box Q test that tests the null hypothesis H_0: the residuals are not correlated, against the alternative that the residuals are correlated. When the H_0 is rejected, the considered model of the time series is not adequate and it needs to be changed.

Zero mean of residuals is tested using the t-test, when we test the hypothesis H_0: the data come from a normal distribution with a mean equal to zero and unknown variance, against the alternative hypothesis H_A: the population distribution does not have a mean equal to zero.

The homoscedasticity (constant variance) of residuals is tested by the two-sample F-test for equal variance. The normality of residuals can be tested by the Kolmogorov–Smirnov (KS) test or the Anderson–Darling (AD) test.

The performance of the model for fitting the data may be also considered by the following measures:

- the root mean square error (RMSE)

$$\text{RMSE}=\sqrt{\frac{1}{n}\sum_{t=1}^{n} e_t^2} \quad (6)$$

- the mean absolute percentage error (MAPE)

$$\text{MAPE}=\frac{1}{n}\cdot\sum_{t=1}^{n}\frac{|e_t|}{y_t}\cdot 100\% \quad (7)$$

- the mean percentage error (MPE)

$$\text{MPE}=\frac{1}{n}\sum_{t=1}^{n}\frac{e_t}{y_t} \quad (8)$$

Here n is sample size.

4. RESULTS

In this section, we summarise the results obtained when modelling the coal and the gas time series, respectively, in accordance with the procedure described in the Methodology section.

4.1. Coal time series

The visualisation of the time series is presented in Fig. 2. As we can see, the series is obviously decreasing with no fluctuations of a fixed frequency.

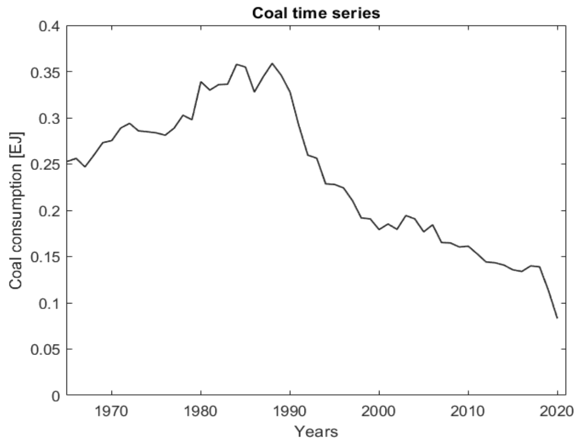

Fig. 2. The time series of coal consumption in Slovakia during the years 1965–2020

The presence of trend is indicated also by the correlogram of the time series (Fig. 3). The slow decrease of the ACF is caused by a strong correlation between the consecutive observations.

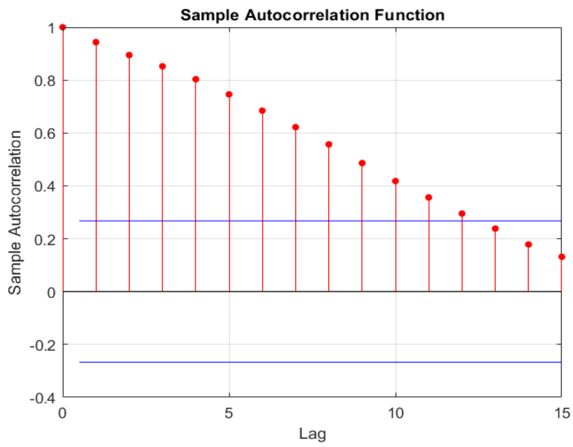

Fig. 3. The correlogram of the coal time series

We conduct the unit root tests on the significance level $\alpha=0.05$. The *p*-value of the ADF test and the KPSS test, respectively, are summarised in Tab. 2.

Tab. 2. Unit root tests for the coal time series

Original time series	ADF test	KPSS test
p-value	0.2845	0.0100

According to the *p*-value of the ADF test, the null hypothesis cannot be rejected on the significance level α=0.05; according to the *p*-value of the KPSS test, we reject the null hypothesis on the significance level α=0.05. The time series is non-stationary.

To eliminate the trend in the data, we replace the original series with the series of differences between the consecutive observations. This time series of first-order differences is also tested for stationarity. The *p*-value of the ADF test and the KPSS test, respectively, are presented in Tab. 3.

Tab. 3. Unit root tests for the first-order difference series (coal)

Series of first-order differences	ADF test	KPSS test
p-value	0.0159	0.0449

According to the *p*-value of the ADF test, we reject the null hypothesis on the significance level α=0.05; according to the *p*-value of the KPSS test, we also reject the null hypothesis on the significance level α=0.05. Because of the conflicting results of both tests for the series of differenced data, we cannot make any conclusions whether this series is stationary or not. Therefore, we calculate the differences of the consecutive observations of the differenced time series and test the stationarity of the time series of second-order differences. We summarise the *p*-value of the ADF test and the KPSS test, respectively, in Tab. 4.

Tab. 4. Unit root tests for the second-order difference series (coal)

Series of second-order differences	ADF test	KPSS test
p-value	0.0010	0.1000

On the significance level $\alpha = 0.05$, we reject the null hypothesis of the ADF test, while we do not reject the null hypothesis of the KPSS test. We may conclude that the series of second-order differences is stationary.

We fit the ARIMA models with parameters considered as follows:

$$d=\{1,2\};\ p=\{0,1,2\};\ q=\{0,1,2\}. \tag{9}$$

The values of parameter d are determined by results of the unit root tests; the values of the other two parameters are considered to not exceed 2 because higher values occur only seldom. The best fitting model is chosen according to the AIC value. The ARIMA models along with their AIC values are in Tab. 5.

Tab. 5. The fitted ARIMA models

ARIMA model	$\log(L)$	AIC
$(1,1,0)$	159.299	−314.597
$(0,1,1)$	159.011	−314.022
$(1,1,1)$	160.896	−315.792
$(2,1,0)$	160.158	−314.315
$(0,1,2)$	159.637	−313.274
$(1,1,2)$	160.937	−313.874
$(2,1,1)$	160.925	−313.849
$(2,1,2)$	162.585	−315.171
$(1,2,0)$	154.658	−305.316
$(0,2,1)$	160.246	−316.492
$(1,2,1)$	160.275	−314.550
$(2,2,0)$	157.471	−308.942
$(0,2,2)$	160.273	−314.546
$(1,2,2)$	160.275	−312.551
$(2,2,1)$	160.465	−312.929
$(2,2,2)$	162.163	−314.327

The smallest value of the AIC is achieved by the MA$(0,2,1)$ model, which means that the second-order differences of time series follow the MA(1) model in the form

$$y_t''=\varepsilon_t - 0.859\varepsilon_{t-1} \tag{10}$$

where y_t'' is a series of second-order differences, $\varepsilon_t, \varepsilon_{t-1}$ are the independent identically distributed error terms with zero mean. The model fitted to the time series is depicted in Fig. 4.

We verify the model by checking the residuals. The results of the tests are summarised in Tab. 6.

Tab. 6. The *p*-values of the tests for verification of the model

Ljung-Box Q test (*p*-value)	t-test (*p*-value)	Two-sample F-test (*p*-value)	AD test (*p*-value)
0.8534	0.4028	0.0626	0.2188

According to the *p*-values of all the tests, we may conclude that on the significance level $\alpha = 0.05$, the residuals of the model are not autocorrelated and are normally distributed with constant variance. Thus, the residual time series is a white noise.

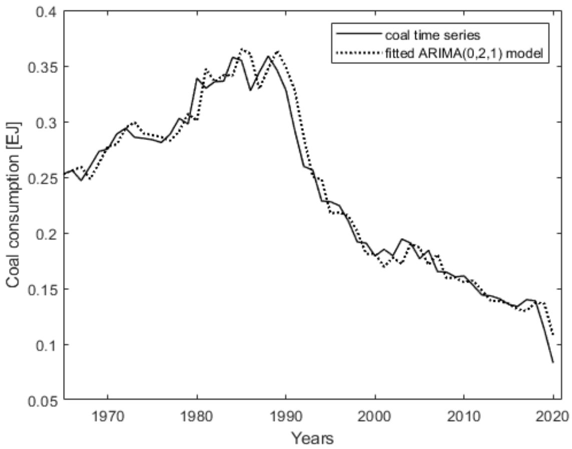

Fig. 4. Model ARIMA$(0,2,1)$ fitted to the coal time series

The performance of the model is assessed by the measures RMSE, MAPE and MPE, respectively; the results are given in Tab. 7. The measure MPE indicates that the majority of errors is negative, which means that the model systematically overestimates the reality. According to MAPE, the mean absolute percentage error between the consumption of coal predicted by the model and the actual consumption is 4.75%.

DOI 10.2478/ama-2023-0004

Tab. 7. Performance of the ARIMA(0,2,1) model for the coal time series

RMSE	MAPE	MPE
0.0138	4.7506	–0.9684

Based on the fitted model, we may forecast future coal consumption. The forecasts for years 2021–2030 are presented in Tab. 8 and visualised in Fig. 5.

Tab. 8. The forecast of coal consumption for years 2021–2030

Year	Point forecast	Lower 95% confidence level	Upper 95% confidence level
2021	0.072525	0.04462	0.10042
2022	0.06207	0.01896	0.10519
2023	0.05163	−0.00573	0.10900
2024	0.04119	−0.03039	0.11277
2025	0.03075	−0.05531	0.11681
2026	0.02031	−0.08063	0.12125
2027	0.00987	−0.10641	0.12614
2028	−0.00057	−0.13267	0.13152
2029	−0.01102	−0.15943	0.13740
2030	−0.02146	−0.18669	0.14378

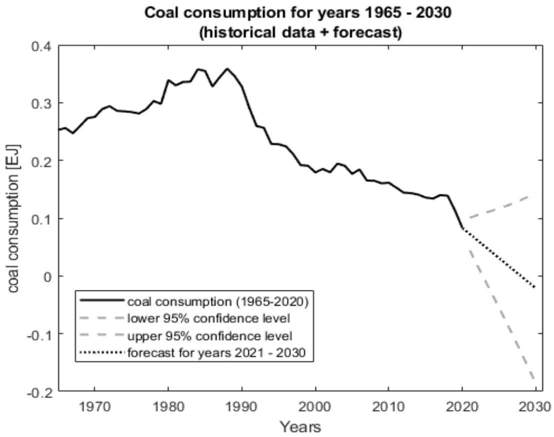

Fig. 5. Coal consumption in years 1965–2030 (actual values and forecast)

4.2. Gas time series

The visualisation of the gas time series is in Fig. 6. As we can see, the series is increasing with no obvious seasonality.

Similarly as in the coal time series, the presence of a trend is indicated also by the correlogram of the time series (Fig. 7) where the ACF only slowly decrease.

We conduct the unit root tests on the significance level $\alpha = 0.05$. The *p*-values of the ADF test and the KPSS test are presented in Tab. 9.

According to the *p*-value of the ADF test, the null hypothesis cannot be rejected on the significance level $\alpha = 0.05$; according to the *p*-value of the KPSS test, we reject the null hypothesis on the significance level $\alpha = 0.05$. This proves our assumption that the time series is non-stationary.

To eliminate the trend in the data, we transform the series by differencing. Then we test the stationarity of the first-order difference series and draw a conclusion from the *p*-values of the ADF test and the KPSS test (Tab. 10).

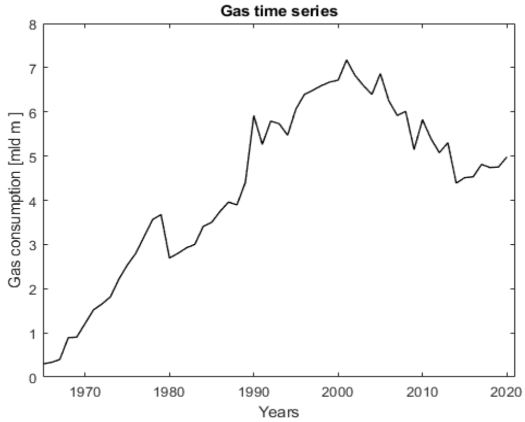

Fig. 6. The time series of gas consumption in Slovakia during the years 1965–2020

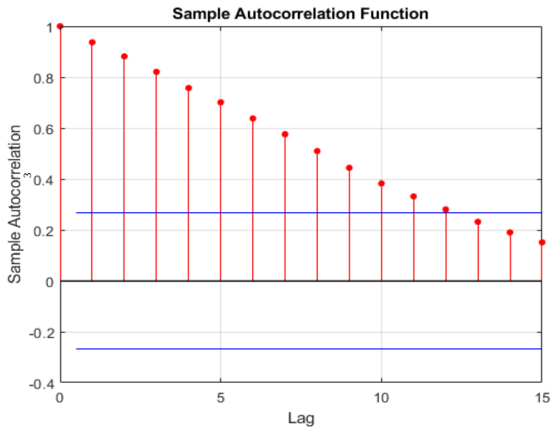

Fig. 7. The correlogram of the gas time series

Tab. 9. Unit root tests for the gas time series

Original time series	ADF test	KPSS test
p-value	0.8200	0.0100

Tab. 10. Unit root tests for the first-order difference series (gas)

First-order difference series	ADF test	KPSS test
p-value	0.0046	0.0327

Just as for the coal time series, according to the *p*-value of the ADF test, we reject the null hypothesis on the significance level $\alpha = 0.05$. According to the *p*-value of the KPSS test we also reject the null hypothesis on the significance level $\alpha = 0.05$. Because of the conflicting results of both tests for the first-order difference series we cannot make any conclusions whether the series is stationary or not. We replace this series with the series of the differences of its consecutive observations and test the stationarity of such second-order difference series. Tab. 11 presents the *p*-values of the ADF test and the KPSS test.

Tab. 11. Unit root tests for the second-order difference series (gas)

Second-order difference series	ADF test	KPSS test
p-value	0.0010	0.1000

On the significance level $\alpha = 0.05$ we reject the null hypothesis of the ADF test, while we do not reject the null hypothesis of the KPSS test. We may conclude that the second-order difference series is stationary.

We fit the ARIMA models with parameters considered as follows:

$$d=\{1,2\};\ p=\{0,1,2\};\ q=\{0,1,2\}. \tag{11}$$

Again, the values of parameter d are determined by results of the unit root tests. The best fitting model is chosen according to the smallest AIC value. The ARIMA models along with their AIC are in Tab. 12.

Tab. 12. The fitted ARIMA models

ARIMA model	$\log(L)$	AIC
$(1,1,0)$	−30.391	64.782
$(0,1,1)$	−30.495	64.990
$(1,1,1)$	−30.324	66.647
$(2,1,0)$	−29.997	65.995
$(0,1,2)$	−29.216	64.432
$(1,1,2)$	−27.788	63.577
$(2,1,1)$	−27.995	63.991
$(2,1,2)$	−27.788	65.576
$(1,2,0)$	−40.226	84.452
$(0,2,1)$	−30.115	64.229
$(1,2,1)$	−29.342	64.685
$(2,2,0)$	−31.455	68.910
$(0,2,2)$	−28.829	63.658
$(1,2,2)$	−28.708	65.415
$(2,2,1)$	−29.285	66.569
$(2,2,2)$	−25.210	60.419

The smallest value of the AIC is obtained by the MA$(2,2,2)$ model, which means that the series of second-order differences follow the ARMA$(2,2)$ model in the form

$$y_t'' = -1.1375 y_{t-1}'' - 0.3978 y_{t-2}'' + \varepsilon_t - 0.8086\varepsilon_{t-2} \tag{12}$$

where y_t'' is the second-order difference series, $\varepsilon_t, \varepsilon_{t-2}$ are the independent identically distributed error terms with zero mean. The model fitted to the time series is shown in Fig. 8.

We verify the model by checking the residuals. The results of the tests are summarised in Tab. 13. According to the *p*-values of the tests, we may conclude that on the significance level $\alpha = 0.05$, the residuals of the model are not autocorrelated, they have constant variance but do not come from the normal distribution $N(0, \sigma^2)$, that is, the residual time series is a white noise, not Gaussian white noise.

The performance of the model is assessed by the measures RMSE, MAPE and MPE; the results are given in Tab. 14.
The value of MPE indicates that the majority of errors is positive, which means that the model systematically underestimates the reality. According to the value of MAPE, the mean absolute percentage error between the consumption of gas predicted by the model and the actual consumption is 7.88%.

Based on the fitted model, we predict the annual gas consumption. The forecasts for years 2021–2030 are given in Tab. 15 and visualised in Fig. 9.

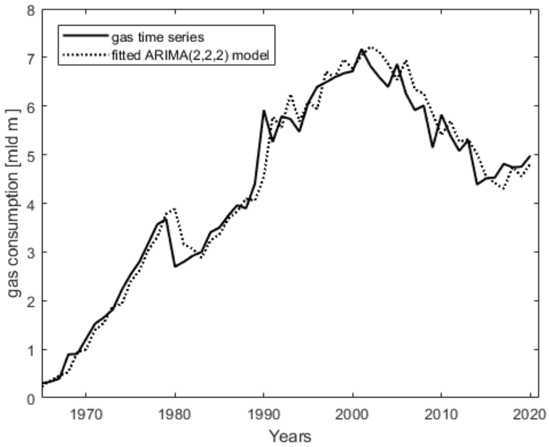

Fig. 8. The model ARIMA$(2,2,2)$ fitted to the gas time series

Tab. 13. The *p*-values of tests for verification of the model

Ljung-Box Q test (*p*-value)	t-test (*p*-value)	Two sample F-test (*p*-value)	AD test (*p*-value)
0.8489	0.5287	0.4288	0.0258

Tab. 14. Performance of the ARIMA(0,2,1) model for the gas time series

RMSE	MAPE	MPE
0.3824	7.8804	0.3135

Tab. 15. The forecast of gas consumption for years 2021–2030

Year	Point forecast	Lower 95% confidence level	Upper 95% confidence level
2021	4.8126	4.0378	5.5875
2022	4.8620	3.7920	5.9320
2023	4.8091	3.5133	6.1048
2024	4.7933	3.1506	6.4360
2025	4.7736	2.8838	6.6634
2026	4.7439	2.5213	6.9665
2027	4.7277	2.2143	7.2411
2028	4.6993	1.8550	7.5436
2029	4.6801	1.5114	7.8489
2030	4.6547	1.1438	8.1656

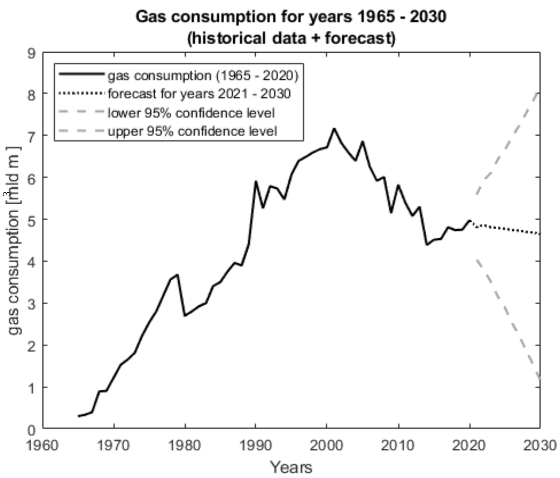

Fig. 9. Gas consumption in years 1965–2030 (actual values and forecast)

5. DISCUSSION AND CONCLUSIONS

In the paper, we modelled the time series of coal and gas consumption, respectively, in Slovakia during the years 1965–2020 by applying the ARIMA(p, d, q) models. Because of the trend in each time series, parameter $d > 0$. After fitting several models with various combinations of parameters p, d, q, we have chosen the ARIMA$(0,2,1)$ model for the coal consumption and the ARIMA$(2,2,2)$ model for the gas consumption, respectively, as they achieved the smallest values of AIC. The results of the Ljung–Box test verified that for each time series, the chosen ARIMA model explains all the autocorrelation in the series, therefore it is adequate for modelling the actual time series and can be used for predicting future values. The values of MAPE less than 10% (4.75% for coal and 7.88% for gas) indicate that the fitted ARIMA models provide reliable predictions.

Based on the constructed forecasts, we can formulate the following conclusions:

- coal consumption shall follow the decrease that has been observed in recent years. According to the forecast, close to zero coal consumption will be achieved between years 2027 and 2028. Such a scenario is in agreement with the obligations of Slovakia to finish the electricity production from coal by 2030 (as electricity production alongside households heating is one of main coal consumers);
- the gas consumption in the next decade exhibits a very mild decrease, almost a stagnation.

Although there is no other model that can be used for comparison, we can compare our predictions of the gas consumption with official predictions reported by the Ministry of Economy of Slovak Republic. The ministry issues annually a Report on the results of gas supply security monitoring (Správa o výsledkoch monitorovania bezpečnosti dodávok plynu), where it is summarised the consumption, the production and the import during the year. In addition, the ministry provides the prognosis of development in the consumption and the production for the following period, including the predictions for the next 5 years. The predictions for years 2021–2025 are presented in Tab. 16. The methodology for obtaining the forecasts declared by the ministry is not available.

Tab. 16. Predictions of gas consumption for years 2021–2025

Year	Gas consumption [10^9 m^3]	
	Predictions from the Ministry of Economy [22]	Point forecasts from the ARIMA(2,2,2) model
2021	5.1	4.8126
2022	5.0	4.8620
2023	5.0	4.8091
2024	5.0	4.7933
2025	5.0	4.7736

According to the report [22], the Ministry anticipates the stagnation of consumption on the level of approx. 5.0 [10^9 m^3] in the upcoming years. In our predictions, we observe that after the increase in previous years, the consumption should start to slowly decrease. This predicted decrease of consumption can be caused by the situation in 2020. The COVID-19 pandemic brought restrictions to our everyday lives, influencing everything, including the industrial sector as the main gas consumer in Slovakia. To avoid the influence of unpredictable changes in 2020, Wang et al. [23, 24] suggested to consider the consumption from a COVID-free scenario simulation instead of the real consumption in 2020. It is of further research to estimate the influence of the pandemic on the future gas consumption, comparing the predictions for the original time series and the time series adjusted by the simulation.

To sum it up, the target to build a prediction model for the coal and the gas consumption, respectively, in Slovakia has been achieved. Both ARIMA models provide very good fit to the time series. Taking these results as reference models, we can carry on with the research in the future by applying other approaches, such as artificial neural networks, grey models, and by building hybrid models in order to improve the fit of the model to the data, and to obtain more precise predictions.

Making responsible energy policy requires trustworthy predictions. Therefore, we hope that the proposed models will be of help to the authorities when preparing future strategies.

REFERENCES

1. Slovak Ministry of Economy. Integrated National Energy and Climate Plan for 2021 to 2030. [Internet] 2019 December [cited 2022 May 31] Available from: https://energy.ec.europa.eu/system/files/202003/sk_final_necp_main_en_0.pdf
2. Brożyna J, Strielkowski W, Fomina A, Nikitina N. Renewable Energy and EU 2020 Target for Energy Efficiency in the Czech Republic and Slovakia. Energies. 2020; 13(4): 965.
3. OKTE, a.s. National Energy Mix. [Internet] 2022 May [cited 2022 May 31] Available from: https://www.okte.sk/en/guarantees-of-origin/statistics/national-energy-mix/
4. IEA. Gas 2020. [Internet] 2020 June [cited 2022 May 31]. Available from: https://iea.blob.core.windows.net/assets/555b268e-5dff-4471-ac1d-9d6bfc71a9dd/Gas_2020.pdf
5. Jandačka J, Holubčík M, Trnka J. Utilization of solid fuels with regard to the transport distances of the raw material. TRANSCOM 2021, Transp Res Proc 2021; 55: 829-836.
6. Nandimandalam H, Gude VG, Marufuzzaman M. Enviromental impact assessment of biomass supported electricity generation for sustainable rural energy systems – A case study of Grenada County, Mississippi, USA. Sci Total Environ. 2022; 802: 149713.
7. Dritsaki C, Niklis D, Stamatiou P. Oil Consumption Forecasting using ARIMA Models: An Empirical Study for Greece. Int J Energy Econ Policy. 2021; 11(4):214-224.
8. Ozturk, S, Ozturk F. Forecasting Energy Consumption of Turkey by ARIMA Model. J Asian Sci Res. 2018; 8(2): 52-60.
9. Akpinar M, Yumusak N. Year ahead demand forecast of city natural gas using seasonal time series methods. Energies. 2016; 9: 727.
10. Chaturvedi S, Rajasekar E, Natarajan S, McCullen N. A comparative assessment of SARIMA, LSTM RNN and Fb Prophet models to forecast total and peak monthly energy demand for India. Energy Policy. 2022; 168: 113097.
11. Manowska A, Rybak A, Dylong A, Pielot J. Forecasting of Natural Gas Consumption in Poland Based on ARIMA-LSTM Hybrid Model. Energies. 2021; 14(24): 8597.
12. Wang X. Research on the prediction of per capita coal consumption based on the ARIMA-BP combined model. Energy Rep. 2022: 8(4): 285-294.
13. Wang Q, Li S, Li R. Forecasting energy demand in China and India: Using single-linear, hybrid-linear, and non-linear time series forecast techniques. Energy. 2018; 161: 821-831.
14. Ma M, Wang Z. Prediction of the energy consumption variation trend in South Africa based on ARIMA, NGM and NGM-ARIMA models. Energies. 2020; 13(1): 10.
15. Pavlicko M, Vojteková M, Blažeková O. Forecasting of electrical energy consumption in Slovakia. Mathematics. 2022; 10: 577.

16. Brabec M, Konár O, Pelikán E, Malý M. A nonlinear mixed effects model for the prediction of natural gas consumption by individual customers. Int J Forecast. 2008; 24: 659-678.
17. Hošovský A, Piteľ J, Adámek M, Mižáková J, Židek K. Comparative study of week-ahead forecasting of daily gas consumption in buildings using regression ARMA/SARMA and genetic-algorithm-optimized regression wavelet neural network models. J Build Eng. 2021; 34: 101955.
18. BP p.l.c. Statistical Review of World Energy – all data, 1965-2020. [Internet] 2021 July [cited 2022 May 29]. Available from: https://www.bp.com/content/dam/bp/business-sites/en/global/corporate/xlsx/energy-economics/statistical-review/bp-stats-review-2021-all-data.xlsx
19. Kwiatkowski D, Phillips PCB, Schmidt P, Shin Y. Testing the null hypothesis of stationarity against the alternative of unit root: How sure are we that economic time series have a unit root? J Econom. 1992; 54(1-3): 159-178.
20. Cipra T. Time Series in Economics and Finance. Cham: Springer Nature Switzerland; 2020. 410p.
21. Hyndman RJ, Athanasopoulos G. Forecasting: Principles and Practice. 2nd ed. Heathmont: OTexts; 2018. 382p.
22. Slovak Ministry of Economy. Report on the results of gas supply security monitoring. [Internet] 2021 July [cited 2022 October 21] Available from: https://www.mhsr.sk/uploads/files/WdL723Kw.pdf?csrt=6552196416131516580
23. Wang Q, Li S, Jiang F. Uncovering the impact of the COVID-19 pandemic on energy consumption: New insight from difference between pandemic-free scenario and actual electricity consumption in China. J Clean Prod. 2021; 313: 127897.
24. Wang Q, Li S, Zhang M, Li R. Impact of COVID-19 pandemic on oil consumption in the United States: A new estimation approach. Energy. 2022; 239: 122280.

This work has been supported by the Slovak Grant Agency KEGA through the project No. 027ŽU-4/2020 Innovation of learning text and implementation of new didactical means to improve the quality of Mathematics II at the university of the technical type and through the project No. 029ŽU-4/2022 Implementation of the principles of blended learning into the teaching of the subject Numerical Methods and Statistics.

Mária Michalková: https://orcid.org/0000-0001-7488-8514

Ivana Pobočíková: https://orcid.org/0000-0003-4357-260X

DOI 10.2478/ama-2023-0005

DESIGN OF A HEIGHT-ADJUSTABLE BOARDING SYSTEM FOR A NEW DOUBLE-DECK RAILWAY VEHICLE

Pavol ŠŤASTNIAK*, Michal RAKÁR, Jakub TÍŽEK****

*Faculty of Mechanical Engineering, University of Žilina, Univerzitná 8215/1, 010 26 Žilina, Slovakia
**Škoda Transportation, 1. máje 3176/102, 709 31 Ostrava, Czech Republic

pavol.stastniak@fstroj.uniza.sk, michal.rakar@skoda.cz, jakub.tizek@skoda.cz

received 27 June 2022, revised 18 October 2022, accepted 6 November 2022

Abstract: This paper deals with a solution for faster and safer boarding and leaving of passengers at railway station platforms from 150 mm to 550 mm higher than the head of the rail. This conception is based on the requirements of railway infrastructure administrators, transporters and also manufacturers of passenger rolling stock. This device is designed for the new double-deck railway vehicle for suburban and regional transport, which fulfils legislative and normative requirements that are specified for the selected area of vehicle construction and operational features. Selected parts of the construction were verified through a series of simulation analyses. This article also includes a study that deals with optimization of the boarding area considering designed changes in the construction of the floor and a draft for modification of the vertical clearance of the boarding entrance area in a rough construction of the vehicle.

Key words: double-deck railway vehicle, boarding system, railway station platform, simulation, FEA

1. INTRODUCTION

Recently, the number of passengers and goods transported by rail has been growing significantly. This can also be seen as a result of the European Union's commitment to carbon neutrality by 2050 [1, 2]. In this case, railway transport becomes friendly, safe and sustainable. This calls for significant renewal, modernization and expansion, in the means of transport and infrastructure [3–9].

One manner of reaching transport efficiency is related to the reduction of transport time. This can be achieved by increasing the maximum speed of vehicles. Another way is connected to lowering the time for boarding and leaving, because it reduces a train's stop time [10]. This is also related to limiting the use of additional stairs and platforms as they are very often not suited to a train and rail platform leading to unsafe situations with respect to health [11, 12].

The European Commission has set in its regulations two platform heights on newly built or reconstructed railway tracks [13, 14]. Subsequently, the development of the vehicles is adapted to these platform heights so that the boarding edge (vehicle floor) is approximately at their level. However, reconstruction of the existing infrastructure is not progressing fast enough to eliminate the problem of platform diversity soon.

Therefore, manufacturers offer various types of vehicles and equipment (e.g. ramps and fixed or moving steps). The paper presents the results of research work on the development of auxiliary equipment for a double-decker railway vehicle for suburban and regional transport. The aim of the paper follows the project of a device for boarding and leaving if the distance between the head of the rail and the height of the platform ranges from 150 mm to 550 mm. This was reached at the requirements of the COMMISSION REGULATION (EU) No 1299/2014 and No 1300/2014 [13, 14] for approval. The article studied verifies whether the boarding area meets the legislative requirements in case the vehicle would be operated on lines with a platform height of between 550 mm and 760 mm above the top of the rail.

2. PLATFORMS FOR VEHICLES USED IN SUBURBAN AND REGIONAL TRANSPORT

The station platform is one of the basic elements of the railway infrastructure because it allows boarding and leaving based on safety rules. It represents a connection between the static and dynamic parts of the transport system, which makes it an important factor for evaluating the safety of the entire transport process.

According to the literature [14], on newly built and upgraded tracks, the nominal platform height should be 550 mm or 760 mm above the top of the rail. Both types of platforms (height of platforms 550 mm and 760 mm) are being used in Germany. In the Czech and Slovak Republics, platforms with a height of 550 mm only are used. In the case of suburban and regional rolling stock, manufacturers ensure to adapt the boarding edge height to the platform height in order to achieve safe and comfortable boarding for passengers [15, 16] (Fig. 1).

In the Czech Republic, there are still a large number of platforms that are <400 mm, which were built many years ago and do not comply with current legislations [13, 14, 17]. For this reason, boarding vehicles with a boarding area adapted for platform heights of 550 mm above the top of rail operated on tracks with platforms <400 mm (e.g. 210 mm) are often uncomfortable.

For this problem, manufacturers are taking action to install fixed (Fig. 2) or movable steps (Fig. 3) [18, 19]. These devices fulfil a safety requirement because they fill the gap between the platform and the boarding area.

Fig. 1. Railway vehicles with adapted boarding–leaving zone

Fig. 2. Fixed step in the railway vehicle Talent of Bombardier Transportation: 1 – boarding area of the vehicle; 2 – fixed step; 3 – platform

If the vehicle is to be operated on tracks with a platform height of 550 mm above the top of rail and the vehicle has a boarding area height adapted to this platform, the movable step (1) (Fig. 3) should be installed just below the boarding area of the vehicle (3) (Fig. 3).

Fig. 3. Extendable steps on the vehicle 14Ev from Škoda Transportation: 1 – movable step; 2 – additional step; 3 – boarding area of the vehicle

When operating a railway vehicle with different platform heights, manufacturers install additional steps (2) (Fig. 3) under the first retractable step. This solution assists passengers in boarding the vehicle from platforms <400 mm above the top of rail.

If the rough construction of the vehicle does not allow placing both steps in the space under the interior floor, then a lower step is installed under the vehicle bottom. This is not very popular, because if the vehicle is operated at low values of temperatures, then snow and ice could limit the movement of the auxiliary step [20].

For these reasons, it is necessary to propose new solutions.

3. TILT PLATFORM CONCEPT

When proposing boarding the vehicle by means of movable steps or adjusting the boarding area, it was necessary to proceed in accordance with the literature [14] and [17].

A level entrance according to the PRM TSI regulations can be considered as the entrance from the platform to the door of the railway vehicle, when the interior of the vehicle boarding area does not contain any steps. The gap between the end plate of the entrance door or also of the extended bridge platform/step and the station platform does not exceed 75 mm measured horizontally and 50 mm measured vertically.

A movable step is in this case defined as a retractable device built into the vehicle below the level of the vehicle door area and is fully automatic and activated in conjunction with the door opening and closing procedures [21].

The auxiliary step must extend before the vehicle door is opened and passengers are allowed to get on/off and conversely, the step can only be retracted if the door is already closed, and it is not possible to enter/exit the vehicle.

In the design of the entrance, stairs are very important parameters, l_2 and l_3 (Fig. 4). Parameter l_2 is the maximum height between the upper surface of the external step and the step inside the vehicle (or the floor) if there are no more steps in the vehicle boarding area. Parameter l_3 represents the minimum depth of the step.

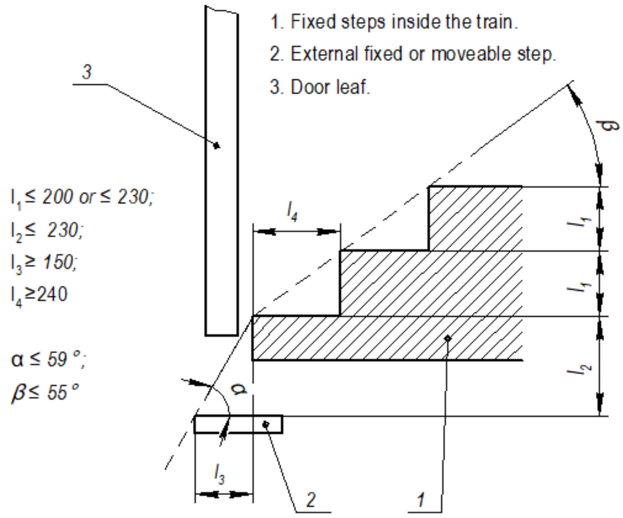

Fig. 4. Dimensional requirements for interior and exterior stairs (STN EN 14752)

It follows from the entry conditions provided that a suitable solution is to use a retractable and folding mechanism that can quickly and safely unfold/fold to the required height above the rail.

The designed height-adjustable boarding platform (1) (Fig. 5), which is installed as a separate device in the vehicle, has dimensions of 1,450 mm x 915 mm x 130 mm. It is a 4-mm thick bent sheet metal, in which holes are cut to lighten the construction. At the top of the height-adjustable boarding platform the original self-supporting EN AW-6060 (AlMgSi) aluminium alloy plate with a 75-mm wide warning strip (2) and part of the vehicle floor (3) is used.

In order to install the boarding platform under the interior floor, it is placed in the rough construction of the vehicle at an angle of 5° in the direction of the floor slope. The maximum permissible height of the module is limited by the height of the milled hole in the rough construction of the railway vehicle (130 mm). The width is also limited to 1,450 mm.

To create sufficient space for the construction of the mechanism, a structural material should have mechanical and physical

DOI 10.2478/ama-2023-0005

properties for resistance on loading and mass, respectively. Therefore, sandwich panels made of EN AW-6060 (AlMgSi) aluminium alloy were selected. The module is mounted to the C profiles of the vehicle by means of profiles and strength screws (Fig. 6).

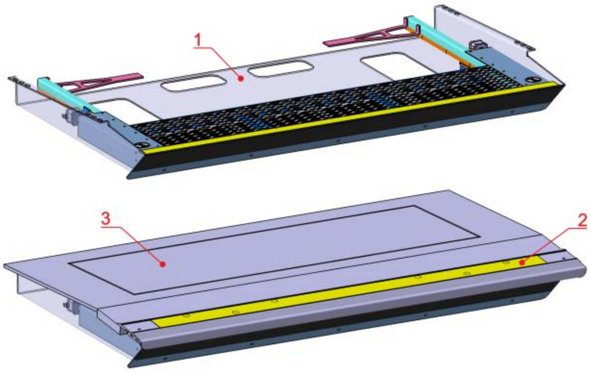

Fig. 5. Main components of the height-adjustable boarding platform for boarding and leaving for a railway vehicle: 1 – the height-adjustable boarding platform; 2 – wide warning strip; 3 – part of the vehicle floor

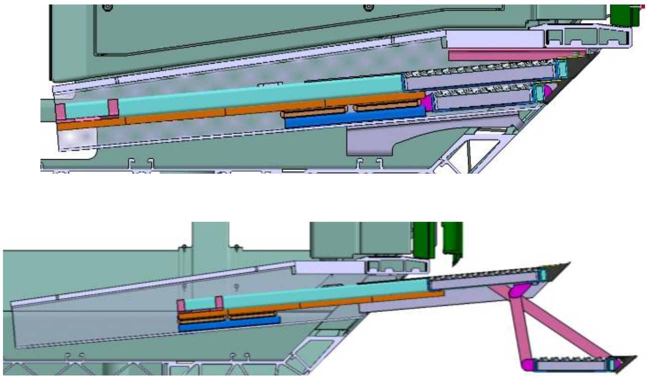

Fig. 6. Tilted lower step-cross section

The construction of the upper and lower step frames (Fig. 7) consists of a welded construction of closed square welded profiles measuring 30 mm x 30 mm with a wall thickness of 3 mm (2), bent L-profiles made of sheet metal 3 mm (3), rectangular welded profile measuring 30 mm x 15 mm with a wall thickness of 2 mm (4), sheets forming a reinforcement 3-mm thick (5) and a plastic plate (1) with a warning yellow strip 45 mm wide.

An important parameter in the design of steps is the mass of the structure, on which the forces acting on the structure will depend:

$$F_s = G_s + F_l, \quad (1)$$

where $G_s = M \cdot g$ – self-weight of the step, N; M – mass of the step, kg; F_l – load from the considered carrying capacity, N.

The studies conducted show that the design of the steps can be made from different materials [22, 23]. These are, for example, various variations of metal or plastic floor gratings, or special aluminium and composite sandwich panels with anti-slip surface treatment that can be used as the filling [22, 23]. The main factors determining the choice of materials of the boarding surface are determined. These factors are divided into several groups:

1. Safety (reliability) factor (f_r), which includes the strength of the material (e.g. plastic, steel, aluminum, etc.) and the coefficient of friction (slip) of the step surface (e.g. smooth anti-slip surfaces).
2. Aesthetic factor (f_a), which includes appearance and practicality (the ability to use steps with different types of shoes, including stilettos).

In accordance with these factors, an objective function has been developed to determine the optimal material of the boarding surface:

$$M(f_r, f_a) \rightarrow min, \quad (2)$$

The physical meaning of the objective function is that when selecting the material for the boarding surface, it is necessary that the mass tends to be a minimum while achieving the maximum safety and comfort.

In accordance with the developed objective function (2), a hot dip galvanized expanded metal grating was suggested. It guarantees low maintenance costs, low weight and at the same time sufficient safety.

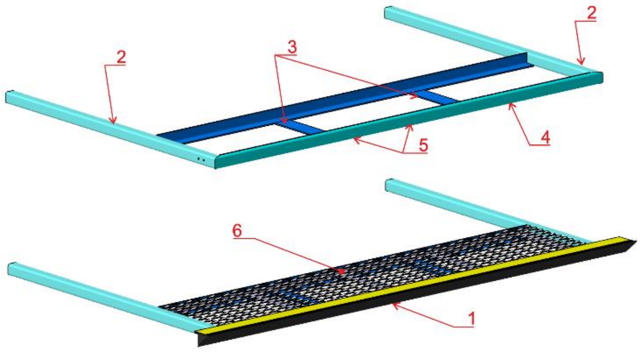

Fig. 7. Sub-components of the upper step: 1 – plastic plate, 2 – welded construction of closed square welded profiles, 3 – bent L-profiles, 4 – rectangular welded profile, 5 – sheets forming a reinforcement, 6 – hot dip galvanized expanded metal

The upper step is ensured by a linear guide (Fig. 8) and consists of the special shape rail (1) and a runner with rolling elements (2). The rails are fixed on the underside of the square profile on both sides of the frame of the upper step. The runners are fastened with screws to a bracket (3) made of 3 mm thick sheet metal. The actuator, which ensures the extension of the upper step, is realized by a DC motor with a toothed belt or a chain.

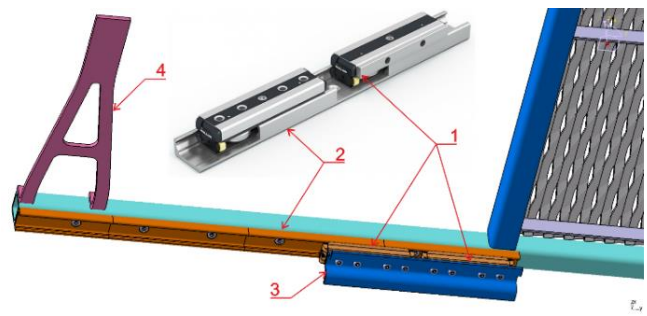

Fig. 8. Details of upper step: 1 – special shape rail, 2 – runner with rolling elements, 3, 4 – bracket

In terms of functionality, simplicity and weight saving of the mechanism, the construction of the lower step is designed as part of the upper step. To help passengers board from the platforms at a height of 550 mm above the top of rail, the upper and lower steps slide out together as one unit. In the case of boarding passengers from platforms 150 mm above the top of rail, after the train stops at the station, the upper step is first extended so that parameter l_3 (150 mm) is observed. Subsequently, the lower step will start to tilt down from the upper step. The mechanism for tilting the step consists of a pair of arms (7) and (8), which are rotatable and mounted on brackets with pins (5), (6), (9) and (10) (Fig. 9).

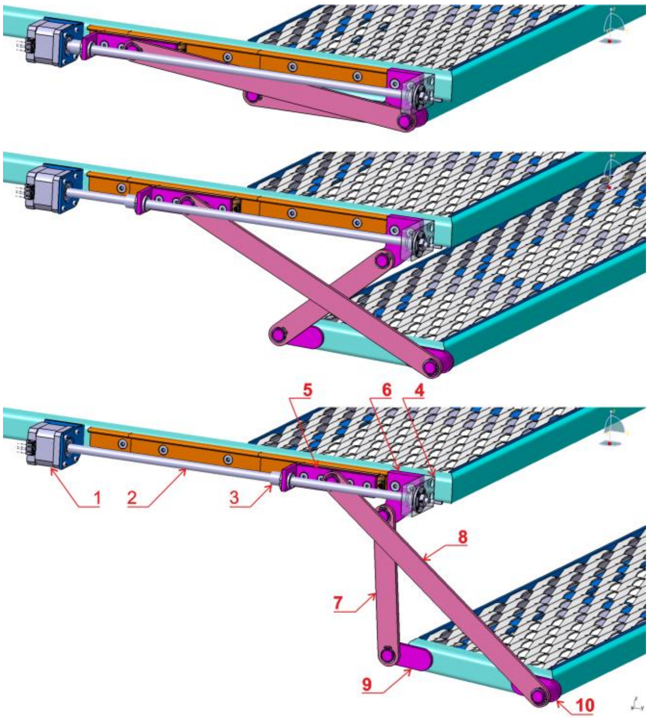

Fig. 9. Tilt mechanism of lower step

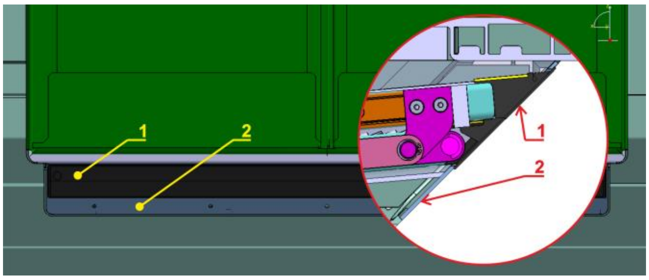

Fig. 10. Details of construction of the vehicle: 1 – non-rigid plate, 2 – sheet metal cover

The profile (5) is installed along a linear guide runner. Also, a nut (2) is attached to the profile (5), into which the screw (3) of the linear drive (1) is screwed. The principle of the lower step tilting function is that after the linear actuator has been actuated, the linear movement of the nut mounted in the profile is transmitted to the linear guide runner due to the rotation of the screw. By moving the arm (8), the force is transmitted to the lower step, and under the influence of the arm guide (7), the lower step is tilted towards the station platform. By suitable adjustment of the lengths of the arms, the lower step must be set not turned by 5° as the upper step, but in a horizontal position for better comfort when boarding the passenger (Fig. 6).

The contact surface with the exterior consists of a pair of non-rigid (e.g. plastic) plates (1) together with a sheet metal cover (2), which forms the filling of the remaining part of the milled hole in the rough construction of the vehicle (Fig. 10).

On the front surface of the plates, an overlap seal is designed, which should slide against the sheet metal cover when the step is inserted into the vehicle and thus seal the gaps between the step plates and the sheet metal cover. Otherwise, rainwater or snow could enter the vehicle and the designed structure, leading to failure of the mechanism. Placing the whole construction (module) inside the vehicle is also advantageous because heat from the interior passes into this space. If the non-rigid plates still freeze, there is a possibility to install the heating on the exposed parts.

4. THE PLATFORM IN FEM APPROACH

For functional and strength analysis, it is important to correctly determine the loads that affect the design of the boarding device [14–26].

Standard [17] defines the value reflecting stress of 4 kN/m^2 in the vertical direction (in the z-axis). It follows that the load value for the lower step is 780 N and for the upper step it is 1,638 N. The selected load value was also determined on the assumption that no more than two passengers could board or leave at the same time through the door of a vehicle with a clear usable width of 1,300 mm. The weight of one passenger according to the literature [17] is equal to 80 kg. After adding up the weight of the passengers and adding the weight within the coefficient of safety, choose a load capacity for both steps at 300 kg.

The strength analysis of the designed construction was conducted in the 22.2 ANSYS software. The 3D model was modified (simplified) in SpaceClaim.

For the strength analysis, parts of the tilting mechanism together with the construction of the lower step frame were selected as key supporting elements. The original tread surface from expanded metal was replaced by a simple plane. Due to the symmetry of the construction a half model for the simulation was used.

The shorter arm bracket is attached to the upper step frame and the longer arm bracket is connected to the linear guide runner. When the step is in the end position, the linear guide runner cannot move because it is held in this position by the linear actuator nut. Therefore, these two elements are considered to be fixed.

A mesh of volume finite elements for analysis of new design of tilt platform by finite element method has been created. The number of elements in the mesh was 48,189 and nodes 141,784. The percentage of elements with an aspect ratio of <3 mm was 74%. The dimensions of the finite element mesh model are at a scale of 1:1 to the dimensions of the structure being analysed. They are used as isoparametric, 20-node and 10-node elements with average size of elements at 2 mm (elements of the tilting mechanism) and 6 mm (other parts). The analysis is performed in a linear region. The distortion of the results of the analysis resulting from the introduction of the simplification mentioned is considered negligible. Consideration is given to the fact that the material is linear, elastic and isotropic.

The main parts of the construction were designed from structural steel of S355J2 (Properties: Min yield strength Re = 355 MPa, min, tensile strength Rm = 470 MPa, Young modulus of

DOI 10.2478/ama-2023-0005

elasticity E = 2.1e^5 MPa, Poisson´s ratio μ = 0.3 and density ρ = 7,850 kg · m^{-3}.
The proposed design for three loading conditions is analysed as follows:

– The first loading condition is according to the standard [17] on the area defined by parameter l_3 and useful step width of 1,300 mm (force value of 780 N in the direction of the *z*-axis). The maximum calculated value of stress is 110 MPa. The most stressed parts of the structure are the bracket with the pin and the upper part of the arm in the area of the hole for locking in the end position (Fig. 11). The largest value of displacement is located in the middle part of the lower step frame.
– The second loading condition is also according to literature [17] for an area of 200 mm x 100 mm at any place on the step surface (force value of 2,000 N in the direction of the z-axis). The maximum value of stress was levelled at 344 MPa (Fig. 12).
– The third loading condition is based on the increased safety factor (force value of 3041.1 N in the direction of the z-axis). The maximum calculated value of stress is close to 350 MPa (Fig. 13).

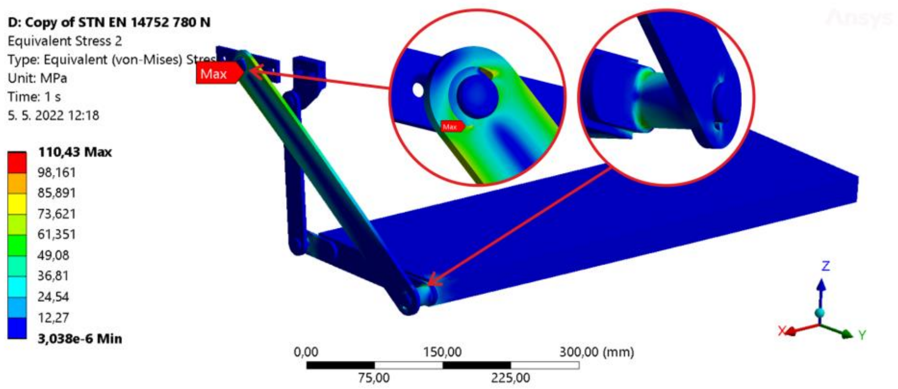

Fig. 11. Mises stress distribution from analysis under loading condition 780 N

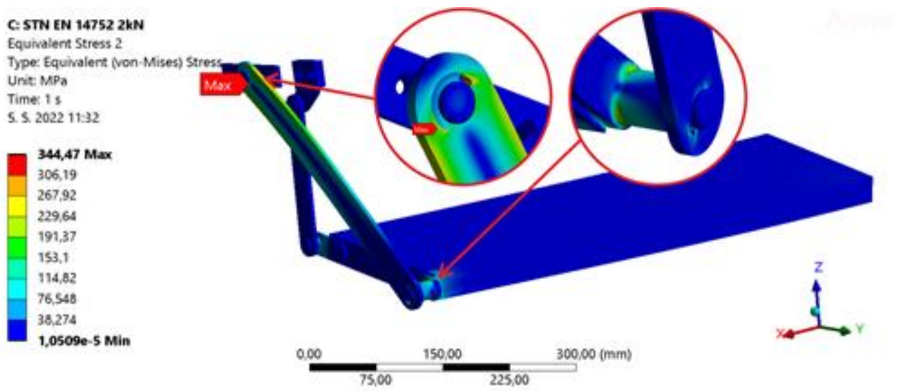

Fig. 12. Mises stress distribution from analysis under loading condition 2,000 N

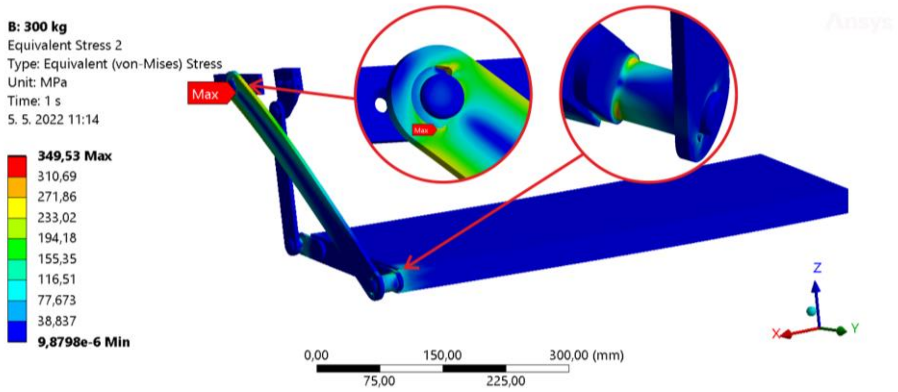

Fig. 13. Mises stress distribution from analysis under loading condition 3,041.1 N

Based on the simulation results, it can be concluded that the construction fulfils the requirements of the current standards because stress values of the second and third conditions are below the yield stress of the material used (Re = 355 MPa). This

sciendo
DOI 10.2478/ama-2023-0005

kind of data follows a static loading, but in the case of cyclic ones the boarding–leaving platform should be recalculated. This means that the problem considered is represented by a multistage numerical procedure and it is added to the next work schedule of the authors.

5. VEHICLE BOARDING AREA STUDY FOR PLATFORMS WITH A HEIGHT OF 760 MM ABOVE TOP OF RAIL

The boarding area of a railway vehicle is designed for platforms at a height of 550 mm above the top of the rail. The maximum value of an operational high of a boarding–leaving plate is expressed as 570 mm above the top of the rail. In a situation, where the vehicle stops at a platform with a maximum value of an operational high of 760 mm above the top of the rail, the height difference between the boarding levels is 190 mm.

This defines parameter δ_{v-} in the TSI PRM regulation [14]. The maximum permissible value of the δ_{v-} is 160 mm. This means that a railway vehicle does not meet the conditions according to the above-mentioned regulation and structural modifications to the vehicle's boarding area are required.

The current floor in the boarding area is sloped at an angle of 8.1° from the boarding edge to the centre and this is levelled in the middle of the vehicle. With reference to the input conditions, it is proposed to move the boarding plate 30 mm higher, that is, to a height of 600 mm above the top of the rail. With this change, the parameter δv– reached the minimum required value. The angle of slope of the ramp (8.5°) was also changed and the horizontal part of the boarding area followed 126 mm compared with the initial one reflecting the value equal to 455 mm (Fig. 14).

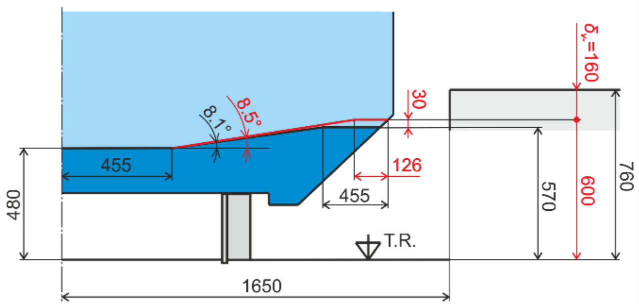

Fig. 14. Changes in the height and slope of the floor of the boarding area on the vehicle: black numbers follow initial dimensions; red numbers represent modified construction dimensions

It was also important to check the vertical clearance of the door. The standard [13] only defines boarding of a vehicle with a higher boarding edge with fixed interior steps from a lower platform (Fig. 15a). However, our case is the opposite: boarding from a higher platform to a vehicle with a lower boarding area that has no interior steps. For this reason, we considered the following:

– The lower line is directed from the edge of the platform to a point located at the end edge of the horizontal part where the floor begins to bend downwards towards the centre of the vehicle.
– The upper line is parallel to the lower line and is positioned to pass through the upper edge of the boarding area of the vehicle (Fig. 15b).

In this case, the useful vertical clearance l_1 has a value of 1,922 mm, which satisfies the condition of at least 1,900 mm, and we assume that a passenger with a height up to the value of parameter l_1 should not be restricted when boarding the vehicle.

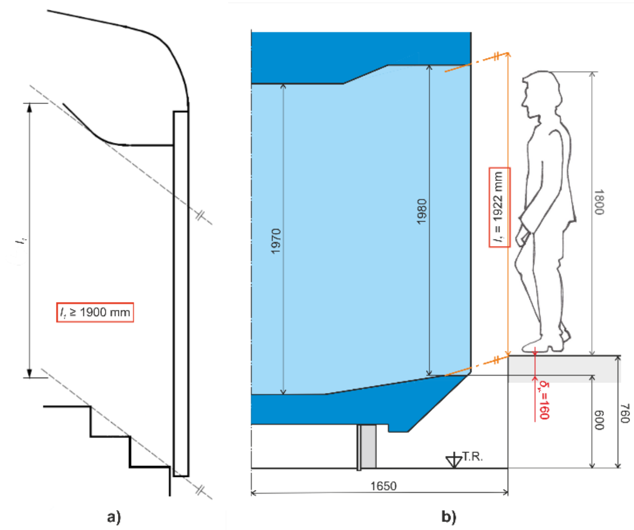

Fig. 15. Checking the vertical clearance of the vehicle's boarding area (a) according to STN EN 14752 and (b) own approach

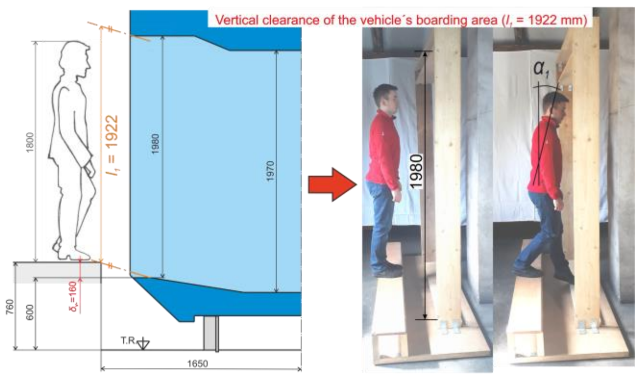

Fig. 16. Vehicle boarding test with vertical clearance l1 = 1,922 mm

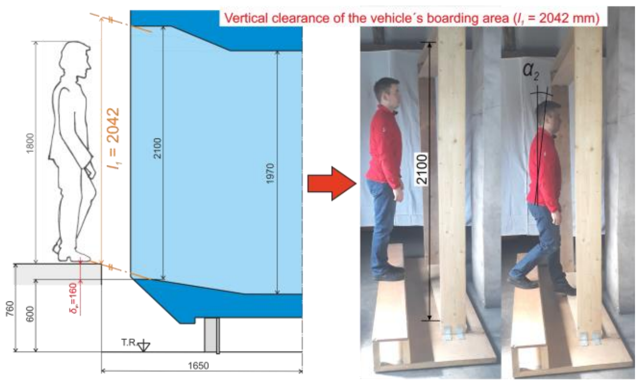

Fig. 17. Vehicle boarding test with vertical clearance l1 = 2,042 mm

However, the edge of the boarding area is above the height of a person standing on the railway platform. This case reflects that the passenger would be affected by his subjective feeling, which would cause him to bow his head when getting into the vehicle.

DOI 10.2478/ama-2023-0005

This idea was verified on a simple model: a vehicle's boarding area and a station platform. The test confirmed that the passenger tends to bow his head when boarding (Fig. 16, α_1).

Therefore, the height of the upper edge of the boarding was represented by 2,042 mm (Fig. 17), wherein $\alpha_2 < \alpha_1$. With this design, the passenger does not need to bow his head when entering the vehicle.

6. SUMMARY

This paper presented a new design of the boarding–leaving device for a railway vehicle at different height levels of platforms. The proposed construction, which was created on the basis of the authors' proposed objective function, combines a system of retractable and tilting steps, thanks to which passengers are boarded from plat-forms with a height ranging from 150 mm to 550 mm above the top of rail in accordance with the required European legislation [13, 17].

Selected parts of the device (a mechanism) which ensured tilting of the lower step was verified by a series of simulation calculations. Based on the FEM results the maximum calculated value of stress for first load conditions is 110 MPa, second is 344 MPa and third is 350 MPa. The most stressed parts of the structure are the bracket with the pin and the upper part of the arm in the area of the hole for locking in the end position. The largest value of displacement is located in the middle part of the lower step frame. Stress value proposed construction for the first, second and third load conditions below the yield stress of the material used (Re = 355 MPa). The designed device meets the current requirements of European legislation and after the optimization of selected structural elements, the prototype can be built and tested.

In the study of different clearance heights of the boarding opening on the model, a clearance height of the boarding opening of 2,100 mm proved to be the best compromise. The useful ground clearance l_1 is 2,042 mm, which meets the requirements of STN EN 14752. The ceiling edge of the boarding opening is located sufficiently above the head of the passenger standing on the platform. The passenger is not limited by the effect caused by the subjective feeling of bowing the head when entering the vehicle.

REFERENCES

1. 2050 long-term strategy. (Internet]. Available from: https://climate.ec.europa.eu/eu-action/climate-strategies-targets/2050-long-term-strategy_en#stakeholder-input (accessed on 1 July 2022).
2. City of Paris: Carbon Neutral by 2050 for a Fair, Inclusive and Resilient Transition | France. (Internet]. https://unfccc.int/climate-action/un-global-climate-action-awards/climate-leaders/city-of-paris (accessed on 1 July 2022).
3. Holloway C, Thoreau R, Roan T-R, Boampong D, Clarke Th, Watts D, Tyler N. Effect of vertical step height on boarding and alighting time of train passengers. Proceedings of the Institution of Mechanical Engineers, Part F: Journal of Rail and Rapid Transit 2016;230(4): 1234-1241. https://doi.org/10.1177/0954409715590480.
4. Thoreau R, Holloway C, Bansal G, Gharatya K, Roan T-R, Tyler N. Train design features affecting boarding and alighting of passengers. Journal of Advanced Transportation. 2016;50(8):2077-2088. Available from: https://doi.org/10.1002/atr.1446.
5. Gerlici J, Gorbunov M, Kravchenko K, Prosvirova O, Lack T. The innovative design of rolling stock brake elements. Communications - Scientific Letters of the University of Žilina. 2017;19(2):23-28.
6. Antony S, Long C, Becky PYL. Mengqiu C, Frank, W. Step-free railway station access in the UK: the value of inclusive design. European Transport Research Review. 2021; 13:1-12. https://doi.org/10.1186/s12544-021-00504-3.
7. Gerlici J, Gorbunov M, Nozhenko O, Pistek V, Kara S, Lack T, Kravchenko K. About creatiion of bogiie of the freiight car. Communications - Scientific Letters of the University of Žilina. 2017;19(2):29-35.
8. Gorbunov M, Gerlici J, Kara S, Nozhenko O, Chernyak G, Kravchenko K, Lack T. New principle schemes of freight cars bogies. Manufacturing Technology. 2018;18(2):233-238. https://doi.org/10.21062/ujep/83.2018/a/1213-2489/MT/18/2/233.
9. National strategy to boost accessibility for disabled passengers. (Internet]. Available from: https://www.gov.uk/government/news/national-strategy-to-boost-accessibility-for-disabled-passengers (accessed on 30 July 2022).
10. Sertler P. How parameters of infrastructure affect design of rolling stock for passenger transport. 21st International Conference on Current Problems in Rail Vehicles. 2013: 77-84.
11. Dižo J, Blatnicky M, Gerlici J, Leitner B, Melnik R, Semenov S, Mikhailov E, Kostrzewski M: Evaluation of ride comfort in a railway passenger car depending on a change of suspension parameters. Sensors. 2021;21(23):8138. https://doi.org/10.3390/s21238138.
12. Chudzikiewicz A, Krzyszkowski A, Stelmach A. Asymmetric threats in terms of safety of railway systems. Transport Problems, 2021;16(3): 131–140. https://doi.org/10.21307/TP-2021-047.
13. Commission regulation (EU) No 1299/2014 on the technical specifications for interoperability relating to the 'infrastructure' subsystem of the rail system in the European Union.
14. Commission regulation (EU) No 1300/2014 on the technical specifications for interoperability relating to accessibility of the Union's rail system for persons with disabilities and persons with reduced mobility.
15. The Disability Discrimination Act (DDA). (Internet]. Available from: https://www.sbb.ch/en/timetable/travel-advice/passengers-with-reduced-mobility/dda.html (accessed on 12 July 2022).
16. Accessible travel. (Internet]. Available from: https://www.sbb.ch/en/timetable/travel-advice/passengers-with-reduced-mobility/accessible-travel.html (accessed on 12 July 2022).
17. STN EN 14752+A1 (2022) Railway applications - Bodyside entrance systems for rolling stock.
18. Kundrata M, Tizek J. Double-deck push-pull trainsests Skoda. 24th International Conference on Current Problems in Rail Vehicles. 2019:389-398.
19. Blatnický M, Dižo J, Sága, M, Gerlici J, Kuba E. Design of a mechanical part of an automated platform for oblique manipulation. Applied Sciences. 2020;10(23):1-24. https://doi.org/10.3390/app10238467.
20. Kurčík P, Blatnický M, Dižo J, Pavlík A, Harušinec J. Design of a technical solution for a metro door system. Transportation Research Procedia.2019;40:67–773. https://doi.org/0.1016/j.trpro.2019.07.108.
Poppeová V, Bulej V, Zahoranský R, Uríček J. Parallel mechanism mechanism and its application in design of machine tool with numerical control. Applied Mechanics and Materials. 2013;282:74-79, 2013. https://doi.org/10.4028/www.scientific.net/AMM.282.74.
22. Fomin O, Gerlici J, Vatulia G, Lovska A, Kravchenko K. Determination of Vertical Accelerations in a Symmetrically Loaded Flat Car with Longitudinal Elastic-Frictional Beams. Symmetry. 2022;14(3):583. https://doi.org/10.3390/sym14030583.
23. Fomin O, Gorbunov M, Gerlici J, Vatulia G, Lovska A, Kravchenko K. Research into the strength of an open wagon with double sidewalls filled with aluminium foam. Materials. 2021;14(12):3420. https://doi.org/10.3390/ma14123420.
24. Koziak S, Chudzikiewicz A, Opala M, Melnik R. Virtual software testing and certification of railway vehicle from the point of view of their dynamics. Transportation Research Procedia. 2019;40:729–736. https://doi.org/10.1016/j.trpro.2019.07.103.

25. Kravchenko K, Gerlici J, Harusinec J, Kravchenko O. Research of the Characteristics of Wheel and Rail Contact under the Influence of Design and Operational Factors. Transport Means - Proceedings of the International Conference, 2021-October. 2021:865–870.
26. Kukulski J; Jacyna, M, Golebiowski P: Finite Element Method in Assessing Strength Properties of a Railway Surface and Its Elements. Symmetry. 2019;11(8):1014. https://doi.org/10.3390/sym11081014

This work was supported by the Cultural and Educational Grant Agency of the Ministry of Education of the Slovak Republic in the project No. KEGA 023ŽU-4/2020: Development of advanced virtual models for studying and investigation of transport means operation characteristics. This research was supported by the Cultural and Educational Grant Agency of the Ministry of Education of the Slovak Republic in the project No. KEGA 036ŽU-4/2021: Implementation of modern methods of computer and experimental analysis of the properties of vehicle components in the education of future vehicle designers.

Pavol Šťastniak: https://orcid.org/0000-0003-1128-7644

Michal Rakár: https://orcid.org/0000-0003-1164-3506

Jakub Tížek: https://orcid.org/0000-0003-2048-7226

DOI 10.2478/ama-2023-0006

A FLYWHEEL-BASED REGENERATIVE BRAKING SYSTEM FOR RAILWAY VEHICLES

Jacek JACKIEWICZ*

*Faculty of Mechatronics, Kazimierz Wielki University, ul. Kopernika 1, 85-074 Bydgoszcz, Poland

jacek.jackiewicz@ukw.edu.pl

received 25 June 2022, revised 30 October 2022, accepted 7 November 2022

Abstract: Regenerative braking is a technique that employs electric motors to convert the dynamic mechanical energy from the motor's spinning rotor and any attached loads into electricity. However, such a type of regenerative braking can only slow but not stop the vehicle because there is too little energy to excite the motor acting as a generator at low speeds. Therefore, this paper presents a unique flywheel-based regenerative braking system for railway vehicles. This system is supposed to meet high safety and comfort expectations in all operating conditions. The braking action control of this system should allow braking of empty or loaded vehicles according to load, the anti-blockage braking action of wheels and prevent wheel-slide during braking or wheel slip during acceleration. The new regenerative braking system under development, like any kinetic energy recovery system, requires the application of continuously variable transmission. The essence of the new solution is to design and build this type of variable transmission using only one planetary gear controlled through the powertrain control module for an electric motor cooperating concurrently. This paper describes complete modelling and simulation realisation on a closed-loop servomotor drive, which cooperates with the variable transmission of the regenerative braking system based on the Scilab/Xcos environment.

Key words: railway brakes, flywheel, regenerative braking system

1. INTRODUCTION

Various railway brakes [1] are used on vehicles of railway trains to enable the deceleration of vehicles and control of acceleration of train cars going down a slope. However, when a train is parked, they are used to keep its carriages immobile. Basic systems of railway brakes can be classified as follows: pneumatic, electric, hydraulic and mechanical. All of these systems can have various designs and structural arrangements.

Suburban trains should provide a short travel time between stations. The high acceleration of the train leaving the station and then a quick reduction of its speed before the next station caused by its braking ensure such a requirement. Therefore, operating at speeds no higher than 180 km/h, the suburban trains have increased numbers of driven wheels or wheelsets in their configurations. In addition, such types of trains are not only equipped with standard pneumatic and electric brakes but can quite often be equipped with rail brakes and eddy current brakes. Anyway, this way of the train moving between stations is associated with substantial energy losses during braking because most brakes use friction between two surfaces pressed together to convert the kinetic energy of the moving vehicles into heat, commonly.

This kinetic energy can be reclaimed and stored in a reusable manner by regenerative braking systems [2]. Increasingly more modern railway vehicles with electric drive systems have regenerative braking systems to not only capture but also apply this available form of power. During braking, due to the principle of reversibility of electrical machines, electric vehicles use their traction motors to convert kinetic energy into electromagnetic energy by switching them into generator operation mode. When electric currents are produced by these dynamo-motors, the electrical energy generated from such a process can be dissipated as heat through brake grid choppers or resistors (i.e., dynamic or rheostatic braking) or can be usefully and beneficially absorbed (i.e., regenerative braking). For electric railway vehicles and systems, regenerative braking offers the capability to return this recovered braking energy to the power supply line. Besides this, the recuperated energy can be stored on the train board automatically. This method of storing energy provides distinct benefits. Namely, the consumption of stored available energy can be as independent as possible from the power supply line, and the entire system can use such energy at any convenient moment. As the application to traction systems is considered 'hybrid', the ability to self-generate power by railway vehicles allows for their less dependence on railway electrification systems.

Hybrid and plug-in hybrid drive systems have become more and more frequent for diesel-electric multiple unit regional railway vehicles [3]. When considering the design of these vehicles, they are similar to locomotives with diesel engines or gas turbines. A significant difference is that hybrid vehicles have additional electric motors besides diesel or gas turbine power units. Electric energy generated in these vehicles can be stored in electric rechargeable batteries, supercapacitors or flywheels. The charging of these components can occur during running at the idle speed of the diesel generator or gas turbine and, moreover, braking when the kinetic energy of train vehicles is transformed into electric power.

Rechargeable batteries are usually used for electrical energy storage through a reversible chemical reaction, which allows the charge to be stored again after the battery has been drained. They can be made from different combinations of electrode materials and electrolytes. However, despite significant investments in research, around the world, for improving batteries, their use has some drawbacks. They are heavy concerning the amount of energy stored per unit mass (i.e., energy density), and their manufacturing is very costly [4]. Most importantly, their utility characteristics can significantly vary with changes in the ambient temperature of operation, which means the operation of hybrid systems equipped with batteries can be unpredictable, both in scorching heat and cold climates. In those climatic conditions, for electric batteries, it is necessary to create advanced systems for maintaining temperatures in their predetermined operating range. It entails an additional cost due to supplementary energy usage.

Aside from the technology of electric rechargeable battery packs, alternate main methods of energy storage captured via regenerative braking are the technology of supercapacitor arrays (which store potential energy depending on their state of electric charging), the technology of rotating flywheels (which store kinetic energy in the form of angular momentum) as well as compressed fluid energy storage systems. The methods of storing energy built on supercapacitors and rotating flywheels perform very reasonably and are less susceptible than electric batteries to the influence of temperature. Supercapacitors can be charged very quickly, and, by their number of cycles of charging and discharging, they have a leading position at the current time. However, supercapacitors have a shortcoming concerning their low specific energy and the limited efficiency time because of linearly reducing their voltage as power is drawn. In turn, the batteries hold their voltage during the discharging period. In the applications used so far, the rotating flywheels have a good enough ability to store energy and a virtually unlimited number of charge cycles. Comparing them with supercapacitors and batteries in terms of size, weight and operation characteristics, they are inferior. Tungsten heavy alloys (WHAs), based on W-Ni-Cu and W-Ni-Fe, belong to a group of two-phase composites [5]. Due to their advantageous combinations of high density, strength and ductility WHAs can be used as basic materials for rotors of flywheels. Moreover, penetrators in all cannon-fired kinetic energy projectiles are made of WHAs and, more often, depleted uranium (DU) alloys, U-3/4Ti, as well. Note the chemical symbol, W, of the rare metal tungsten comes from its old Swedish name, wolfram.

Nowadays, flywheels offer a reliable and durable solution for storing kinetic energy. Such a storing energy method has the potential to bring significant efficiency gains and cost reductions for mass rapid transit networks [6]. The key to efficiency improvements in rail transport is to provide a local energy storage capability, which can capture and store energy produced by braking systems and deliver it on demand to reduce the power required for an accelerating train. Moreover, any flywheel-based regeneration system can stabilise the traction power system voltage by eliminating voltage sags and peaks appearing when braking energy is dissipated through brake resistors [7, 8]. Flywheel-based energy storage technology is both proven and mature. Such technology provides a low-risk and low-cost solution as well. Flywheels have a high level of reliability, durability, and availability. They can operate continuously with two-minute minimum headways of trains without compromising product life [9, 10].

The performance of a mechanical energy storage system in the form of a flywheel depends on the properties of the used drivetrain. In [11], Read compared the operation of two drive transmission options, considering the efficiency of energy recovery from the flywheel. He examined two representative drive transmission methods: (a) electric powertrain (consisting of motor/generator, power electronics, motor, and final drive) and (b) mechanical toroidal continuously variable transmission with the final drive. These drivetrains can change seamlessly through a continuous range of gear ratios. However, they operate with efficiencies that do not exceed more than 80%. Additionally, as stated by Zhang et al. [12], control is crucial to guarantee the performance of any flywheel energy storage system.

Because of the above, the primary goal of this paper is to present a new concept of a regenerative braking system based on a flywheel. At the same time, the proposed new solution is to improve the energy efficiency of the mechanical continuously variable transmission conveying the propulsion between the flywheel and the wheels of the rail vehicle. This solution requires the design of a new control system for a servo motor that should smoothly change the gear ratio between active and passive shafts of the planetary gear to maintain a constant command value for the drive torque.

2. NEW KINETIC ENERGY STORAGE SYSTEM ABOARD RAILWAY VEHICLES

Increasing the acceleration and deceleration of trains within a railway network can improve the performance of railway passenger transport. Such a requirement is particularly desirable for urban, suburban, and regional trains, which should feature relatively high acceleration and deceleration. Passenger comfort must be additionally considered when designing railway transit systems for their performance and cost-effectiveness. It should be kept in mind that with high accelerations and decelerations of railway vehicles, the risk of passengers losing their balance and falling is also increased [13]. Between two adjacent stations, any train's run can be divided into three stages: (i) starting from the station to accelerate to a stable cruise speed, (ii) running at the cruise speed for some time, and (iii) decelerating and stopping at the next station in an interval.

This work intends to create an effective regenerative braking system for self-propelled railway vehicles. Since most railway vehicles are powered by electricity supplied through overhead contact lines or diesel engines, which are turbocharging except for a few, this recuperating braking system will be appropriate for both these drive types. Moreover, this system is incorporated into all rail vehicles, which can accelerate and decelerate quickly.

However, achieving a tractive effort diagram similar to that which can be obtainable with the electric traction systems operating so far poses a problem for vehicles powered only by diesel engines. Namely, the piston engines cannot be started under load, cannot reverse rotation direction, and do not provide a constant starting tractive effort. Therefore, transmission is necessary between the diesel engine and the railway wheels. Most diesel locomotives are diesel-electric [14]. They have all the components of a series hybrid transmission to make the drive systems more flexible and environmentally friendly. For that reason, a hybrid drive system that uses an onboard flywheel-based rechargeable energy storage system is taken here as a starting point because it can be used in both electric multiple units and electro-diesel multiple units. Recovering kinetic energy via a flywheel through regenerative braking seems promising for self-propelled railway vehicles with frequent starts/stops (see [15, 16]). Such a system in railway vehicles will have a meaningful effect on

DOI 10.2478/ama-2023-0006

energy saving; it can also drive systems to become more flexible and, at the same time, environmentally friendly. However, like any kinetic energy recovery system, the new regenerative braking system requires the application of continuously variable transmission. The essence of the new solution is to design and build this type of variable transmission using only one planetary gear controlled through the powertrain control module for a FAULHABER DC servo motor with an integrated motion controller [17], cooperating concurrently.

Fig. 1 shows a schematic representation of the hybrid traction system, which combines a motor-generator (MG) power source with the new braking energy recovery system for the electric multiple-unit bogie. The energy recovery system is mainly composed of the assembly of two flywheels, the control clutch 1, the bevel gear transmission, and the clutch 2, as a coupling device. The assembly of flywheels is used for energy storage. Both of these flywheels operate in vacuum containers. The first differential transmission is utilised to change smoothly the varying gear ratio between the powertrain and assembly of two flywheels by applying theservo motor. The clutch 2 is used to control processes of engagement, release, and sliding friction of connection between the flywheel energy storage system and drive transmission of the electric multiple-unit bogie. When electric multiple units are used for braking, the clutch is engaged gradually, and the flywheels are accelerated. If the flywheels accelerate to a certain borderline degree, the clutch is disconnected, and the flywheels rotate at a high speed in the vacuum chamber.

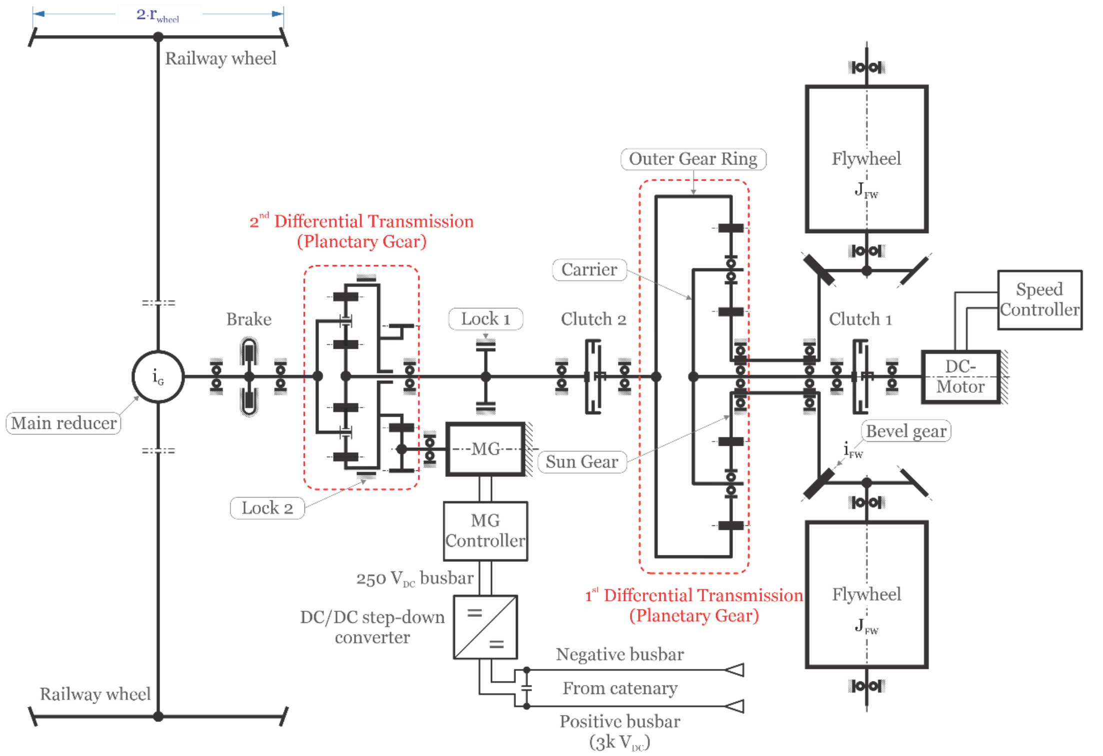

Fig. 1. Hybrid traction system, which combines motor-generator power source with mechanical flywheel energy storage system

As shown in the figure above, both differential transmissions comprise three shafts – the sun gear, the planet carrier, and the external ring gear. During regenerative braking, the three-shaft operation mode of the first planetary gear is used, in which two shafts of the outer ring and the carrier are driven, and the sun shaft is the driver. In such a case, the planetary gearset operates as a summation gear train.

Planetary gearsets are characterised by their high efficiency with the transfer of torque of large values, even in small construction spaces. They are suitable for clockwise or counter-clockwise use and in alternating, constant, and intermittent operations.

According to the analytical method of Willis [18], if the angular velocities of the two input shafts of the planetary gearset are known, the angular velocity of the output shaft can be determined by the following equation:

$$\omega_{\mathrm{C}}^{(i)}=\frac{\mathrm{N}_{\mathrm{S}}^{(i)}}{\mathrm{N}_{\mathrm{R}}^{(i)}+\mathrm{N}_{\mathrm{S}}^{(i)}}\,\omega_{\mathrm{S}}^{(i)}+\frac{\mathrm{N}_{\mathrm{R}}^{(i)}}{\mathrm{N}_{\mathrm{R}}^{(i)}+\mathrm{N}_{\mathrm{S}}^{(i)}}\,\omega_{\mathrm{R}}^{(i)}\ , \qquad (1)$$

where $\omega_{\mathrm{C}}^{(i)}$, $\omega_{\mathrm{S}}^{(i)}$, and $\omega_{\mathrm{R}}^{(i)}$ are the angular velocities of the planet carrier, sun gear, and ring, respectively. In turn, $\mathrm{N}_{\mathrm{S}}^{(i)}$ and $\mathrm{N}_{\mathrm{R}}^{(i)}$ are the numbers of teeth of the sun gear and ring, respectively. In Eq. (1), the superscript, $^{(i)}$, denotes the differential transmission number.

Let's assume for a while that all gear pairs of the first differential transmission are operating with 100% efficiency. If this is the case, the total power entering and leaving the gearbox must also add up to zero [19] as follows:

$$\mathrm{M}_{\mathrm{C}}^{(i)}\omega_{\mathrm{C}}^{(i)}+\mathrm{M}_{\mathrm{S}}^{(i)}\omega_{\mathrm{S}}^{(i)}+\mathrm{M}_{\mathrm{R}}^{(i)}\omega_{\mathrm{R}}^{(i)}=0\ , \qquad (2)$$

where $\mathrm{M}_{\mathrm{C}}^{(i)}$, $\mathrm{M}_{\mathrm{S}}^{(i)}$ and $\mathrm{M}_{\mathrm{R}}^{(i)}$ determine the torque of the carrier, torque of the sun, and the torque of the ring (annulus), respectively. Moreover, to ensure invariable values of the following torques: $\mathrm{M}_{\mathrm{C}}^{(1)}$, $\mathrm{M}_{\mathrm{S}}^{(1)}$, and $\mathrm{M}_{\mathrm{R}}^{(1)}$ during deceleration or braking of the railway vehicle, the angular accelerations of the three main components of the planetary gearset (i.e., $\dot{\omega}_{\mathrm{C}}^{(1)}$, $\dot{\omega}_{\mathrm{S}}^{(1)}$, and $\dot{\omega}_{\mathrm{R}}^{(1)}$) should also be constant. Hence, the differentiation of both sides of Eq. (2) gives

$$\mathrm{M}_{\mathrm{C}}^{(1)}\dot{\omega}_{\mathrm{C}}^{(1)}+\mathrm{M}_{\mathrm{S}}^{(1)}\dot{\omega}_{\mathrm{S}}^{(1)}+\mathrm{M}_{\mathrm{R}}^{(1)}\dot{\omega}_{\mathrm{R}}^{(1)}=0\,. \tag{3}$$

The above condition is necessary to meet because according to Newton's Second Law of Motion in rotation, the net torque, M_{FW}, on the rotating mass with variable angular speed, $\omega_{\mathrm{FW}}(t)$, and mass moment of inertia, J_{FW}, causes it to accelerate with angular acceleration, $\varepsilon_{\mathrm{FW}}\overset{\mathrm{def}}{=}\dot{\omega}_{\mathrm{FW}}$:

$$M_{\mathrm{FW}}=\mathrm{J}_{\mathrm{FW}}\cdot\varepsilon_{\mathrm{FW}}\,. \tag{4}$$

As shown in Fig. 1, $\omega_{\mathrm{FW}}=\mathrm{i}_{\mathrm{FW}}\cdot\omega_{\mathrm{S}}^{(1)}$, where i_{FW} = 4.245 is the bevel gear ratio. For the first planetary gear, the teeth # of the sun is $\mathrm{N}_{\mathrm{S}}^{(1)}$ = 37, the teeth # of the ring is $\mathrm{N}_{\mathrm{R}}^{(1)}$ = 73.

To obtain greater efficiency of the drive transmission of the mechanical flywheel energy storage system proposed here than in the known solutions used so far, it is necessary that the value of the moment, $\mathrm{M}_{\mathrm{C}}^{(1)}$, should be close to zero. In this case, the flow of kinetic energy during the charging and discharging of such a variant of the so-called 'mechanical' battery will take place with very little loss.

The required value of the angular acceleration, $\varepsilon_{\mathrm{R}}^{(1)}\overset{\mathrm{def}}{=}\dot{\omega}_{\mathrm{R}}^{(1)}$, and the value of the torque, $\mathrm{M}_{\mathrm{R}}^{(1)}$, can be determined for given values of deceleration or acceleration of the rail vehicle and based on the analysis of its drive system. Then, considering Eqs (3) and (4), the angular acceleration, $\varepsilon_{\mathrm{S}}^{(1)}\overset{\mathrm{def}}{=}\dot{\omega}_{\mathrm{S}}^{(1)}$, and the torque, $\mathrm{M}_{\mathrm{S}}^{(1)}$, should be determined. Thus, using Eq. (1), the required value of the angular acceleration, $\varepsilon_{\mathrm{C}}^{(1)}\overset{\mathrm{def}}{=}\dot{\omega}_{\mathrm{C}}^{(1)}$, can be established, as well as the range of angular velocities of the carrier shaft from its initial to final values. Therefore, the control strategy for the FAULHABER DC servo motor to determine its desired changes of angular velocity and acceleration (or deceleration, as well) has a dramatic impact on the performance of this system, which constitutes the first differential transmission.

Similar to the first differential transmission, the second one is the speed-coupling unit, which constitutes the hybrid drivetrain.

In Fig. 1, the flywheel energy storage system supplies power to the sun gear through a clutch and transmission. The second differential transmission is used to modify the speed-torque characteristics to match the traction requirements. For this planetary gear, the teeth # of the sun is $\mathrm{N}_{\mathrm{S}}^{(2)}$ = 30, the teeth # of the ring is $\mathrm{N}_{\mathrm{R}}^{(2)}$ = 76.

The electric motor-generator supplies power to the ring gear of the second planetary gear. Lock 1 and lock 2 are used respectively to lock the sun gear and ring gear to the standstill frame of the vehicle to satisfy the different operation mode requirements. The following operation modes can be distinguished [20]:

- Hybrid traction: When lock 1 and lock 2 are released (the sun gear and ring gear can rotate), both the flywheel energy storage system and motor generator supply positive torque (positive power) to the driven wheels.
- Flywheel energy storage system alone traction or alone regenerative braking: When lock 2 locks the ring gear to the vehicle frame and lock 1 is released, only the flywheel energy storage system supplies power to the driven wheels or performs regenerative braking.
- Motor-generator alone traction: When lock 1 locks the sun gear to the vehicle frame (clutch 2 is disengaged) and lock 2 is released, only the motor-generator supplies power to the driven wheels.
- Motor-generator alone regenerative braking: When lock 1 is set in locking state, the clutch 2 is disengaged, and the motor-generator is controlled in regenerating operation (negative torque), the kinetic energy of the vehicle can be transferred by the electric system to the catenary.
- Supplying electric energy to the catenary from the flywheel energy storage system: When lock 1 and lock 2 are released, the rail vehicle brake is locked, and the flywheel energy storage system supplies positive power to the railway traction network.

The following condition, $\varepsilon_{\mathrm{R}}^{(2)}=\varepsilon_{\mathrm{S}}^{(2)}=\varepsilon_{\mathrm{C}}^{(2)}$, is assumed for the hybrid traction mode, which can be performed during acceleration or deceleration. Note that $\mathrm{M}_{\mathrm{C}}^{(2)}=\mathrm{M}_{\mathrm{wheels}}/\mathrm{i}_{\mathrm{G}}$, where $\mathrm{M}_{\mathrm{wheels}}$ is the total torque transmitted by railway wheels of one drive axle, and i_{G} = 2.39 is the final drive ratio.

3. CONCEPT OF THE CONTROL SYSTEM OF THE DC SERVO MOTOR

Correct operation of the flywheel-based regenerative braking system requires designing and building a reliable control system for the DC motorafterward. This motor can easily be speed-controlled by modifying the supply voltage providing a consistent amount of torque over its entire speed range.

The first step to designing a closed-loop control system is to identify a mathematical representation of the DC motor [21]. The DC motor can be best represented by a transfer function of a complex variable, s. The transfer function, which diagram block is shown in Fig. 2, provides a mathematical description for the DC motor that relates input voltage, $\mathcal{V}_{\mathrm{m}}(s)$, to the angular velocity of the motor shaft, $\Omega_{\mathrm{m}}(s)$. Note that the angular velocity is $\omega_{\mathrm{m}}(t)\overset{\mathrm{def}}{=}\dot{\theta}_{\mathrm{m}}(t)$, where θ_{m} is the angular position of the motor shaft. $\Omega_{\mathrm{m}}(s)$ and $\mathcal{V}_{\mathrm{m}}(s)$ are the signal Laplace transforms of $\omega_{\mathrm{m}}(t)$ and $v_{\mathrm{m}}(t)$, respectively.

Hence, the following equation represents the model of the DC motor:

$$\frac{\Omega_{\mathrm{m}}(s)}{\mathcal{V}_{\mathrm{m}}(s)}=\frac{\mathrm{K}_{\mathrm{m}}}{\mathrm{J}_{\mathrm{eq}}\mathrm{R}_{\mathrm{m}}s+\mathrm{K}_{\mathrm{m}}^{2}}\,, \tag{5}$$

where K_{m} = 0.028 Vs/rad, R_{m} = 3.3 Ω, and J_{eq} = 9.64·10-6 kg·m2 are the motor back ElectroMotive Force (EMF) constant, motor armature resistance, and equivalent moment of inertia, respectively.

The next step is to choose a control method and design a controller. The feedback system in Fig. 2 is a single-loop feedback system with a proportional-integral-derivative (PID) controller, which the controller gains (i.e., k_{P}, k_{D}, and k_{I}) should be determined to satisfy all design specifications. This closed-loop control system uses the measurement of the output and feedback of the angular motor shaft position signal, θ_{m}, to compare it with the desired input (reference or command), θ_{d}. Since the intended purpose of the control is to simultaneously determine the desired angular velocity, $\omega_{\mathrm{d}}(t)$, and the angular acceleration (or deceleration) of the motor shaft, ε_{d}, this concept of the single-input, single-output (SISO) control system is inadequate here.

DOI 10.2478/ama-2023-0006

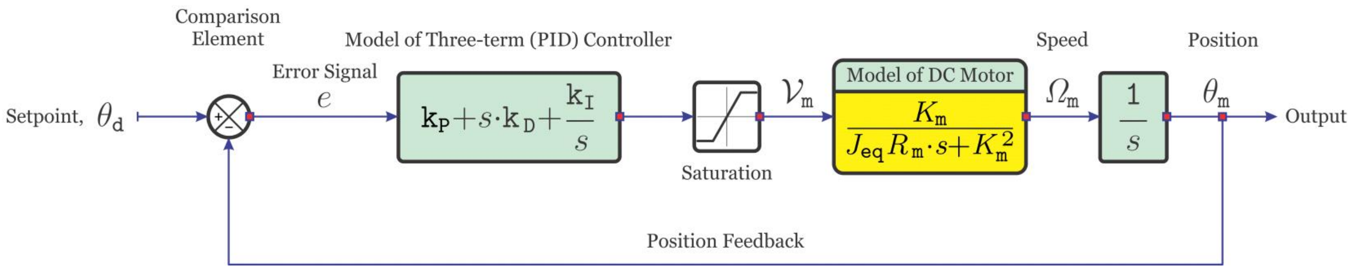

Fig. 2. Schematic of a closed-loop control system for the DC motor with PID controller. PID, proportional-integral-derivative

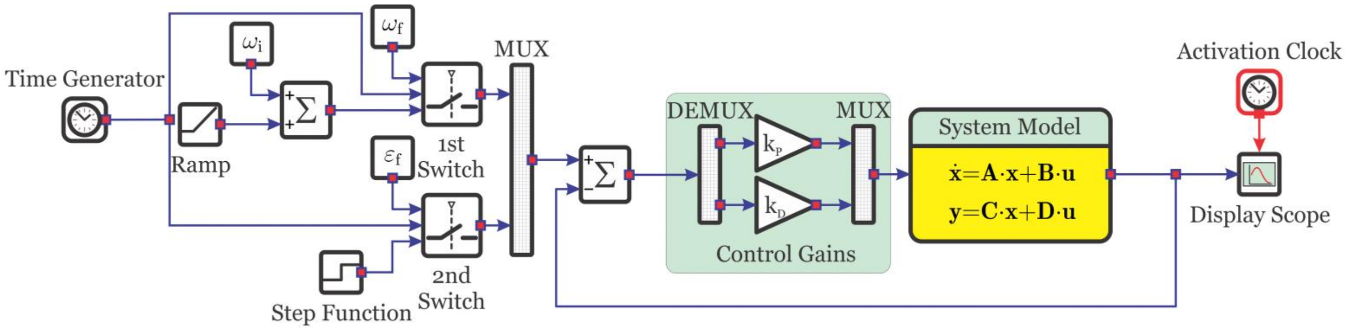

Fig. 3. Conceptual design configuration for the state-space PD feedback control. PD, proportional-derivative

Given the transfer function of the SISO system, $\Omega_m(s)/\mathcal{V}_m(s)$, it can be obtained from its multiple input-output (MIMO) state-space representations [22, 23], which is represented by the following equations:

$$\dot{\mathbf{x}}(t) = \mathbf{A} \cdot \mathbf{x}(t) + \mathbf{B} \cdot \mathbf{u}(t)\,, \tag{6}$$

$$\mathbf{y}(t) = \mathbf{C} \cdot \mathbf{x}(t) + \mathbf{D} \cdot \mathbf{u}(t)\,, \tag{7}$$

for $t \geq t_0$ and initial conditions $\mathbf{x}(t_0)$, where $\mathbf{A}$, $\mathbf{B}$, $\mathbf{C}$, and $\mathbf{D}$ are the system, input, output, and feedforward matrixes, respectively. In Eqs (6) and (7), $\mathbf{x}(t)$ is the state vector, $\dot{\mathbf{x}}(t)$ is the derivative of the state vector to time, $\mathbf{y}(t)$ is the output vector, and $\mathbf{u}(t)$ is the input (or control) vector. Eq. (6) is called the state differential equation, and Eq. (7) is the output equation.

Using Eq. (5), the transfer function of the DC motor can be converted to the state-space representation as follows

$$\begin{Bmatrix} \dot{\omega}(t) \\ \dot{\varepsilon}(t) \end{Bmatrix} = \begin{bmatrix} \frac{-K_m^2}{J_{eq} R_m} & 0 \\ 0 & \frac{-K_m^2}{J_{eq} R_m} \end{bmatrix} \begin{Bmatrix} \omega(t) \\ \varepsilon(t) \end{Bmatrix} + \\ + \begin{bmatrix} \frac{K_m}{J_{eq} R_m} & 0 \\ 0 & \frac{K_m}{J_{eq} R_m} \end{bmatrix} \begin{Bmatrix} \mathcal{V}_m(t) \\ \dot{\mathcal{V}}_m(t) \end{Bmatrix}, \tag{8}$$

$$\begin{Bmatrix} \omega(t) \\ \varepsilon(t) \end{Bmatrix} = \begin{bmatrix} 1 & 0 \\ 0 & 1 \end{bmatrix} \begin{Bmatrix} \omega(t) \\ \varepsilon(t) \end{Bmatrix}. \tag{9}$$

After coupling with a proportional- derivative (PD) compensator, as shown in Fig. 3, the above model creates a control system that meets the design assumptions regarding the possibility of simultaneous control of the variable linearly angular velocity of the electric motor shaft, $\omega(t)$, for a predetermined constant angular acceleration (or deceleration), $\varepsilon(t)$. In the block diagram performed by Xcos/Scilab software of Fig. 3, ε_f stands for the constant acceleration (or deceleration) in the assumed period, and ω_i and ω_f stand for the initial and final velocities, respectively. In Fig. 3, k_P = 100 and k_D = 10 denotes the proportional and derivative gains, respectively.

4. COMPUTATIONAL RESULTS

The new energy recovery hybrid system with flywheels can use various operation modes listed in Section 2. Of these five strategies, let's look at the second one, i.e., 'flywheel energy storage system alone traction or alone regenerative braking'.

For computer simulations, parameters of a typical high-speed railway multiple unit train, i.e., CRH380A, are selected from Appendix A of [24]. The maximum operating speed of the train CRH380A can be up to 380 km / h. However, its regular operating speed is 350 km / h.

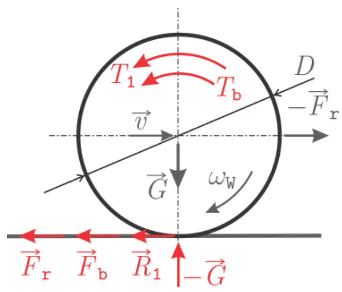

Fig. 4. Forces acting on a rotating wheel during braking

The emergency braking deceleration of some trains reaches 1.4 m/s2, and the standard braking deceleration is 1.1 m/s2. However, according to data in Table 1 presented in [25], the vehicle Sheffield Supertram (Siemens-Düwag) can brake with a deceleration of 3 m/s2 using emergency track brakes. But their use carries a high risk of passenger injury.

DOI 10.2478/ama-2023-0006

Tab. 1. Example maximum accelerations for railway vehicles in Great Britain

Vehicle	Maximum acceleration (m/s²)		
	Traction	Service brakes	Emergency brakes
Class 390 Pendolino (intercity EMU)	0.37	0.88	1.18
Class 156 Super Sprinter (regional DMU)	0.75	0.7–0.8	0.7–0.8
Class 323 (suburban EMU)	0.99	0.88	1.18
London Underground 1992 tube stock	1.3	1.15	1.4
Tyne and Wear Metrocar	1.0	1.15	2.1 (*)
Manchester tram (Ansaldo T-68)	1.3	1.3	2.6 (*)
Sheffield Supertram (Siemens-Düwag)	1.3	1.5	3.0 (*)
Croydon tram (Bombardier FLEXITY)	1.2	1.3	2.73 (*)
Nottingham tram (Bombardier)	1.2	1.4	2.5 (*)

(*) As experience has shown, emergency track brakes are used as a last resort because their use carries a high risk of passenger injury.

The distribution of the forces acting on the braked wheel is depicted in Fig. 4. The wheel is subject to the following forces:

– the vertical forces $\vec{G}$ and $-\vec{G}$, considered in the cases of load-bearing and traction wheels,
– the resisting torque T_1, corresponding to the resistance $\vec{R}_1$,
– the braking torque $T_\mathrm{b} = F_\mathrm{b} \cdot \mathrm{D}/2$ (The overall reaction of the ground on the wheel is thus given by the resistance force $\vec{F}_\mathrm{r} = \vec{F}_\mathrm{b} + \vec{R}_1$),
– the horizontal force $-\vec{F}_\mathrm{r}$ applied to the spindle in the direction of motion, which is equal in magnitude to the ground reaction $\vec{F}_\mathrm{r}$.

Given that all driving and load-bearing wheelsets of the train are always braked, for adhesion conditions to apply, it is necessary that

$$F_\mathrm{b} \leq f(v) \cdot G \,, \tag{10}$$

where $f(v)$ is the coefficient of friction between the shoe and the rail, which depends on train speed, v.

Example 1: Regenerative braking of the multiple unit train from a speed of 50–0 m/s (all wheels at each bogie are braked in a regenerative manner with the train deceleration, aD = 1 m/s2)

In braking a train, the braking forces have to be applied to the wheels rapidly, systematically, and under control to prevent derailments. The braking operation should not be damaging to the train and its passengers. Under normal conditions, during braking, efforts should be taken to avoid any discomfort to the passengers, and if at all, it should be kept to the barest minimum.

The brake time is $t = V_0/a \cdot t$ = 50 s, and the brake distance $s = V_0 \cdot t - ½ \cdot a_\mathrm{D} \cdot t^2$ = 1250 m. Given that $\mathrm{m_{CAR}}$= 52362 kg, the total brake force per one car $F_\mathrm{b} = \mathrm{m_{CAR}} \cdot a$ = 52362 N, and the brake energy, $W_\mathrm{b} = F_\mathrm{b} \cdot s$ = 65452500 J. Because of the small moment of the inertia of the car wheels compared to the flywheels, the contribution of the wheel's change of energy is not significant. The wheel radius is $\mathrm{r_{wheel}}$ = 0.43 m and the moment of the inertia of both the same flywheels is $\mathrm{J_{FW}}$ = 5 kg·m2. The initial speed of the flywheels is ω_FW= 0 rad/s. Furthermore, the stored kinetic energy in both the flywheels is E_K = 65452500 J. Fig. 5 shows how the angular velocities of the ring, sun gear, and planet carrier of the first differential transmission are changed during braking. Fig. 6 shows the implementation of planet carrier control by the FAULHABER DC servo motor with an integrated motion controller during braking.

The torque values are as follows: $\mathrm{M_C^{(1)}} \approx$ 0 N·m, $\mathrm{M_R^{(1)}}$ = 1333.1 N·m and $\mathrm{M_S^{(1)}}$ = -1536 N·m. The ratio of the second planetary gear is constant and equals $\omega_\mathrm{S}^{(2)}/\omega_\mathrm{C}^{(2)}$ = 3.5333.

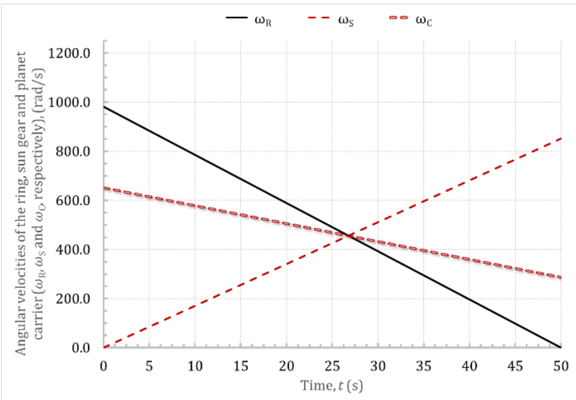

Fig. 5. Changes in the angular velocities of the ring, sun gear, and planet carrier during braking (Example 1)

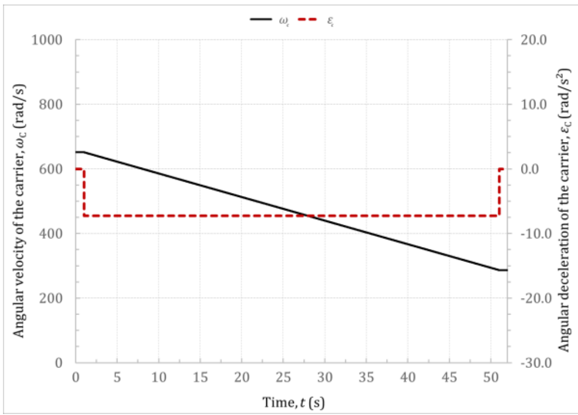

Fig. 6. Course of planet carrier control by the electric motor MG during braking (Example 1)

Example 2: Regenerative emergency braking of the multiple unit train from a speed of 50–0 m/s (all wheels at each bogie are braked in a regenerative manner with the train deceleration, aD = 3 m/s2)

DOI 10.2478/ama-2023-0006

The brake time is $t = V_0/a \cdot t$ = 16.67 s, and the brake distance $s = V_0 \cdot t - ½ \cdot a_D \cdot t^2$ = 416.67 m. The total brake force per one car $F_b = m_{CAR} \cdot a$ = 157084.74 N, and the brake energy, $W_b = F_b \cdot s$ = 65452500 J. The initial speed of the flywheels is ω_{FW} = 0 rad/s. Furthermore, the stored kinetic energy in both the flywheels is E_K = 65452500 J. Fig. 7 shows how the angular velocities of the ring, sun gear, and planet carrier have changed during braking. Fig. 8 shows the implementation of planet carrier control by the FAULHABER DC servo motor during braking.

The torque values are as follows: $M_C^{(1)} \approx 0$ N·m, $M_R^{(1)}$ = 3999.4 N·m and $M_S^{(1)}$ = -4607.9 N·m. The ratio of the second planetary gear is the same as in the previous example and equals $\omega_S^{(2)}/\omega_C^{(2)}$ = 3.5333.

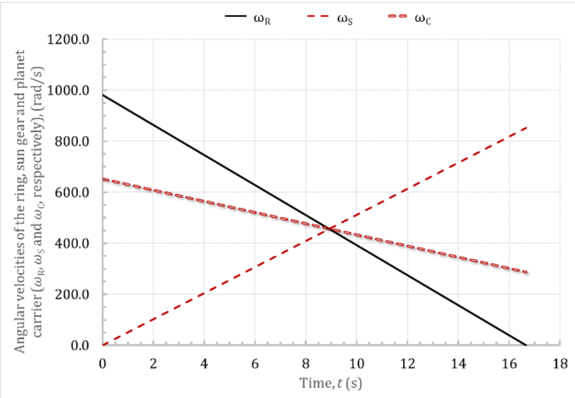

Fig. 7. Changes in the angular velocities of the ring, sun gear, and planet carrier during braking (Example 2)

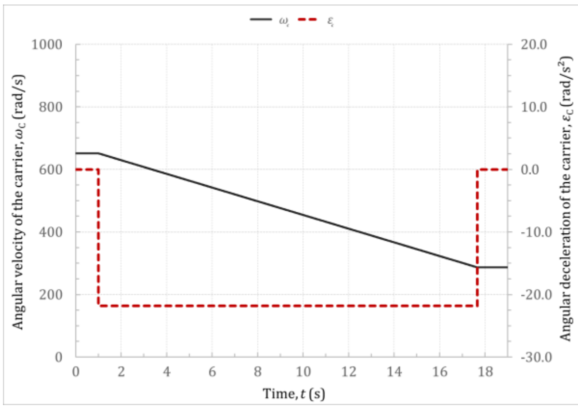

Fig. 8. Course of planet carrier control by the electric motor MG during braking (Example 2)

Example 3: Acceleration of the multiple unit train using only the energy stored in the flywheels moving from a speed of 0–50 m/s (the train acceleration, a = 1 m/s2)

The accelerating time is t = 50 s, and the traveled distance $s = ½ \cdot a \cdot t^2$ = 1250 m. The consumed kinetic energy from both the flywheels is E_K = 65452500 J. Fig. 9 shows how the angular velocities of the ring, sun gear, and planet carrier have changed during acceleration. Fig. 10 shows the implementation of planet carrier control by the FAULHABER DC servo motor during acceleration.

The torque values are as follows: $M_C^{(1)} \approx 0$ N·m, $M_S^{(1)}$ = 1536 N·m and $M_R^{(1)}$ = -1333.1 N·m. The ratio of the second planetary gear is also the same as in the previous example and equals $\omega_S^{(2)}/\omega_C^{(2)}$ = 3.5333.

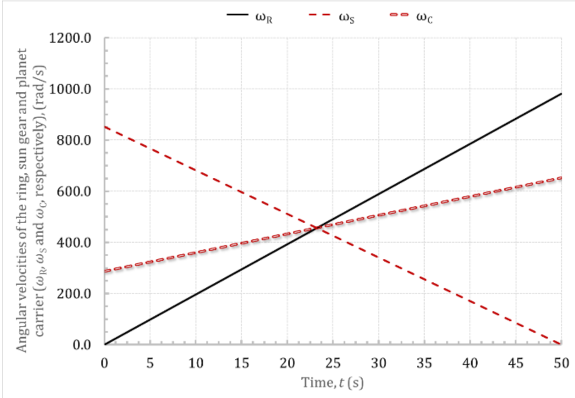

Fig. 9. Changes in the angular velocities of the ring, sun gear, and planet carrier during accelerating (Example 3)

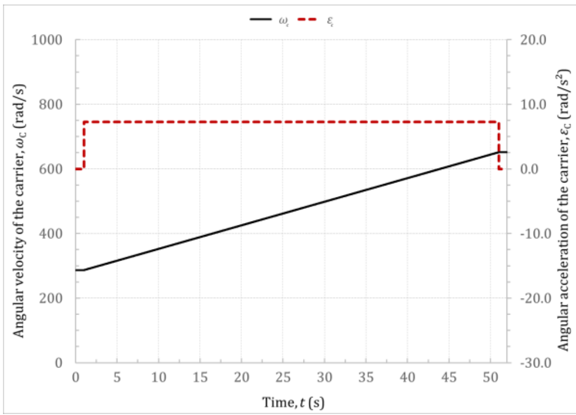

Fig. 10. Course of planet carrier control by the electric motor MG during accelerating (Example 3)

5. CONCLUSIONS

The article describes the new concept of a regenerative braking system based on flywheels, which gives a chance to introduce a more effective solution than the previously known ones. The new mechanical hybrid kinetic energy recovery system is designed under the design process of mechatronic systems. The proposed system uses new innovative, continuously variable transmission to discharge and charge the 'mechanical' batteries. This innovative transmission method offers the opportunity to obtain more desirable energy savings than before during the regenerative braking of electric multi-unit trains.

It is easy to notice that the use of a mechatronic approach during designing a new energy recovery hybrid system with flywheels significantly simplified the mechanical structure of this system. The control system of the new regenerative braking method is less complicated even compared to the control of continuously variable toroidal gears. It is an additional advantage of this solution.

The proposed system provides the ability of rail vehicles to reuse braking energy which is not lost but stored in the flywheels. However, as it has been established for railway vehicles operating at speeds up to 200 km/h, about 40% of the energy is consumed for traction (i.e., lost during variation of the kinetic energy of vehicles). Another 40% of the energy is spent by natural oscillations of the running gear and their interconnections between cars (see [26, 27]). Of the remaining 20%, 10% is consumed to overcome the frictional forces in the systems and components of railway vehicles and the interaction forces between wheels and rails, and the remainder of 10% is used to overcome air resistance.

REFERENCES

1. Spiryagin M, Cole C, Sun YQ, McClanachan M, Spiryagin V, McSweeney T. Design and simulation of rail vehicles. Boca Raton: CRC press; 2014.
2. Latto L. Regenerative braking systems in rail applications [Internet]. 2014 [cited 2022 June 20]. Available from: https://connectorsupplier.com/regenerative-braking-systems-rail-applications/
3. Kapetanović M, Vajihi M, Goverde RM. Analysis of hybrid and plug-In hybrid alternative propulsion systems for regional diesel-electric multiple unit trains. Energies. 2021; 14(18): 5920. Available from: https://doi.org/10.3390/en14185920
4. Duffner F, Mauler L, Wentker M, Leker J, Winter M. Large-scale automotive battery cell manufacturing: Analyzing strategic and operational effects on manufacturing costs. International Journal of Production Economics. 2021; 232: 107982. Available from: https://doi.org/10.1016/j.ijpe.2020.107982
5. Şahin Y. Recent progress in processing of tungsten heavy alloys. Journal of Powder Technology. 2014; Hindawi Publishing Corporation. Article ID 764306. Available from: http: //dx.doi.org /10.1155/ 2014/764306
6. Morant S. Flywheel technology generates energy efficiencies for metros. International Railway Journal [Internet]. 2017 [cited 2022 June 20]. Available from: https://www.railjournal.com/in_depth/ flywheel-technology-generates-energy-efficiencies-for- metros/
7. Khodaparastan M, Mohamed A. Flywheel vs. supercapacitor as wayside energy storage for electric rail transit systems. Inventions. 2019; 4(4): 62.
8. Qu X, Tian L, Li J, Lou C, Jiang T. Research on charging and discharging strategies of regenerative braking energy recovery system for metro flywheel. In: 3rd Asia energy and electrical engineering symposium (AEEES). IEEE. 2021: 1087-1095.
9. Meishner F, Sauer DU. Wayside energy recovery systems in DC urban railway grids. ETransportation. 2019; 1: 100001.
10. VYCON. Vycon - the proven flywheel energy storage system for rail [Internet]. 2017 [cited 2022 June 20]. Available from: https://vyconenergy.com/2017/03/13/vycon-showcases-flywheel-energy-storage-system-for-metro-rail-power-regeneration-at-asia-pacific-rail-expo/
11. Read M. Flywheel energy storage systems for rail. Doctoral dissertation. London: Imperial College; 2011.
12. Zhang JW, Wang YH, Liu GC, Tian GZ. A review of control strategies for flywheel energy storage system and a case study with matrix converter. Energy Reports. 2022; 8: 3948-3963.
13. Wu Q, Li Y, Dan P. Optimization of urban rail transit station spacing for minimizing passenger travel time. Journal of Rail Transport Planning & Management. 2022; 22: 100317. Available from: https://doi.org/ 10.1016/j.jrtpm.2022.100317
14. Brenna M, Foiadelli F, Zaninelli D. Electrical railway transportation systems. Hoboken, New Jersey: Wiley; 2018.
15. Sardar A, Dey RK, Muttana SB. A deep dive into kinetic energy recovery systems—Part 1. Auto Tech Review. 2015; 4(6): 20-25.
16. Sardar A, Dey RK, Muttana SB. A deep dive into kinetic energy recovery systems—Part 2. Auto Tech Review. 2015; 4(7): 20-24.
17. Faulhaber. DC-Motors with integrated Electronics. Technical information [Internet]. 2022 [cited 2022 June 20]. Available from: www.faulhaber-group.com
18. Arnaudo K, Karaivanov DP. Planetary gear trains. Boca Raton: CRC Press; 2019.
19. Machowski J, Lubosny Z, Bialek JW, Bumby JR. Power system dynamics: stability and control. Hoboken: Wiley; 2020.
20. Emadi, A. (Ed.). Handbook of automotive power electronics and motor drives. Boca Raton: CRC press; 2017.
21. Teach tough concepts: Closed-loop control with LabVIEW and a DC motor [Internet]. 2020 [cited 2022 June 20]. Available from: https: //knowledge.ni.com/KnowledgeArticleDetails?id=kA03q000000YHx8CAG&l=en-US
22. Dorf RC, Bishop RH. Modern control systems. 14th ed. Harlow: Pearson Education; 2022.
23. Jackiewicz J. Optimal control of automotive multivariable dynamical systems. In: Awrejcewicz J, editor. Dynamical systems theory and applications. Cham: Springer; 2017. p. 151–168.
24. Zhai W. Vehicle–track coupled dynamics: theory and applications. Singapore: Springer; 2020.
25. Powell, JP, Palacín R. Passenger stability within moving railway vehicles: Limits on maximum longitudinal acceleration.Urban Rail Transit. 2015; 1(2): 95-103.
26. Jackiewicz J. Coupler force reduction method for multiple-unit trains using a new hierarchical control system. Railway Engineering Science. 2021; 29: 163-182. Available from: https: //link.springer.com/article/ 10.1007/s40534-021-00239-w
27. Jackiewicz, J. Modeling the longitudinal dynamics of electric multiple units with Xcos/Scilab software. In: IOP conference series: Materials science and engineering. 2021; 1199(1): 012066. Available from: https://iopscience.iop.org/article/ 10.1088/1757-899X/1199/1/012066/meta

Jacek Jackiewicz: https://orcid.org/0000-0001-7284-7639

DOI 10.2478/ama-2023-0007

INVESTIGATION OF DRIVING STABILITY OF A VEHICLE–TRAILER COMBINATION DEPENDING ON THE LOAD'S POSITION WITHIN THE TRAILER

Ján DIŽO*, Miroslav BLATNICKÝ*, Paweł DROŹDZIEL**
Rafał MELNIK*, Jacek CABAN**, Adam KAFRIK***

*Faculty of Mechanical Engineering, University of Žilina, Univerzitná 8215/1, 010 26 Žilina, Slovakia
**Faculty of Mechanical Engineering, Lublin University of Technology, ul. Nadbystrzycka 36, 20-618 Lublin, Poland
***Faculty of Computer Science and Technology, Lomza State University of Applied Sciences,
ul. Akademicka 14, 18-400 Łomża, Poland

jan.dizo@fstroj.uniza.sk, miroslav.blatnicky@fstroj.uniza.sk, p.drozdziel@pollub.pl,
rmelnik@ansl.edu.pl, j.caban@pollub.pl, kafrik@uniza.sk

received 27 June 2022, revised 5 November 2022, accepted 27 November 2022

Abstract: Passenger cars are a means of transportation used widely for various purposes. The category that a vehicle belongs to is largely responsible for determining its size and storage capacity. There are situations when the capacity of a passenger vehicle is not sufficient. On the one hand, this insufficient capacity is related to a paucity in the space needed for stowing luggage. It is possible to mount a rooftop cargo carrier or a roof basket on the roof of a vehicle. If a vehicle is equipped with a towbar, a towbar cargo carrier can be used for improving its space capacity. These accessories, however, offer limited additional space, and the maximal load is determined by the maximal payload of the concerned vehicle. If, on the other hand, there is a requirement for transporting a load with a mass or dimensions that are greater than what could be supported using these accessories, then, provided the vehicle is equipped with a towbar, a trailer represents an elegant solution for such demanding requirements. A standard flat trailer allows the transportation of goods of various characters, such as goods on pallets, bulk material, etc. However, the towing of a trailer changes the distribution of the loads, together with changes of loads of individual axes of the vehicle–trailer axles. The distribution of the loads is one of the key factors affecting the driving properties of a vehicle–trailer combination in terms of driving stability, which is mainly a function of the distribution of the load on the trailer. This research introduces a study into how the distribution of the load on a trailer influences the driving stability of a vehicle–trailer combination. The research activities are based on simulation computations performed in a commercial multibody software. While the results presented in the article are reached for a particular vehicle–trailer combination as well as for a particular set of driving conditions, the applicability of the findings can also be extended more generally to the impact that the load distributions corresponding to various vehicle–trailer combinations have on the related parameters and other driving properties.

Key words: driving stability, vehicle–trailer combination, multibody simulation

1. INTRODUCTION

Trailers are used for transport of goods for shorter as well as longer distances. An important reason why trailers were developed and why their use still finds widespread prevalence is the steadily increasing need for transport, specifically the transport of cargo whose volume and weight exceed what could possibly be supported by the transport capacities typically associated with the engines of road vehicles.

Modelling and simulation is very important for science and research. Mechanical engineers use virtual models and software for modelling of road vehicles every day and these constitute an inseparable part of their work activities. These models allow the investigation of reactions and responses of road vehicles or road vehicle–trailer combinations to changes of input parameters, their driving properties and other factors, and additionally allow researchers to ascertain various means by which a reduction can be achieved in the cost associated with development and testing [1–3]. It is possible to obtain valuable information about an investigated subject in relatively short time. In this work, the investigation undertaken concerns the driving stability of a vehicle–trailer combination that is exposed to various effects, such as different roadway surface qualities, load distributions, driving speeds and other parameters [1, 4].

The main objective of this research is to analyse the driving properties of a vehicle with a trailer depending on a position of the load on a trailer loading area. The research is performed using a commercial multibody software, Simpack. It has been necessary to input to this software the researchers' own model of a vehicle and a trailer.

Although a number of studies have been conducted with regard to the influence that the driving properties of vehicle–trailer combinations exert on these vehicles in a state of motion, some characteristics, such as the dimensions, weight and occasionally other parameters, are specific for a particular combination.

There are various scientific works focussing on the investigation of the driving properties of vehicle–trailer combinations. They are aimed at assessing the manoeuvrability, handling, braking properties and behaviour of vehicle–trailer combinations. These researches are performed in various ways, such as by means of simulation computations, experimental tests, analytical models and other similar methods [5–8]. As the mentioned studies have shown, the driving properties of vehicle–trailer combinations are often and also significantly influenced by braking during driving manoeuvres [9–12]. However, in our research, the effects of braking during a movement of a vehicle–trailer combination are not investigated. This is because our research aims to ascertain the exact moment when, given that it is travelling at a constant driving speed, a vehicle–trailer combination comes into an unstable movement. On one hand, the multibody model allows the definition of a braking of the combination; however, on the other hand, the authors of the present study do not have access to the representative data, which would enable a driver's behaviour to be simulated as part of the overall simulated operational situations [10, 13, 14]. This matter can be a subject of study for future research. Further, the investigated vehicle–trailer combination is not equipped with a braking system (i.e. it does not have an overrun brake) [9, 15–17], and therefore, the braking operation has not been considered at all during simulated manoeuvres comprising the present study.

2. SIMULATION COMPUTATION OF A VEHICLE–TRAILER COMBINATION

A simulation involves experimentation with a virtual computation model, which represents a real vehicle. The goal is to optimise its properties before the final production. A simulation is widely accepted as a scientific method, and it is an apparatus of almost every scientific activity. While the accuracy obtained as a result of performing experimentation under actual real-world conditions is certainly desirable, the particular circumstances under which experiments are performed may not in themselves be adequately representative of the real-world conditions prevailing for the duration of time to which the research findings are sought to be extrapolated. For this reason, real-world experimentation may fail to manifest findings representing true, exact, structured and systematic facts, which necessities the use of simulations. A simulation works with a certain model of a vehicle, i.e. with an idealised form of a real vehicle. It can be understood that a simulation is an experiment with a model.

In the present study, simulation computation has been performed using Simpack software. It is a multibody software that enables virtual models of vehicles and vehicle combinations to be set-up, including nonlinearities [18–20]. A created MBS (multibody system) model of a vehicle and a trailer consists of rigid bodies interconnected by force elements. These force elements include massless components of a model, such as coil springs, hydraulic dampers, further torsion bars, components of wheels' suspension systems and others. Moreover, in the case of road vehicles, the Simpack software offers special force elements, which include models for tyre–road contact.

3. RESEARCH OF DRIVING OF A VEHICLE WITH A TRAILER WITH VARIOUS POSITIONS OF A LOAD

In practice, many accidents happen because a driver does not distribute a load on a loading area of a trailer to a proper position. These accidents are observed mostly in the case of passenger cars to which a single-axle trailer has been attached. In the case of single-axle trailers, drivers should ensure that a proper load will act upon a towbar. This maximal load is defined in a road law [21]. However, many drivers are not able to estimate this load, which leads either to an overload of a towbar in a vertical direction or to a towbar load that is too small [22–24]. A towbar overload can cause problems with the suspension system of a tow vehicle's rear axle. However, an even bigger problem can occur, if the centre of gravity (CoG) of the load, or of the entire trailer, is situated behind the trailer axle. Depending of the total weight of the trailer, this can cause the load distribution to become precariously skewed in such a way that the rear axle of the vehicle bears the least load, which can seriously compromise the steerability of the vehicle; this phenomenon is indeed the result of several serious road accidents. In particular, some instances of particular vulnerability for the loss of steerability to take place are driving in a curve and driving over road irregularities; and other circumstances, such as taking a sharp turn, could also be responsible for loss of vehicle control while attempting steering [25–28]. Accordingly, using simulation with the Simpack software, the present research introduces the results of analyses of various driving situations of a vehicle–trailer combination.

During investigation of the dynamics of vehicles or vehicle–trailer combinations, various output quantities are evaluated. From the dynamics point of view, acceleration signals are the most important. These signals pertain to accelerations in various locations of a vehicle [29]. These locations are chosen in such a way that the driving comfort can be evaluated [30–33]. Other quantities are forces, which most often pertain to the driving safety. In the presented research, the signals of accelerations would not find a direct application to the investigated phenomenon, i.e. the driving safety and driving stability of the vehicle–trailer combination [34–36]. Therefore, the wheel forces have been chosen as the main output parameters. In mentioning these forces, we refer to the lateral wheel forces between the trailer tyre and the roadway surface. In principle, either a left or a right wheel can be evaluated. In our case, we have decided to evaluate the lateral forces of the left wheel.

It is important to estimate the limit value of these forces. It can be assessed from multiple points of view. The limit value of the lateral wheel force has been estimated as the zero value of this force. This stance is an outcome of the fact that zero lateral force means slipping a wheel on the roadway surface, i.e. the danger of an accident. There has not been estimated any other limit value for the lateral wheel force.

3.1. An MBS model of a vehicle–trailer combination

A road model has been selected from the Simpack model database. Subsequently, CAD (computer-aided design) models of individual bodies of the passenger car and the single-axle trailer, such as car bodywork, wheels, the trailer frame and others have been imported to a model. Mechanical and kinematic joints have been defined between:
- a trailer towing bar and a trailer frame;
- a vehicle bodywork and a suspension system;
- a suspension system and a wheel; and
- a wheel and a roadway surface.

A vehicle–trailer combination model is shown in Fig. 1.

DOI 10.2478/ama-2023-0007

Fig. 2 depicts selected dimensions of the vehicle–trailer combination, and the basic parameters of the towing vehicle are listed in Tab. 1.

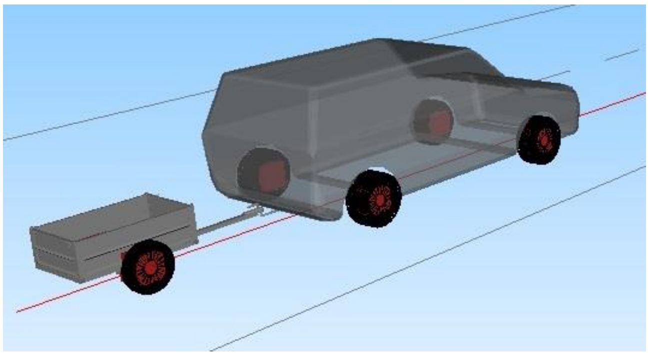

Fig. 1. A vehicle–trailer combination model

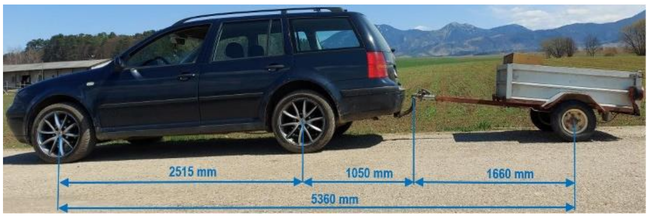

Fig. 2. Dimensions of the vehicle–trailer combination

Tab. 1. Parameters of the towing vehicle

Parameter	Value (mm)
Length	4,397
Height	1,473
Width	1,735
Wheelbase	2,515

The superstructure of the trailer has dimensions of 1,300 mm (the length) and 1,000 mm (the width).

Within the research, various driving situations have been evaluated. These have been observed with reference to the output parameters total vertical force and lateral force. Further, the research has investigated a situation of driving in a curve when a load with the total weight of 220 kg has been placed on the trailer loading area. The vehicle–trailer combination has been driving on the road at the speed of 55 km/h and the load has been positioned in such a way that the CoG of the load is located:

– in the front part of the trailer;
– in the rear part of the trailer; or
– behind the trailer.

Moreover, the research investigates a maximal speed, at which a vehicle–trailer combination is able to drive in a curve safely. The vehicle–trailer combination has been driving on a road with a specified geometry. The road geometry has been created based on experiences of researchers and it has not corresponded to any real road. The road profile has been chosen in such a manner that the equanimity or steadiness of the movement of the vehicle–trailer combination would be disturbed even under optimal driving conditions. The road geometry in the horizontal plane is shown in Figs. 3 and 4; from these images, we infer the road curvatures in the corresponding locations. Additionally, the road tracking in the Simpack software is depicted in Fig. 5.

The modelled road profile is comprised of several sections, which are the following: a straight section of 20 m, a right-handed curve with a radius of 30 m, a left-handed curve with a radius of 20 m, a straight section of 10 m and finally two curves – firstly a left-handed curve and then a right-handed one, each with the radius of 20 m. Fig. 3 provides the view from below to the road profile (as the software renders it).

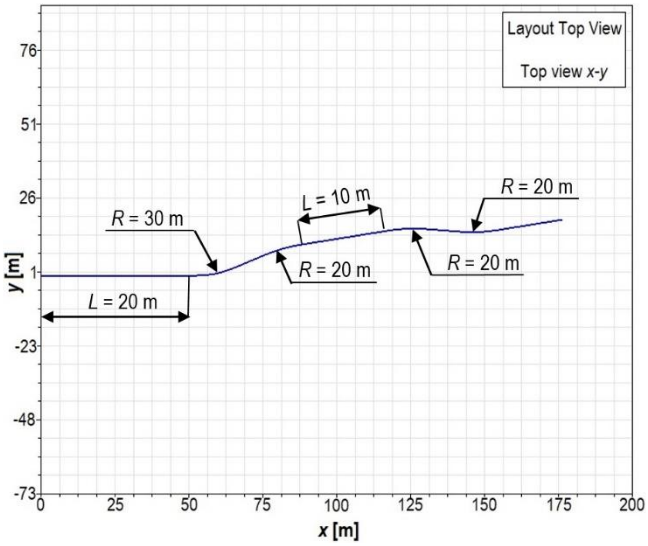

Fig. 3. Road geometry shown in a horizontal plane

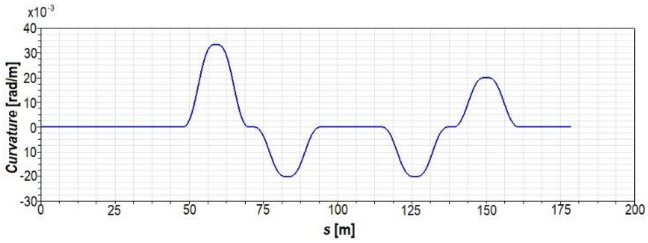

Fig. 4. The curvature of the created road

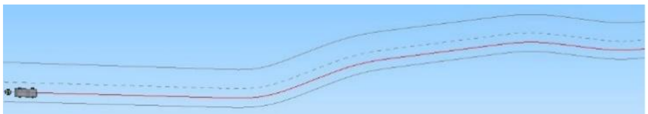

Fig. 5. A testing road in the Simpack software

An important element of simulation-based computations of movement of a vehicle (or an entire vehicle–trailer combination) is a model of tyre–road contact. There are several models of tyre–road contacts that are available for researchers to study, as well as available in the used Simpack software. In our case, a tyre–road model called the Pajecka contact model has been used [37, 38]. The parameters are defined through a text file, which has been used in conjunction with a setting win-dow applicable to this modelling element

The defined tyre–road model includes parameters for dimensions of tyres, vertical and lateral stiffness of tyres, damping coefficients, roadway surface coefficients and others. In the created vehicle–trailer combination, three different tyre–road models have been applied, namely for the front wheels of the vehicle, for the

DOI 10.2478/ama-2023-0007

rear wheels of the vehicle and for the trailer wheels. While the tyre model of the trailer wheels has been very different in comparison with the tyre models of the vehicle, the tyre models of the front and rear wheels have differed only in having stiffness values and damping coefficients that are slightly different from each other, and this minute difference was caused by variations in the tyres' air pressure values. The friction coefficient has been set to the value of 0.75 for all tyre–road contacts [37–40].

3.2. The CoG of the load located in the front part of the trailer

The trailer has been loaded with a load of 220 kg. The curb weight of the trailer is 180 kg, and together with the load, this gives a total weight of 400 kg. The driving speed of the vehicle–trailer combination has been set to a value of 55 km/h. The load has been deposited in the front part of the trailer. A comparison between an actual vehicle–trailer combination operating under real-world conditions, and the same combination according to the MBS model employed in the present research, is shown in Figs. 6 and 7.

Fig. 6. A real vehicle–trailer combination with the load deposited in the front part of the trailer

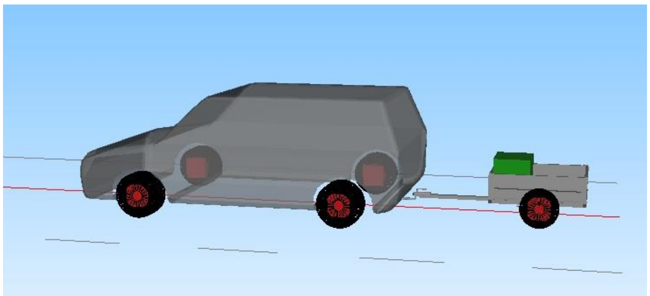

Fig. 7. An MBS model of a vehicle–trailer combination with the load deposited in the front part of the trailer

In this case, in order to determine the optimal position within the trailer in which the load may be de-posited, it is first necessary to obtain the maximum permissible load that can be borne by the towing ball of the vehicle. For the chosen vehicle, 75 kg is pre-scribed as the maximal permissible vertical load. The same load can be represented as 735.75 N in terms of force (together with the gravitational acceler-ation being considered at g = 9.81 m/s2). The CoG of the trailer is given by its design, and it is located 115 mm in front of the axle (in the driving direction). If the dimensions of the trailer and the vehicle–trailer combination (Fig. 2) were considered, then, for our particular case corresponding to a load of 220 kg, the maximum allowable distance within which the CoG needs to be located would be 471.82 mm in front of the trailer axle. The internal length of the superstructure of the trailer and the dimensions of the designed load allow the load to be placed in such a position that the CoG of the trailer is located 400 mm in front of the trailer axle. This is depicted in Figs. 6 and 7. It means that the permissible vertical load of the towing ball of the vehicle of 735.75 N is not exceeded.

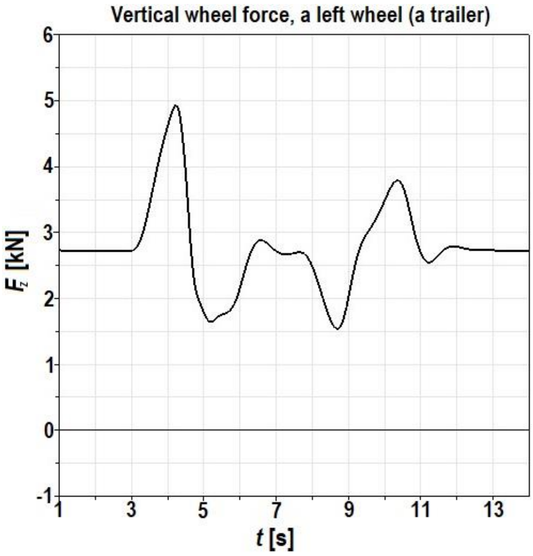

Fig. 8. A waveform of the total vertical wheel force of the trailer (a left wheel), with the load located in the front part of the trailer

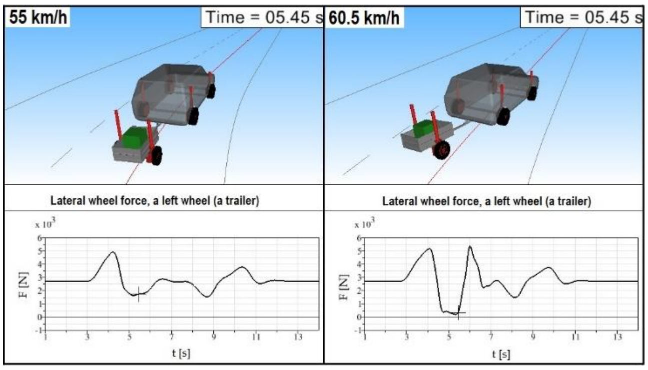

Fig. 9. A comparison of situations for the driving speeds of 55 km/h and 60.5 km/h

The results of a waveform of the vertical wheel force of the left wheel of the trailer (shown in Fig. 8) demonstrate that a vehicle–trailer combination has been able to safety drive in the curve. Further, 60.5 km/h has been identified as the maximal speed at which a vehicle–trailer combination with the described configura-tion is able to safely drive along the given curve. The speed of 61 km/h leads to the loss of wheel–road contact and skid occurs. A comparison of the total vertical force of the trailer wheel for two different speeds is shown in Fig. 9.

3.3. The CoG of the load located in the rear part of the trailer

For investigating the driving properties of the vehicle–trailer combination, this time with the load placed in the rear, a load quantity was chosen such that the total weight amounted to the same 220 kg, and the chosen driving speed also remained the same at 55 km/h. Again, the driving of the vehicle–trailer combination on the same road and with the same curves' radii has been investigated. Figs. 10 and 11 illustrate a comparison of a real vehicle–trailer combination with an MBS model, with the load deposited in the rear part of the trailer.

Fig. 10. A real vehicle–trailer combination with the load deposited in the rear part of the trailer

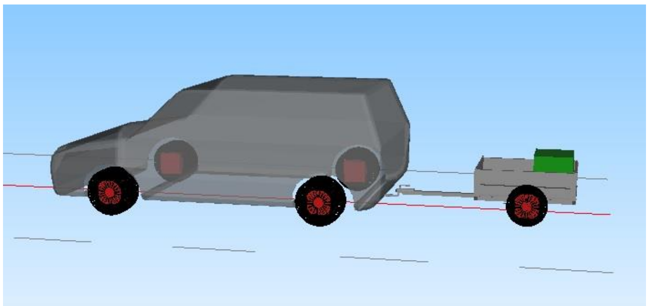

Fig. 11. An MBS model of a vehicle–trailer combination with the load deposited in the rear part of the trailer

Based on the calculated output parameters, it is ascertained that the vehicle–trailer combination is able to drive through the curve safely. On the one hand, the trailer was moving in a slight oscillating movement in the horizontal plane; however, on the other hand, after overcoming the curve, the drive of the vehicle–trailer combination was stabilised.

The acting of the total vertical wheel force between a wheel of the trailer and the road is depicted in Fig. 12.

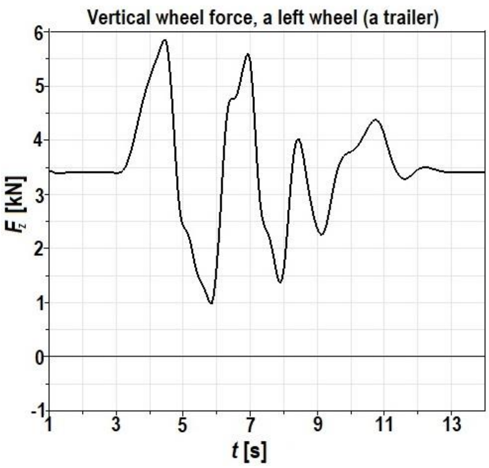

Fig. 12. A waveform of the total vertical wheel force of the trailer, with the load located in the rear part of the trailer.

3.4. The CoG of the load located behind the trailer

This is a case of load-carrying involving a trailer, wherein the driver uses the trailer to transport lengthy items, such as wooden beams, metal plates or rods or other similar objects. In such a case, the CoG of the load is usually located behind the trailer, as can be seen in Fig. 13. A multibody model of the vehicle–trailer combination with the load situated behind the trailer is depicted in Fig. 14.

Fig. 13. A real vehicle–trailer combination with the CoG of the load situated behind the trailer

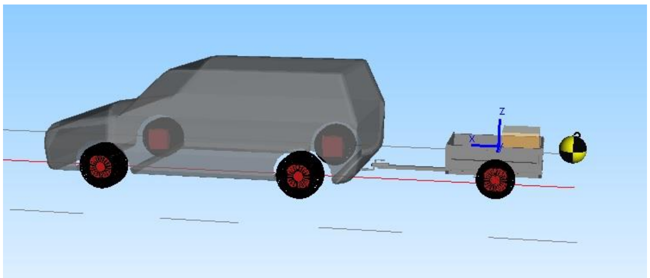

Fig. 14. An MBS model of a vehicle–trailer combination with the CoG load situated behind the trailer

The parameters of the load and the inputs for the simulation have again been the same, i.e. the total weight (the sum of the curb and load weights) has been set as 220 kg and the driving speed has been set as 55 km/h. The CoG of the load located behind the trailer is marked by a black-yellow sphere (Fig. 14).

The passage of the vehicle–trailer combination along the same path as in the previous cases has been examined.

The vehicle–trailer combination has not passed the test of driving in curves. When it was moving along the first curve, a skid occurred and the vehicle–trailer combination was ejected out of the road (Fig. 15). A waveform of the total vertical force on the left wheel of the trailer is shown in Fig. 15. As can be seen, the vertical wheel force in the time interval 6.5–8 s equals 0, which means that no lateral force could be generated, resultant to which the trailer slides to the side.

For this case, a waveform of the lateral wheel force of the left rear wheel of the vehicle is shown in Fig. 16. This waveform reveals that the rear part of the vehicle oscillates around a mean value. Practically, this corresponds to the oscillating movement of the rear part of the vehicle, and this movement of the vehicle is uncontrolled. Due to the described facts (trailer dimensions, load dimension, the permissible vertical load of the towing ball and the load value), the position of the load presented in Section 3.2 is recommended for these particular conditions.

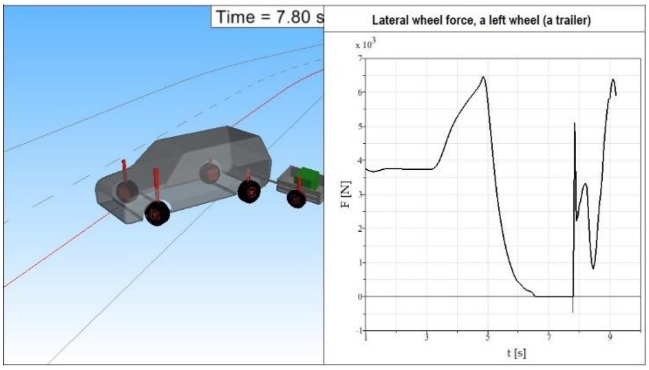

Fig. 15. A waveform of the wheel force of the trailer, a left wheel

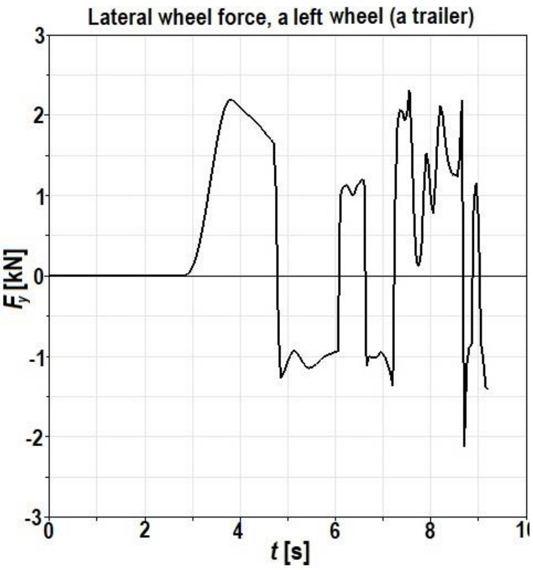

Fig. 16. A waveform of the lateral wheel force of the trailer, with the CoG of the load located behind the trailer

The future research in this field will be focussed on performing simulations with vehicle–trailer combinations with different parameters, i.e. for vehicles and trailers of different categories. Further, the multibody model can be improved by implementation of flexible bodies. Such a multibody model will better represent some structural properties of a vehicle, a trailer or even both.

As is obvious, the presented results are obtained from simulation-based computations. The credibility of simulation-based computations should be verified through comparisons with the results of experimental tests [9, 29]. Such tests can be performed using a real vehicle–trailer combination or, alternatively, using a scale model [41]. Each of these approaches has its own advantages and disadvantages depending on the point of view. While experiments deploying a real vehicle-and-trailer pair provide actual results, results derived from tests performed using a scale model need to undergo a certain process of conversion before they can be compared with parameters pertaining to real vehicles. In terms of safety and financial costs, scale models appear more advantageous, because an expensive infrastructure would be required for conducting tests with real vehicles (a road without public traffic, a vehicle and trailer with a safety system in a case of overturning, etc.) [42].

4. CONCLUSIONS

The main goal of the paper was to investigate the dependence of the driving properties of a vehicle–trailer combination on the load positions. The work consisted in creating the CAD models of a vehicle and a trailer. Subsequently, these CAD models of vehicles were implemented within the framework of the MBS software Simpack. After defining the mass and inertia parameters of the vehicles, various simulation computations were performed.

Three possibilities of depositing a load on the loading area of a trailer were compared. It has been discovered during the research that a small change in driving speed and in the position of the load can cause a deterioration of driving properties in terms of driving stability, i.e. can result in the vehicle–trailer combination sliding off the road or even overturning.

Using an MBS software such as Simpack, it is possible to relatively easily introduce changes in the various driving situations and parameters concerning the investigated vehicles. Such an exercise is helpful for evaluating and assessing the driving properties of vehicles without calling forth the risk that would be involved in performing dangerous driving manoeuvres with a real vehicle–trailer combination.

The simulations demonstrated in the present study, performed with the use of MBS software, have revealed the most dangerous position that can be used for depositing a load on a trailer, together with more favourable positions. The obtained results and findings introduce a more general benefit, in that it can be assumed that vehicle–trailer combinations with different parameters (with regard to vehicle and a trailer dimensions) will also behave in a similar way. A driver must avoid a situation wherein the CoG of the load on the trailer is situated behind the trailer axle, even behind the trailer itself. Such a position of the load leads to a considerable lightening of the weight-burden of the rear axle of the towing vehicle, and driving at a higher speed in this condition can thus result in a dangerous accident.

REFERENCES

1. Gerlici J, Sakhno V, Yefymenko A, Verbitskii V, Kravchenko A, Kravchenko K. The stability analysis of two-wheeled vehicle model. MATEC Web of Conference. 2018; 157: 1-10. https://doi.org/10.1051/matecconf/201815701007
2. Aldughaiyem A, Salamah YB, Ahmad I. Control Design and Assessment for a revesing tractor – trailer system using a cascade controller. Applied Sciences [Internet]. 2021 Nov 11; 11(22): 10634. Available form: https://doi.org/10.3390/app112210634
3. Mikhailov AV, Zhigulskaya AI, Kasakov YA. Modeling of peat tractor semi-trailer motion. International Conference Aviation Engineering and Transportatin (AviaEnT 2020), September 21-26, 2020, Irkutsk, Russia. https://doi.org/10.1088/1757-899X/1061/1/012026
4. Milani S, Unlusoy YS, Marzbani H, Jazar RN. Semitrailer Steering control for improved articulated vehicle manoeuvrability and stability. Nonlinear Engineering. 2019; 8(1): 568-581. https://doi.org/10.1515/nleng-2018-0124
5. Emheisen MA, Emirler MT, Ozkan B. Lateral stability control of articulated heavy vehicles based on active steering system. International Journal of Mechanical Engineering and Robotics Research. 2022; 11(8): 575-582. https://doi.org/10.18178/ijmerr.11.8.575-582
6. Chen Y, Peterson AW, Zhang C, Ahmdian M. A simulation-based comparative study on lateral characteristics of trucks with double and triple trailers. International Journal of Vehicle Safety. 2019; 11(2): 136-157. https://doi.org/10.1504/IJVS.2019.101857

7. Mataras DA, Luque P, Alonso M. Phase plane analysis applied to non-explicit multibody vehicle models. Multibody System Dynamics. 2022; 56(2): 173-188. https://doi.org/10.1007/s11044-022-09846-9
8. Hussain K, Stein W, Day AJ. Modelling commercial vehicle handling and rolling stability. Proceedings of the Institution of Mechanical Engineers, Part K: Journal of Multi-body Dynamics. 2005; 219(4): 357-369. https://doi.org/10.1243/146441905X48707
9. Marienka P, Francak M, Jagelcak J, Synak F. Comparison of braking characteristics of solo vehicle and selected types of vehicle combinations. Horizons of Autonomous Mobility in Europe (LOGI 2019), November 14-15, 2019, České Budějovice, Czech Republic. https://doi.org/10.1016/j.trpro.2020.02.007
10. Damjanovic M, Zeljko S, Stanimirovic D, Tanackov I, Marinkovic D. Impact of the number of vehicles on traffic safety: Multiphase modeling. Facta Universitatis Series: Mechanical Engineering. 2022; 20(1): 177-197. https://doi.org/10.22190/FUME220215012D
11. Skrucany T, Vrabel J, Kazimir P. The influence of the cargo weight and its position on the braking characteristics of light commercial vehicles. Open Engineering, 2020; 10(1): 154-165. https://doi.org/10.1515/eng-2020-0024
12. Vrabel J, Skrucany T, Bartuska L, Koprna J. Movement analysis of the semitrailer with the tank-container at hard braking – the case study. 4th International Conference of Computational Methods in Engineering Science (CMES 2019), November 21-23, 2019, Kazimierz Dolny, Poland. https://doi.org/10.1088/1757-899X/710/1/012025
13. Mattas K, Albano G, Riccardo D, Galassi MCh, Suarez-Bertoa R, Sandor V, Ciuffo B. Driver models for the definition of safety requirements of automated vehicles in international regulations. Application to motorway driving conditions. Accident Analysis and Prevention. 2022; 174: 1-16. https://doi.org/10.1016/j.aap.2022.106743
14. Gechev T, Mruzek M, Barta D. Comparison of real driving cycles and consumed braking power in suburban Slovakian driving. 9th International Scientific Conference on Aeronautics, Automotive and Railway Engineering and Technologies (Bultrans 2017), September 11-13, 2017, Sozopol, Bulgaria. https://doi.org/10.1051/matecconf/201713302003
15. Yevtushenko, A., Kuciej, M., Topczewska, K.: Analytical model for investigation of the effect of friction power on temperature in the disk brake. Advances in Mechanical Engineering. 2017; 9(12): 1-12. https://doi.org/10.1177/1687814017744095
16. Yevtushenko A, Kuciej M, Topczewska K. Analytical model to investigate distributions of the thermal stresses in the pad and disk for different temporal profiles of friction power. Advances in Mechanical Engineering. 2018; 10(10): 1-10. https://doi.org/10.1177/1687814018806670
17. Koch S, Koppen E, Grabner N, von Wagner U. On the influence of multiple equilibrium positions on brake noise. Facta Universitatis Series: Mechanical Engineering. 2021; 19(4): 613-632. https://doi.org/10.22190/FUME210106020K
18. Bai Z, Lu Y, Li Y. Method of improving lateral stability by using additional yaw moment of semi-trailer. Energies [Internet]. 2020 Nov 30; 13(23):6317. Available from: https://doi.org/10.3390/en13236317
19. Lack T, Gerlici J. Analysis of vehicles dynamic properties from the point of view of passenger comfort. Communication – Scientific Letters of the University of Zilina. 2008; 10(3): 10-18. https://doi.org/10.26552/com.C.2008.3.10-18
20. Rigatos G, Siano P, Wira P, Busawon K, Binns R. A nonlinear H-infinity control approach for autonomous truck and trailer systems. Unmanned Systems. 2020; 8(1): 49-69. https://doi.org/10.1142/S2301385020500041
21. Road traffic act No. 8/2009.
22. Wang D, Chen S, Zhang W, Du D. The roll stability analysis of semi-trailer based on the wheel force. Computers, Materials and Continua. 2022; 71(1): 1837-1848. https://doi.org10.32604/cmc.2022.023033
23. Chajkin AP, Dobretsov RY, Sokolova VA, Teterina IA, Kamenchukov AV, Tiknonov EA, Bazykin VI. Mathematical model for assessing lateral stability of articulated tracked vehicles. 3rd International Scientific Conference on Applied Pysics, Information Technologies and Engineering (APITECH-III 2021), September 24 – October 3, 2021, Krasnoyarsk, Russia. https://doi.org/10.1088/1742-6596/2094/4/042005
24. Voros I, Takacs D. The effects of trailer towing on the dynamics of a lane-keeping controller. ASME 2020 Dynamic Systems and Control Conference. Virtual, Online, 2020. https://doi.org/10.1115/DSCC2020-3141
25. Vasko M, Leitner B, Saga M. Computational fatigue damage prediction of the lorry frames under stochastic random excitation. Communication – Scientific Letters of the University of Žilina. 2010; 12(4): 62-67.
26. Lot R, Massaro M. A symbolic approach to the multibody modeling of road vehicles. International Journal of Applied Mechanics [Internet]. 2017 Jul 1; 9(5):1750068. Available from: https://doi.org/10.1142/S1758825117500685
27. Xing J. Determination of instability critical speed of articulated vehicle on ramp section based on response surface method. International Conference on Mechanical Engineering, Intelligent Manufacturing and Automation Technology (MEMAT 2021), April 23-25, 2021, Guilin, China. https://doi.org10.1088/1742-6596/1939/1/012075
28. Zhang Q, Su Ch, Zhou Y, Zhang Ch, Ding J, Wang Y. Numerical investigation on handling stability of a heavy tractor semi-trailer under crosswind. Applied Sciences [Internet]. 2020 May 26; 10(11):3672. Available from: https://doi.org/10.3390/app10113672
29. Jagelcak J, Gnap J, Kuba O, Frnda J, Kostrzewski M. Determination of turning radius and lateral acceleration of vehicle by GNSS/INS sensor. Sensors [Internet]. 2022 Mar 16; 22(6):2298. Available from: https://www.mdpi.com/1424-8220/22/6/2298
30. Guo R, Siquan L, Zulin H, Xu L. Study on Vehicle-road interaction for autonomous driving. Sustainability [Internet]. 2022 Sep 14; 14(18):11693. Available from: https://www.mdpi.com/2071-1050/14/18/11693
31. Yang Z, Wang L, Liu F, Li Z. Nonlinear dynamic analysis of constant-speed and variable-speed of autonomous vehicle passing uneven road. Journal of Vibroengineering. 2022; 24(4): 726-744. https://doi.org/10.21595/jve.2022.22250
32. Lack T, Gerlici J. Analysis of vehicles dynamic properties from: The point of view of passenger comfort. Communications – Scientific Letters of the University of Žilina. 2008; 10(3): 10-18.
33. Gerlici J, Lack T, Ondrova Z. Evaluation of comfort for passengers of railway vehicles. Communications – Scientific Letters of the University of Žilina. 2007; 9(4): 44-49.
34. De Bernardis, M., Rini, G., Bottiglione, F., Hartavi, A.E., Sorniotti, A.: On nonlinear model predictive direct yaw moment control for trailer sway mitigation. Vehicle System Dynamics. 2022; in press: 1-27. https://doi.org/10.1080/00423114.2022.2054352
35. Zhou S, Zhang S. Study on tractor semi-trailer roll stability control. The Open Mechanical Engineering Journal. 2014; 8(A238): 238-242. https://doi.org/10.2174/1874155x01408010238
36. Koszałka G, Zniszczynski A. A simulation study on the manoeuverability of a large size semitrailer. Transport. 2016; 31(4): 408-415. https://doi.org/10.3846/16484142.2015.1057224
37. Pacejka H. Modeling of the as a vehicle component with applications. CCG-Course V2.01, Carl-Cranz-Gesellschaft. 1982.
38. Rill G. Sophisticated but quite simple contact calculation for handling tire models. Multibody System Dynamics. 2019; 45(2): 131-153. https://doi.org/10.1007/s11044-018-9629-4
39. Nunic ZB, Ajanovic M, Miletic D, Lojic R. Determination of the rolling resistance coefficient under different traffic conditions. Facta Universitatis Series: Mechanical Engineering. 2020; 18(4): 653-664. https://doi.org/10.22190/FUME181116015N
40. Istenik R, Barta D, Mucha W. Influence of the wheels on the automobile dynamics. Komunikacie. 2004; 6(1): 26-28.
41. Car trailer fail – car accident in Poland. 2022; Online, [cited 2022-11-04]: Available on: https://www.youtube.com/watch?v=mfLnLwFcSBc
42. Tongue weight safety demonstration. 2022; Online, [cited 2022-11-04]: Available on: https://www.youtube.com/watch?v=w9Dgxe584Ss

This work was supported by the Cultural and Educational Grant Agency of the Ministry of Education of the Slovak Republic as part of the projects 'Development of advanced virtual models for studying and investigation of transport means' operation characteristics' (No. KEGA 023ŽU-4/2020) and 'Implementation of modern methods of computer and experimental analysis of the properties of vehicle components in the education of future vehicle designers' (No. KEGA 036ŽU-4/2021).

Ján Dižo: https://orcid.org/0000-0001-9433-392X

Miroslav Blatnický: https://orcid.org/0000-0003-3936-7507

Paweł Droździel: https://orcid.org/0000-0003-2187-1633

Rafał Melnik: https://orcid.org/0000-0003-2900-784X

Jacek Caban: https://orcid.org/0000-0002-7546-8703

Adam Kafrik: https://orcid.org/0000-0002-8710-1546

DOI 10.2478/ama-2023-0008

ANALYTICAL APPROACH FOR VEHICLE BODY STRUCTURES BEHAVIOUR UNDER CRASH AT ASPECTS OF OVERLOADING AND CRUMPLE ZONE LENGTH

Dariusz KURPISZ*, Maciej OBST*, Tadeusz SZYMCZAK, Radosław WILDE*****

*Institute of Applied Mechanics, Poznan University of Technology, ul. Jana Pawła II 24, 60-965 Poznan, Poland
**Motor Transport Institute, ul. Jagiellonska 80, 03-301 Warszawa, Poland
***Łukasiewicz Research Network - Poznań Institute of Technology, ul. Ewarysta Estkowskiego 6, 61-755 Poznan, Poland

dariusz.kurpisz@put.poznan.pl, maciej.obst@put.poznan.pl,
tadeusz.szymczak@its.waw.pl, radoslaw.wilde@pit.lukasiewicz.gov.pl

received 22 August 2022, revised 1 December 2022, accepted 1 December 2022

Abstract: Road safety problem is still topical, especially since the number of vehicles and the volume of traffic are increasing. It is possible to increase the safety of road users through systemic changes in many areas related to transport. The deformation of the vehicle body during an accident has an impact on the loads acting on the passengers. Vehicle body deformation depends on complex parameters, and knowledge of these parameters is essential for designing crumple zones and the accident reconstruction process. Knowledge of the mechanical parameters of the vehicle structure during deformation is also a reference to passenger injury indicators assessment. This paper reports results from the analytical approach for determining the protection level of personal vehicles. The proposed conception is based on the results from the static stiffness characteristic of the Ford Taurus, which gives the possibility of phenomenological and simple body crumple analytical description at a speed equal to 10 km/h, 40 km/h, 56 km/h and 60 km/h, which is an original part of the work. The approach enables us to describe the vehicle crash by focusing on variations of deformation in time, stiffness, vehicle collision time (duration), deceleration and dynamic crash force. Basing on the body stiffness data of the personal vehicle, the length of the deformation zone in the front of the car and the maximum values of force at the crash for a speed of 60 km/h are presented. Results obtained by the authors show that is possible to estimate the overloading level during the crash time of a vehicle based on the stiffness characteristic of the car body. The proposed methodology can be developed and the advantage of the presented procedure is an uncomplicated useful tool for solving complex problems of a vehicle crash.

Key words: crash test, car body stiffness, overload, dynamic force

1. INTRODUCTION

Road safety is constantly considered by engineers and researchers' groups for the design of modern cars at increasing the protection level against a crash. This becomes also more significant because the number of vehicles is increasing. The importance of this problem can be proved by the development of passive safety protection systems, gaining its expression among others in the number of published research results. They focus not only on the assessment of the impact of seat belts functioning on the passenger's body [1–6], the concepts of its improvement [6], manufacturing, testing [7,8,9], minimizing the risk of injury [10] but also the overloads and zone size crush [11].

Regardless of the passive safety systems used, the body structure and the resulting rigidity play a key role. Sauders et al. [12] analysed the rear impact resistance of seats used in passenger cars. Advances in the design of car seats have been noted, however, there are cases where seats aren't sufficiently resistant to accident overloads. Of course, there exists a correlation between the dynamic crumple stiffness of the car's body and dynamic forces operating on the seats and passengers. Sugimoto et al. [13] pointed out the problem of the conducted crash tests to real road accidents. The work presents the results of vehicle-to-vehicle crash tests, especially in the situation when cars have different weights. The question was asked about the reasons for the differences between a crash test and a real accident. Attention was also paid to the problem of cars hitting energy-consuming barriers. Citing the results of research conducted in the USA, it was noted that there is a strong correlation between the mass and the stiffness of the vehicle. The authors defined car body stiffness as the slope of the loading on the chassis as derived from an accelerometer attached to the cabin floor on the chassis. Witteman [14] also researched the weight influence of the crash car process. Pointed out the event of a vehicle with a mass >1,500 kg colliding with a honeycomb structure, the test results are different from real collisions. Jawad and Saad [15] described a problem of different mass of vehicle compatibility during a crash. The phenomenon of deformation of the body structure during frontal collisions was investigated. Simulation result for the dynamic behaviour of the crumple zone was presented. Also investigated relation between car crash parameters and passengers' injury criteria. Sadeghipour in his doctoral dissertation [16] considered the problem of the compatibility of cars in Europe during a collision. The author noted that the crash tests of the 1980s and 1990s are not effective in testing modern cars. Due to the high cost of crash tests, the author has conducted extensive finite element method analysis. Barbat et al. [17] conducted research also related to the compatibility of vehicles during a crash. Authors paid attention that geometric interaction, vehicle mass and body stiffness are decision parameters in the vehicle deformation process. The FEM method was used for model simulations. Subramaniam et al. [18] investigated the compatibility of crumple zones and according to the authors, the structural compliance of the crush zones of various cars can improve road safety. In road accident crash analysis and vehicle deformation, the popular method is energy-based analysis. Żuchowski [19] researched the dependence of the impact force on the deformation of the car's body based on energy methods. The case of a car hitting an energy-consuming barrier was considered and for applied simplified linear model identification parameters, the results of crash tests of three different cars were used. Differences in the design of the front body parts of cars manufactured today and 20 or 30 years ago were noted, which is important in assessing the speed of the collision. The author also commented on the issue related to the car's body dynamic stiffness during an impact. The described method was analyzed for three popular cars: Toyota Echo, Honda Accord and Ford Escape. Leibowitz's PhD dissertation [20] is thematically related to the analytical and experimental methodology of car crash energy calculation based on body deformation stiffness. Based on NCAP NHTSA tests data frontal body structure was modelled. Attention was drawn to the necessity of experimental tests to determine the stiffness characteristics of vehicle bodies. The author used the 3D scanning method for more accurate measurement of the deformed body. The author drew attention to the current industry standard for crash energy calculation which is based on the assumed linear relationship of energy and vehicle crush. The body stiffness calculation was based on NHTSA's Full Frontal NCAP. Neades in his doctoral dissertation [21] described the mechanics of the vehicle movement in the aftermath of the crash. A new methodology was proposed to describe the total work of the deformation zone to a particular vehicle. The advantage of the proposed method is the incorporation of restitution effects and the obtained results are identical to those obtained based on the momentum. Khattab's PhD thesis [22] described the problem of controlling energy dissipation of passive and adaptable energy absorbers during crumple zone deformation depending on the vehicle speed during a collision. Different mechanisms of impact energy dissipation have been highlighted. Tests of the damping elements used in the construction of the car body were carried out. McCoy et al. [23] considered the problem of stiffness of additional steel elements attached to the front of the car body. It was noted that additional elements or covers attached to the body result in a change in the frontal body stiffness. The authors determined the stiffness coefficients of the described additional body elements and compared them to frontal body stiffness. Chen [24] tested the dynamical properties, and the damping behaviour of structures filled with aluminium foams was carried out. Hollowell et al. [25] described and analysed several crash test procedures. Brell [26] described factors that affect crumple zone deformation and response. Impact on passengers during a collision is also presented. The author described the instantaneous stiffness of the crumple zone. Research is also focused on collision modelling. Lukoševičius et al. [27] presented three and four mass dynamic models of crumple zone for passenger cars during a frontal impact. The linear stiffness in the initial stage of the vehicle body deformation and then the ideal plastic deformation of the crush zone were assumed resulting in the body stiffness which then increases to infinity. The necessity to use nonlinear relations for stiffness at higher collision velocities was pointed out. Pahlavani and Marzbanrad [28] presented a 12-degree model of a vehicle for a frontal crash, and composed model based on basic rheological material models such as spring, dumper and Maxwell body. The result obtained by model analysis was compared to experimental crash tests. Munyazikwiye et al. [29] presented a mathematical model of the frontal crash of vehicle-to-vehicle. The model is based on the mass of the crashed cars and linear Kelvin elements which represent the mechanical properties of the crumple zones. Wiacek et al. [30] studied the impact of modern materials such as high-strength steel and aluminium on a car's body structure stiffness. The authors used four methods for car body stiffness calculation based on cars produced between 2002 and 2014. Data were taken from NCAP frontal crash experimental. A very interesting problem was raised by Sungho and HaengMuk [31] who investigated the problem related to vehicle bodies after crash repair. Using the technical data of a popular personal car, simulation research was carried out. The authors noted the reduction in the strength of the repaired body and the change in stiffness to the vehicle that did not crash. Prochowski et al. [32] investigated side-impact vehicle crash in terms of accident reconstructions. Based on experimental results, deformation and stiffness parameters were estimated.

Sahraeia et al. [11] presented results of the impact that linked the stiffness of the frontal structure of the car to the risk of injuries of passengers in the rear seats. The stiffness of the structure can be improved by applying high-strength steel or by increasing the thickness of the sheets which was investigated by Wiacek et al. Vehicle stiffness can be also controlled by profiles shape which was described by Obst et al. [33, 34].

Car accidents are also a problem of passenger injuries the scope of which also depends to a large extent on the mechanical properties of the vehicle crush zone.

The simulations on the MADYMO mannequin showed an increase in the incidence of head injuries from 4.8% (at 1,000 N/mm stiffness) to 24.2% (at 2,356 N/mm stiffness). Additionally, the risk of chest injuries increased from 9.1% to 11.8%. According to the authors, additional measures should be introduced to protect passengers seated on the rear seats when the stiffness of the vehicle increases. Such safeguards may be applied using additional airbags or active seat belts. The comparison of the injuries of passengers seated in the front seats with the injuries of passengers seated in the rear seats was investigated by Mitchell et al. [35].

Bunketorp and Elisson [36] pointed out that further analysis of the resulting injuries with particular attention to angular deformation and translation should be followed.

A reduction of consequences due to vehicles crash requires employing more energy-absorbing elements which was described by Szeszycki [37]. However, the practical use of these components can be achieved at low speeds such as no more than 30 km/h. At higher values of the physical quantity, absorbers in the body structure of the front of the vehicle play an important role because they carry the impact energy by cracking, deforming and collapsing thereby saving passengers.

Because all the aforementioned test bench methods sometimes show far-reaching and difficult-to-estimate discrepancies with the actual impact effects, which in terms of initial conditions may significantly differ from those assumed experimentally, and the only reliable characteristic is obtained in the static longitudinal compression test of the car body, so the dependence of the force

DOI 10.2478/ama-2023-0008

on the length of the crumple zone is reasonable to describe the behaviour of the vehicle based on these characteristics.
Additionally, the widely used definitions of mean values of car body stiffness may not be an optimal approach because it does not take into consideration the local values of stiffness and their influence on instant acceleration.

The aim of this paper is focused on analysing the differences between the equivalent quasi-constant dynamic stiffness of the front vehicle body structure and the instant stiffness, in terms of the length of the crumple zone and the maximal overloading occurring during the frontal impact of the car into a stiff obstacle. It is also an attempt at a simple, based on a static characteristic, mathematical description of the deceleration generated during the collision process, which is also the original part of the work. The proposed simple analytical methodology can be of course developed in parallel to the crash test of real cars. Based on the proposed model, more advanced analysis is possible if for example we have data on the dynamic stiffness of the car's crumple zone. Presented solutions can be adopted for analysis of rear crash problems, in case of facial impact. It is worth noting that the proposed simple analytical model is handy which in the case of engineering practice is an excellent analytical tool.

To the fact that detailed experimental data on the static vehicle front body stiffness are not generally available, it was decided to use the characteristics of Ford Taurus presented by Sahraeia et al. As a result, the lengths of the frontal vehicle body deformation zones and the maximal overloading values at impact for the car speed of 10 km/h, 40 km/h, 56 km/h (Euro NCAP "The European New Car Assessment Programme" test) and 60 km/h were determined analytically and numerically.

2. THE PHENOMENOLOGICAL METHOD

A used method of investigation was the phenomenological approach, applied to experimental characteristics, taken from Ref. [11]. The experimental results of the static compression of the Ford Taurus whole car body structure, provided the relation between force and displacement. The approximation of discussed relation lets to formulate the differential equation of the car body motion, during face collision with the rigid obstacle. The solution of the discussed equation, complemented by the boundary conditions (like mass and initial velocity) gives the functions describing the length of the crash zone, deceleration and in consequence impact force.

Let us take into consideration the collision process of a car with mass m [kg], initial velocity V_0 [m/s] and body stiffness k [kN/mm], with an infinitely stiff undeformable obstacle. In the case of a small number of protective elements, the impact energy is directly absorbed by the vehicle's superstructure at an unknown and difficult-to-estimate force. It is influenced by both, the construction and speed of the car. Protective components must determine the maximum values of overloading at the moment of the collision, and the length of the crumple zone. Each of these quantities is closely related to the probability of the survival chance of the driver and passengers. Nevertheless, the amount of experimental data on the vehicle body characteristics is still not enough. However, in Ref. [11], the behaviour of the Ford Taurus during the collision is discussed in details.

In Fig. 1, we can see that the car's body response to the crash is in a form of an increasing relationship between force and displacement with oscillations, indicating variations in a range of deformation zones. This makes it difficult to elaborate in detail on the car's behaviour during the crash. Therefore, this relationship can be presented in a straight line. The characteristic wave of the graph is associated with the deformation of the car body resulting in complex blocking and destruction of its overlapping elements. Besides the knowledge of this stage is well represented by the relationship between force and displacement as well as the deformed components as a function of the observed behaviour is irregular. Therefore, the force versus displacement under a crash can be approximated linearly as follows:

$$F(b) = kb, \tag{1}$$

where: k is the stiffness coefficient (slope of the straight line on Fig. 1, $k \approx 1\,[\mathrm{kN}/\mathrm{mm}]$), b [mm] is the depth of the crash zone from the point of contact between the front bumper and the obstacle.

The discussed situation is illustrated in Fig. 2.

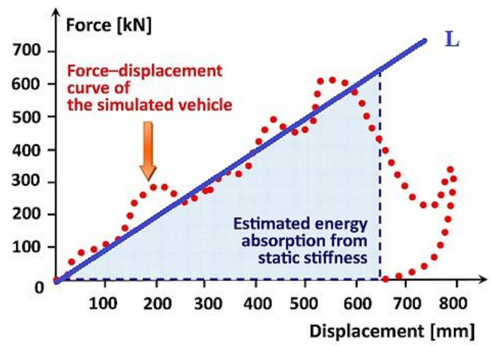

Fig. 1. Variations of force versus displacement for the Ford Taurus crash test. Data taken from Ref. [11]

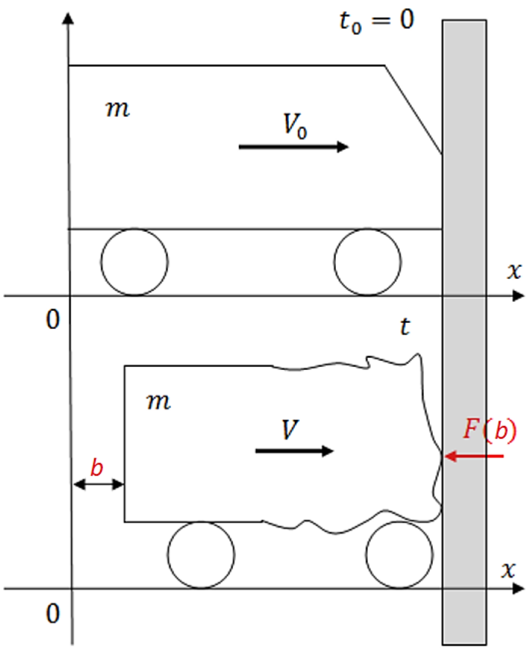

Fig. 2. The car body in two stages of a crash test on an undeformable obstacle: (a) in the initial stage without any deformation and (b) in the further stage at elastic and plastic deformation

Using Newton's second law, we receive:

$$ma = -F(b), \tag{2}$$

or equivalently in differential form:

$$m\frac{d^2b}{dt^2} = -F(b), \tag{3}$$

$$mV\frac{dV}{db} = -F(b), \tag{4}$$

where $V\left[\frac{m}{s}\right]$ and $a\left[\frac{m}{s^2}\right]$ are the velocity and deceleration during the collision, respectively.

Using Eq. (1) and making some transformations the following equation can be obtained:

$$V^2 = \frac{-k}{m}b^2 + C. \tag{5}$$

Velocity $V_0\left[\frac{m}{s}\right]$ at the beginning of the collision process satisfy the following assumption: $V_0 = V(0)$, therefore $C = {V_0}^2$, which in turn means:

$$V(b) = \sqrt{{V_0}^2 - \frac{k}{m}b^2}. \tag{6}$$

Eq. (6) specifies the speed of oncoming movement as a function of path s destroying the deformable compartment of the body of the vehicle.

From a practical point of view, a more meaningful equation is one that shows the dependence of the path of destruction of the deformable compartment of the body of the vehicle as a function of time.

From the fact that $V(b) = \frac{db}{dt}$ the following relationship can be written:

$$\frac{db}{dt} = \sqrt{{V_0}^2 - \frac{k}{m}b^2} \tag{7}$$

and after transformations, as follows:

$$\arcsin\left(\sqrt{\frac{k}{m{V_0}^2}}b\right) = \sqrt{\frac{k}{m}}t + D. \tag{8}$$

Because in time of the contact of the front part of the body of the car and undeformable obstacle, the body deformation equals zero, therefore $b(0) = 0$. After transformations $D = 0$, and finally as below:

$$b = V_0\sqrt{\frac{m}{k}} \cdot \sin\left(\sqrt{\frac{k}{m}}t\right). \tag{9}$$

Differentiating the obtained equation after time we get:

$$V = \frac{db}{dt} = V_0 \cdot \cos\left(\sqrt{\frac{k}{m}}t\right), \tag{10}$$

and hence:

$$a = \frac{dV}{dt} = -V_0 \cdot \sqrt{\frac{k}{m}} \cdot \sin\left(\sqrt{\frac{k}{m}}t\right), \tag{11}$$

The vehicle stops during the crash when $V = 0$. The time of the collision process can be written as:

$$t = \frac{\pi}{2}\sqrt{\frac{m}{k}}. \tag{12}$$

In that time the maximal deceleration occurs if:

$$a_{\max} = -V_0 \cdot \sqrt{\frac{k}{m}}, \tag{13}$$

and the impact force can be expressed as follows:

$$F_{\max} = m \cdot a_{\max} = -\sqrt{mk} \cdot V_0. \tag{14}$$

The deceleration value Eq. (13) is only an approximation and may significantly differ from the maximum peak, which is significantly influenced by the detailed characteristics of the body deformation (body structure and used components, types of engineering materials, operational conditions), impact speed and the associated effect of dynamic stiffness oscillation and many other minor factors. To get a result that is closer to the realistic model of the destruction of the body while crashing on a rigid obstacle the static characteristics of the body of the Ford Taurus car were used [11].

Using the differential equation of the motion during a vehicle collision with a rigid obstacle and making the transformations the following formula is obtained:

$$\frac{1}{2}mV^2 = -\int_0^b F(l)dl, \tag{15}$$

where the right side of the above equation contains everything, which is responsible for longitudinal car body static reaction. Introduced this way the phenomenological conception eliminates the necessity of knowledge about experimental car body parameters like stiffness and damping coefficients. Those parameters are neglected, when someone decides to use the multimas model in analytical crumple zone modelling, like Lukoševičius et al. [27] and can be determined in the numerical way (FEM "Finite Element Method" investigations), like work of Lankarani and McCoy [23]. Applying the initial condition $V(0) = V_o$ the following equation can be received:

$$V = \sqrt{{V_o}^2 - \frac{2}{m}\int_0^b F(l)dl}. \tag{16}$$

The total depth $\hat{b}$ of the zone (crumple) of controlled destruction of the front part of the body of the vehicle is obtained by solving the following equation:

$$V(\hat{b}) = 0, \tag{17}$$

Eq. (16) allows us to determine the speed as a function of the current depth of the deformed vehicle body compartment. However, it does not provide information about the variability of discussed velocity in time, and thus makes it impossible to estimate the delay.

Applying the left side of Eq. (16) to the definition of instantaneous speed we get:

$$\frac{db}{dt} = \sqrt{{V_o}^2 - \frac{2}{m}\int_0^b F(l)dl}, \tag{18}$$

and finally:

$$t = \int_0^b \frac{db}{\sqrt{{V_o}^2 - \frac{2}{m}\int_0^b F(l)dl}}. \tag{19}$$

As we can see that Eq. (19) is different compared with Eq. (12) because $F(t)$ is non-linear.
Marking the right side of equality Eq. (19) by $G(b)$ we get:

$$t = G(b) - G(0), \tag{20}$$

and finally after some transformations:

$$b = G^{-1}(t). \tag{21}$$

Thus, the change in delay and speed as a function of time is:

$$\tilde{a}(t) = \frac{-F\left(G^{-1}(t)\right)}{m}, \tag{22}$$

$$\tilde{V}(t) = V_o + \int_0^t \tilde{a}(l)dl. \tag{23}$$

3. RESULTS OF COMPUTATIONS

The authors have decided to present two previously shown approaches of $F(t)$, i.e. the first based on approximation Eq. (1) of the experimental characteristics of static body rigidity and the second as an exact reconstruction without referring to the approximating function relying only on the experimental data set.

The depth of the stopping distance, speed and deceleration (during a collision) as a function of time was determined in two ways: using Eqs (10–12) and (21–23).

The approximate value of the static body characteristic was assumed at the level $k = 1\left[\frac{\text{kN}}{\text{mm}}\right]$, when we used the experimental characteristics, the corresponding velocity value during the impact was determined from Eq. (10).

Based on Fig. 1, the body stiffness of the Ford Taurus car (year 2004, weight 1,740 kg) was reproduced and then the relationship between the speed V during the collision and its duration was numerically elaborated using Eq. (16). The elaborated plots are illustrated in Figs. 3 and 4.

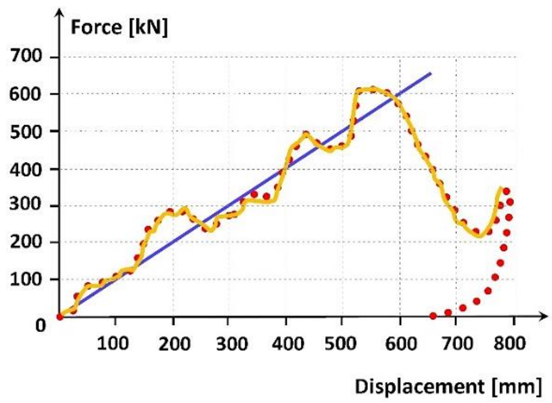

Fig. 3. Superimposition of the reading graph (orange line) on the original body characteristics – data taken from Ref. [11] (red dots represents continuous data) and its linear approximation

Variations of the deformation zone depth were determined at two approaches, expressing the sensitivity of the relationship on the proposed method (Fig. 4). Differences between these results were clearly visible at a speed exceeding 50 km/h. In the case of the relationship between the depth of a deformation zone and time, the differences in the two approaches were not significant Fig. 5. At the speed of 60 km/h the first and second iteration expressed not the same values in s(t) and time (Fig. 5). Variations of the speed versus time during the crash were sensitive to the approach stage (Fig. 6). This was expressed by differences in the value of time, taking 30%.

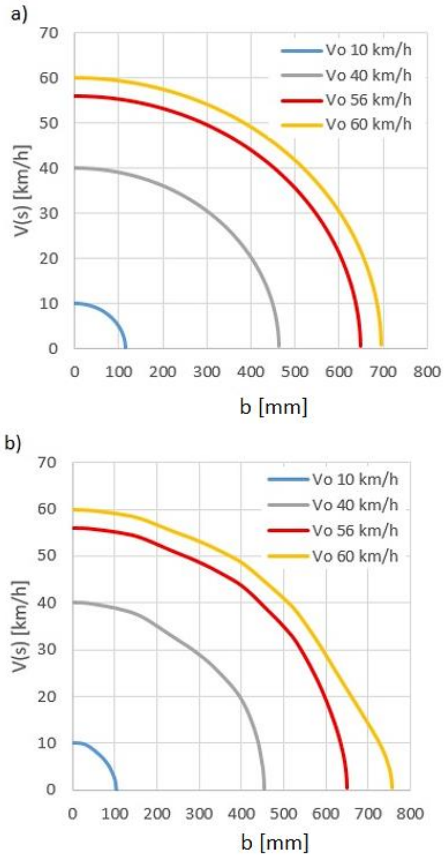

Fig. 4. Car speed as a function of the current crumple depth determined using the first approach (a) and the second approach (b) at the four values of initial speed: 10 km/h, 40 km/h, 56 km/h and 60 km/h

Summarizing the results shown in Figs. 4–7 is worth emphasizing the approximation of the static characteristics of the car body using a straight line:
– does not significantly affect the depth of the crumple zone (Fig. 5),
– influences the time (duration) of the collision, which is independent of the initial speed (Fig. 6),
– significantly changes the relationship of deceleration-time (Fig. 7).

The local maxima, presented in Fig. 7(b), are strongly correlated with the course of the static characteristic versus time shown in Ref. [11].

The results obtained on the basis of the static characteristics and the formulas expressed by Eqs (15)–(23) as well as the relationship versus time are compared with data from the experiment (Fig. 8).

It is observable, that approximation by the use of static vehicle body stiffness characteristics, gives results comparable with the experiment (the model year 2000). The plot of acceleration value (red line determined by the authors) is similar to over plots. The non-linearity and pulsating value of deceleration is a direct consequence of the changeable static and dynamic stiffness of the vehicle body, which is a very accomplished structure. It can be explained based on structural features of the components (manufacturing state) against crash because their mechanical parameters and geometry follow the static stiffness at a not significant speed in a car accident while in the case of a crash at dynamic conditions, significant differences occurred in cross-sections and length of elements leading to a local concentration of permanent deformation, fracturing and collapsing as a final stage. Therefore, different values of force and deformation at crashing can be evidenced. From the practical point of view, it means the crumple zones at the initial state and after an accident at permanent deformation will express significantly different behaviour if a vehicle was repaired in a process with drawing and straightening. It can be connected with a vehicle history and operating condition such as a small collision, i.e. crumple zones of pure cars can be more deformable absorbing a higher level of energy and saving passengers compared to the exploited elements, at the same crush zone design. This means that the zone exhaustion state with deformation will occur earlier than its counterpart without loading history. As a result, the occupied zone of the exploited vehicle will be subjected to loading faster. Additionally, the behaviour of older cars is different from younger ones to the application of modern structural materials such as high-strength steel [38, 39]. Worth noticing that dynamic stiffness is very demanding because the experiment is very expensive due to the permanent deformation of the tested object which does not enable it to use again. Therefore, capturing details from this kind of test is very difficult.

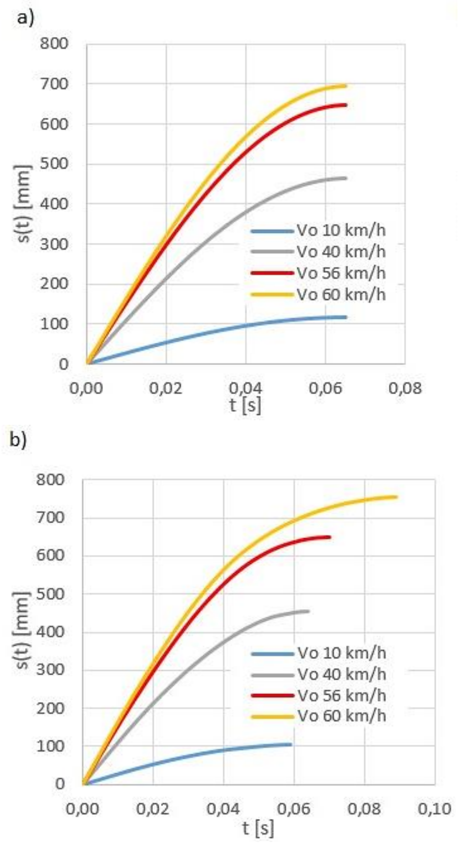

Fig. 5. Depth of the crumple zone as a time function for first approach (a) and second approach (b) captured at the initial speed of car equal to 10 km/h, 40 km/h, 56 km/h and 60 km/h

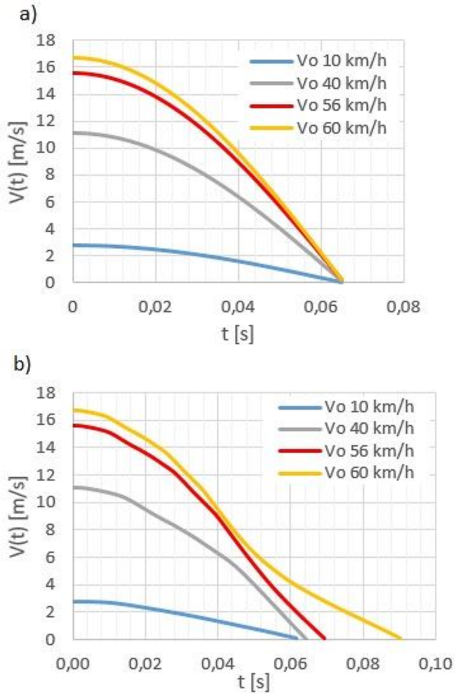

Fig. 6. Car speed versus time during a collision for the first approach (a) and second approach (b) at the initial speed of the car: 10 km/h, 40 km/h, 56 km/h and 60 km/h

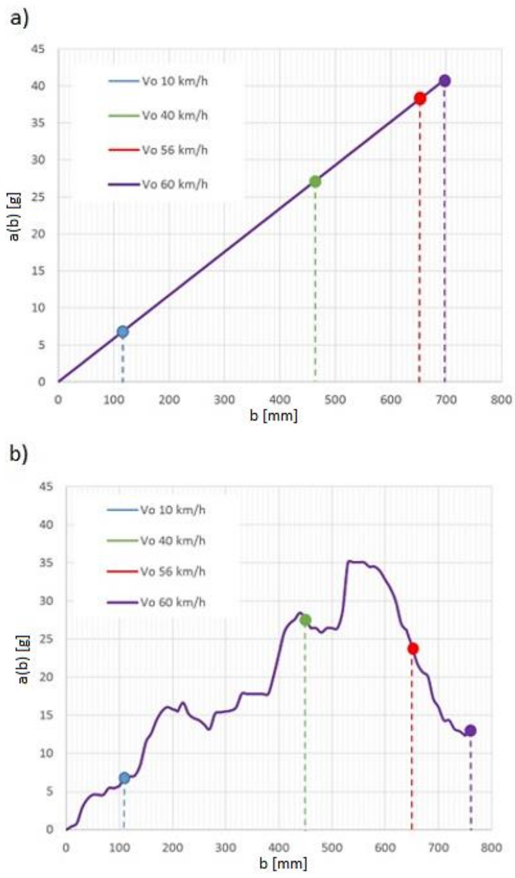

Fig. 7. Deceleration for the first approach (a) and the second approach (b) at the initial speed of the car taking off at 10 km/h, 40 km/h, 56 km/h and 60 km/h

DOI 10.2478/ama-2023-0008

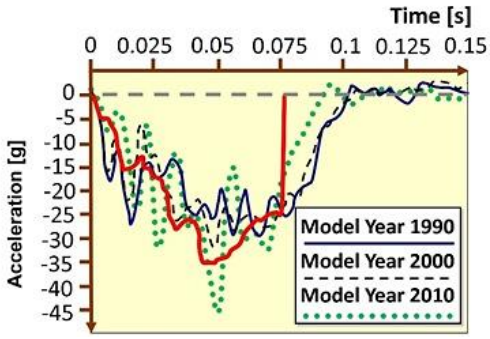

Fig. 8. Comparison of the results determined by means of the authors's approach (red line) and data taken from Ref. [11]

To clarity the comparison between static and dynamic stiffness (determined based on Fig. 8) was shown in Fig. 9. It is based on patterns:

$$\begin{cases} F(t) = m \cdot a(t) \\ b(t) = \int_0^t a(l)dl \end{cases} \Rightarrow F(b) \tag{24}$$

where points of characteristics' a(t) are directly taken from Fig. 8.

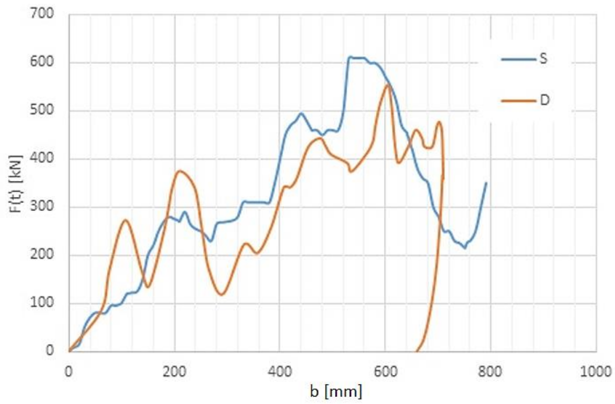

Fig. 9. Comparison of static (S) and dynamic (D) stiffness (impact velocity 56 km/h) of Ford Taurus

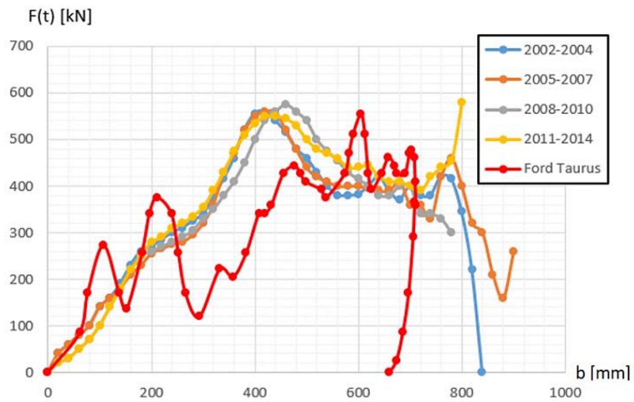

Fig. 10. Comparison of dynamic (D) stiffness (impact velocity 56 km/h) of Ford Taurus and experimental stiffness of series personal cars produced in years 2002–2014 according to Ref. [37]

It is important to note, that the static stiffness is a little bit large compared to dynamic stiffness, which is a known phenomenon described by Wiacek et al. [37]. In consequence, deceleration calculated by the use of static characteristics describes possibly the worst situation. Hence the assessment based on such type of approach is much more conservative.

The relation's shape and maximum force value on the discussed plot are comparable to those mentioned in Ref. [37] (see Fig. 10).

4.CONCLUSIONS

The conducted analytical modelling of the process of the frontal collision of a car with a rigid obstacle allows concluding that the quasistatic characteristic of the body stiffness is a sufficient tool to describe the phenomena occurring during dynamic loading, in the basic scope. It gives results comparable to the experimental ones (Fig. 8), which takes place when we use variable static stiffness in the modeling. Carrying out an analogous line of reasoning for the quasistatic averaged stiffness leads to a difference in the range of instantaneous deceleration values, with the results obtained for the actual stiffness (Fig. 7), although on the other hand, it does not cause a significant change in the length of the crush zone and the duration of the collision.

The lower values of dynamic stiffness, compared to the static one, can be justified by the immediate degradation of some elements of the body during dynamic loading.

Although the effects of a collision cannot be predicted with accuracy, the use of the phenomenological concept of the analytical description of this phenomenon allows us to satisfactorily determine the maximum value of the instantaneous delay, which is critical due to possible injuries to passengers (overloading effect).

The influence of the difference between vehicle body static and dynamic stiffness on the values of deceleration during the crash event is still not sufficiently presented, therefore this stage is selected for further investigations.

The presented way of approach can be used for any other car. However, knowledge about car body stiffness, is strictly recommended. The discussed Ford Taurus is only an example, illustrating the proposed method.

REFERENCES

1. Łabęcka M., Żaba C., Lorkiewicz-Muszyńska D., Świderski P., Mularski A., Kołowski J. Fatal injuries of organs situated in the neck caused by fastened seat belts. Arch. Med. Sąd. Kryminol. 2011;LXI: 170-175 (in Polish).
2. Dubois D., Zellmer H., Markiewicz E. Experimental and numerical analysis of seat belt bunching phenomenon. International Journal of Impact Engineering. 2009; 36: 763-774. https://doi.org/10.1016/j.ijimpeng.2008.11.006
3. Reeda M.P., Ebert S. M., Sherwood Ch.P., Klinich K.D., Manary M.A. Evaluation of the static belt fit provided by belt-positioning booster seats. Accident Analysis and Prevention. 2009;41: 598-607. https://doi.org/10.1016/j.aap.2009.02.009
4. Houten R.V., Reagan I. J., Hilton B.W. Increasing seat belt use: Two field experiments to test engineering-based behavioral interventions. Transportation Research, Part F. 2014;23:133-146. https://doi.org/10.1016/j.trf.2013.12.018

5. Joszko K., Wolański W., Gzik M., Żuchowski A. Experimental and modelling investigation of effective protection the passengers in the rear seats during car accident. Modelowanie Inżynierskie. 2015;25 (56): 48-57 (in Polish).
6. Kang H.-S., Cho H.-Y., Lee S.-K., Shon J.-H. Development of an index for the sound and haptic quality of a seat belt. Applied Acoustics. 2015;99: 145-154. https://doi.org/10.1016/j.apacoust.2015.06.006
7. Li Z., Yu Q., Zhao X., Yu M., Shi P., Yan C. Crashworthiness and lightweight optimization to applied multiple materials and foam-filled front end structure of auto-body. Advances in Mechanical Engineering. 2017;9(8): 1-21. https://doi.org/10.1177/1687814017702806
8. Liang C., Wang C., J., Nguyen V., B., English M., Mynors D. (2017). Experimental and numerical study on crashworthiness of cold-formed dimpled steel columns. Thin-Walled Structures. 2017;112: 83-91. https://doi.org/10.1016/j.tws.2016.12.020
9. Kotełko M. Load capacity and failure mechanisms of thin-walled structures, WNT Warszawa, Poland (in Polish); 2017.
10. Kent R.W., Purtsezov S.V., Pilkey W.D. Limiting performance analysis of a seat belt system with slack. International Journal of Impact Engineering. 2007;34: 1382-1395. https://doi.org/10.1016/j.ijimpeng.2006.07.002
11. Sahraeia E., Digges K., Marzougui D., Roddis K. High strength steels, stiffness of vehicle front-end structure, and risk of injury to rear seat occupants. Accident Analysis and Prevention. 2014; 66: 43-54. https://doi.org/10.1016/j.aap.2014.01.004
12. Saunders J.W., Molino L.N., Kuppa S., McKoy F.L., Performance of seating systems in a FMVSS no. 301 rear impact crash test. Computer Systems Management, Inc. USA, Paper Number 248.
13. Sugimoto T., Kadotani Y., Ohmura S. The offset crash test – a comparative analysis of test methods. Honda R&D Co., Ltd. Japan, Paper Number 98-S I-0-08, 1998.
14. Witteman, W. J. Improved vehicle crashworthiness design by control of the energy absorption for different collision situations. Technische Universiteit Eindhoven, 1999. https://doi.org/10.6100/IR518429
15. Jawad, Saad A.W. Compatibility study in frontal collisions – mass and stiffness ratio. ACME Department, University of Hertfordshire, United Kingdom, Paper Number 98-SI-O-14; 1998.
16. Sadeghipour E. A New Approach to Assess and Optimize the Frontal Crash Compatibility of Vehicle Structures with Focus on the European Fleet of Passenger Car. PhD thesis, Technical University of Munich; 2017.
17. Barbat S., Li X., Prasad P. Vehicle to vehicle front to side crash analysis using a CAE based methodology. Passive Safety Research and Advanced Engineering, Ford Motor Company, United States, Paper Number 07-0347; 2007
18. Subramaniam K., Mukul Verma M., Rajesh Nagappala R., Ronald Tedesco R., Louis Carlin L. Evaluation of stiffness matching concepts for vehicle safety improvement. General Motors Corporation, USA, Paper Number 07-0112.
19. Żuchowski A. The use of energy methods at the calculation of vehicle impact velocity. The Archives of Automotive Engineering – Archiwum Motoryzacji. 2015;68(2): 85-111.
20. Leibowitz B. Method for Computing Motor Vehicle Crash Energy Based on Detailed Crush Data and Stiffness Values. PhD thesis. Johns Hopkins University, USA; 2014.
21. Neades J.G.J. Developments in Road Vehicle Crush Analysis for Forensic Collision Investigation. PhD thesis. De Montfort University; 2011.
22. Khattab A. Abd El-R. Investigation of an adaptable crash energy management system to enhance vehicle crashworthiness. PhD thesis. Concordia University Montreal, Quebec, Canada; 2010.
23. McCoy M.L., Lankarani H.M. Determination of the crush stiffness coefficients of a typical aftermarket frontal protective guard used in light trucks and vans with comparisons between guard stiffness and frontal vehicle crush coefficients. Proc. IMechE Vol. 220 Part D: J. Automobile Engineering. 2006;220(8): 1073-1084. https://doi.org/10.1243/09544070D19003
24. Chen W. Crashworthiness Optimization of Ultralight Metal Structures. PhD thesis. Massachusetts Institute of Technology; 2001.
25. Hollowell W.T., Gabler H. C., Stucki S.L., Summers S., Hackney J.R. Updated review of potential test procedures for FMVSS no. 208 NHTSA 1999.
26. Brell E. Simplified models of vehicle impact for injury mitigation. PhD thesis. School of Urban Development. Queensland University of Technology; 2005.
27. Lukoševičius V., Keršys R., Keršys A., Makaras R., Jablonskytė J. (2020). Three and four mass models for vehicle front crumple zone. Transport Problems. 2020;15(3). doi: 10.21307/tp-2020-035.
28. Pahlavani M., Marzbanrad J. Crashworthiness study of a full vehicle-lumped model using parameters optimization. International Journal of Crashworthiness, 2015;20(6): 573-591. http://dx.doi.org/10.1080/13588265.2015.1068910
29. Munyazikwiye B.B., Karimi H.R., Robbersmyr K.G. Optimization of Vehicle-to-Vehicle Frontal Crash Model Based on Measured Data Using Genetic Algorithm. IEEE Accesss. Digital Object Identifier. 2017;5: 3131-3138. doi: 10.1109/ACCESS.2017.2671357
30. Wiacek Ch., Nagabhushana V., Rockwell T., Summers S., Zhao L., Collins L.A. Evaluation of frontal crash stiffness measures from the U.S. new car assessment program. Paper Number 15-0257; 2015.
31. Kim S., Cho H. A study on the stiffness change of a passenger car's front frame body before and after a collision accident. International Journal of Mechanical Engineering and Robotics Research. 2021;10(5): 270-275. doi: 10.18178/ijmerr.10.5.270-275
32. Prochowski L., Ziubiński M., Pusty T. Experimental and analytic determining of the characteristics of deformation and side stiffness of a motor car body based on results of side-impact crash tests. International Automotive Conference (KONMOT2018). IOP Conf. Series: Materials Science and Engineering 421 (2018) 032025. doi:10.1088/1757-899X/421/3/032025
33. Obst M., Kurpisz D., Paczos P. The experimental and analytical investigations of tension phenomenon of thin-walled cold formed channel beams subjected to four-point bending. Thin Walled Structures. 2016; 106: 179-186. https://doi.org/10.1016/j.tws.2016.05.002
34. Obst M., Rodak M., Paczos P. Limit load of cold formed thin-walled nonstandard channel beams. Journal of Theoretical and Applied Mechanics. 2016;54(4): 1369-1377. doi: 10.15632/jtam-pl.54.4.1369
35. Mitchell R.J., Bambach M.R., Toson B. Injury risk for matched front and rear seat car passengers by injury severity and crash type: An exploratory study. Accident Analysis and Prevention. 2015;82: 171-179. https://doi.org/10.1016/j.aap.2015.05.023
36. Bunketorp O.B., Elisson L.K. Cervical status after neck sprains in frontal and rear-end car impacts injury. Int. J. Care Injured. 2012; 43: 423-430. https://doi.org/10.1016/j.injury.2011.05.020
37. Szeszycki A. Project of the collision energy absorber for the Formula Student vehicle, Engineering Thesis Poznan University of Technology (in Polish); 2020.
38. Matlock D.K., Speer J.G., de Moor E. Recent AHSS developments for automotive applications: processing, microstructures, and properties. Addressing Key Technology Gaps in Implementing Advanced High-Strength Steels for Automotive Light Weighting February 9-10, 2012, USCAR Offices, Southfield, MI.
39. Chatterjee D. Behind the development of advanced high strength steel (AHSS) including stainless steel for automotive and structural applications - an overview. Materials Science and Metallurgy Engineering, 2017; 4(1): 1-15. doi: 10.12691/msme-4-1-1

Dariusz Kurpisz: https://orcid.org/0000-0003-2233-8638

Maciej Obst: https://orcid.org/0000-0001-6555-6198

Tadeusz Szymczak: https://orcid.org/0000-0003-2533-7200

Radosław Wilde: https://orcid.org/0000-0002-6237-2294

DOI 10.2478/ama-2023-0009

THERMAL PERFORMANCE OF THE THERMAL STORAGE ENERGY WITH PHASE CHANGE MATERIAL

Paweł BAŁON*, Bartłomiej KIEŁBASA*, Łukasz KOWALSKI*, Robert SMUSZ**

*AGH University of Science and Technology, Faculty of Mechanical Engineering and Robotics,
al. Mickiewicza 30-B2, 30-059 Kraków, Poland
** Rzeszów University of Technology, ZT, Aleja Powstańców Warszawy 12, 35-959 Rzeszów, Poland

balonpawel@gmail.com, bartek.kielbasa@gmail.com, lkowalski@agh.edu.pl, robsmusz@prz.edu.pl

received 11 September 2022, revised 18 November 2022, accepted 2 December 2022

Abstract: Values of energy supply and demand vary within the same timeframe and are not equal. Consequently, to minimise the amount of energy wasted, there is a need to use various types of energy storing systems. Recently, one can observe a trend in which phase change materials (PCM) have gained popularity as materials that can store an excess of heat energy. In this research, the authors analysed paraffin wax (cheese wax)'s capability as a PCM energy storing material for a low temperature energy-storage device. Due to the relatively low thermal conductivity of wax, the authors also analysed open-cell ceramic Al2O3/SiC composite foams' (in which the PCM was dispersed) influence on heat exchange process. Thermal analysis on paraffin wax was performed, determining its specific heat in liquid and solid state, latent heat (LH) of melting, melting temperature and thermal conductivity. Thermal tests were also performed on thermal energy container (with built-in PCM and ceramic foams) for transient heat transfer. Heat transfer coefficient and value of accumulated energy amount were determined.

Key words: energy storage, phase change material, PCM, heat accumulation

1. INTRODUCTION

Energy accumulation plays an important role in sustainable utilisation of available energy sources and in improving their efficiency [1]. It happens due to some energy sources being available for limited timeframes, such as solar energy and waste heat emitted by machines, home appliances and buildings [1]. Phase change materials (PCM) provide the opportunity to accumulate such heat energy because of their relatively large values of latent heat (LH). Energy accumulation systems utilising PCM are characterised by ability to store or release large amounts of energy, maintaining almost constant temperature value when the phase transition occurs. They are used in multiple fields: solar energy (solar water heating, solar air heating [2, 3, 4], solar power plants [4]), construction of passive and active energy-storage systems [5], photovoltaic panel cooling [6], electronics [7], automotive industry [8], space heating and domestic hot water systems [9], space cooling systems [10], spacecraft industry, food industry, for biomedical appliances and intelligent textiles. The first studies in the literature dealing with PCM are dated back to the '40s of the preceding century [11], but only the energy crisis during the '70s led to their utilisation as thermal energy storages (TES) that can release sensitive heat (SH) or LH, and visibly increased PCMs' importance for energy management [12, 13]. PCMs can be grouped based on their origin as organic, non-organic or eutectic mixtures. Organic PCMs can be further divided into paraffins, fatty acids and ionic liquids. Inorganic PCMs are mostly salts, their hydrates and eutectic mixtures created with them. They are typically characterised by high values of enthalpy of fusion, a small range of phase transition temperature and higher – in comparison with organic PCMs – thermal conductivity coefficients. However, inorganics are not thermally stable during phase transition – they undergo segregation and might be supercooled. Such occurrences can cause corrosion of PCM containers. Organic PCMs have a relatively high value of LH, are chemically stable and their melting temperature can be controlled by regulation of carbon atoms' amount in chain during the synthesis process. The disadvantages of using organic PCMs include their tendency to change volume during melting, as well as low thermal conductivity coefficients. For example, salt's hydrates have thermal conductivity coefficients within the range of 0.4–0.7 W/(mK) [14] while organics have it in the range of 0.15–0.3 W/(mK) [15]. Organics don't cause corrosion, are non-toxic and the supercooling effect during phase change is relatively small in their case. Organic PCMs are readily available in relatively low prices, characterised by a wide range of work temperatures to choose from, chemically stable and safe to use with drinking water and various other materials [16]. Given the small thermal conductivity coefficients of the materials discussed above, the issue of intensifying heat transfer presents a scientific problem. One of its solutions is to disperse the material in another body, which is able to transfer the heat well (such as metals and their alloys). The conducting material can be structured as a frame, net, porous foam etc., with copper and aluminium foams or expanded graphite allowing mention as examples. Porous ceramic materials can also be used. Additionally, PCM containers can be equipped with parts that intensify the heat exchange process, such as ribbed structures [17, 18, 19, 20], metal meshes and rings. Another way to intensify the heat exchange rate is the utilisation of nanomaterials mixed with PCMs to increase the thermal conductivity coefficient of such blends in comparison with the raw material [21, 22, 23]. The container shape plays a major role in the heat exchange process as well, e.g. a container shaped as a cylindrical ring displays better thermal characteristics than a spherical one of the same volume.

In this research, the authors used ceramic open-cell composite foams of Al2O3/SiC. The advantage of using such foams is their low weight in comparison with metallic foams, as well as a lower price. It has to be noted that, unfortunately, the heat transfer coefficient for ceramic foams is lower than that for foams based e.g. on aluminium alloy or copper.

Pure Al2O3 has a thermal conductivity coefficient of 18 W/mK [24], which can be increased by adding SiC to the material up to 35 W/mK, with a 43% SiC weight admixture [25].

Utilisation of a ceramic array should perceptibly increase the heat exchange rate during the charging process of a container with PCM. It should lower the time required to charge and discharge the heat energy from and into the PCM heat accumulation system.

2. THERMAL PROPERTIES OF THE PCM

In this research, paraffin (cheese) wax was used as PCM, and it is composed of refined petroleum slack and beeswax. Paraffins are materials consisting of saturated carbon–hydrogen chains (with CnH2n+2 formula) integrated with branched, straight and ring-like (aromatics) structures, which are produced by the distillation of crude oil. Both the melting point temperature and LH of fusion increase with chain length. For an n in between 5 and 17, they are liquid at room temperature, while those with an n higher than 17 manifest in the form of solids. With an increasing number of carbon atoms, the melting temperature of paraffin waxes is also increased. Solid paraffin waxes are a mixture of hydrocarbons (iso-alkanes and cycloalkanes). For this reason, it is also difficult to accurately determine the molar mass of paraffins. Cheese wax is considered non-toxic, which is important for PCM TES that are intended for application in drinking water preparation. This type of paraffin (cheese wax) is used to protect cheese. No legal restrictions apply and they can be used as a PCM in domestic hot water tanks, without additional tests and approvals. And this is very important from a practical point of view.

Concerning the present study, the first measurements performed were those of specific heat, LH and phase transition temperature. Specific heat measurements of the discussed PCM were performed using a differential scanning calorimeter (DSC) Mettler-Toledo DSC 822e with IntraCooler Haake EK 90/MT under a nitrogen atmosphere (60 ml/min flow speed) [Fig. 1]. The test was performed using standard DSC aluminium crucibles with a 40 µl volume. Temperature appreciation speed was set to 10 °C/min. Specific heat measurements were performed in accordance with recommendations in the literature [26, 27].

Specific heat measurement was performed using an indirect method with a sapphire calibration constant temperature growth rate of 10 °C /min and heat flux (HF) being the directly measured value [28].

Samples of a weight between 5 mg and 20 mg were taken from provided material (Fig. 2).

In the first experimental step, the heat rate with an empty container (HF_{cr}^{exp}) was recorded. After placing the sample in the crucible, the measurement was repeated, obtaining HF readings of samples with crucibles HF_{pr+cr}^{exp} . HF for the sample follows the formula:

$$HF_{pr}^{exp} = HF_{pr+cr}^{exp} - HF_{cr}^{exp} . \tag{1}$$

Fig. 1. DSC DSC822e and crucibles used. DSC, differential scanning calorimeter

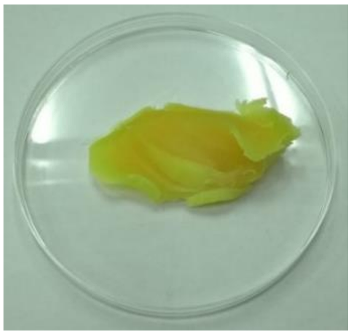

Fig. 2. Plastic wax analysed in the research

In the next step, heat rate on the reference material (sapphire) HF_{sap}^{exp} was measured. The reference material was a sapphire disc with a diameter of 7 mm, which was directly analysed in the calorimeter's chamber. HF_{sap}^{exp} was obtained by subtracting the HF signal for sapphire from the signal measured with the device's chamber when it was empty. It allowed determination of the specific heat of the reference sample, following the formula:

$$c_{p_{sap}}^{exp} = \frac{HF_{sap}^{exp}}{m_{sap}\,\beta}, \tag{2}$$

where HF_{sap}^{exp} represents the heat rate with the reference sample (mW), m_{sap} the reference sample's weight (mg) and ß the rate of temperature change during the test (K/min).

Afterwards, the correction factor K, used to account for heat loss to the environment, was calculated:

$$K = \frac{c_{p_{sap}}^{lit}}{c_{p_{sap}}^{exp}}, \tag{3}$$

where $c_{p_{sap}}^{lit}$ represents the standardised specific heat of a sapphire reference (J/[gK]) [28].

The experimental value of the specific heat of the samples was determined using Eq. (1) and in compliance with the following relationship:

DOI 10.2478/ama-2023-0009

$$c_{p_{pr}}^{exp} = \frac{HF_{pr}^{exp}}{m_{pr}\,\beta}, \tag{4}$$

where: m_{pr} represents the sample weight (mg), and $ß$ the rate of temperature change during the test (K/min).

Weights of wax samples and the sapphire reference sample were measured using an analytical balance. The specific heat of PCM samples was calculated using the following relationship:

$$c_{p_{pr}}^{cor} = c_{p_{pr}}^{exp}\,K, \tag{5}$$

where: $c_{p_{pr}}^{cor}$ represents the sample's specific heat after correction (J/[gK]).

Fig. 3 presents the DSC thermograph of a HF signal measured for the wax sample after subtracting the signal measured with the empty crucible.

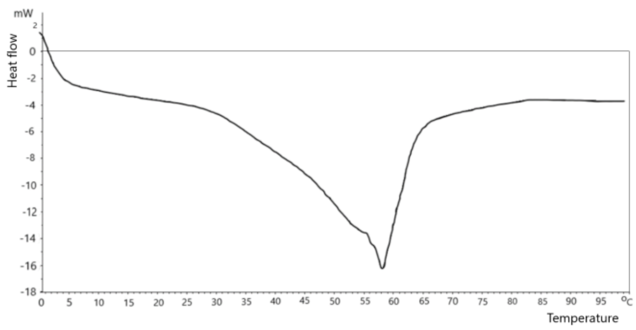

Fig. 3. Wax DSC thermogram – identification of specific heat. DSC, differential scanning calorimeter

Values of the specific heat of PCM specimens calculated using the procedure described above are presented in Fig. 4 (for solid and liquid states of the material).

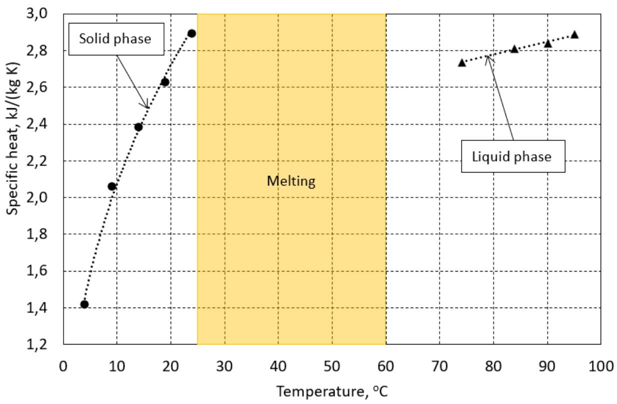

Fig. 4. Specific heat of wax vs. temperature

For the solid phase, a major increase of heat capacity is perceptible in the dependence of temperature, achieving the value of 2.9 kJ/(kgK) in 25 °C. A relatively small increase of specific heat can be observed for the material in its liquid state.

Tab. 1. Specific heat capacity of the paraffin wax [29]

Melting temperature (°C)	Specific heat capacity (kJ/kgK)	
	Solid	Liquid
32–32.1	1.92	3.26

The measured average specific heat for the solid phase amounts to 2.3 kJ/kgK and is slightly higher than the data presented in the literature [29].

In turn, for the liquid phase, the measured average specific heat is 2.99 kJ/kgK, which is less than the value presented in the literature [29]. The discrepancies are probably due to the different carbon–hydrogen chains' structure of the paraffin in the solid state and the fact that the tested sample is composed of refined petroleum slack and beeswax. This is also evidenced by the higher melting point, as shown in Tab. 1.

The LH of melting and melting temperature for the analysed material were determined using DSC analysis in compliance with the standards presented in the literature [30, 31, 32], with indium being used as a reference material for determination of the LH of melting.

$$L = L_c \frac{m_c\,A}{m\,A_c} \tag{6}$$

where: L represents the LH of melting for the sample, L_c the LH of melting for the reference material, m the specimen weight, m_c the reference weight, A the surface area under the HF graph (as marked in Fig. 5) for the sample and A_c the area on the HF graph for the reference material.

A temperature range for this measurement was selected based on the sample's material characteristics. Tests were carried out through the aid of the same calorimeter as for previous trials (Mettler-Toledo DSC822e, in nitrogen with its flow speed equal to 60 ml/min), using an IntraCooler device.

As visible in Fig. 5, DSC analysis of the wax sample showed a single-step melting process with very small differences between the heating cycles. For each of the tests, there is one peak in the melting process. The peak on each DSC curve represents a phase change. As can be seen in Fig. 5, due to the presence of multicomponent hydrocarbon isomers, paraffin does not have a clear (sharp) melting temperature. The melting process of wax does not occur in a constant temperature, but rather in a range of temperature values, which starts at 25 °C and ends at 60 °C. In the initial part of the transition, the LH is relatively small, while soaring LH values can be observed at 53 °C, which corresponds to the calculated melting temperature of the tested PCM.

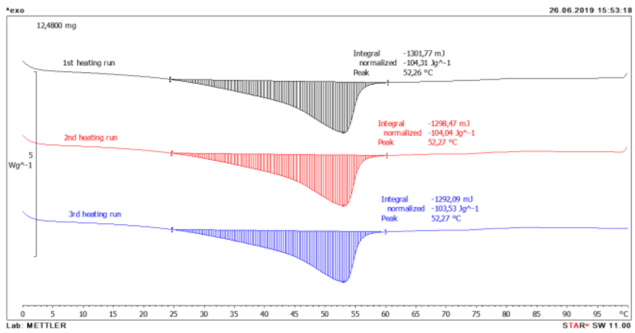

Fig. 5. Wax DSC thermograms – identification of the latent and melting temperatures. DSC, differential scanning calorimeter

To determine the LH of melting of PCM, three tests were performed, and their results are presented in Tab. 2. Small differences in the calculated LH lead to the conclusion that the phase-change and thermal properties of the material are stable, making it suitable for use in TES systems.

Tab. 3 shows the properties of the paraffins. Compared to the values measured in this study, the melting enthalpy of paraffins is more than twice as high. This is because, as mentioned before, paraffins consist of carbon–hydrogen chains and this may indicate shorter chains for the tested sample. Therefore, the LH of the cheese wax is much lower.

Tab. 2. Results of measuring the melting point and LH of the paraffin wax

Test No.	Melting temperature (°C)	LH (kJ/kg)
1	52.3	104.31
2	52.3	104.04
3	52.3	103.53
Mean	**52.3**	**104.0**

LH, latent heat

Tab. 3. The thermal properties of paraffins

Paraffin	No. of carbon atoms in one molecule	Melting temp. (°C)	LH (kJ/kg)	Density (kg/m^3)
n-Nonadecane	19	32	222	785
n-Eicozane	20	36.6	247	788
n-Heneicozane	21	40.2	213	791
n-Docozane	22	44	249	794
n-Trikozane	23	47.5	234	796
n-Tetracozane	24	50.6	255	799
n-Pentacozane	25	53.5	238	801
n-Hexacozane	26	56.3	256	803
n-Heptacozane	27	58.8	235	779
n-Oktacozane	28	41.2	254	806
n-Nonacozane	29	63.4	239	808
n-Triacontane	30	65.4	252	775

LH, latent heat

Uncertainty in measurement of specific heat and LH was estimated using the procedures described in the literature [33, 34]. Complex standard uncertainty was calculated according to the formula:

$$u_c(Y) = \sqrt{\sum_{j=1}^{n}\left(\frac{\partial Y}{\partial X_i}\, u(X_i)\right)^2} \tag{7}$$

where: $u(X_i)$ represents standard uncertainties of partial measurements and $u_c(Y)$ total complex standard uncertainty.

The following factors influence the uncertainty in determination of the specific heat and the LH of fusion: repeatability of heat power measurements for an empty cell, empty crucibles, sample and sapphire, and determination of the mass of the sample, sapphire and indium. The uncertainty in the heat power measurement is ±0.1 mW. The error of mass measurement with the analytical balance was determined at the level of ±0.01 mg. The uncertainty in the specific heat and the LH of fusion for the thermal power was estimated at the level of ±3%. In the next step, measurements of PCM's thermal conductivity coefficient were carried out using a KD2 thermal properties analyser (Decagon Devices Inc.) This device can be used to measure properties of solid, loose and liquid materials [35]. The method of calculating the thermal conductivity coefficient is based on solving temperature functions:

– For heating phase:

$$T(t) = m_0 + m_2\, t + m_3\, ln(t) \text{ for } 0 < t \le t_h, \tag{8}$$

– For cooling phase:

$$T(t) = m_1 + m_2 t + m_3\, ln\left(\frac{t}{t-t_h}\right) \quad \text{for } t > t_h\ , \tag{9}$$

$$k = \frac{q}{4\pi\, m_3} \tag{10}$$

where: T(t) represents the temperature of a linear heat source, $m_0, m_1, m_2\ and\ m_3$ indicate constants, m_0 should be interpreted as the environment temperature during the heating phase considering contact resistance, m_2 the velocity of environment temperature drift, m_3 the slope of temperature function vs. $ln(t)$, k the thermal conductivity coefficient, q the power of this linear heat source and t_h the operating time of the linear heat source.

By registering temperature change over time and approximating the collected data with Eqs (8) and (9), it is possible to determine the thermal conductivity coefficient value. To measure the thermal conductivity of PCM in the liquid and solid states, a KS-1 measurement probe (length 60 mm and diameter 1.3 mm) was used. The probe enables measurement of the thermal conductivity coefficient of solids and liquids in the range of 0.02–2.00 W/(mK) within a temperature range of –50 °C to 150 °C, with a ±5% accuracy in the range 0.2–2.0 W/(mK), and ±0.01% in the range 0.02–0.2 W/(mK) [36].

The analysed wax samples in glass vials were placed in a water bath, controlling the water temperature, as indicated in Fig. 6. After reaching thermal equilibrium of the system, four measurements were performed for each analysed temperature value. The results of the experiment are indicated in Fig. 7. The solid phase measurements exhibited a strong temperature dependency, where thermal conductivity peaked at 35 °C, possibly due to the solid–solid structural transition [37].

One can observe that the thermal conductivity almost doubled during the melting process, in comparison with the commencement of the experiment, at which time this value was recorded at 25 °C. It was seen during melting that the sample was highly viscous with a mush-like characteristic. It was observed that for paraffins with a higher melting temperature, there occur both structural and state changes [37, 38], similar to this case. In general, for paraffins with a higher melting point, there may be another "phase", consisting of solid flakes (particles) and liquid cells, which is called the mush phase. During structural change, a single phase undergoes thermal excitation, which results in the conversion (rebuilding) of the internal structures of the paraffin, and this is known as the solid–solid phase change.

The structure of the carbon–hydrogen chains changes and might have affected how energy is transferred between solid particles of the paraffin wax (molecular mechanism of heat conduction in a solid) [39].

Therefore, a strong increase in the heat conductivity coefficient during melting is the result of the reconstruction of the paraffin structure. This phenomenon is correlated with the structural change. After finalising the structural transition, thermal conductivity decreases to its minimal value for liquid wax, and then slowly increases with temperature. With the appearance of cells containing a liquid phase, convective heat exchange processes begin to dominate. This causes a strong decrease in the thermal conductivity of the paraffin wax. The particular values of this phenomenon are presented in Tab. 4.

DOI 10.2478/ama-2023-0009

Tab. 4. Thermal conductivity of the paraffin wax

Melting temperature (°C)	Thermal conductivity (kJ/kgK)		Reference
	Solid	Liquid	
32–32.1	0.514	0.224	Francis Agyenim
51.8	0.233	n/a	Mohamed Lachheb
53–57	0.26	0.16	Vahit Saydam

The measured values of the thermal conductivity coefficient for the solid phase that find mention in the literature [40, 41] are observed to be much higher than the values reported in the present study. The probable cause of these higher values might be the fact of the measurement having been made already, at the beginning of the phase transition. As can be seen from Fig. 7, there is a rapid increase in the thermal conductivity coefficient between the temperatures of 25.2 °C and 25.6 °C.

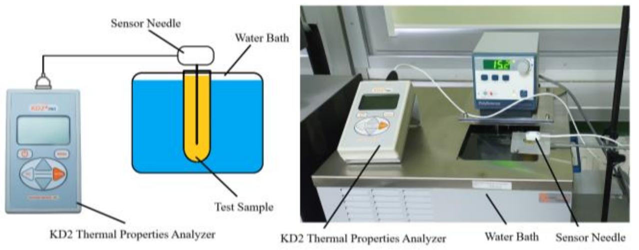

Fig. 6. Schematic diagram of thermal conductivity test equipment

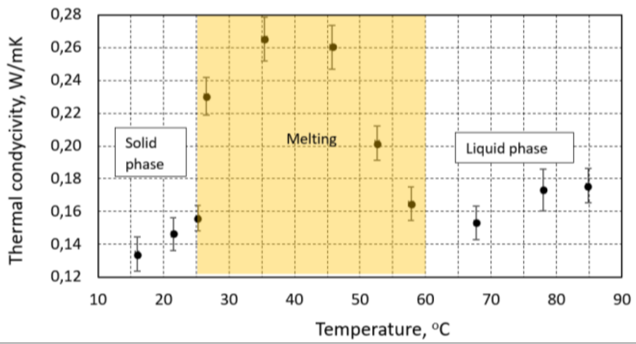

Fig. 7. Thermal conductivity of the wax vs. temperature

Standard uncertainty was calculated in accordance with recommendations in the literature, and its values are presented in Tab. 5.

Tab. 5. The melting point and the LH of the wax

Temperature (°C)	Standard uncertainty in the temperature (°C)	Thermal conductivity (W/[mK])	Standard uncertainty in the thermal conductivity (W/[mK])
16.0	0.30	0.134	0.010
21.5	0.26	0.146	0.010
25.2	0.27	0.156	0.008
26.5	0.30	0.230	0.012
35.4	0.37	0.265	0.013
45.7	0.30	0.260	0.013
52.6	0.28	0.202	0.010
57.8	0.36	0.165	0.010
67.7	0.33	0.153	0.010
78.0	0.28	0.173	0.013
84.8	0.28	0.176	0.010

LH, latent heat

The last determined material parameter was the density of the wax in its solid state and at a temperature of 22 °C. The value was determined using an analytical scale and with manual measurement of a cylindrical specimen. The obtained density value was 909 kg/m3 with an uncertainty of ±1%.

3. THERMAL PERFORMANCE OF THE STORAGE CONTAINER WITH PCM AND CERAMIC FOAM

In the following step, the authors researched the thermal properties of PCM dispersed in Al2O3/SiC composite foams, utilising an experimental TES system with a measurement setup designed for the purpose. Porosity of the foam was determined using optical analysis [42] with a help of open source software [43]. One of the most frequently used methods of porosity measurement is the Archimedes method, applied according to the EN 623-2 standard [44]. However, if the pore size is >200 μm, this method is not recommended for porosity measurements. In this case, the pore sizes were in the range of 1.5–3.0 mm. Therefore, the optical technique was used to measure the porosity of the Al2O3/SiC composite. This measuring technique is successfully used to determine the porosity of building materials, rocks, etc. The samples were photographed in a high resolution. Then, to further clean the image, a threshold value was set using an open-source photo editing software (ImageJ, an image processing program), so that any given pixel was either white or black (Fig. 8).

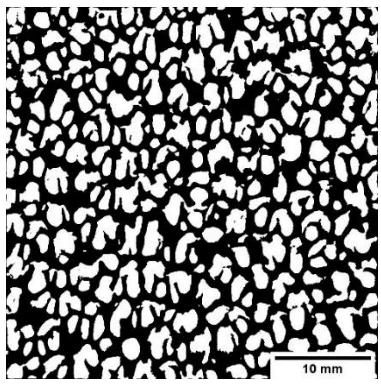

Fig. 8. Photographed image of ceramic foam (pores are white)

Then, the area of the pores and the skeleton was measured, and on this basis, the porosity was determined. Three samples of the foam were appraised to obtain a mean porosity of 48%. Then, the foam was placed in a cuboidal container (with a volume of 2.3 l), and filled with cheese wax afterwards (Fig. 9). The container was placed inside a case, which made it easier to mount probes and measurement devices to the rig and enable water-flow inside. During tests, the “hot” side of the rig was heated with flowing liquid (water), and the “cold” side was thermally insulated. A thin HF meter (OMEGA®, with 5% declared measurement uncertainty) was fixed to the "hot" side of the PCM container, in addition to the installation of two K-type thermocouples with which to measure the container's surface temperature. Additionally, three K-type thermocouples were installed in the space between the device's case and the container, to measure the flowing fluid's temperature. Five K-type thermocouples were also placed on the "cold" container's side.

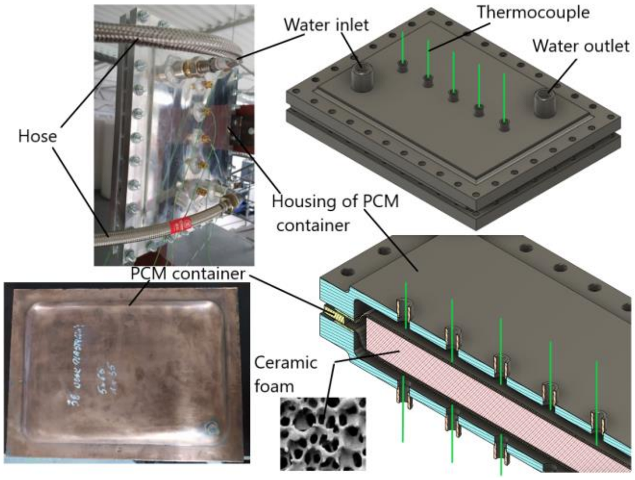

Fig. 9. View of the measuring section and the PCM container. PCM, phase change material

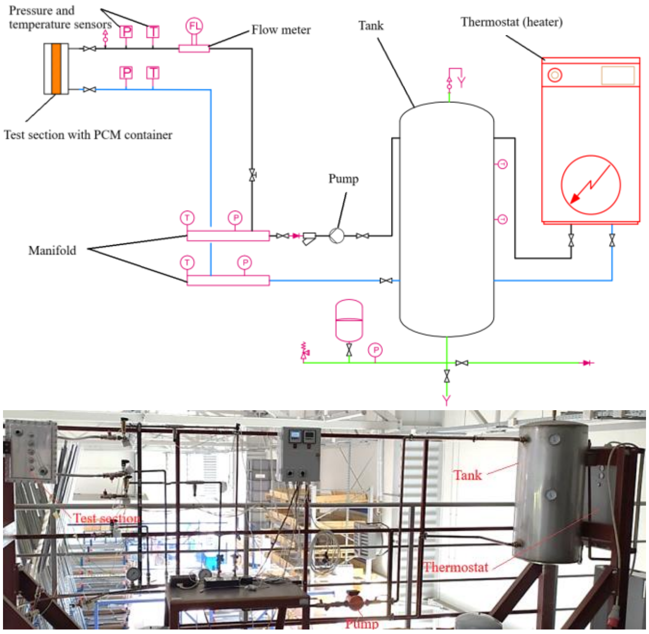

Fig. 10. Simplified scheme of the experimental stand

The test section was integrated into the experimental stand (Fig. 10). The stand consists of main parts such as: buffer tank, measurement/test section, pump and thermostat (heater). The buffer tank is included in the setup to maintain the stability and uniformity of the temperature at which hot water is supplied to the test section. The liquid's flow rate through the measurement section was regulated using a valve, and measured with a TecFluid TM44 turbine flowmeter. The temperatures on the inlet and outlet of the test section were measured using Pt100 thermistors, while the water-pressures at these same locations were read using WIKA piezoelectric transducers. For data acquisition, a DATAQ® Instruments GL820 midi Logger was used.

For the duration of the trials, the following parameters were logged:

– the test section's inlet and outlet temperatures;
– the water-pressures of the inlet and outlet;
– the volumetric flow rate;
– the temperature of the PCM container's external surfaces;
– the temperature of the surrounding environment; and
– the HF.

The data obtained were recorded in a text file. The main objective of this study was to determine the heat exchange conditions prevailing during the TES charging process and the amount of accumulated heat energy. To obtain the heat transfer coefficient, HF density on the container's surface was measured along with the temperatures of the fluid and of the aforementioned surface, with the liquid's volumetric flow rate being ascertained at 0.57 m3/h.

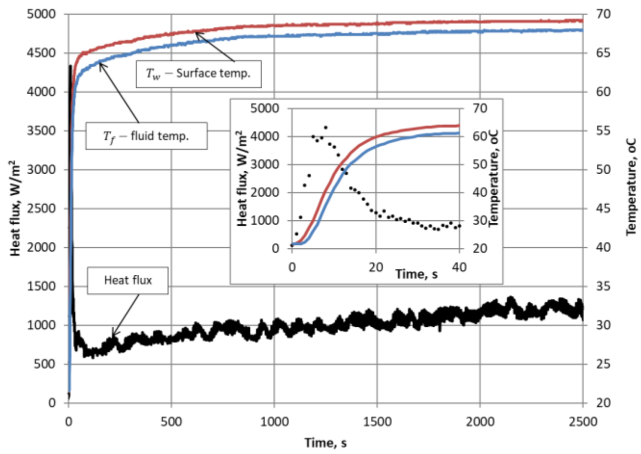

Fig. 11. HF density, fluid and surface temperature vs. time. HF, heat flux

At the beginning of the charging process, the HF from water to the PCM container grows rapidly, as shown in Fig. 11. This phenomenon is followed by a similar-in-size fast decrease and stabilisation of the parameter, with a slight increase over time. The initial growth of HF can be explained by the large difference between the temperatures of the container and the liquid at the beginning of a charging process. During forced convection, the temperature difference between the fluid and the wall is the main driving force in the process of thermal energy transport. Moreover, in the initial heat transfer process, the thickness of the thermal boundary layer is small. The thermal resistance of the boundary layer is very low and therefore the transfer coefficient attains high values. After the system's temperature becomes regulated, the "driving force" behind this HF's spike decreases. This is due to the stabilisation and growth in the thickness of the thermal boundary layer. The function of heat transfer coefficient in time was determined using the following formula:

$$h(t) = \frac{q(t)}{T_f(t) - T_w(t)}, \tag{11}$$

where: $h(t)$ represents the transient heat transfer coefficient, $q(t)$ the HF, $T_f(t)$ the temperature of the liquid and $T_w(t)$ the container's wall temperature.

Change of the heat transfer coefficient across time is presented in Fig. 11. Similarly as with the HF density graph, a spike of the coefficient's value is observed at the beginning of the process. It

DOI 10.2478/ama-2023-0009

can be explained by the relatively small thickness of the container's wall, enabling rapid heat exchange with large temperature differences of the container and a medium. The slight increase of the coefficient's value afterwards can be caused by a decrease in the fluid's viscosity at the container's surface as it accumulates more energy, intensifying fluid transport momentum.

The mean value of heat transfer coefficient $\bar{h}$ was calculated as a mean of the function:

$$\bar{h} = \frac{1}{t}\int_0^t \frac{q(t)\,dt}{T_f(t) - T_w(t)} \tag{12}$$

where: *t* indicates time.

The mean heat transfer coefficient calculated for a timeframe between 0 s and 2,500 s is 780 W/m2 K, proving that the heat exchange process is laminar.

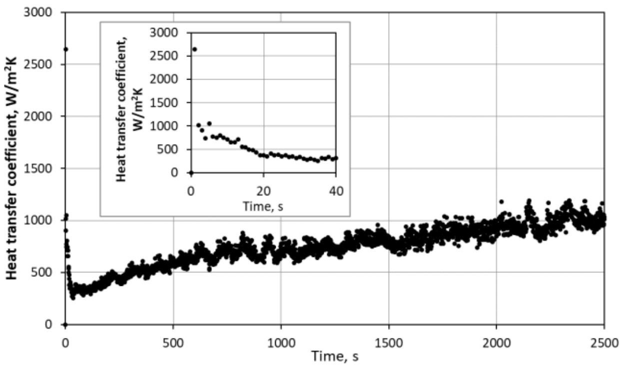

Fig. 12. Instantaneous value of the heat transfer coefficient

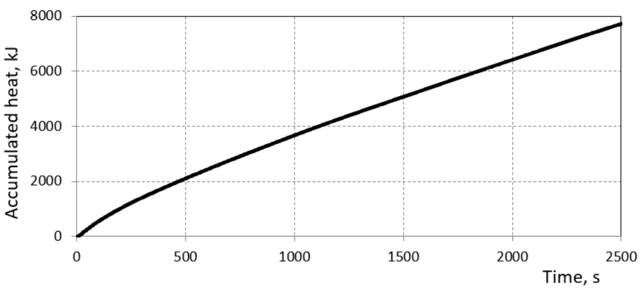

Fig. 13. The amount of accumulated heat

The amount of heat accumulated during charging process (Q) was calculated based on the relation:

$$Q = \int_0^t \rho\, c\, \dot{V}\, [T_{in}(t) - T_{out}(t)]\, dt \tag{13}$$

where: $\rho\, c$ represents the volumetric heat capacity of water, $\dot{V}$ water's volumetric flowrate, T_{out} temperature of water in the test section's outlet and T_{in} temperature of water in the test section's inlet. Water's volumetric heat capacity, which is a product of specific heat and density, was calculated, based on literature data [44, 45], to be the following:

$$\rho\, c = 4211.7 - 1.6796\, T_{av} \tag{14}$$

where: T_{av} temperature is an arithmetic mean of inlet's and outlet's liquid temperatures.

The determined amount of accumulated heat is presented on graph (Fig. 13). As visible, the amount of heat accumulated is an ascending linear function of time, except the beginning of the charging process. The slope of the curve presented in Fig. 13 depends on the heat capacity of the paraffin as well as on the heat transfer coefficient. The higher intensity of heat accumulation observed in the initial phase (Fig. 13) is related to higher values of the heat transfer coefficient, as shown in Fig. 12. The use of ceramic foam eliminates the effect (local change of the curve slope) related to the phase change [46, 47, 48].

4. SUMMARY

In this study, the authors carried out research on the thermal properties of a PCM – specifically wax. In the dominant majority of publications focussed on PCM materials, the description of the thermophysical properties is limited to information concerning only the LH, melting point temperature and (less often) the thermal conductivity coefficient (for the solid and liquid phases). There is a noticeable absence of complete information on changes in thermophysical properties during the phase change. Therefore, in this study, detailed thermophysical studies were carried out during the wax melting process. In particular, the temperature range in which the phase change occurs was precisely determined. This is important for the correct design of thermal energy accumulation systems.

Specific heat was determined for the material's solid and liquid states. In the material's solid state, a strong increase of specific heat capacity in relation to temperature increase is observed, reaching 2.9 kJ/(kgK) at a temperature of 25 °C. In the material's liquid state, a slight and approximately linear increase of specific heat with temperature growth was observed. DSC analysis revealed a one-stage melting process of the discussed substance, with very small differences in material behaviour during multiple subsequent heating cycles. The melting process of the analysed PCM occurs gradually in a range of temperatures starting at 25 °C and concluding at 60 °C. At the beginning of a melting process, the intensity of phase change LH's emission is relatively small. Vigorous increase of this value can be observed at 53 °C, which corresponds to the melting temperature determined in this research. The melting temperature and LH of melting were also determined as 52.3 °C and 104.0 kJ/(kgK), respectively. Omittable value differences for the LH of melting between different specimens shows that the analysed material possesses stable thermal properties. This is important for design purposes connected with TES devices and systems.

The heat transfer coefficient of wax was measured. Its value perceptibly varies with temperature changes. Above the temperature of 25 °C, it starts growing rapidly, to reach a value that is almost double its initial value, due to the material's phase transition. After a liquid phase appears, the heat transfer coefficient rapidly decreases and afterwards slightly grows with further temperature increase. The thermal analysis of a transient process of charging a PCM container filled with ceramic foam and wax was carried out. The analysis revealed that the value of the heat transfer coefficient grows rapidly at the beginning of the charging process, a phenomenon possibly caused by the small thickness of the near-wall thermal layer. This layer increases its thickness with time, thereby causing an associated decrease in the coefficient's value. Slight and steady growth of the coefficient afterwards can be caused by a decrease in the liquid's viscosity in the near-wall area.

REFERENCES

1. Tao YB, He Y-L. A review of phase change material and performance enhancement method for latent heat storage system. Renew. Sustain. Energy Rev. 2018; 93: 245–259.
2. Farid MM, Khudhair AM, Siddique AK Razack, Al-Hallaj S. A review on phase change energy storage: materials and applications. Energy Conversion and Management. 2004; 45:1597–1615.
3. Sharma A, Tyagi VV, Chen CR, Buddhi D. Review on thermal energy storage with phase change materials and applications. Renewable and Sustainable Energy Reviews. 2009; 13: 318–345.
4. Agyenim F, Hewitt N, Eames P, Smyth M. A review of materials, heat transfer and phase change problem formulation for latent heat thermal energy storage systems (LHTESS). Renewable and Sustainable Energy Reviews. 2010; 14: 615–628.
5. Kalnæs SE, Jelle BP. Phase change materials and products for building applications: A state-of-the-art review and future research opportunities. Energy and Buildings. 2015; 94: 150–176.
6. Chandel SS, Agarwal T. Review of current state of research on energy storage, toxicity, health, hazards and commercialization of phase changing materials. Renewable and Sustainable Energy Reviews. 2017; 67:581–596.
7. Ren Q, Guo P, Zhu J. Thermal management of electronic devices using pin-fin based cascade microencapsulated PCM/expanded graphite composite. Int J Heat Mass Transf. 2020; 149:119199.
8. Pielichowska K, Pielichowski K. Phase change materials for thermal energy storage. Progress in Materials Science. 2014; 65: 67–123.
9. Douvi E, Pagkalos C, Dogkas G, Koukou MK, Stathopoulos VN, Caouris Y, Vrachopoulos MG. Phase change materials in solar domestic hot water systems: A review. International Journal of Thermofluids. 2021; 10:100075.
10. Souayfane F, Fardoun F, Biwole P-H. Phase change materials (PCM) for cooling applications in buildings: A review. Energy and Buildings. 2016; 129: 396-431.
11. Nair AM, Wilson C, Huang MJ, Griffiths P, Hewitt N. Phase change materials in building integrated space heating and domestic hot water applications: A review. Journal of Energy Storage. 2022; 54:105227.
12. Schaetzle WJ. Thermal energy storage in aquifers: design and applications. 1980; New York: Pergamon.
13. Schmidt FW. Thermal energy storage and regeneration. 1981; New York: McGraw-Hill.
14. Naplocha K., et al. Effects of cellular metals on the performances and durability of composite heat storage systems. Int. J. Heat Mass Transf. 2017; 117:1214-1219.
15. Libeer W, et al. Two-phase heat and mass transfer of phase change materials in thermal management systems. Int. J. Heat Mass Transf. 2016; 10: 215-223.
16. Pagkalos C, et al. Evaluation of water and paraffin PCM as storage media for use in thermal energy storage applications: a numerical approach. 2020; Int. J. Thermofluids 1–2.
17. Telkes M, Raymond E. Storing solar heat in chemicals—a report on the Dover house. Heat Vent. 1949; 46(11):80–86.
18. Quenel J, Atakan B. Heat flux in latent thermal energy storage systems: the influence of fins, thermal conductivity and driving temperature difference. Heat Mass Transfer. 2022. https://doi.org/10.1007/s00231-022-03220-3
19. Yang X, Yu J, Xiao T, Hu Z, He Y-L. Design and operating evaluation of a finned shell-and-tube thermal energy storage unit filled with metal foam. Appl. Energy. 2020; 261:114385.
20. Acir A, Canli ME. Investigation of Fin Application Effects on Melting Time in a Latent Thermal Energy Storage System with Phase Change Material (PCM). Applied Thermal Engineering. 2018.
21. Aramesh M, Shabani B. Metal foams application to enhance the thermal performance of phase change materials: A review of experimental studies to understand the mechanisms. Journal of Energy Storage. 2022; 50:104650.
22. Tao YB, He YL. A review of phase change material and performance enhancement method for latent heat storage system. Renewable and Sustainable Energy Reviews. 2018; 93: 245–259.
23. Tariq SL, Ali HM, Akram MA, Janjua MM, Ahmadlouydarab M. Nanoparticles enhanced phase change materials (NePCMs)-A recent review. Applied Thermal Engineering. Applied Thermal Engineering. 2020; 176:115305.
24. Jianfeng WU, Yang ZHOU, Mengke SUN, Xiaohong XU, Kezhong TIAN, Jiaqi YU. Mechanical Properties and Microstructure of Al2O3/SiC Composite Ceramics for Solar Heat Absorber. Journal of Wuhan University of Technology-Mater. Sci. Ed.:615-623.
25. Devaiah M, Comparison of Thermal Conductivity Experimental Results of SICP/AL2O3 Ceramic Matrix Composites with Mathematical Modeling. International Journal of Applied Engineering Research. 2018; 13(6): 3784-3788.
26. DIN 51007 General principles of differential thermal analysis.
27. ISO 11357-4 Plastics. Differential scanning calorimetry (DSC). Part 4: Determination of specific heat capacity.
28. Ditmars DA, et al. Jour. Res. National Bureau of Standards. 1982; 87(2):159-163.
29. Agyenim F, Hewitt N, Eames P, Smyth M. A review of materials, heat transfer and phase change problem formulation for latent heat thermal energy storage systems (LHTESS). Renewable and Sustainable Energy Reviews. 2010; 14: 615–628.
30. Paris J, Falardeau M, Villeneuve C. Thermal storage by latent heat: a viable option for energy conservation in buildings. Energy Sources. 1993; 15: 85–93.
31. ISO 11357-3 Plastics — Differential scanning calorimetry (DSC) — Part 3: Determination of temperature and enthalpy of melting and crystallization.
32. Eysel W; Breuer KH. The calorimetric calibration of differential scanning calorimetry cells. Thermochim. Acta. 1982; 57(3): 317-329.
33. Coleman HW, Steele WG. Experimentation, Validation, and Uncertainty Analysis for Engineers, third ed. John Wiley & Sons, Inc, 2009.
34. Evaluation of measurement data — Guide to the expression of uncertainty in measurement, GUM; 2008.
35. KD2 Pro Thermal Properties Analyzer Operator's Manual. Version 10. Decagon Devices. Inc.; 2011.
36. Wang J, Xie H, Xin Z., Thermal properties of paraffin based composites containingmulti-walled carbon nanotubes, Thermochimica Acta. 2009; 488:39-42.
37. Gulfam R, Zhang P, Meng Z. Advanced thermal systems driven by paraon-based phase change materials - A review. Applied Energy. 2019; 238: 582-611.
38. Gulfam R, Zhang P, Meng Z., Phase-Change Slippery Liquid-Infused Porous Surfaces with Thermo-Responsive Wetting and Shedding States. ACS Appl. Mater. Interfaces. 2020; 12: 34306−34316
39. Saydam V, Duan X. Dispersing Different Nanoparticles in Paraffin Wax as Enhanced Phase Change Materials – A Study on the Stability Issue. Journal of Thermal Analysis and Calorimetry volume. 2019; 135: 1135-1144.
40. Lachheb M, Karkri M, Albouchi F, Ben Nasrallah S, Fois M, Sobolciak P.Thermal properties measurement and heat storage analysis of paraffin/graphite composite phase change material. Composites: Part B 66. 2014: 518–525.
41. de Vries DA. A nonstationary method for determining thermal conductivity of soil in situ. Soil Sci. 1952; 73:83-9.
42. D. Martin III Bradley, J. Putman, Nigel B.Kaye: Using image analysis to measure the porosity distribution of a porous pavement, Construction and Building Materials, Volume 48, November 2013, pp. 210-217

DOI 10.2478/ama-2023-0009

43. Image Processing and Analysis in Java-ImageJ. Available from: https://imagej.nih.gov/ij/index.html
44. EN 623-2 Advanced technical ceramics. Monolithic ceramics. General and textural properties. Determination of density and porosity.
45. IAPWS Industrial Formulation 1997 for the Thermodynamic Properties of Water and Steam. In: International Steam Tables. Springer. Berlin, Heidelberg. 2018.
46. Sun X, Chu Y, Medina MA, Mo Y, Fan S, Liao S. Experimental investigations on the thermal behavior of phase change material (PCM) in ventilated slabs. Applied Thermal Engineering. 2014; Volume 148; 5:1359-1369.
47. Bałon P., Kiełbasa B., Kowalski Ł., Smusz R., Case Study on the In_ uence of Forming Parameters on Complex Shape Part Deformation, Advances in Science and Technology Research Journal 2022, 16(6):204–213
48. Wilk J., Bałon P., Smusz R., Rejman E., Świątoniowski A., Kiełbasa B., Szostak J., Cieślik J., Kowalski Ł., Thermal Stratification in the Storage Tank, Procedia Manufacturing, 2020; 47:998–1003

The research activities comprised in this study were carried out within the LIDER IX project entitled “Development of an innovative modular energy storage system using phase change materials” (No. 0004/L-9/17/NCBIR/2018), financed by the National Centre for Research and Development.

Paweł Bałon: https://orcid.org/0000-0003-3136-7908

Bartłomiej Kiełbasa: https://orcid.org/0000-0002-3116-2251

Łukasz Kowalski: https://orcid.org/0000-0002-2866-9000

Robert Smusz: https://orcid.org/0000-0001-7369-1162

ASSESSMENT OF THE IMPACT OF WEAR AND TEAR OF RUBBER ELEMENTS IN TRACKED MECHANISM ON THE DYNAMIC LOADS OF HIGH-SPEED TRACKED VEHICLES

Piotr RYBAK*, Zdzisław HRYCIÓW*, Bogusław MICHAŁOWSKI*, Andrzej WIŚNIEWSKI*

*Faculty of Mechanical Engineering, Military University of Technology, ul. gen. Sylwestra Kaliskiego 2, 00-908 Warszawa, Poland

piotr.rybak@wat.edu.pl, zdzislaw.hryciow@wat.edu.pl, boguslaw.michalowski@wat.edu.pl, wisniewski.andrzej@wat.edu.pl

received 12 October 2022, revised 25 November 2022, accepted 12 December 2022

Abstract: The operation of high-speed tracked vehicles takes place in difficult terrain conditions. Hence, to obtain a high operational reliability, the design or modernisation process must be precise and should consider even the slightest details. The article presents issues related to the problem of formulating vehicle models using partial models of flexible elements used in tracked mechanisms. Changes occurring in the shape and properties of elements such as track pads and roadwheel bandages as a consequence of operating conditions are presented. These changes are reflected in the presented elastic–damping characteristics of components of the crawler mechanism. Numerical studies have shown that deterioration of chassis suspension components after a significant mileage may increase dynamic loads (forces) acting on the running gear. Increased forces in the running gear naturally result in increased stresses in the road surface on which the vehicle is travelling, which can pose a danger (or excessive wear and tear) to road infrastructure components such as culverts, bridges and viaducts. In the literature, model tests of objects are carried out on models that represent new vehicles, and the characteristics of the adopted elements correspond to elements not affected by the process and operating conditions. Its influence should not be ignored in the design, testing and running of a special vehicle. The tracked mechanism, as running gear, is designed for special high-speed vehicles for off-road and off-road driving. Its design ensures high off-road traversability. The dynamic loads originating from off-road driving are superimposed on those generated by the engine, drive train and interaction of the tracks with the roadwheels, sprocket, idler and supporting tracks return rollers.

Key words: maintenance, tracked mechanism, rubber elements, roadwheel, high-speed tracked vehicle, characteristics, modelling

1. INTRODUCTION

The issues related to the tracked vehicle operation are described infrequently and to a rather limited extent in the literature. The authors of most publications consider and analyse the problems experienced in tracked vehicles in industrial applications, e.g., see literature [1, 2] or civil applications, e.g., see literature [3, 4]. In high-speed tracked vehicles (HSTVs), the issue is even more complex. It requires considering several factors that affect the effectiveness and safety of the execution of tasks. The operating conditions (terrain, climatic and meteorological conditions, and dust) are important, a general description of which is included in the literature [5]. An interesting approach to the problem, the influence of vehicle operating time, is presented in the literature [6], where the impact of wear and tear of suspension elements on the dynamic loads of the vehicle is considered. Research on prototype crawler pads of crawler track links is presented in the literature [7]. An analysis of the elastomeric cover pad wear and tear process has been shown to indicate its applicability in HSTVs. The issue of vehicle operational safety and dynamic loads affecting this safety is described in the literature [8, 9]. The papers [10, 11] present the results of numerical tests of vehicle models with crawler tracks that differ in the way the links are connected. Their effects have been analysed on the dynamic loads of the vehicle body when passing over road bumps. The paper [12] describes a model of the interaction of the track–wheel–terrain system and presents the results of model tests for two types of rubber continuous and metal multi-part crawler track belts. In the paper [13], the modelling process and results of load tests that occur on a crawler track with different ways to connect the links are presented. Dynamic forces acting on the vehicle running gear during driving focused on a crawler track were measured in experimental research, the results of which are presented in the paper [14]. The authors proposed and tested the concept of an active mechanism compensating force tension in the tracks. The research was carried out by using numerical analysis. The presented results point towards the reduction in crawler track dynamic tension magnitudes and stability improvement of the tracked mechanism. In the paper [15], a bench testing solution for the analysis of various load conditions of a rubber crawler track is presented. Particular attention has been focused on the forces and stresses that occur in it. The results obtained from the calculation have been compared with the experimental data, and good consistency has been obtained. The methods of calculation of the internal resistance of elements in tracked vehicles are considered in the paper [16]. Various models of roadwheel rolling resistance, rubber track belt bending and crawler track resistance are presented. The authors of the study concluded that the various existing models lead to inconsistent results, especially due to the lack of sufficient data in the case of conventional rubber tracks. In the paper [17], the double roadwheel resistance model including a rubber double band is presented. Resistance is calculated as the total of roadwheel and track contact and the friction of wheel and track guide lugs. The model includes vertical and lateral loads of roadwheels, non-uniform pressure and relation of normal forces between the roadwheel and track guide lugs. As result of experimental and model investigations, solutions to reduce losses in running gear are proposed. The interaction of the elements of the crawler track mechanism with the ground using simplified substitute models has been presented in the papers [18, 19]. The calculation results have been validated with data from the literature and with the results obtained from detailed calculations of the models.

The crawler track mechanism is a running system in which the driving force generated by the engine, which causes the vehicle to move, is intermediated by the crawler tracks to the ground [20]. The high-speed tracked vehicle (HSTV) is a vehicle that develops a running speed of >25 km/h. With a gross vehicle weight of up to 70 t (tonne), such vehicles can reach speeds of up to 75 km/h on paved roads and up to 55 km/h off-road. Such conditions result in increasingly complex dynamic loads of high intensity and random varying parameters.

It is usually assumed that the elastic and damping properties of suspension elements remain essentially unchanged in the lifetime of the track running gear system, whereas the elastic and damping properties of rubber elements of crawler track mechanisms change quite significantly due to wear and tear, mechanical damage, temperature effects and the operating environment. The literature presents results mainly obtained from model tests of new vehicles. For example, the papers [21–23] present models and results of analysis of the interaction of crawler tracks with different types of ground. On the contrary, the paper [24] analyses the effect of the arrangement of shock absorbers on the dynamic loads acting on the tracked vehicle. Some parameters or characteristics are assumed to be invariant during the operating process, while others are ignored. The results of numerical investigations of the 2S1 tracked mechanism with modified suspension are presented in the paper [25]. Torsion bars are replaced with hyperbolic springs. As the result of the proposed modifications improved the stability of the vehicle and reduced the interior and the exterior volume of the vehicle suspension. In the paper [26], a vehicle has been analysed in which the stiffness of the new rubber bandages of the roadwheels has been included, neglecting their damping. In the paper [23, 27], a tracked vehicle model has been used for simulation studies to assess the effects of the terrain geometry, soil characteristics and speed on vehicle performance.

Articles considering the impact of ageing wear and tear of rubber elements in the running gear of tracked vehicles on dynamic loads of HSTVs, such as medium tanks, and its impact on the environment are uncommon. This applies particularly to rubber bands on roadwheels and rubber pads on tracks.

It can be considered that the studies carried out do not take account of the changes in the properties of the elements of the crawler track mechanism of the vehicles, especially in those elements where rubber is used. These changes are due to the distance travelled, speed of travel, type of ground, weather conditions and material ageing. It can be assumed that the material used in this study fills the gap well in this field area.

The genesis of the undertaken topic is the process of modernisation of combat vehicles. It originates in the necessity of improvement of the safety of the crew, leading to an increase in the sprung mass and engine horsepower. As a consequence, roadwheel rolling resistance and dynamic loads or running gear increase.

This study aims to evaluate the effect of wear and tear of rubber elements in the running gear occurring during typical vehicle operation conditions on the change in dynamic loads acting on the vehicle chassis, hull and crew.

2. OPERATING LOADS OF VEHICLE RUNNING GEAR

The natural operating conditions of the HSTV are shown in Fig. 1. The main loads on the crawler track mechanism and the intensity of wear of its elements depend, among other things, on the mass of the vehicle m_b [kg], time of use t [h], running speed v [m/s], steering angular velocity ω [1/s], temperature Δt [°C], pretension of crawler tracks P_w [N], height of ground bumps h [m], their distribution and length l_p [m], type of ground (sand, clay, rocks, etc.) f_{gr} and physical properties of construction materials WM. Thus, its durability T is mainly a function of factors such as in Eq. (1):

$$T = f(m_b, t, y, v, \omega, \Delta t, P_w, l_p, f_{gr}, WM) \tag{1}$$

The design pre-tension of the P_W crawler track belt is given by Eq. (2):

$$P_W = \frac{\rho \cdot g \cdot l^2}{8 \cdot f} \tag{2}$$

where ρ is the unit mass of the crawler track [kg/m], g is the acceleration due to gravity [m/s²], l is the length of the freely hanging section of the crawler track [m] and f is the deflection arrow [m]. The pre-tension of the crawler track should meet the following condition: $f_{min} \leq f \leq f_{max}$ (where f_{min} is the deflection arrow at the minimum tension and f_{max} is the deflection arrow at the maximum tension).

(a)  (b) 

Fig. 1. Natural conditions for the movement of special vehicles: (a) cornering on a paved road and (b) unsurfaced road

Only the tracked vehicle contains a road that can be assumed to have an infinite length. Crawler track belts are unfolded in front of roadwheels, smoothing out the bumps to overcome. After the last wheel has passed, they are taken up from the ground, rewound and unfolded again. The large load-bearing surface of the crawler tracks (Fig. 2) provides vehicles considerable weight with a low average unit pressure ps Eq. (3), as follows:

$$p_s = \frac{G}{2 \cdot F} = \frac{m_b \cdot g}{2 \cdot L_0 \cdot b} \tag{3}$$

where G is the force of gravity of the vehicle, F is the area of the lower track branches, L_0 is the length of contact between the lower track and the ground, b is the width of the track and g is gravitational acceleration.

Contemporary HSTVs up to 40 t have an average unit pressure on the deformable ground of p_s = (40–70) kPa. The average unit pressure of vehicles >40 t is in the range p_S = (75–100) kPa. The tactical and technical requirements for HSTVs >40 t impose a prerequisite that average pressures should not exceed $p_s \leq 85$ kPa. For wheeled vehicles (including multi-axle vehicles), the pressure value is much higher and is in the range p_s = (170–350) kPa [8]. An increase in specific pressures increases the ground resistance force F_{gr} Eq. (4), as follows:

$$F_{gr} = Z \cdot f_{gr} = G \cdot f_{gr} \cdot \cos\alpha \tag{4}$$

where f_{gr} is the ground resistance coefficient, N is the normal reaction and α is the road slope angle.

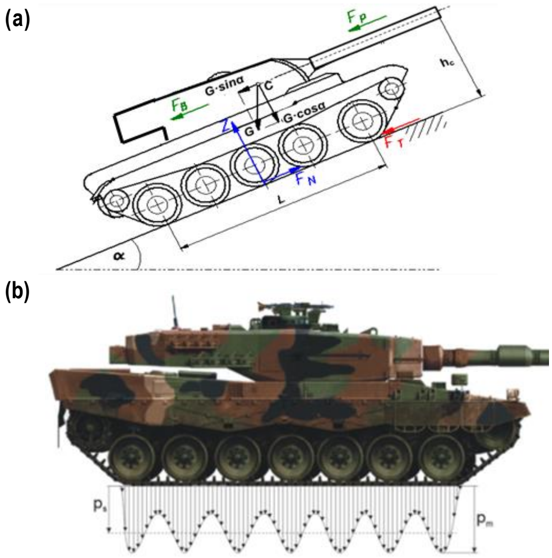

Fig. 2. Diagram showing the interaction of the crawler track mechanism with the ground: (a) diagram of the forces acting on the HSTV and (b) distribution of ground pressures: pm – maximum value, ps – average value

The pressure value p_s combined with the high ground adhesion F_φ Eq. (5) makes it much easier for tracked vehicles to navigate in difficult terrain conditions (φ is the coefficient of adhesion of crawler tracks to the ground).

$$F_\varphi = 0.65 \cdot G \cdot \varphi \tag{5}$$

Some of the data and results of the studies and analyses, due to the status of the vehicles analysed, are characterised by a certain sensitivity value. It should be assumed that they have qualitative, rather than quantitative, qualities.

3. RUBBER ELEMENTS IN THE CRAWLER TRACK RUNNING MECHANISM AND ITS EXTERNAL FACTORS OF WEAR

In motor vehicles, rubber elements (with different shapes, material compositions, manufacturing methods and characteristics) are used extensively, whereas in HSTVs, some of the rubber elements are quite different from the typical rubber elements and have a special role in the operating process. Those are integral parts of the assemblies and elements of the crawler track mechanism subjected to complex dynamic loads in the surrounding environment. Some of the structural assemblies of the crawler track mechanism that use rubber with given properties, shape and geometry are shown in Figs. 3–8. Fig. 3 shows a roadwheel with a vulcanised rubber band of the appropriate thickness and width (these parameters depend on the weight and inertia of the vehicle, the number of roadwheels and the model of interaction of the crawler track with the ground). The use of external rubber bandages enables:

– a reduction in the amount of heat liberated by the friction of the rubber band against the track links compared to pure steel wheels;
– a reduction in the dynamic loads acting on the vehicle hull and crew;
– a reduction in the noise level during driving; and
– a reduction in the amount of heat released during the friction of the rubber band against the crawler track belts compared to steel-rimmed wheels featuring internal shock absorption.

Fig. 4 shows sections of the crawler track belts and links used in HSTVs, with a crawler track of the hinge type (Fig. 4a) and a crawler track of the link type (Fig. 4b).

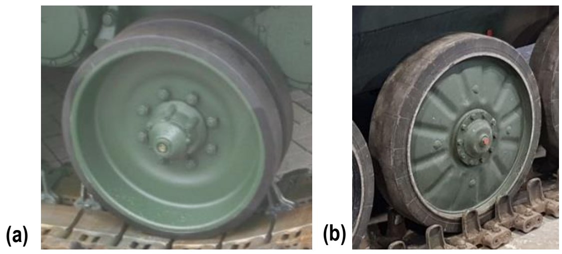

Fig. 3. Roadwheel with an outer rubber band: (a) double outer rubber band and (b) single outer rubber band

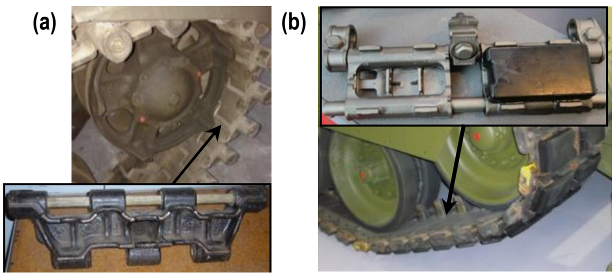

Fig. 4. Hinge (a) and link (b) types of crawler tracks

The links of the crawler track of the hinge type, with a weight of up to 16 kg, are connected by a single pin (Fig. 4a), whereas the links of the crawler track of the link type, with a mass of up to 24 kg, are connected by two pins (Fig. 4b). The links rotate relative to each other by deforming the rubber bushings in a torsional manner, forming the so-called closed joint. To reduce the load on the bushings and reduce the energy loss while driving, the links are connected at an appropriate angle when assembled (angle α in Fig. 5).

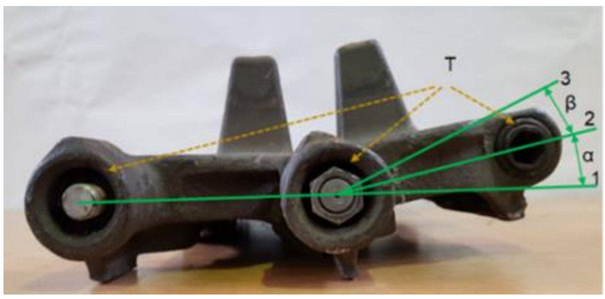

Fig. 5. Crawler track links with a rubber and metal joint: T – rubber-metal bushings, 1 – line parallel to the ground surface, 2 – line of zero torsional stress, 3 – line of maximum torsional stress, α – mounting angle of links, β – angle of maximum relative rotation of links

DOI 10.2478/ama-2023-0010

In the HSTV crawler tracks, interchangeable link cover pads of the crawler track are used (Fig. 6), which can be fixed in an elastic holder (Fig. 6a) or with a screw (Fig. 6b).

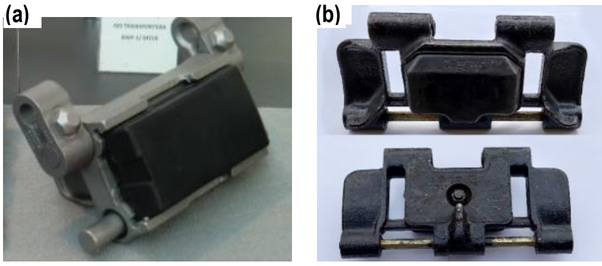

Fig. 6. Link cover pads of the HSTV crawler tracks fixed: (a) pressed into guides and (b) screwed into the socket

Rubber cover pads of crawler tracks contribute to the ability to be driven on public roads (by reducing pavement loads) as follows: a reduction in the amount of heat released when the cover plate is in friction with the ground compared to a metal crawler track, a reduction in vehicle slip-on paved surfaces, a reduction in the noise level when driving, a reduction in dynamic loads when driving off-road, an increase in grip on hard rough pavement and a reduction in grip on soft ground. On vehicles where roadwheels have a reduced thickness band in addition to cover plates, rubber cushions may be used on the inner surfaces of the links, as shown in Fig. 7.

Fig. 7. Rubber cushions on the inner surface of the links of crawler tracks

During the operation of HSTVs, insufficient resistance of some elements of the crawler track mechanisms to complex operating loads can be observed. This affects the durability and reliability not only of the crawler track mechanism but also of other vehicle units and systems. The aforementioned applies to both the cover pads of the crawler track links, which have a specified odometer reading of 1,000–1,500 km, and the bandages of roadwheel, whose wear and tear and failure rate depend on the intensity of use, dynamic loads, ambient and operating temperatures. Examples of damage to bandages and cover plates are shown in Figs. 8a and 9. When driving on a hard, rough road surface:

– rubber track pad plates are subject to abrasive wear and tear during cornering (Fig. 1a), and the weight of the links and crawler tracks may change (also by tearing out rubber fragments – Fig. 8b);
– rubber track pads plate, as a result of wear and tear, can cause a reduction in the thickness of the damping layer and an increase in the noise level during dynamic driving may occur (the cause for this phenomenon is the uneven weight distribution in the link. In the link, different inertial forces act on the pins, drive wheels, directional wheels, roadwheels and support rollers); and
– rubber track pad plates can cause a risk of loss of stability at high speeds in curvilinear motion.

On deformable ground:

– rubber cover pads have an impact on running resistance, depending on the shape and geometry of the link and the cover pads and their degree of wear and tear;
– during dynamic driving and cornering, the track is at risk of dropping or tipping over on the dry, turf-covered ground.

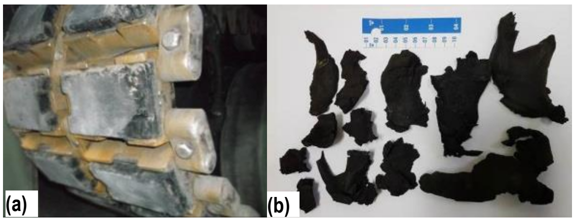

Fig. 8. Rubber cover plates: (a) with varying degree of wear and tear and (b) torn out rubber pad fragments

A confirmation of the considerable load on the links of crawler tracks and their wear during an interaction with the ground is shown in Fig. 9, where Fig. 9a shows a link of a new metal crawler track, while Fig. 9b after greater mileage. The abrasive wear of the ground grapples is visible.

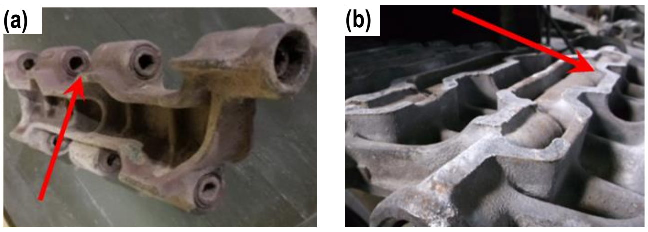

Fig. 9. Working surfaces of metal ground gripples of links. (a) new link and (b) used link

An important element that affects the efficiency and durability of crawler track belts is the link joints. The introduction of rubber and metal joints has, irrespective of the type of crawler track, eliminated the possibility of direct engagement between pins and link lugs in highly abrasive environments.

The rubber bandages of the roadwheels carry complex dynamic loads in the radial, circumferential and transverse directions when the vehicle is in motion. Roadwheels may also be exposed to external mechanical sources such as stones, debris and rocks. This process also generates thermal loads, which can have a significant impact on the elastic properties of rubber. The result of the aforementioned impacts is damage to the bandages. Examples of the most common damage cases are shown in Fig. 10. The running conditions of special HSTVs, in military applications, pose some challenges to vehicle designers and manufacturers. The rubber used for the structural elements of the crawler track mechanism must meet the assumed requirements and be characterised by appropriate properties, especially within scope of:

– high resistance to mechanical stress (compression, tension, impact, chipping, tearing);
– good energy absorption (vibro-insulating properties) to reduce dynamic loads on the vehicle hull and crew;
– high abrasion resistance;
– high adhesion to metals (vulcanising properties);

– high thermal resistance (non-combustible or self-extinguishing); and
– good thermal conductivity, heat dissipation into the superstructure (load-bearing wheel rim, base of cover plate, etc.) and environmental resistance (ageing, exposure to operating fluids).

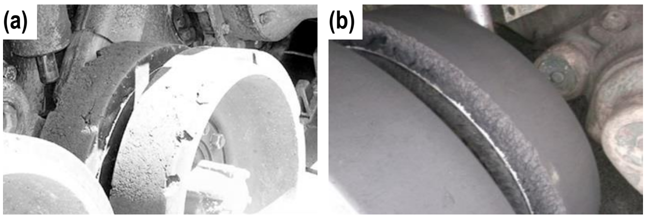

Fig. 10. Damage to the rubber bands of the load-bearing wheels: (a) abrasive and mechanical wear and (b) interaction of the track guide ridges and devulcanisation of the bandage from the rim

The change in the elastic and damping (ED-RP) properties of the rubber elements of the crawler track mechanism after a significant mileage is the result of the impact of a number of factors. The main factors are summarised in the following Eq. (6):

$$ED - RP = f(WM, shape\ (a\ x\ b\ x\ c), t_e, v, P_{ks}, P_w, P_k, P_o, \sigma_z, \Delta t) \quad (6)$$

where *WM* is the physical properties of the material, *a* x *b* x *c* is the *(length x width x height)* dimensions of cover plate [m], t_e is the time of use [h], *s* is the mileage [km], P_{ks} is the static load [kN], P_k is the crawler track tension from driving force [kN], P_k is the crawler track tension resulting from centrifugal force [kN], σ_z is stresses and Δt is the temperature increment.

4. METHODOLOGY

4.1. Experimental setup

The models for testing should be built on the actual characteristics of elements and also with an observation of changes occurring during day-to-day running. To identify the relevant parameters of selected rubber elements, bench tests have been conducted. The tests were carried out on an Instron 8802 machine. Each of the test objects was subjected to deflection from 5 mm to 14 mm, with a frequency in the range of 0.1–2 Hz. For each variant, 10 load cycles have been carried out. Fig. 11a shows the test bench while testing a sample of a roadwheel with a rubber bandage, and Fig. 11b shows the test bench with a rubber pad during axial compression. The initial deflection of the rubber pad was 7 mm.

The stiffness (*k*) of the elements under test is determined from the elastic characteristics for the static equilibrium position, from the following Eq. (7):

$$k = \frac{\Delta P}{\Delta f} \quad (7)$$

or determined by Young's modulus of the sample material of the element, obtained from the following Eq. (8) [28]:

$$k = \frac{E \cdot A}{h} \quad (8)$$

where *P* is the element load [kN], f is the displacement [mm], E is the determined Young's modulus [MPa], A is the surface area of the sample [mm^2] and h is the height of the sample [mm].

The dispersion coefficient ψ is determined from the following Eq. (9):

$$\Psi = \frac{\Delta W}{W} \quad (9)$$

where ΔW is the value of energy dispersed during one vibration cycle [J] and W is the value of energy supplied to the system during this vibration cycle [J].

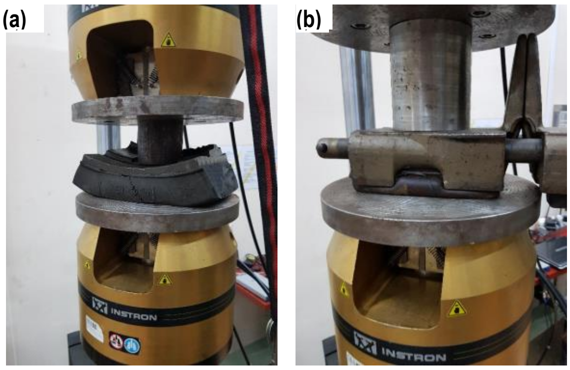

Fig. 11. Bench testing of elements of crawler track mechanism: (a) a sample of roadwheel with rubber bandage and (b) a rubber pad

4.2. Numerical model

Depending on the purpose of the study, vehicle models are characterised by varying degrees of complexity. These can be discrete models with one, two and a finite number of degrees of freedom or models developed and analysed by FEM [29]. Partial models can be used to analyse complex dynamic objects such as HSTVs, as demonstrated in the paper [30].

Fig. 12 shows a model of the high-speed tracked vehicle adopted for the analysis. The relevant partial models of the susceptible elements of the crawler track mechanism have been distinguished in it.

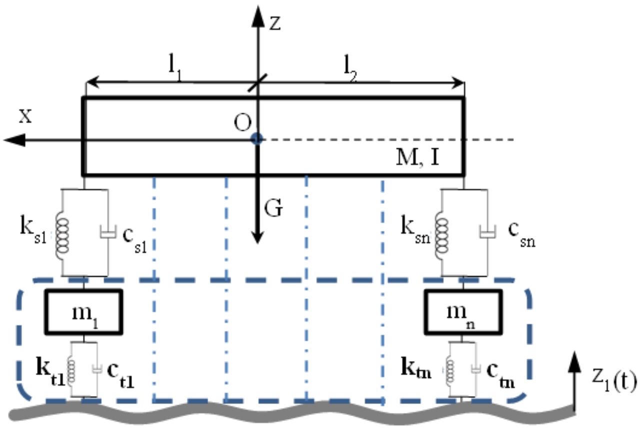

Fig. 12. HSTV model: M – body mass, I – body moment of inertia, G – gravity, k_{s1}, ..., k_{sn} – spring stiffness of the suspension, c_{s1}, ..., c_{sn} – suspension damping, k_{t1}, ..., k_{tn} – stiffness, c_{t1}, ..., c_{tn} – damping of the rubber elements of the crawler track mechanism, and n – number of roadwheels at one side

The equation of motion of the vehicle is given by the following Eq. (10):

DOI 10.2478/ama-2023-0010

$$\boldsymbol{M}\ddot{q} + \boldsymbol{C}\dot{q} + \boldsymbol{K}q = \boldsymbol{F}\Psi = \frac{\Delta W}{W} \tag{10}$$

where *M* is the diagonal inertia matrix of the system, q is the generalised displacement vector, *C* is the damping matrix, *K* is the stiffness matrix and *F* is the generalised force vector resulting from the kinematic excitations acting on the wheels.

Numerical investigations were performed with the original finite element code. In the investigation, there were 18 degrees of freedom, including vertical displacement of wheels Eq. (12), the hull and the driver seat Eq. (2), and rotations along the longitudinal (x) and traversal (y) axes of the vehicle hull Eq. (2) and the driver seat Eq. (2). The model includes non-linear sprung and damping characteristics of vehicle suspension. The test object has been the hypothetical HSTV with a mass of 42 t, the moment of inertia I_x=92,000 kg/m^2 and I_y=190,000 kg/m^2 based on the undercarriage of a medium-sized tank, and running speed of 30 km/h on a non-deformable road with a single obstacle in the form of two road bumps, first in the shape of (1-cos) function (obstacle A) and second in form of a triangular prism shape (obstacle B).

The shape of the first obstacle is given by Eq. (11), while the second by Eq. (12):

$$z(t) = \begin{cases} \frac{h}{2}\cdot\left(1 - cos\cdot\left(\frac{2\cdot\pi\cdot V\cdot t}{L_b}\right)\right), & t \le \frac{L_b}{V} \\ 0, & t > \frac{L_b}{V} \end{cases} \tag{11}$$

where h is the obstacle height [m], V is the driving speed [m/s] and L_b is the obstacle length [m].

$$z(t) = \begin{cases} \frac{h\cdot\mathrm{V}\cdot\mathrm{t}}{L_p}, & t \le \frac{L_p}{V} \\ \frac{h}{L_p}(2\cdot\mathrm{L} - \mathrm{V}\cdot\mathrm{t}), & \frac{L_p}{V} < t \le \frac{2\cdot L_p}{V} \\ 0, & t > \frac{2\cdot L_p}{V} \end{cases} \tag{12}$$

where L_p is the half of total obstacle length [m].

Both had a height of 0.15 m and a length of 1 m. Model studies can also be carried out for other obstacle profiles such as threshold, sinusoidal track also combined with kinematic shape with pseudo-random distribution (various quality road).

5. RESEARCH RESULTS

5.1. Experimental investigation

Fig. 13 shows the results of measurements not subjected to additional processing steps. The graph also shows the deflection spike near zero load force, caused by the detachment of the rubber pad from the stand base. The stiffness characteristic presented in Fig. 14 is not suitable for implementation in the numerical investigation. One cycle was selected from the recorded trial, then the approximations for force load and unload phases were determined with an average curve, and an area of the hysteresis loop corresponding to the dissipation energy was determined.

The aforementioned procedure was applied both for rubber pads and a section of roadwheel with a rubber bandage. The numerical study assumes the implementation of the running system as a substitute model. The rubber band works in series with the rubber pad in the vehicle running system. Fig. 15 shows individual characteristics, where blue denotes a new rubber pad (RP1), green denotes a new rubber band (RB) and resultant characteristic and yellow denotes a series connection (RP1 and RB). Fig. 16 shows individual characteristics, where blue denotes a used rubber pad (RP2), green denotes a new rubber band (RB) and resultant characteristic, and yellow denotes a series connection (RP2 and RB).

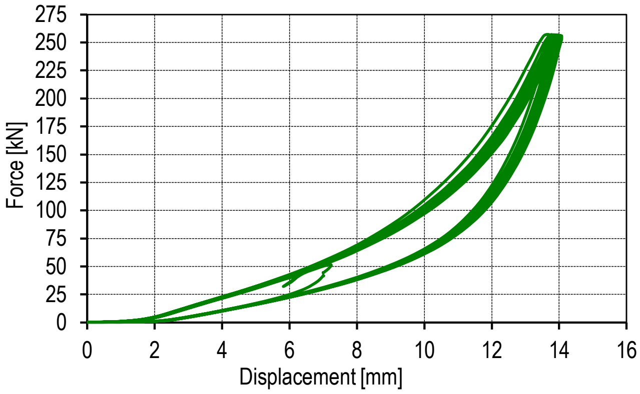

Fig. 13. Stiffness characteristic for the new rubber pad consisting of ten cycles

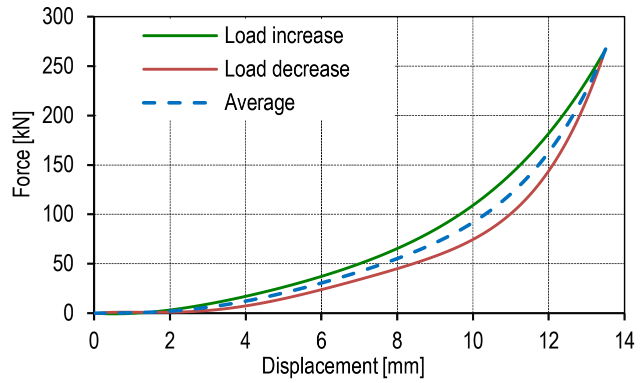

Fig. 14. Processed stiffness characteristic: force load (green line), force unload (brown line) and suitable for numerical investigation form visible as a dashed line

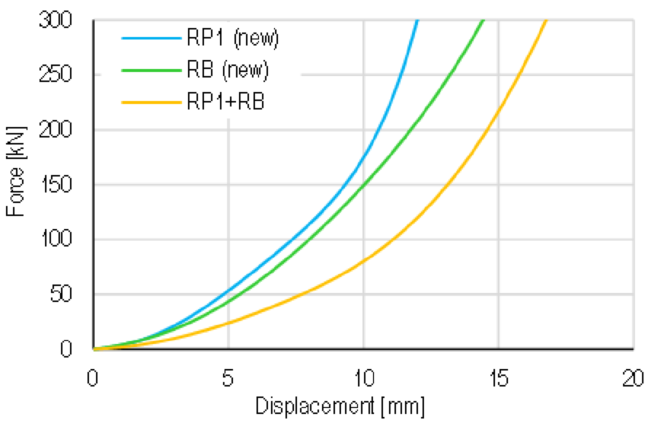

Fig. 15. Approximated stiffness characteristics: blue line – new rubber pad, green – new rubber band, yellow – resultant characteristic

DOI 10.2478/ama-2023-0010 acta mechanica et automatica, vol.17 no.1 (2023)

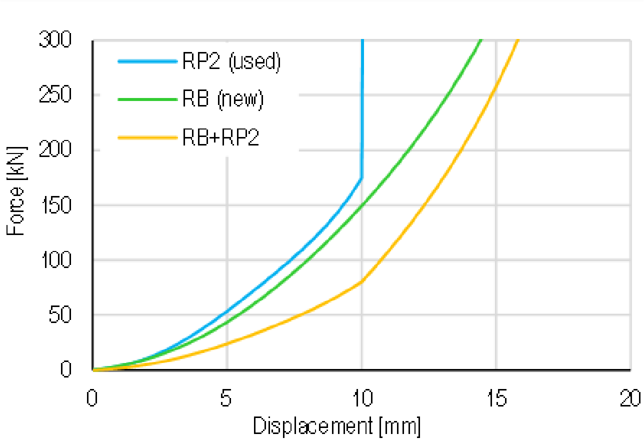

Fig. 16. Approximated stiffness characteristics: blue line – used rubber pad, green – new rubber band, yellow – resultant characteristic

5.2. Model research

Model tests have several advantages: they are non-destructive, enable a multivariate analysis in a short time, do not require a large investment and are safe. Depending on the specific characteristics of the elastic and damping elements present in the crawler track mechanism, it is possible to determine, at each stage of operation, the loads on the hull as well as the driver, the dynamic reactions of the load-bearing wheels and the deflection of the rubber bandage, allowing the determination of ground loads. Examples of the dynamic load patterns from the tests for the rubber elements analysed – new and after the run – are shown in Figs. 17 and 18.

The main part of Fig. 17a shows the acceleration waveforms of six roadwheels when passing a single A-type obstacle for a new rubber band and new rubber pad configuration (conf. I). Sections of the graph enclosed by a dashed red line shows acceleration waveforms of peak areas for the new rubber band and used rubber pad configuration (conf. II). In case of conf. I, high acceleration values are observed when the first, second and sixth roadwheels are running into an obstacle. Deceleration values occurring are similar levels except for the first roadwheel (lowest deceleration value of 241 m/s^2) and sixth roadwheel (highest deceleration value of 255 m/s^2). In case of conf. II, waveform patterns are similar. The highest acceleration values are observed for the first, second and sixth roadwheels, higher by an average of around 7.2%. In the case of deceleration values, extreme values were observed for the first and sixth roadwheels. The lowest deceleration value was observed for the first roadwheel (212 m/s^2), while the highest deceleration value was observed for the sixth roadwheel (239 m/s^2). This is equivalent to a change of 12% and 6.3%. Tab. 1 summarises the detailed acceleration, and deceleration values and their percentages for the compared configurations, respectively.

The main part of Fig. 17b shows waveforms of forces transmitted by six roadwheels when passing a single A-type obstacle for a new rubber band and new rubber pad configuration (conf. I). Sections of the graph enclosed by a dashed red line shows force waveform peak areas for a new rubber band and used rubber pad configuration (conf. II). In case of conf. I, the highest force values are observed when the first, second and sixth roadwheels are running into an obstacle. The maximum force value is ≈108 kN. For the same wheels, a reduction in the transmitted force to zero is observed. This is equivalent to the condition in which the roadwheels become detached from the road surface. In case of conf. II, waveform patterns are similar. The highest values of force transmission are observed for the first, second and sixth roadwheels, higher by an average of around 3.3%. For the first, second and sixth roadwheels, detachment from surface was also observed. Tab. 2 summarises the detailed extreme force values and their percentages for the compared configurations.

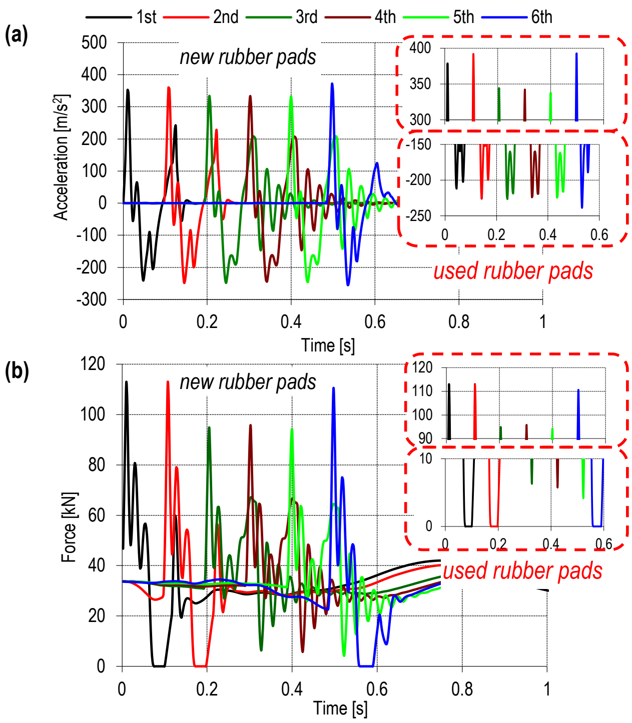

Fig. 17. Vertical acceleration waveforms of roadwheels passing a single A-type obstacle for conf. I (a) and conf. II in section of graph enclosed by a dashed red line. Force exerted on roadwheels for conf. I (b) and conf. II in section of graph enclosed by dashed red line

Tab. 1. Roadwheel vertical acceleration peak values and relative differences for tested configurations: a new rubber pad[1] and worn-out rubber pad[2]

Roadwheel number	Acceleration [m/s^2]				|Difference| [%]	
	max[1]	max[2]	min[1]	min[2]		
1st	352	378	–241	–212	7.4	12.0
2nd	360	391	–248	–226	8.6	8.9
3rd	334	344	–248	–226	3.0	8.9
4th	334	341	–245	–224	2.1	8.6
5th	332	336	–246	–224	1.2	8.9
6th	372	393	–255	–239	5.6	6.3

[1]conf. I: new rubber band, new rubber pad.
[2]conf. II: new rubber band, used rubber pad

Tab. 3 summarises the data covering the maximum and minimum values of rubber deflection (for the equivalent stiffness characteristics, the determination is shown in the fourth section). Tab. 3 confirms the detachment of the first, second and sixth roadwheels in both scenarios. The highest deflection values are observed for these roadwheels. In the case of the third and fourth roadwheels, both minimum and maximum deflection values are

DOI 10.2478/ama-2023-0010

similar. In the case of the fifth roadwheel, smaller deflection peak values were observed (0.5 mm). The two tested configurations showed an impact of rubber pad wear on the working range (deflection). In the case of the second, third and fourth roadwheels, a minimum deflection value increase for conf. II about 42.1% was observed. A maximum deflection change of values is an order of magnitude lower and decreased by about 1%. A greater change was observed for the first, second and sixth roadwheels, a decrease by an average of 5%.

The condition of the rubber elements has an impact on loads acting on roadwheels and suspensions but did not significantly affect the loads acting on the vehicle hull and the driver.

Tab. 2. Peak values and relative differences of force exerted on roadwheel for tested configurations: a new rubber pad[1] and worn-out rubber pad[2]

Roadwheel number	1st	2nd	3rd	4th	5th	6th
F_{max}^1 [kN]	108	108	93	94.2	93.2	107
F_{max}^2 [kN]	113	113	94.9	95.7	94.1	111
|Difference| [%]	4.63	4.63	2.04	1.59	0.97	3.74
F_{max}^1 [kN]	0*	0*	5.63	5.00	3.48	0*
F_{max}^2 [kN]	0*	0*	6.29	5.74	4.20	0*
|Difference| [%]	N.A.	N.A.	11.7	14.8	20.7	N.A.

[1]conf. I: new rubber band, new rubber pad.
[2]conf. II: new rubber band, used rubber pad
*Detachment of the roadwheel from the ground.
N.A. – not applicable.

Tab. 3. Rubber deflection peak values and relative differences for tested configurations: a new rubber pad[1] and worn-out rubber pad[2]

Roadwheel number	Deflection [mm]				|Difference| [%]	
	max[1]	max[2]	min[1]	min[2]	min	max
1st	0*	0*	–11.4	–11.0	N.A.	3.86
2nd	0*	0*	–11.4	–11.0	N.A.	4.18
3rd	–2.1	–2.9	–10.5	–10.4	38.1	0.91
4th	–2.0	–2.7	–10.6	–10.5	35.0	1.23
5th	–1.5	–2.3	–10.6	–10.4	53.3	1.39
6th	0*	0*	–11.2	–11.0	N.A.	2.52

[1]conf. I: new rubber band, new rubber pad.
[2]conf. II: new rubber band, used rubber pad
*Undeformed rubber (detachment of roadwheel from the ground).
N.A. – not applicable.

The main part of Fig. 18a shows acceleration waveforms of six roadwheels when passing a single B-type obstacle for a new rubber band and new rubber pad configuration (conf. I). Sections of the graph enclosed by a dashed red line shows acceleration waveform peak areas for a new rubber band and used rubber pad configuration (conf. II). In case of conf. I, significantly higher acceleration values are observed for the third, fourth and sixth roadwheels overcoming an obstacle.

Deceleration values are similar, except for the first (lowest deceleration value of 476 m/s^2) and second roadwheels (highest deceleration value of 461 m/s^2). In case of conf. II, waveform patterns are similar. The highest acceleration values are observed for the third, fourth and fifth roadwheels, higher by an average of around 1.9%. In the case of deceleration values, extreme values were observed for the first and second roadwheels. The lowest deceleration value was observed for the fifth roadwheel (416 m/s^2), while the highest deceleration value was observed for the first roadwheel (472 m/s^2). This is equivalent to a change of 1.96% and 0.84%. Tab. 4 summarises the detailed acceleration and deceleration values and their percentages for the compared configurations. The main part of Fig. 18b shows waveforms of forces transmitted by six roadwheels when passing a single B-type obstacle for a new rubber band and new rubber pad configuration (conf. I). Sections of the graph enclosed by a dashed red line show force waveform peak areas for a new rubber band and used rubber pad configuration (conf. II). In case of conf. I, significantly higher force values are observed when the third, fourth and fifth roadwheels are overcoming an obstacle. The maximum force value is ≈200 kN. For all wheels, a reduction in the transmitted force to zero is observed. This is equivalent to the condition in which the roadwheels become detached from the road surface.

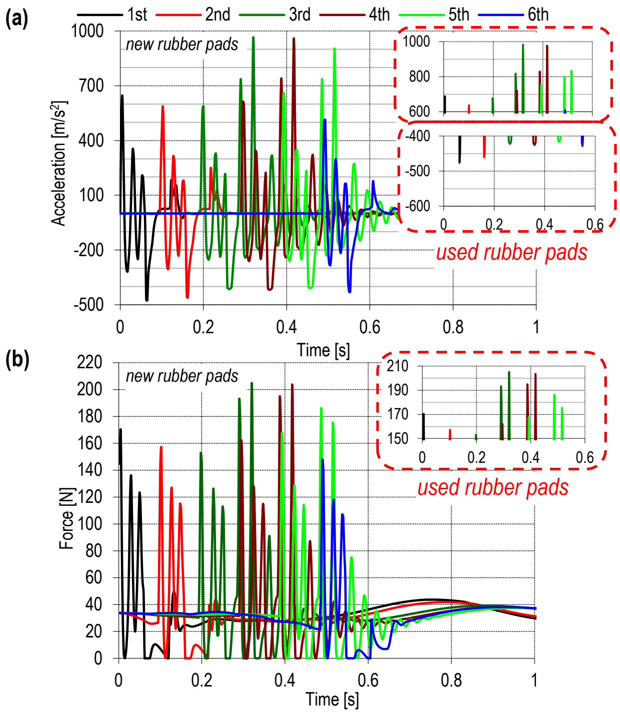

Fig. 18. Vertical acceleration waveforms of roadwheels passing a single B-type obstacle for conf. I (a) and conf. II in the section of graph enclosed by a dashed red line. Force exerted on roadwheels for conf. I (b) and conf. II in the section of graph enclosed by a dashed red line

In case of conf. II, waveform patterns are similar. The highest values of force transmission are observed for the third, fourth and sixth roadwheels, higher by an average of around 1.6%. The highest percentage increase was observed for the sixth roadwheel. The value of the force increased by 10.7%. For all roadwheels, detachment from surface was also observed. Tab. 5 summarises the detailed extreme force values and their percentages for the compared configurations.

Tab. 6 summarises data covering the maximum and minimum values of rubber deflection (for the equivalent stiffness characteristics, the determination is shown in the fourth section). Tabs. 5

and 6 confirms the detachment of all roadwheels in both scenarios. The highest deflection values are observed for the third and fourth roadwheels. In the case of the first, second and fifth roadwheels, the maximum deflection was smaller. The smallest deflection, lower by about 2 mm, was observed for the sixth roadwheel. In both configurations, detachment of roadwheels occurred. The impact of rubber pad wear on the working range (deflection) was observed for all roadwheels. Maximum deflection values decreased overall by 5.1%. The highest percentage decrease was observed for the third and fourth roadwheels.

The condition of the rubber elements has an impact on loads acting on roadwheels and its suspensions but did not significantly affect the loads acting on the vehicle hull and the driver.

Tab. 4. Roadwheel vertical acceleration peak values and relative differences for tested configurations: a new rubber pad[1] and worn-out rubber pad[2]

Roadwheel number	Acceleration [m/s²]				|Difference| [%]	
	max[1]	max[2]	min[1]	min[2]	min	max
1st	646	683	–476	–472	5.73	0.84
2nd	586	629	–461	–458	7.34	0.65
3rd	966	980	–414	–422	1.45	1.93
4th	958	977	–418	–425	1.98	1.67
5th	904	827	–408	–416	8.52	1.96
6th	513	605	–430	–428	17.9	0.47

[1]conf. I: new rubber band, new rubber pad.
[2]conf. II: new rubber band, used rubber pad

Tab. 5. Peak values and relative differences of force exerted on roadwheel for tested configurations: a new rubber pad[1] and worn-out rubber pad[2]

Roadwheel number	1st	2nd	3rd	4th	5th	6th
F_{max}[1] [kN]	161	148	202	200	188	133
F_{max}[2] [kN]	168	156	204	204	185	147
|Difference| [%]	4.43	5.48	1.47	1.87	1.34	10.7
F_{max}[1] [kN]	0*	0*	0*	0*	0*	0*
F_{max}[2] [kN]	0*	0*	0*	0*	0*	0*
|Difference| [%]	N.A.	N.A.	N.A.	N.A.	N.A.	N.A.

[1]conf. I: new rubber band, new rubber pad.
[2]conf. II: new rubber band, used rubber pad
*Detachment of the roadwheel from the ground.
N.A. – not applicable.

Tab. 6. Rubber deflection peak values and relative differences for tested configurations: a new rubber pad[1] and worn-out rubber pad[2]

Roadwheel number	Deflection [mm]				|Difference| [%]	
	min[1]	min[2]	max[1]	max[2]	min	max
1st	0*	0*	–13.4	–12.8	N.A.	4.48
2nd	0*	0*	–12.9	–12.5	N.A.	3.10
3rd	0*	0*	–14.4	–13.4	N.A.	6.94
4th	0*	0*	–14.4	–13.4	N.A.	6.94
5th	0*	0*	–13.9	–13.3	N.A.	4.32
6th	0*	0*	–12.5	–11.9	N.A.	4.80

[1]conf. I: new rubber band, new rubber pad.
[2]conf. II: new rubber band, used rubber pad
*Undeformed rubber (detachment of roadwheel from the ground).
N.A. – not applicable.

6. SUMMARY AND FINAL FINDINGS

The elasticity characteristics obtained indicate a change in the properties of rubber as a construction material. The degree of change depends on the running conditions, terrain and meteorological conditions, as well as its intensity and exposure time.

This article demonstrates that during the operation of high-speed tracked vehicles, there is intensive wear of the rubber material used in the crawler track mechanism assemblies. The shape, geometry, properties and elastic and damping characteristics change. Deterioration of the elastic damping properties of rubber elements in the suspension components does not necessarily eliminate the vehicle from further use. However, it may be one of the causes of accelerated wear of other elements or assemblies. Monitoring changes in parameters describing the properties of elements of the crawler track mechanism make it possible to build models with high accuracy corresponding to the test objects (HSTV) and to determine loads close to the real ones. As a result, it makes it possible to carry out model tests on new objects, as well as after a run undergoing modification or modernisation.

Intense wear and tear of rubber elements used in crawler track mechanisms leading to the deterioration of their elastic–damping properties indicate the relevance of further investigation of this phenomenon. This particularly concerns the durability and reliability of cover plates of crawler tracks, and load-bearing wheel counter-measurements may be suggested:

1. Selection of the shape and dimensions of the rubber elements to reduce the running resistance in rectilinear and curvilinear motions and the loads resulting from these forces.
2. Modification of the composition of the mixture from which the rubber elements of the crawler mechanism are made. This could be a direction related to the use of rubber mixtures with a graphene admixture [31].

The aforementioned measures should positively influence the technical characteristics of high-speed tracked vehicles by, for example, increasing the traction properties, reliability and durability of the internal equipment assemblies. Efforts in this direction should also have the effect of reducing vehicle maintenance and operating costs.

REFERENCES

1. Djurić R, Milis Avljević V. Investigation of the relationship between reliability of track mechanism and mineral dust content in rocks of lignite open pits. Maintenance and Reliability. 2016; 18 (1): 142-150.
2. Grygier D. The impact of operation of elastomeric track chains on the selected properties of the steel cord wires. Maintenance and Reliability. 2017; 19 (1): 95-101.
3. Dudziński P, Kosiara A, Konieczny A. Wirtualne prototypowanie nowej generacji układu jezdnego na gąsienicach elastomerowych do zastosowań arktycznych. Postępy Nauki i Techniki. 2012; 14: 64-74.
4. Czabanowski R. Numeryczna analiza obciążeń wybranych elementów podwozia z gąsienicami elastomerowymi. Przegląd Mechaniczny. 2010; nr 7-8: 30-36.
5. Dziubak T. The effects of dust extraction on multi-cyclone and non-woven fabric panel filter performance in the air filters used in special vehicles. Maintenance and Reliability. 2016; 18 (3): 348-357.
6. Gniłka J, Mężyk A. Experimental identification and selection of dynamic properties of a high-speed tracked vehicle suspension system. Maintenance and Reliability. 2017; vol. 19 (1): 108-113.
7. Bogucki R. Badania prototypów nakładek elastomerowych na człony taśm gąsienicowych. Szybkobieżne Pojazdy Gąsienicowe. 2013; 1 (32): 37-46.

8. Rybak P. Tracked or Wheeled Chassis. Journal of Kones Powertrain and Transport. 2007; 14 (3):527-536.
9. Rybak P. Operating loads of impulse nature acting on the special equipment of the combat vehicles. Maintenance and Reliability. 2014; 16 (3): 347-353.
10. Campanelli M, Shabana AA, Choi JH. Chain vibration and dynamic stress in three-dimensional multibody tracked vehicles. Multibody System Dynamics. 1998; 2**:** 277–316.
11. Lee K. A numerical method for dynamic analysis of tracked vehicles of high mobility. KSME International Journal. 2000; 14 (10): 1028-1040.
12. Ma ZD, Perkins NC. A super-element of track-wheel-terrain interaction for dynamic simulation of tracked vehicles. Multibody System Dynamics. 2006; 15: 351–372.
13. Wallin M, Aboubakr AK, Jayakumar P,·Letherwood MD,·Gorsich DJ,·Hamed A,·Shaban A. A comparative study of joint formulations: application to multibody system tracked vehicles. Nonlinear Dynamics. 2013; 74 (3): 783–800.
14. Wang P, Rui X, Yu H. Study on dynamic track tension control for high-speed tracked vehicles. Mechanical Systems and Signal Processing. 2019; 132: 277-292. Available from: doi.org/10.1016/j.ymssp.2019.06.031
15. Wang Z, Lv H, Zhou X, Chen Z, Yang Y. Design and Modeling of a Test Bench for Dual-Motor Electric Drive Tracked Vehicles Based on a Dynamic Load Emulation Method. Sensor. 2018; 18: 1-20.
16. Dudziński P, Chołodowski J. A method for predicting the internal motion resistance of rubber-tracked undercarriages, Pt. 1. A review of the state-of-the-art methods for modeling the internal resistance of tracked vehicles. Journal of Terramechanics. 2021; 96: 81-100. Available from: doi.org/10.1016/j.jterra.2021.02.006
17. Chołodowski J, Dudziński P, Ketting M. A method for predicting the internal motion resistance of rubber-tracked undercarriages, Pt. 3. A research on bending resistance of rubber tracks. Journal of Terramechanics. 2021; 97: 71-103. Available from: https://doi.org/10.1016/j.jterra.2021.02.005
18. Liu W, Cheng K, Wang J. Failure analysis of the rubber track of a tracked transporter. Advances in Mechanical Engineering. 2018; 10 (7): 1–8.
19. Gat G, Franco Y, Shmulevich I. Fast dynamic modeling for off-road track vehicles. Journal of Terramechanics. 2020; 92: 1-12. Available from: doi: 10.1016/j.jterra.2020.09.001.
20. Burdziński Z. Teoria ruchu pojazdu gąsienicowego. Warszawa: WKŁ; 1972.
21. Mahalingam I, Padmanabhan C. A novel alternate multibody model for the longitudinal and ride dynamics of a tracked vehicle. Vehicle System Dynamics. 2021; 59(3): 433-457.
22. Edwin P, Shankar K, Kannan K. Soft soil track interaction modeling in single rigid body tracked vehicle models. J Terramechanics. 2018; 77:1-14.
23. Sandu C, Freeman JS. Military tracked vehicle model. Part I: Multibody dynamics formulation.Int J Veh Syst Model Test. 2005; 1(1-3):48–67.
24. Janarthanan B, Padmanabhan C, Sujatha C. Longitudinal dynamics of a tracked vehicle:simulation and experiment. J Terramechanics. 2012;49(2):63-72.
25. Nabagło T, Jurkiewicz A, Kowal J. Modeling verification of an advanced torsional spring for tracked vehicle suspension in 2S1 vehicle model. Engineering Structures. 2021; 229: 111623.
26. Ata WG, Oyadiji SO. An investigation into the effect of suspension configurations on the performance of tracked vehicles traversing bump terrains. Vehicle System Dynamics. 2014; 52(7): 1-25.
27. Sandu C, Freeman JS. Military tracked vehicle model. Part II: Case study. Int J Veh Syst Model Test. 2005;1(1-3):216-231.
28. Budynas R, Nisbett K. Shigley's Mechanical Engineering Design. McGraw Hill Education; 2019.
29. Borkowski W, Rybak P, Hryciów Z. Modele częściowe w analizie obciążeń struktur nośnych wozów bojowych. Biuletyn Wojskowej Akademii Technicznej. 2006; 55(4):221-232.
30. Hryciów Z; Małachowski J; Rybak P, Wiśniewski A. Research of Vibrations of an armoured Personnel Carrier Hull with FE Implementation. Materials. 2021; 14,6807:1-18. Available from: doi.org/10.3390/ma14226807.
31. Hebda M, Łopata A. Grafen – materiał przyszłości. Czasopismo Techniczne. Mechanika. 2012; R. 109, Z. 22, 8-M: 45-53.

Piotr Rybak: https://orcid.org/0000-0002-7063-9913

Zdzisław Hryciów: https://orcid.org/0000-0002-6281-1883

Bogusław Michałowski: https://orcid.org/0000-0002-5793-2744

Andrzej Wiśniewski: https://orcid.org/0000-0002-2089-1942

sciendo

DOI 10.2478/ama-2023-0011 acta mechanica et automatica, vol.17 no.1 (2023)

EXPERIMENTAL ANALYSIS OF TRANSVERSE STIFFNESS DISTRIBUTION OF HELICAL COMPRESSION SPRINGS

Robert BARAN*, Krzysztof MICHALCZYK*, Mariusz WARZECHA*

*Faculty of Mechanical Engineering and Robotics, Department of Machine Design and Maintenance,
AGH University of Science and Technology, al. Mickiewicza 30, 30-059 Kraków, Poland

rbaran@agh.edu.pl, kmichal@agh.edu.pl, mwarzech@agh.edu.pl

received 27 September 2022, revised 13 December 2022, accepted 13 December 2022

Abstract: This paper presents the results of an experimental analysis of the distribution of transverse stiffness of cylindrical compression helical springs with selected values of geometric parameters. The influence of the number of active coils and the design of the end coils on the transverse stiffness distribution was investigated. Experimental tests were carried out for 18 sets of spring samples that differed in the number of active coils, end-coil design and spring index, and three measurements were taken per sample, at two values of static axial deflection. The transverse stiffnesses in the radial directions were tested at every 30° angle. A total of 1,296 measurements were taken, from which the transverse stiffness distributions were determined. It was shown that depending on the direction of deflection, the differences between the highest and lowest value of transverse stiffness of a given spring can exceed 25%. The experimental results were compared with the results of the formulas for transverse stiffness available in the literature. It was shown that in the case of springs with a small number of active coils, discrepancies between the average transverse stiffness of a given spring and the transverse stiffness calculated based on literature relations can reach several tens of percent. Analysis of the results of the tests carried out allowed conclusions to be drawn, making it possible to estimate the suitability of a given computational model for determining the transverse stiffness of a spring with given geometrical parameters.

Key words: helical spring, coil spring, transverse stiffness, end coils, stiffness distribution

1. INTRODUCTION

Cylindrical compression helical springs are widely used in mechanical systems as energy-storing components. Among the broad range of their applications, those requiring knowledge of the transverse stiffness of the spring pose immense challenges. Examples of such applications are vibratory conveyors [1], railroad bogies [2, 3], or vibration absorbers [4]. To support mechanical engineers in the design of such systems, many studies have been published in recent decades; mainly focusing on analytical models enabling the calculation of spring characteristics.

The published analytical models are generally based on simplifications and are therefore prone to errors. Yıldırım [5] reported differences between the results of the experiments and those obtained by elementary relationships for the static characteristics of cylindrical compression helical springs. Furthermore, Paredes [6] pointed out that the spring rate relationships available in the literature are characterised by sufficient accuracy only for springs with a coil number of not <5. The quoted work presented the results of experimental research on the axial compression of springs with two different ends (closed and ground ends and closed and not ground ends). Based on these results, a modification of the formulas for the number of active coils was proposed. Liu and Kim [7] analysed the effect of end coils on the natural frequencies of longitudinal vibration. They proposed a modification of the conventional analytical model in which the fixed boundary points at the ends of active coils were replaced by torsional stiffness elements, representing the end coils. The inclusion of end coils in the calculations produced outcomes closer to the experimental results than the conventional model. The problem of transverse vibrations of cylindrical compression helical springs, which is of significant practical importance, was approached in many studies. Haringx [8] proposed a fundamental model of spring treated as an equivalent column, with the reference to the issue of its elastic stability and natural vibration frequencies. He assumed that spring has flat wound end coils with no contact with active coils. The model of the equivalent column was used by Wittrick [9] for the problem of spring vibration, including coupling between the longitudinal and torsional forms of vibration. The aforementioned coupling phenomenon was also considered in the work [10], in which the authors studied the wave phenomena occurring in a spring with a constant lead angle. The purpose of the work [11] was the unified dynamic analysis and dynamic criteria of stability for helical springs with the application of an equivalent beam model. Mottershead [12] proposed a new finite element modelling the coil or a part of a coil of a helical spring, whilst Taktak et al. [13] proposed a new finite element modelling the total behaviour of a helical spring. In all the cited works, the issue of the influence of end coils on transverse stiffness was neglected or subjected to only a partial analysis, as in paper [8]. The problem of the influence of passive coils on the frequency of transverse natural vibrations has been emphasised by Michalczyk [14] where, using numerical methods, significant discrepancies were shown between results obtained for springs differing in the end-coils shape. The same phenomenon was demonstrated experimentally by Michalczyk and Bera [15]. This influence is mainly related to the elastic susceptibility of passive coils.

DOI 10.2478/ama-2023-0011

To ensure the stable operation of cylindrical compression helical springs, their ends should be closed and ground – this is form D according to ISO 2162-2:1993. For durability reasons, the EN13298:2003 standard specifies that the extremity of each end coil should have, after the grinding, a thickness between 3 mm and one-quarter of the wire cross-section. In extreme cases, the contact line between the end coil and the adjacent active coil can take the form of a point. In this case, the concentration of contact stresses and wire abrasion have a negative effect on the fatigue strength of the spring [16]. Increasing the contact length between the end and active coils has a positive effect on contact stresses but at the same time increases the mounting space of the spring.

Effects related to the length of the contact line between the end coils and adjacent active coils are neglected in the models currently used to calculate the transverse stiffness of cylindrical compression helical springs. The transverse stiffness values determined on their basis have a uniform distribution in all directions perpendicular to the spring axis. The problem of nonuniformity of stiffness distribution in the direction perpendicular to the spring axis is important in suspension systems of vibrating machines and rail vehicles. The springs are placed in holders in the appropriate position to eliminate the differences in transverse stiffness and eccentricity in the transmission of axial force. Any positioning of the springs in relation to each other could cause an uneven distribution of vibrations, manifesting itself in driving discomfort, or even damage to the suspension by spring failure, usually in the area of the end coil [17]. In addition, in the case of sets of coaxially aligned springs, there is a risk of collision between the inner and outer springs. This phenomenon is especially dangerous for those springs, especially the inner one, which is the most loaded [18].

Despite the extensive literature on the static and dynamic properties of helical springs, the impact of the shape of the end coil on these properties has not been fully explained. The significance of this impact increases with the decreasing number of active coils.

This paper aims to investigate the effect of contact line length between end coils and adjacent active coils and the number of active coils on the transverse stiffness distribution of springs, and to investigate the relationship between experimental results and those of known computational models from the literature. This will improve the cylindrical compression helical spring design process for applications where transverse stiffness is an important aspect. The experimental results presented in this paper, together with a description of the geometry of the springs tested, can also provide a benchmark for validating numerical models of springs.

2. METHODOLOGY

2.1. Sample selection – geometrical and material properties

To carry out the tests, springs with parameters determined by a strict mathematical model were designed. Each spring has end coils on both sides with the same pitch as the wire diameter, and active coils in the middle part with a determined working pitch. The spring wire axis is rounded with a fixed radius at the pitch change point. Each of these spring sections was described by mathematical equations and then a path was generated using the Python programming language to represent the spring wire axis. To examine the influence of the contact line length on the stiffness distributions, three forms of end coils were designed as shown in Fig. 1.

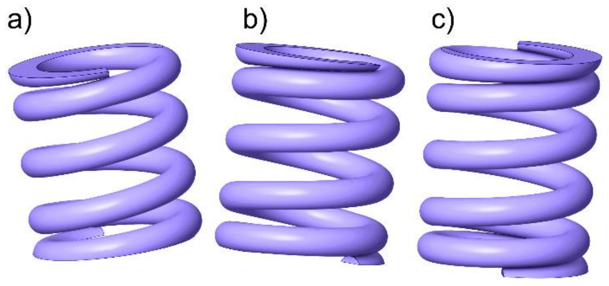

Fig. 1. Closed and ground end coil with (a) point contact with active coils, (b) with contact at 0.25 of coil length and (c) with contact at 0.5 of coil length

Fig. 1a shows a spring with point contact between passive and active coils. The number of passive coils of this spring is 2. Fig. 1b presents a model of a spring for which the contact line length between coils on each side equals 0.25 of a coil and the number of passive coils equals 2.5. Fig. 1c presents a spring with contact line length of 0.5 of a coil on each side and the number of passive coils equals 3. For the sake of simplicity, in the following part of the paper, the forms of end coils shown in Fig. 1a will be denoted as e1, the forms shown in Fig. 1b will be denoted as e2, and the forms shown in Fig. 1c will be denoted as e3. The pitch of the spring in the active area in the unloaded condition was 10 mm for all springs. As mentioned above, a lower number of active coils increases the influence of end coils on the static characteristics of cylindrical compression helical springs. Considering this fact and taking into account the design space of various applications, three different numbers na of active coils were selected for analysis: 2.5, 2.75 and 3. Moreover, two different spring indexes C were considered: 5 and 7.

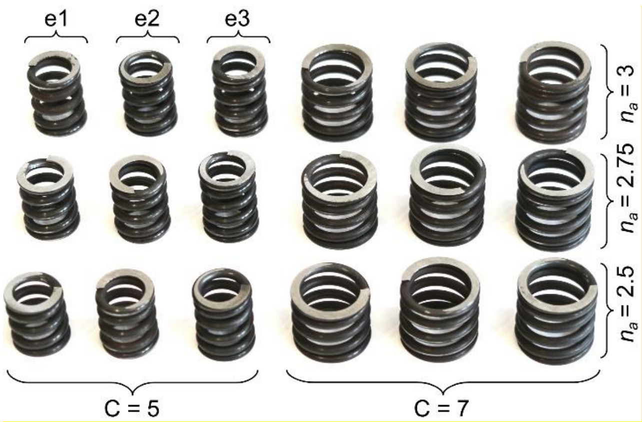

Fig. 1. Single samples intended for laboratory research

Tab. 1. Parameters of spring samples selected for experimental testing

Active coils	n_a = 2.5						n_a = 2.75						n_a = 3					
End-coil shape	e1		e2		e3		e1		e2		e3		e1		e2		e3	
Spring index C	5	7	5	7	5	7	5	7	5	7	5	7	5	7	5	7	5	7

DOI 10.2478/ama-2023-0011 acta mechanica et automatica, vol.17 no.1 (2023)

The springs used in the experiments were manufactured by a supplier under the EN 13906-1:2013 standard. All springs were coiled from wire with a diameter dw = 5 mm made of 55CrSi FD Becrosi 26 spring steel, which complies with the EN-10270-2 standard. The modulus of elasticity in tension E and the modulus of elasticity in shear G for this material were 206 GPa and 79.5 GPa, respectively. After winding, the springs were tempered at 220°C for 15 minutes, then the end coils were ground to ¾ of the circumference and subjected again to the same heat treatment. All 18 combinations of the spring parameters listed above are shown in Tab. 1. Fig. 2 shows a set of 18 spring samples to be tested with the parameters listed in Tab. 1.

2.2. Test setting

The tests were carried out using an HT-2402 testing machine from Hung Ta Instrument Co., Ltd., Taiwan, equipped with a CL16md 5kN load cell from ZEPWN, Poland, of the precision class 0.5 according to ISO 376 (Fig. 3a).

To measure the transverse stiffness of a spring, the spring must be preloaded before applying a force perpendicular to its axis. To enable such measurements, an adapter device was designed and built (Fig. 3b). The adapter was made based on 45 mm x 45 mm strut profiles with high axial and flexural stiffness. Its design minimises the loads transferred from the tested springs to its components, so the elastic deformation of the adapter is negligibly small compared to that of the tested springs.

To achieve axial preload of spring 1, the distance between brackets 2 and 3 was adjusted by moving bracket 2 with the help of a screw fitted with knob 6. Once the correct axial spring compression was achieved, measured using a digital caliper, bracket 2 was fixed. The force transverse to the axis of the spring was applied by pressing the head of the testing machine against rail 4 in the direction indicated by the red arrow in Fig. 3b. Rail 4 was assembled to the HIWIN HGW15CC linear guideway 5.

a)

b)

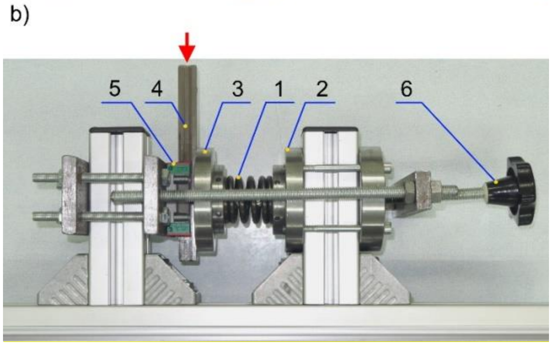

Fig. 3. The test stand (a) and adapter (b) for measuring transverse stiffness

A similar design solution for a fatigue test bench for railway springs is presented in paper [19], while paper [20] describes a bench that only allows the axial stiffness testing of the springs.

The pretension force applied to the spring causes motion resistance in the linear guideway of the adapter. This resistance results in forces which can influence measurements of the spring transverse stiffness. To assess whether those forces are significant or can simply be omitted, additional tests were performed. For those tests, the adapter device was modified. The main modification was the inclusion of a second, identical linear bearing. Therefore, during the tests, the motion resistance of both linear bearings was measured simultaneously. The tests were carried out at spring pretension nominal values of 125 N, 250 N, 500 N, 750 N and 1,000 N, which approximately covers the entire range of loads acting on the linear bearing during the tests of their transverse stiffness. Fig. 4a shows the registered resistance force values for an exemplary test with a pretension force equal to 1,000 N. The tests consisted of forcing both guides to move by a value of 10 mm with a rate of 6 mm/min and recording the resistance force. Each test was repeated five times for a given load value. The obtained results allowed the calculation of the average linear bearing resistance force as shown in Fig. 4b. The largest average drag force of two linear bearings did not exceed 9 N. Due to the small values of the resistance forces of a single linear bearing, these forces were omitted from the calculations.

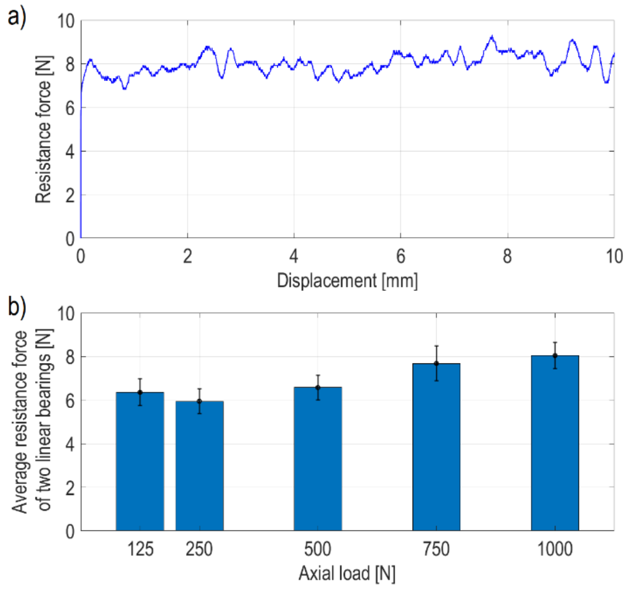

Fig. 4. Example record: (a) variation of the resistance force as a function of bearing displacement, with an axial load of 1,000 N; (b) average resistance forces of two linear bearings for five different axial loads

2.3. Transverse stiffness tests

Transverse stiffness measurements were carried out on axially compressed springs. The value of axial compression corresponded to 25% (denoted as c25) and 50% (denoted as c50) of the total clearance between the active coils. This way of achieving the axial load made it possible to apply a proportional load to each spring and therefore enabled a comparison of the results obtained. The transverse deflection was selected so that the maximum tangential stress did not exceed the value of 50% of ultimate

DOI 10.2478/ama-2023-0011

stress in the worst case. The second condition for the selection of the transverse deflection is the condition of stability, necessary for the spring ends resting on their supports. This condition is formulated in the EN 13906-1:2013 (E) standard:

$$F_Q \cdot \frac{L}{2} \leq F_0 \cdot \frac{D-s_Q}{2} \quad (1)$$

where: F_0 is the axial force, F_Q is the lateral force, L is the total spring length, D represents the nominal spring diameter and s_Q is the transverse deflection. As a result of trial calculations, it was assumed that the maximum transverse displacement of the moving end of the spring during the experiment would be 0.0933 of the axial deflection. The axial deflection values and the corresponding transverse deflection values are presented in Tab. 2.

Tab. 1. The values of transverse deflections for each number of active coils and the value of axial deflections

Active coils	n_a = 2.5	n_a = 2.75	n_a = 3
Axial deflection [mm] (c25)	3.13	3.44	3.75
Transverse deflection [mm] (c25)	2.04	2.25	2.45
Axial deflection [mm] (c50)	6.25	6.88	7.50
Transverse deflection [mm] (c50)	1.75	1.92	2.10

For each spring, at the given preload, 12 measurements were made by changing the direction of the transverse load. To achieve this, the tested spring was rotated with respect to the test stand with angular increments of 30°. Each measurement at a fixed angle value was repeated three times, and then the average value from these measurements was calculated. The arrangement of load directions and spring geometry is presented in Fig. 5.

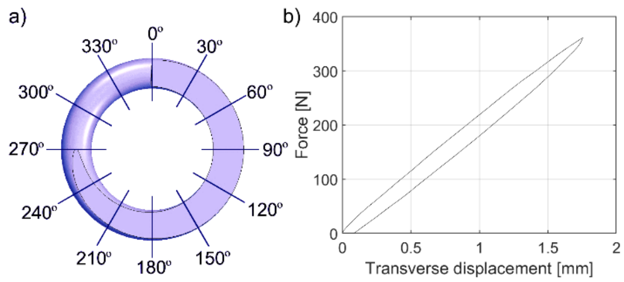

Fig. 2. An angular coordinate system (a) defining transverse load directions in subsequent tests of transverse stiffness for a single spring (view from the sliding support side) and (b) sample test record for measuring the transverse stiffness of a spring

The transverse stiffness was determined as the quotient of the maximum transverse force to the corresponding maximum deflection. Although inequality Eq. (1) was satisfied for all the experimental conditions shown in Tab. 2, some springs in the tests at c25 axial deflection lost stability at certain angular positions before reaching the maximum assumed value of lateral deflection. In these cases, the stiffness was determined from the stable part of the characteristic. The total number of transverse stiffness measurements taken was 1,296.

3. RESULTS AND DISCUSSION

3.1. Results of the Experiments

The transverse stiffness distributions as a function of the direction of the transverse force (see Fig. 5a) obtained based on the experiments under axial deflection c50 are shown in Figs. 6–8. The transverse stiffness at individual points in those figures is average values with standard deviation for three measurements of each spring. The results are repeatable because the coefficient of variation for each measurement point did not exceed 2%. This shows sufficient accuracy in measuring transverse stiffness with the use of the designed stand, which means the possibility of concluding based on these tests. Fig. 6 shows the transverse stiffness distribution for springs with n_a = 2.5, Fig. 7 shows the transverse stiffness distribution for springs with n_a = 2.75 and Fig. 8 shows the analogical plots for springs with n_a = 3.

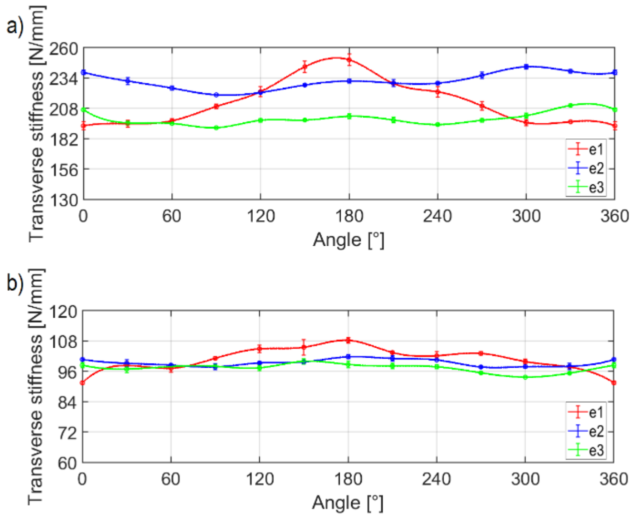

Fig. 6. Transverse stiffness distribution for springs with na = 2.5, and spring index (a) C = 5 and (b) C = 7

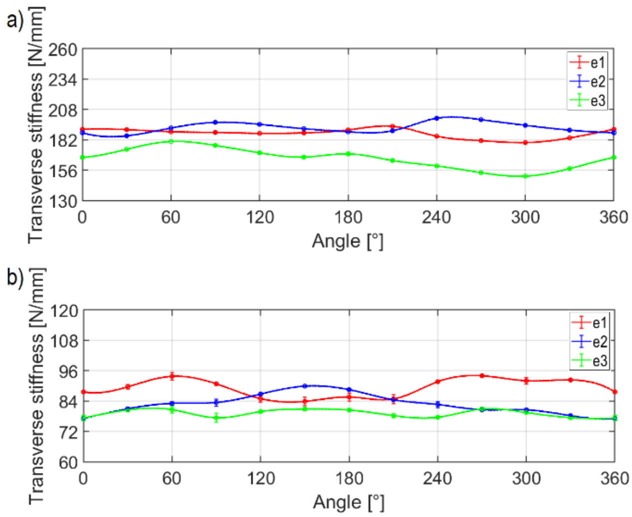

Fig. 7. Transverse stiffness distribution for springs with na = 2.75, and spring index (a) C = 5 and (b) C = 7

DOI 10.2478/ama-2023-0011 acta mechanica et automatica, vol.17 no.1 (2023)

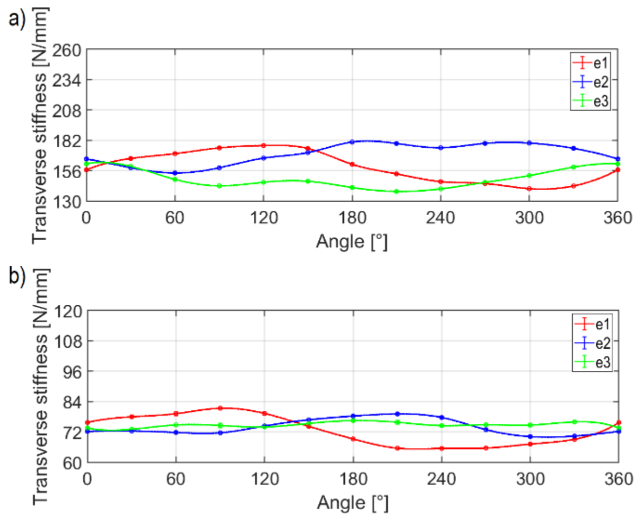

Fig. 8. Transverse stiffness distribution for springs with na = 3, and spring index (a) C = 5 and (b) C = 7

As is evident from Figs. 6–8, the transverse stiffness was significantly dependent on the direction of the applied force. This phenomenon is a consequence of changes in the geometry of the spring's end coils and their mutual positioning.

The measurement data presented in Figs. 6–8 revealed the influence of the design of the end coils of the spring on its transverse stiffness. It can be seen that increasing the number of passive coils from e1 to e3 is not necessarily accompanied by a reduction in spring transverse stiffness.

For a more precise comparison of the results obtained, their statistical parameters were calculated (Tabs. 3 and 4). They allow the variability of the stiffness distribution on the circumference of the spring to be assessed and to indicate the influence of the shape of the end coils, the partial number of active coils and the spring index on this distribution. The relative gap that occurs in the last column in Tabs. 3 and 4 is calculated as the gap between the maximum and minimum stiffness values in the entire 360° range divided by the mean stiffness value. The coefficient of variation shown in Tabs. 3 and 4 relates to the variation of the stiffness distribution as a function of load angle.

Tab. 3. Statistical analysis of transverse stiffness distribution for the c25 axial load

Spring index C	Number of active coils n_a	End-coil shape	Mean transverse stiffness [N/mm]	Coefficient of variation [%]	Maximum value N/mm] / (angle of occurrence)	Minimum value N/mm] / (angle of occurrence)	Relative gap [%]
5	2.5	e1	164	3.8	175/0°	153/300°	13.7
		e2	186	5.0	209/0°	170/270°	21.5
		e3	163	4.1	176/210°	153/120°	14.4
5	2.75	e1	154	7.4	171/60°	136/150°	22.7
		e2	160	3.5	170/150°	151/240°	11.9
		e3	137	3.5	148/150°	132/270°	11.7
5	3	e1	127	4.6	138/120°	118/30°	16.3
		e2	142	5.6	154/180°	130/60°	17.2
		e3	125	1.5	128/330°	121/300°	5.4
7	2.5	e1	84	3.2	87/90°	78/270°	11.3
		e2	85	4.9	91/60°	78/300°	14.8
		e3	80	6.6	92/210°	70/300°	26.7
7	2.75	e1	78	7.7	88/60°	71/150°	21.5
		e2	75	4.5	83/150°	72/30°	14.6
		e3	69	4.5	74/60°	64/180°	13.3
7	3	e1	71	2.1	73/30°	68/300°	6.8
		e2	66	3.2	68/300°	61/0°	12.0
		e3	67	2.4	69/180°	64/240°	7.6

Tab. 2. Statistical analysis of transverse stiffness distribution for the c50 axial load

Spring index C	Number of active coils n_a	End-coil shape	Mean transverse stiffness [N/mm]	Coefficient of variation [%]	Maximum value N/mm] / (angle of occurence)	Minimum value N/mm] / (angle of occurrence)	Relative gap [%]
5	2.5	e1	214	9.2	250/180°	193/0°	26.5
		e2	231	3.2	244/300°	220/90°	10.4
		e3	199	2.7	210/330°	191/90°	9.6
5	2.75	e1	187	2.2	194/210°	180/300°	7.4
		e2	193	2.4	200/240°	185/30°	7.8
		e3	166	5.5	181/60°	151/300°	17.8
5	3	e1	159	8.6	177/120°	141/300°	23.2
		e2	170	5.5	180/180°	154/60°	15.5
		e3	149	5.3	162/0°	138/210°	15.9
7	2.5	e1	101	4.5	108/180°	91/0°	16.6
		e2	99	1.4	102/180°	98/270°	4.0
		e3	97	1.8	100/150°	94/300°	6.4
7	2.75	e1	89	4.2	94/270°	84/150°	11.3
		e2	83	4.7	90/150°	77/0°	15.4
		e3	79	1.9	81/270°	77/0°	4.4
7	3	e1	72	8.4	81/90°	65/240°	21.9
		e2	74	4.3	79/210°	70/300°	12.1
		e3	75	1.3	76/180°	73/30°	4.6

By analysing the results in Tabs. 3 and 4, it can be seen that both at axial deflection c25 and c50, the differences between the maximum and minimum values of transverse stiffness for a single spring can exceed 25% of its average stiffness. Axial deflection significantly affects the stiffness distribution as it changes the partial number of active coils. This can be seen in the example of a spring with index C = 7, na = 2.5 and end-coil shape e3, for which the relative gap is 26.7% at axial deflection c25 and at axial deflection c50 the relative gap is only 6.4%. The calculation of the coefficient of variation showed that the variability of the transverse stiffness distribution on the circumference of the spring does not exceed 10% for the geometric and measurement parameters adopted.

In the case of springs with index C = 7, no significant effect of end-coil design on stiffness was observed, while in the case of springs with C = 5, the effect is distinct. The springs with index C

DOI 10.2478/ama-2023-0011

= 5 and the end-coil design e2 showed significantly higher stiffness than the springs with the end-coil shapes e1 and e3.

Analysing the angular coordinates of the occurrence of maximum and minimum stiffnesses, no clear trend can be observed regarding the influence of geometrical parameters. This is because each deflection closes a different number of active coils, which translates into a different stiffness for individual directions of the transverse load.

3.2. Analysis of results and comparison with results of analytical formulas

The measurement data presented in Section 3.1 showed a relatively large variation in the transverse stiffness with the change in the direction of the load force. By contrast, the analytical equations available in the literature assume a constant value of transverse stiffness RQ. To confront those values with the measurement data, the most renowned analytical formulas of Gross, Wahl, and Haringx (the latter used in the EN 13906-1:2013 standard) were selected. These formulas are presented below. Transverse stiffness according to Gross [21]:

$$R_Q = \frac{1}{\frac{1}{F_0}\cdot\left[\frac{2}{\frac{F_0}{\sqrt{\alpha\left(1-\frac{F_0}{\beta}\right)}}}\cdot\tan\left(\frac{h}{2}\cdot\sqrt{\frac{F_0}{\alpha\left(1-\frac{F_0}{\beta}\right)}}\right)-h\right]+\frac{h}{\beta}} \tag{2}$$

where: F0 is the axial force, h is the length of the loaded spring.

The quantities α and β are the bending and shearing stiffnesses, respectively:

$$\alpha = \frac{2\cdot h\cdot J\cdot E\cdot G}{\pi\cdot n_a\cdot\frac{D}{2}\cdot(2G+E)} \tag{3}$$

$$\beta = \frac{E\cdot h\cdot J}{\pi\cdot n_a\cdot\left(\frac{D}{2}\right)^3} \tag{4}$$

In Eqs (3) and (4), E represents Young's modulus, G is the shear modulus, J is the second moment of the cross-section area of the wire, and D is the nominal diameter of the spring.
Below, the Wahl [22] method is presented:

$$R_Q = \left(1-\frac{2\cdot F_0}{\beta\left(\sqrt{1+\frac{4\cdot\pi^2\cdot\alpha}{h^2\cdot\beta}}-1\right)}\right)\cdot\left(\frac{h^3}{12\cdot\alpha}+\frac{h}{\beta}\right)^{-1} \tag{5}$$

Calculation by Haringx [8]:

$$R_Q = \frac{F_0}{h\left(\left(1+\frac{F_0}{\beta}\right)\frac{\tan\left(\frac{1}{2}h\sqrt{\frac{F_0}{\alpha}\left(1+\frac{F_0}{\beta}\right)}\right)}{\frac{1}{2}h\sqrt{\frac{F_0}{\alpha}\left(1+\frac{F_0}{\beta}\right)}}-1\right)} \tag{6}$$

The computational model proposed by Haringx [8] was used in the transverse stiffness calculation method presented in the EN 13906-1:2013 standard. The calculation formulas in this standard can be presented in the following form:

$$R_Q = \frac{\gamma}{h}\cdot\eta \tag{7}$$

where:

$$\eta = \xi\left[\xi-1+\frac{\frac{1}{\lambda}}{\frac{1}{2}+\frac{G}{E}}\cdot\sqrt{\left(\frac{1}{2}+\frac{G}{E}\right)\left(\frac{G}{E}+\frac{1-\xi}{\xi}\right)}\cdot\tan\left(\lambda\cdot\xi\cdot\sqrt{\left(\frac{1}{2}+\frac{G}{E}\right)\left(\frac{G}{E}+\frac{1-\xi}{\xi}\right)}\right)\right]^{-1} \tag{8}$$

$$\gamma = \frac{G\cdot h\cdot J}{\pi\cdot n_a\cdot\left(\frac{D}{2}\right)^3} \tag{9}$$

where ξ represents the relative axial deflection of the spring, λ is the spring slenderness defined as a quotient of a spring free length to its mean diameter, and γ represents the compression stiffness of the spring.

Since the EN 13906-1:2013 standard uses the Haringx model, the results obtained using Eq. (7) are the same as the results obtained using Eq. (6). The results based on Eqs (8) and (9) were compared with the values measured during the tests. The experimental results were averaged and given statistical parameters. The results obtained for the axial load c25 are presented in Tab. 5 and for the axial load c50 in Tab. 6. For each stiffness value calculated based on a given method, the relative change between the experimental result and the result of this method is given in parentheses.

As shown in Tabs. 5 and 6, analytical methods generally underestimate stiffness values, especially for springs with index C = 5. The comparison presented demonstrated that analytical relations give only approximate values of the spring transverse stiffness, which may not be sufficient for precise designs. Moreover, they give different values, leaving the designer with the problem of choosing one of them.

Tab. 3. Comparison of the mean values of the measured transverse stiffness (for c25 axial deflection) and their deviations from the calculations by analytical methods

Spring index C	Number of active coils n_a	End-coil shape	Mean transverse stiffness [N/mm]	Gross method [N/mm]	Wahl method [N/mm]	Haringx method [N/mm] (and PN EN 13906:2013)
5	2.5	e1	164	190 (16%)	163 (0%)	186 (14%)
		e2	186	174 (–7%)	150 (–19%)	170 (–9%)
		e3	163	158 (–3%)	138 (–15%)	155 (–5%)
5	2.75	e1	154	159 (3%)	135 (–12%)	155 (1%)
		e2	160	145 (–10%)	124 (–22%)	141 (–12%)
		e3	137	132 (–4%)	115 (–16%)	129 (–6%)
5	3	e1	127	133 (5%)	113 (–11%)	130 (2%)
		e2	142	122 (–14%)	104 (–27%)	119 (–16%)
		e3	125	111 (–11%)	96 (–23%)	109 (–13%)
7	2.5	e1	84	95 (14%)	93 (11%)	94 (12%)

		e2	85	89 (6%)	87 (3%)	88 (4%)
		e3	80	84 (5%)	82 (3%)	83 (4%)
7	2.75	e1	78	82 (5%)	79 (2%)	80 (3%)
		e2	75	77 (2%)	75 (–1%)	75 (0%)
		e3	69	72 (4%)	70 (2%)	71 (3%)
7	3	e1	71	71 (0%)	69 (–3%)	69 (–2%)
		e2	66	66 (0%)	64 (–2%)	65 (–1%)
		e3	67	62 (–7%)	60 (–10%)	61 (–9%)

Tab. 4. Comparison of the mean values of the measured transverse stiffness (for the c50 axial deflection) and their deviations from the calculations using analytical methods

Spring index C	**Number of active coils n_a**	**End-coil shape**	**Mean transverse stiffness [N/mm]**	**Gross method [N/mm]**	**Wahl method [N/mm]**	**Haringx method [N/mm] (and PN EN 13906:2013)**
5	2.5	e1	214	202 (–5%)	190 (–11%)	194 (–9%)
		e2	231	184 (–21%)	172 (–25%)	176 (–24%)
		e3	199	167 (–16%)	157 (–21%)	160 (–20%)
5	2.75	e1	187	169 (–10%)	158 (–16%)	162 (–14%)
		e2	193	153 (–21%)	143 (–26%)	146 (–24%)
		e3	166	139 (–16%)	130 (–22%)	133 (–20%)
5	3	e1	159	142 (–11%)	132 (–17%)	135 (–15%)
		e2	170	128 (–25%)	120 (–30%)	122 (–28%)
		e3	149	116 (–22%)	108 (–27%)	111 (–25%)
7	2.5	e1	101	100 (–1%)	95 (–6%)	97 (–4%)
		e2	99	94 (–5%)	89 (–10%)	91 (–8%)
		e3	97	88 (–9%)	84 (–14%)	86 (–12%)
7	2.75	e1	89	86 (–3%)	82 (–9%)	84 (–6%)
		e2	83	81 (–3%)	77 (–8%)	78 (–6%)
		e3	79	76 (–4%)	72 (–9%)	73 (–7%)
7	**3**	**e1**	**72**	**75 (3%)**	**71 (–3%)**	**72 (0%)**
		e2	74	70 (–5%)	66 (–11%)	62 (–17%)
		e3	75	66 (–12%)	62 (–17%)	63 (–15%)

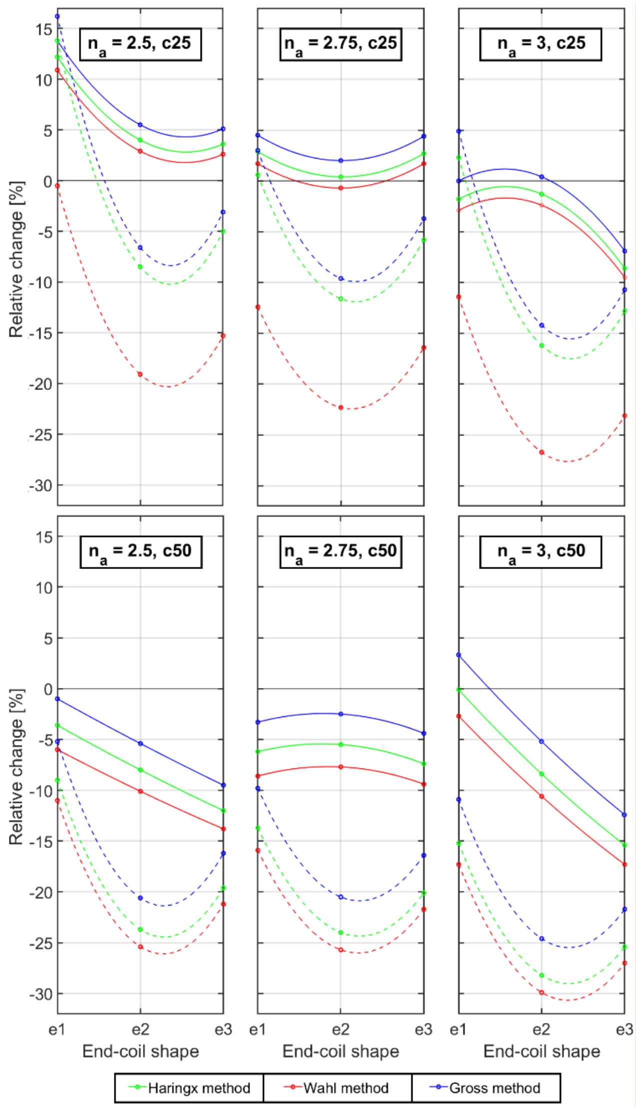

Fig. 3. Relative change between the stiffness values obtained from the experiments and the stiffness values calculated by the methods cited. Solid lines correspond to springs with index C = 7 and dashed lines to springs with index C = 5

This phenomenon is presented in Fig. 9, where an analysis of the effect of the design of the end-coils, the number of active coils and the compression value on the relative difference between the results of Eqs (2), (5) and (7) and the experimental results is presented. In most of the cases studied, the Gross method gives the closest results to the experimental results, but even for this method the discrepancies with the experimental results often exceed 20%. An increase in axial deflection is accompanied by an increase in the discrepancy between the formula results and the experimental results. This trend was confirmed by the results of additional tests on the transverse stiffness of springs with index C = 5, the number of active coils na = 2.5 and the end-coil design e1, e2, and e3 at 37.5% axial deflection. Due to the scope of this

DOI 10.2478/ama-2023-0011

work, the detailed results of these additional studies are not presented in this paper.

The analysis carried out showed that the effect of end-coil design on the discrepancy between formula results and experimental results is greatest for full (n_a = 3) or half (n_a = 2.5) number of active coils. In the case of springs with an intermediate number of coils (n_a = 2.75), this influence was the smallest, in particular for springs with C = 7. It can also be seen that the stiffnesses calculated using the Gross method are always the highest and the Wahl method the lowest. The Haringx method gives intermediate results.

4. CONCLUSIONS

This paper presents the results of transverse stiffness tests on cylindrical helical compression springs. Approximately 1,300 measurements were made with 18 springs differing in end-coil design, the number of active coils, and the spring index. An analysis of these results was carried out and compared with the results of computational models available in the literature. The analysis showed that the transverse stiffness of a cylindrical compression helical spring can show significant differences depending on the direction of the transverse force. In the cases studied, the largest difference between the maximum and minimum stiffness of a single spring reached a value of 26% of the average value of this stiffness. This phenomenon is not taken into account in the computational models present in the literature, which are based on the equivalent column concept, according to which the transverse stiffness of a spring does not depend on the direction of application of the transverse load.

A comparison of the average stiffnesses calculated from the experiments with the results of the calculation models available in the literature showed that the relative differences exceeded 25% in many cases. Under real-world conditions, a spring is generally loaded transversely in some fixed direction on which its transverse stiffness is, for example, the highest. Therefore, the differences between the stiffness calculated from one of the cited calculation methods and the actual spring stiffness may be even greater.

Axial deflection affects the actual number of active coils and thus changes the distribution of the spring's transverse stiffness. Therefore, the influence of the end-coil design on the nature of this distribution cannot be unambiguously determined. However, research has shown that the design of the end coils has the greatest effect on the average stiffness value for springs with a smaller index and, at the same time, a larger lead angle. It has been shown that the effect of the end coil design on the transverse stiffness is greater when the spring has a half or full number of active coils, but less for springs with an intermediate number of these coils.

Research also showed that fulfilling the condition defined in the EN 13906-1 standard for stable transverse operation of the spring does not guarantee such operation, and a new relation needs to be formulated, taking into account the influence of the end-coil design on the stability of the spring under transverse loading conditions.

This research showed that a detailed analysis must be performed during the design of a spring for a precise application. In the case of short springs, it is necessary to perform tests and determine the characteristics of the designed spring. The results of the transverse stiffness measurements presented in this paper can serve as a benchmark for the validation of FEM numerical models.

REFERENCES

1. Cieplok G, Wójcik K. Conditions for self-synchronization of inertial vibrators of vibratory conveyors in general motion. Journal of Theoretical and Applied Mechanics. 2020;58(2): 513–524. https://doi.org/10.15632/jtam-pl/119023
2. Lee CM, Goverdovskiy VN. A multi-stage high-speed railroad vibration isolation system with 'negative' stiffness. Journal of Sound and Vibration. 2012;331(4): 914–921. https://doi.org/10.1016/j.jsv.2011.09.014
3. Lu Z., Wang X., Yue K., Wei J., Yang Z. Coupling model and vibration simulations of railway vehicles and running gear bearings with multitype defects. Mechanism and Machine Theory. 2021;157: 104215.https://doi.org/10.1016/j.mechmachtheory.2020.104215
4. Vazquez-Gonzalez B., Silva-Navarro G. Evaluation of the Autoparametric Pendulum Vibration Absorber for a Duffing System. Shock and Vibration. 2008;15(3–4): 355–368. https://doi.org/10.1155/2008/827129
5. Yıldırım V. Exact Determination of the Global Tip Deflection of both Close-Coiled and Open-Coiled Cylindrical Helical Compression Springs having Arbitrary Doubly-Symmetric Cross-Sections. International Journal of Mechanical Sciences. 2016;115–116: 280–298. https://doi.org/10.1016/j.ijmecsci.2016.06.022
6. Paredes M. Enhanced Formulae for Determining Both Free Length and Rate of Cylindrical Compression Springs. Journal of Mechanical Design. 2016;138(2): 021404.https://doi.org/10.1115/1.4032094
7. Liu H., Kim D. Effects of end Coils on the Natural Frequency of Automotive Engine Valve Springs. International Journal of Automotive Technology. 2009;10(4): 413–420. https://doi.org/10.1007/s12239-009-0047-8
8. Haringx J. A. On Highly Compressible Helical Springs and Rubber Rods, and their Application for Vibration-Free Mountings. Philips research reports. 1949;4: 49–80.
9. Wittrick W. H. On Elastic Wave Propagation in Helical Springs. International Journal of Mechanical Sciences. 1966;8(1): 25–47. https://doi.org/10.1016/0020-7403(66)90061-0
10. Jiang W., Jones W. K., Wang T. L., Wu K. H. Free Vibration of Helical Springs. Journal of Applied Mechanics.1991;58(1): 222–228.https://doi.org/10.1115/1.2897154
11. Kobelev V. Effect of Static Axial Compression on the Natural Frequencies of Helical Springs. Multidiscipline Modeling in Materials and Structures. 2014;10: 379–398. https://doi.org/10.1108/MMMS-12-2013-0078
12. Mottershead J. E. Finite Elements for Dynamical Analysis of Helical Rods. International Journal of Mechanical Sciences. 1980;22(5): 267–283. https://doi.org/10.1016/0020-7403(80)90028-4
13. Taktak M., Dammak F., Abid S., Haddar M. A Finite Element for Dynamic Analysis of a Cylindrical Isotropic Helical Spring. Journal of Me-chanics of Materials and Structures. 2008;3(4): 641–658. http://doi.org/10.2140/jomms.2008.3.641
14. Michalczyk K. Analysis of Lateral Vibrations of the Axially Loaded Helical Spring. Journal of Theoretical and Applied Mechanics. 2015;53(3): 745-755. https://doi.org/10.15632/jtam-pl.53.3.745
15. Michalczyk K., Bera P. A Simple Formula for Predicting the First Natural Frequency of Transverse Vibrations of Axially Loaded Helical Springs. Journal of Theoretical and Applied Mechanics. 2019;57(3): 779–790. https://doi.org/10.15632/jtam-pl/110243
16. Berger C., Kaiser B. Results of Very High Cycle Fatigue Tests on Helical Compression Springs. International Journal of Fatigue. 2006;28(11): 1658–1663. https://doi.org/10.1016/j.ijfatigue.2006.02.046
17. Zhou C. et al. An Investigation of Abnormal Vibration – Induced Coil Spring Failure in Metro Vehicles. Engineering Failure Analysis. 2020;108: 104238. https://doi.org/10.1016/j.engfailanal.2019.104238

DOI 10.2478/ama-2023-0011 acta mechanica et automatica, vol.17 no.1 (2023)

18. Sobaś M. Analysis of the Suspension of Freight Wagons Bogies Type Y25. Pojazdy Szynowe. 2014;3: 33–44.
19. Swacha P., Kotyk M., Ziółkowski W., Stachowiak R. Stand for testing the fatigue life of compression springs. Developments in Mechanical Engineering. 2021;17(9): 73–85. https://doi.org/10.37660/dme.2021.17.9.6
20. Czaban J., Szpica D. The didactic stand to test of spring elements in vehicle suspension. Acta Mechanica et Automatica. 2009;3(1): 33–35.
21. Gross S. Berechnung und Gestaltung von Metallfedern, Springer-Verlag Berlin Heidelberg GmbH. 1951.
22. Wahl A. M. Mechanical Springs. Penton Publishing Company. 1944.

This work was supported by the AGH University of Science and Technology under research program No. 16.16.130.942.

Robert Baran: https://orcid.org/0000-0002-0711-230X

Krzysztof Michalczyk: https://orcid.org/0000-0002-1024-5947

Mariusz Warzecha: https://orcid.org/0000-0002-7417-1561

DOI 10.2478/ama-2023-0012

RESEARCH OF DYNAMIC PROCESSES IN AN ANVIL DURING A COLLISION WITH A SAMPLE

Yuriy PYR'YEV*, Andrzej PENKUL, Leszek CYBULA****

*Faculty of Mechanical and Industrial Engineering, Institute of Mechanics and Printing, Department of Printing Technologies,
Warsaw University of Technology, ul. Konwiktorska 2, 00-217 Warsaw, Poland
**Faculty of Mechanical and Industrial Engineering, Institute of Mechanics and Printing,
Department of Mechanics and Weaponry Technology, Warsaw University of Technology, ul. Narbutta 85, 02-524 Warsaw, Poland

yuriy.pyryev@pw.edu.pl, andrzej.penkul@pw.edu.pl, leszek.cybula@pw.edu.pl

received 3 October 2022, revised 15 December 2022, accepted 18 December 2022

Abstract: The paper concerns modelling the dynamics of the contact system of the tested sample with an elastic half-space (anvil) during their collision. The original elements in the paper include the proposed general approach to solving the problem of contact dynamics. The presented approach consists in determining the force of impact on the sample during the collision and the joint solution of the problem for the tested sample and the problem for an elastic semi-space under the conditions of the assumptions of Hertz's theory. The resulting interaction forces allow the determination of displacements and stresses.

Keywords: collision, test sample, anvil, half-space, elastic waves, impact speed, Hertz's theory

1. INTRODUCTION

The purpose of the paper is to analyse the wave phenomena occurring during the impact of the test sample against the anvil (elastic half-space) and to develop a method for calculating the parameters of selected physical quantities occurring in the anvil and the sample (projectile [1]) in the initial period after the impact.

Experimental database used as input (comparative) data were the impact tests of the Taylor bar. The impact test was proposed by Taylor [1], Whiffin [2] and Carrington and Gayler [3] as an experimental method of measuring the dynamic yield strength Ryd of elastic-plastic materials [1–3].

Many examples of shock-type transient processes with high strain rates can be found in the field of artillery [4–7] and in the study of seismology, earthquake engineering, dynamic soil-substrate interaction and terrain characteristics, and in mathematical modelling of the erosion process.

The problem of collision of elastic bodies with regard to their deformation has a rich history. The elementary collision theory uses the restitution factor Rf as a key parameter characterizing the deformation properties of colliding bodies and does not reflect various features of the internal state of the bodies [8, 9].

Saint-Venant [10], considering the propagation of longitudinal waves, considered the axial impact of the rods. It turned out that the theoretically determined time of collision differs significantly from the time obtained during the experiment. The reason for these differences is the inability to ensure the perfect flatness of the rod ends.

Hertz [11], based on Boussinesq's [12] research on the deformation of an elastic half-space, solved the problem of direct central collision of spheres with elastic properties, considering only local static deformations (ignoring wave propagation). In this case, the agreement between the theoretical and experimental collision times turned out to be good. Hertz's theory of impacts is used in practice to determine the stresses during interactions of two bodies with each other [13].

Sears [14] combined the Saint-Venant and Hertz approaches and considered the influence of the spherical shape of the rod ends on the obtained results. In these studies, he took into account both local deformations and wave propagation. This approach led to a good agreement of theoretical and experimental results and is used in many subsequent works [15, 16].

Kil'chevskii [8] modified Hertz's theory by combining it with Saint-Venant's theory.

The theory of crossbeam impact comes from Timoshenko et al. [17].

The problem concerning the phenomena occurring in an elastic semi-space hit by a moving mass on the surface has been investigated, e.g., in articles [18–24].

Kubenko [19] presented an overview of the approaches to study the impact of a blunted elastic body on the surface of an elastic medium. Mathematically, the problem is generally formulated as the non-stationary mixed boundary problem of continuum mechanics in which the unknown contact boundary changes with time and space.

The collision process between a blunted body and an elastic medium always includes a supersonic stage, during which the boundary value problem can be formulated as non-mixed and thus solved with simpler methods [19, 20].

In the paper [21], the problem of the linear theory of elasticity concerning the response of the elastic surface of the half-space to the normal impact of the indenter was considered.

In the paper [22], an exact analytical solution of the problem was obtained for the impact of a rigid mass on a semi-infinite elastic rod by a Kelvin-Voigt linear element.

The impact of the super seismic phase on the collision process immediately after the first contact is investigated within the

sciendo
DOI 10.2478/ama-2023-0012 acta mechanica et automatica, vol.17 no.1 (2023)

framework of Hertz's theory of impacts in the paper [20]. For small values of the αA parameter (defined in point 4), the influence of the super seismic state on the course of the impact can be neglected.

Ruta and Szydło [25] presented a method enabling the conversion of the results of the dynamic weight test into a static model. This paper presents an analytical solution to the problem of half-space vibrations caused by the shock pulse.

In the paper [26], the ground was modelled as an idealised elastodynamic half-space, and its sound emission during the collision of the object with the ground was analysed.

Since the classic work of Lamb [27] on the transient elastic response of a half-space resulting from the sudden application of a normal surface line and point loads, significant progress has been made in solving this class of elastodynamic problems [28].

Beginning with the ground-breaking work [27], Lamb's problem, which relates to the dynamic response on the free surface of an elastic half-space resulting from a time-dependent point pulse on a free surface, has become a classic subject of numerous theoretical seismology studies. Cagniard [29] presented a complicated method using the Laplace transform over time and presented the final solutions in the time domain. Thanks to the modification made by de Hoop [30], it became an appropriate way to solve the Lamb problem, which is now referred to as the 'Cagniard-de Hoop method'. The problem was taken up again by Sánchez-Sesma et al. [31] who provided a full set of formulas with an exact solution for any source and recipient location. Pak and Bai [32] presented an improved but compact analytical formula of the elastodynamic response in the time domain of a three-dimensional half-space subjected to an arbitrary distribution of internal or surface forces. For a surface point pulse operating on a 3D medium, Pekeris [33] gave a closed solution for a vertical point source, and Mooney [28] extended the results for vertical loads by any Poisson's ratio, ignoring the radial component.

Kausel [34, 35] dealt with the problem of Lamb applied to the soil, horizontal and vertical point load applied to the surface of an elastic, homogeneous half-space with any Poisson's ratio. A compact set of unambiguous space time formulas was presented for the following problems: all response functions for receivers placed on the surface of the half-space and at the depth under the load, i.e., along the epicentral axis.

Emami and Eskandari-Ghadi [36] presented a history of this problem, from its earlier stages to more recent research, by outlining and discussing the various rigorous approaches and methods of solving that have been suggested so far.

We shall consider the collision of elastic bodies (Figs. 1 and 2). The study will be conducted with the basic geometric assumptions of Hertz's theory [11].

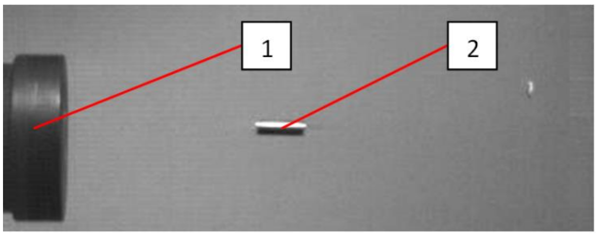

Fig. 1. View of the sample on the flight path before hitting the anvil: (1) anvil and (2) research sample

We limit ourselves to considering the direct interaction of the central bodies, i.e., we assume that they are the resultant of the dynamic contact pressures applied to the colliding bodies, directed along a straight line connecting their centres of inertia and coinciding with the normal to the compression surface at the point of initial contact of the non-deformed surface of these bodies.

Fig. 2. The sample at the moment it hits the anvil

This simplifying assumption will allow us to take into account only one component of the displacements of bodies at the point coinciding with the point of their initial contact.

2. IMPACT PROBLEM STATEMENT

Let us assume that a heavy body hits the half-space and has V_0 velocity when it contacts the surface of the half-space. Under the influence of an impact in a half-space and in a striking sample of r_0 radius, local deformations will be created, and, additionally, vibrations of the half-space will arise. Let us assume that the friction between the contacting surfaces is negligible, and the material of the elastic space with Young's modulus E and Poisson's ratio v does not undergo plastic deformation or fracture.

The assumption about the elastic behaviour of metal anvil (target) can be extended to the case of real processes, when only local plastic deformations occur in the material, limited by the proximity of the starting point of contact; moreover, the energy needed to create a residual indentation is only a small fraction of the initial kinetic energy [18].

By continuing the contact of the impact sample with the half-space, the displacements of the sample will consist of a part dependent on local compression and a part determined by dynamic deflections of the half-space. As is known, the dynamic deflections of the half-space satisfy the differential Eq. (1).

2.1. Mathematical model of the anvil

The point source causes the appearance of volumetric longitudinal (P) and shear (S) waves and Rayleigh (R) waves. Lamb [27] considered two external problems of wave propagation in an isotropic elastic half-space from a normally applied concentrated force to a free force. The solution of these problems in the paper [37] has been reduced to wave equations due to the scalar and vector potential.

We consider the anvil as an elastic half-space that is rigidly fixed in a housing that is struck by the test sample. We can consider the anvil as half-space until reflected waves do not appear.

Let us consider in a cylindrical coordinate system (r, θ, z) a half-space $(0 \leq z < \infty)$, where r is radius, θ is angle and z is coordinate, as shown in Fig. 3. The medium is assumed to be homogeneous and isotropic. Axially symmetric non-stationary loads depending on position and time act on the surface $p(r, t)$

DOI 10.2478/ama-2023-0012

with relative spatial distribution $Z(r)$ and the resultant $P(t)$, i.e., $p(r, t) = Z(r)P(t)$ in time $t > 0$. As a result of this action, there is a vector field of displacement in the structure $U \equiv (u, v, w)$, where u, v and w are the components of the displacement vector on the axis, r, θ and z. Due to the axisymmetric stress distribution, displacements, strains and stresses will be independent of the θ angle. We have $U \equiv (u, 0, w)$.

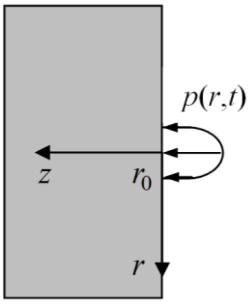

Fig. 3. Physical model of an anvil (elastic half-space) with a surface area load with r_0 radius

An elastic half-space is characterised by the velocities of longitudinal (P) c_1 and shear (S) c_2 waves or the Lame constants λ, μ and density ρ, which are related by dependencies

$$c_1 = \sqrt{\frac{\lambda+2\mu}{\rho}},\ c_2 = \sqrt{\frac{\mu}{\rho}}$$

On the free surface of the medium, stresses $\sigma_{zr}, \sigma_{z\theta}$ and σ_{zz} are either converted to zero or take values corresponding to a given limit load.

We assume that the medium is at rest when $t < 0$, and in the initial moment, $t = 0$, where the axisymmetric source of disturbances starts to work $p(r,t) = Z(r)P(t)$.

As a rule, the forces arising during an impact $P(t)$ (impact force, life force) are not known in advance; they must be determined in the problem-solving process, and only in some cases can they be considered predetermined.

The discussed issue boils down to solving Lamé displacement equations in a cylindrical coordinate system [38]:

$$(\lambda + 2\mu)\left(\frac{\partial^2 u}{\partial r^2} + \frac{1}{r}\frac{\partial u}{\partial r} - \frac{u}{r^2}\right) + \mu\frac{\partial^2 u}{\partial z^2} + (\lambda + \mu)\frac{\partial^2 w}{\partial r\,\partial z} = \rho\frac{\partial^2 u}{\partial t^2},$$
$$(\lambda + \mu)\left(\frac{\partial^2 u}{\partial r\,\partial z} + \frac{1}{r}\frac{\partial u}{\partial r}\right) + \mu\left(\frac{\partial^2 w}{\partial r^2} + \frac{1}{r}\frac{\partial w}{\partial r}\right) + (\lambda + 2\mu)\frac{\partial^2 w}{\partial z^2} = \rho\frac{\partial^2 w}{\partial t^2},$$
$$0 \le z < \infty,\ 0 \le r < \infty \tag{1}$$

at boundary conditions:

$$\sigma_{zz}(r,0,t) = -p(r,t) = -P(t)Z(r),\ z = 0 \tag{2}$$

$$\sigma_{rz}(r,0,t) = 0,\ z = 0 \tag{3}$$

$$u,\ w \to 0,\ z \to \infty \tag{4}$$

and the initial conditions [37]:

$$u = 0,\ \frac{\partial u}{\partial t} = 0,\ \ w = 0,\ \frac{\partial w}{\partial t} = 0,\ t < 0 \tag{5}$$

$p(t, r)$ is the contact pressure density distributed over the contact area $\omega(t)$. Due to the axis of symmetry, $\omega(t)$ is a circle with a radius $a(t)$. We assume that the contact area does not change with time, and from the beginning, the $a(t)$ radius is equal to r_0.

We will consider the sources $Z(r)$ on the surface for which the following condition is met:

$$2\pi\int_0^\infty p(r,t)r\,dr = P(t) \tag{6}$$

where [13]

$$Z(r) = \frac{1}{\pi r_0^2}\frac{3}{2}\sqrt{\left(1 - \frac{r^2}{r_0^2}\right)H\left(1 - \frac{r^2}{r_0^2}\right)}. \tag{7}$$

where $H(t)$ Heaviside function: $H(t) = 0$ for $t < 0$, $H(t) = 1$ for $t \ge 0$.

2.2. Mathematical model of a sample hitting an anvil

In the study to determine the impact of half-space, the system of equations describing the behaviour of waves in the half-space integrates simultaneously with the equation of motion of the sample and the condition of compliance of displacements. The last one takes into account a contact approximation of a sample with mass m_1 and half space. One of the ends of the cylindrical rod is hemispherical. We will consider that for the considered impact of the test sample; the contact approximation can be determined on the basis of the solution to the dynamic problem of Hertz for pressing a ball into an elastic half-space [13].

Let us denote, after Timoshenko [17], the total displacement of the hitting body (projectile [1]) from the start of the impact as $h(t)$ and local compression as α_H. Then, of course [17, 39]

$$h = \alpha_H + w \tag{8}$$

where $w = w(0, 0, t)$ is deflection of the elastic semi-space surface under the sample. The displacement $h(t)$ satisfies the differential equation of motion

$$m_1\frac{d^2h(t)}{dt^2} = -P(t) \tag{9}$$

under initial conditions:

$$h(0) = 0,\ \frac{dh}{dt} = V_0,\ t = 0 \tag{10}$$

Here, $P(t)$ is the resultant of the contact pressure.
In the following part, we assume that

$$\frac{m_1}{P}\frac{\partial^2 w_e}{\partial t^2} \ll 1 \tag{11}$$

where $w_e(r,z,t)$ characterises the relative displacement of the sample elements due to its deformation.

3. SOLUTION METHOD

3.1. Key relationships for an elastic half-space

Having a solution for a concentrated force acting on a half-space boundary, the superposition method allows us to find displacements and stresses arising under the action of a load distributed in a circle [25]. This article uses a different approach [40] to find the stress-strain state of a half-space. Applying the Laplace and Hankel transformations to Eq. (1) and considering the homogeneous initial condition (5), we receive linear differential equations with respect to the variable z. Since the solution of these equations depends on four unknowns, they are found using four boundary conditions (2)–(4). By applying the inverse Laplace and Hankel transformations, we obtain the searched dependencies. Displacements u, w and stresses can be expressed by the Duhamel integral

$$\{u(r,z,t),w(r,z,t)\}=\int_0^t\{u_\delta(r,z,t-t'),w_\delta(r,z,t-t')\}\cdot P(t')dt'=\{u_\delta(r,z,t),w_\delta(r,z,t)\}*P(t) \quad (12)$$

$$\{\sigma_{zz},\sigma_{rr},\sigma_{\theta\theta},\sigma_{rz}\}=\{\sigma_{zz,\delta},\sigma_{rr,\delta},\sigma_{\theta\theta,\delta},\sigma_{rz,\delta}\}*P(t) \quad (13)$$

where $u_\delta(r,z,t)$ and $w_\delta(r,z,t)$ are solutions to problems (1)–(6) for the impulse function $P(t)=\delta(t)$: $\delta(t)=\infty$ for $t=0$, $\delta(t)=0$ for $t\neq 0$ and

$$\int_{-\infty}^{+\infty}\delta(t)dt=1, \quad (14)$$

Eqs (12) and (13) give a convolution of two causal functions. Applying the Laplace and Hankel integral transformations to the considered problems (1)–(6) [37], e.g., for displacement $w_\delta(r,z,t)$, the equations can be written as follows:

$$w_\delta^L(r,z,s)=\int_0^\infty w_\delta(r,z,t)e^{-st}dt \quad (15)$$

$$w_\delta^{LH}(k,z,s)=\int_0^\infty w_\delta^L(r,z,s)rJ_0(kr)dr \quad (16)$$

we get a solution to the problem of the following form [40]:

$$\{u_\delta,w_\delta\}=\frac{1}{2\pi i}\int_{c_0-i\infty}^{c_0+i\infty}\{u_\delta^L,w_\delta^L\}e^{st}ds \quad (17)$$

$$\{\sigma_{zz,\delta},\sigma_{rr,\delta},\sigma_{rz,\delta}\}=\frac{1}{2\pi i}\int_{c_0-i\infty}^{c_0+i\infty}\{\sigma_{zz,\delta}^L,\sigma_{rr,\delta}^L,\sigma_{rz,\delta}^L\}e^{st}ds \quad (18)$$

where

$$\{w_\delta^L,\sigma_{zz,\delta}^L\}=\int_0^\infty\{w_\delta^{LH},\sigma_{zz,\delta}^{LH}\}Z^H(k)kJ_0(kr)dk \quad (19)$$

$$\{u_\delta^L,\sigma_{rz,\delta}^L\}=\int_0^\infty\{u_\delta^{LH},\sigma_{rz,\delta}^{LH}\}Z^H(k)kJ_1(kr)dk \quad (20)$$

$$\sigma_{rr,\delta}^L=\int_0^\infty\sigma_{rr,\delta}^{LH0}Z^HkJ_0(kr)dk+\frac{1}{r}\int_0^\infty\sigma_{rr,\delta}^{LH1}Z^HkJ_1(kr)dk \quad (21)$$

$J_n(kr)$ is a Bessel function of the first kind of order n (n = 0, 1, …); c_0 is a real number so that the contour path of integration is in the region of convergence of $u_\delta^{LH}(k,z,s)$, $w_\delta^{LH}(k,z,s)$.

Integral expressions in Eqs (19)–(21) marked with '*LH*' have the following form [40]:

$$u_\delta^{LH}(k,z,s)=\frac{(\gamma e^{-\alpha z}-2\alpha\beta e^{-\beta z})k}{\mu D(k,s)} \quad (22)$$

$$w_\delta^{LH}(k,z,s)=\frac{(\gamma e^{-\alpha z}-2k^2e^{-\beta z})\alpha}{\mu D(k,s)} \quad (23)$$

$$\sigma_{zz,\delta}^{LH}(k,z,s)=-\frac{(\gamma^2e^{-\alpha z}-2\alpha\beta k^2e^{-\beta z})}{D(k,s)} \quad (24)$$

$$\sigma_{rz,\delta}^{LH}(k,z,s)=\frac{(-e^{-\alpha z}+e^{-\beta z})2\alpha\gamma k}{D(k,s)} \quad (25)$$

$$\sigma_{rr,\delta}^{LH0}(k,z,s)=\frac{\gamma\left(2k^2-(\lambda/\mu)c_1^{-2}s^2\right)e^{-\alpha z}-4\alpha\beta k^2e^{-\beta z})}{D(k,s)} \quad (26)$$

$$\sigma_{rr,\delta}^{LH1}(k,z,s)=\frac{(-2\gamma e^{-\alpha z}+4\alpha\beta e^{-\beta z})k}{D(k,s)} \quad (27)$$

$$D(k,s)=\gamma^2-4\alpha\beta k^2,\ \gamma=2k^2+c_2^{-2}s^2 \quad (28)$$

$$\alpha=\sqrt{k^2+c_1^{-2}s^2},\ \beta=\sqrt{k^2+c_2^{-2}s^2},\ \mathrm{Re}\alpha>0,\ \mathrm{Re}\beta>0 \quad (29)$$

Hankel transform $Z^H(k)$ of the $Z(r)$ source on the surface Eq. (7):

$$Z^H(k)=\frac{3(\sin(r_0k)-r_0k\cos(r_0k))}{2\pi r_0^3k^3} \quad (30)$$

In order to receive the function $w_\delta(0,0,t)$ for the initial moment $t\to 0$, we find the properties of the Laplace transform for $s\to\infty$

$$w_\delta^{LH}(k,z,s)=\frac{c_2^2e^{-\frac{zs}{c_1}}}{\mu c_1}\left(\frac{1}{s}-\frac{c_1zk^2}{2s^2}+\cdots\right)-\frac{2c_2^4k^2e^{-\frac{zs}{c_2}}}{\mu c_1s^3},\ s\to\infty \quad (31)$$

In the initial moment,

$$w_\delta(0,0,t)=\frac{c_2^2}{\mu c_1}H(t)Z(0),\ t\to 0 \quad (32)$$

$$\sigma_{zz,\delta}(0,z,t)=-\delta(t-z/c_1)Z(0),\ t-z/c_1\to 0 \quad (33)$$

Asymptotics Eq. (33) shows that for the calculation of stresses, it is better to use the following equation:

$$\sigma_{zz}(r,z,t)=\int_0^t\sigma_{zz,H}(r,z,t-t')\frac{d}{dt'}P(t')dt' \quad (34)$$

where $\sigma_{zz,H}(k,z,s)=\sigma_{zz,\delta}(k,z,s)/s$.
$c_2/c_1=\sqrt{(1-2\nu)/(2-2\nu)}$

The calculations of the inverse integral Laplace and Hankel transformations were performed in the same way as in the paper [40].

3.2. Solution method for the research sample

Integrating the Eq. (9) using the Laplace transform and the initial condition (10), we obtain the following equation:

$$h(t)=V_0t-\frac{1}{m_1}\int_0^t(t-t')P(t')dt' \quad (35)$$

On the other hand, according to the theory of Hertz [13], we can assume the following equation:

$$\alpha_H=(P/K)^{2/3}=k_0P^{2/3}\text{ or }P=K\alpha_H^{3/2} \quad (36)$$

where K is determined from the equation [13]

$$K=\frac{4E^*\sqrt{r_0}}{3},\ k_0=K^{-2/3},\ \frac{1}{E^*}=\frac{1-\nu_1^2}{E_1}+\frac{1-\nu^2}{E} \quad (37)$$

Considering Eqs (8), (35) and (36), we obtain the equation:

$$V_0t-\frac{1}{m_1}\int_0^t(t-t')P(t')dt'=k_0P(t)^{2/3}+w(0,0,t) \quad (38)$$

At the moment of time, $t=t_n=n\Delta t$, where n = 0, 1, 2, …, where Δt integration time is assumed to take place

$$V_0t_n-\frac{1}{m_1}\int_0^{t_n}(t_n-t')P(t')dt'=k_0P(t_n)^{2/3}+w_n \quad (39)$$

where $w_n=w(0,0,t_{n-1})$.

In the initial moment $t=0$ ($n=0$), sample displacement $h=0$, displacement of half-space $w=0$ and sample speed $v=V_0$.

In moment $t=t_1$ ($n=1$), sample displacement is $h(t_1)=h_1=V_0\,t_1$, deflection of half-space is $w(0,0,t_0)=w_1=0$, impact force (pressure) is $P(t_1)=P_1=K\,(h_1)^{3/2}$, acceleration of the sample is $a_1=-P_1/m_1$ and sample speed is $v(t_1)=v_1=V_0$.

In moment $t=t_2$ ($n=2$), sample displacement is $h(t_2)=h_2=h_1+v_1\,\Delta t+a_1(\Delta t)^2/2$, deflection of half-space is $w(0,0,t_1)=w_2$, impact force (pressure) is $P(t_2)=P_2=K\,(h_2-w_2)^{3/2}$, acceleration of the sample is $a_2=-P_2/m_1$ and sample speed is $v(t_2)=v_2=v_1+a_1\Delta t$.

The further course of the calculations is obvious. Let us write directly the formulas related to the nth stage:

$$h(t_n)=h_n=h_{n-1}+v_{n-1}\Delta t+a_{n-1}(\Delta t)^2/2 \quad (40)$$

$$w_n=\Delta t\sum_{m=1}^{n-2}w_\delta(0,0,t_{n-1}-t_m)\,P_m+\frac{\Delta t}{2}w_\delta(0,0,0)P_{n-1} \quad (41)$$

$$P(t_n)=P_n=K(h_n-w_n)^{3/2} \quad (42)$$

$$a_n=-P_n/m_1 \quad (43)$$

$$v(t_n)=v_n=v_{n-1}+a_{n-1}\Delta t \quad (44)$$

DOI 10.2478/ama-2023-0012

4. NUMERICAL RESULTS

A numerical analysis of the collision of a copper test sample with a steel anvil was carried out. The parameters are given in Tab. 1. The mass of the tested sample is m_1 = 0.0122 kg, sample radius is r_0 = 0.004 m and collision speed is V_0 = 100 m/s.

Tab. 1. Mechanical properties of steel and copper

Properties	Copper	Steel
Longitudinal wave speed c_1 [m/s]	4,597	5,994
Shear wave speed c_2 [m/s]	2,263	3,204
Density ρ [kg/m^3]	8,960	7,830
Coefficient λ [GPa]	97.53	120.6
Shear modulus of elasticity G, μ [GPa]	45.9	80.4
Poisson number ν [–]	0.34	0.3
Young's module E [GPa]	123	209
Yield point R_y [MPa]	57	1,000
Tensile strength R_m [MPa]	227	1,200

For the problem under consideration [21], the $\alpha_A = (\pi\rho r_0^3/m_1)^{1/2}(V_0/c_1)^{3/2} = 0.785\cdot 10^{-3}$ parameter was calculated. Due to the low value of α_A, the influence of the super-seismic state on the course of the impact can be neglected as a whole.

Figs. 4 and 5 show the time courses of the characteristics of the test specimen during the collision. You can see that initially the force of influence on the sample $P(t)$, sample displacement $h(t)$ and deflection of half-space $w(t)$ during the collision increase and reach their maximum values. The sample speed $v(t)$ initially drops to zero at time t'_s. The diagram of the relationship $P(t)$ is shown in Fig. 4. Since the Hertz model describes elastic deformations, the $P(t)$ diagram is symmetrical about the vertical axis passing through the point (t'_s, P_{max}) ($t_s = 2\,t'_s$), where t_s is the collision time. When the force of the effect on the sample $P(t_s) = 0$, then $h - w = 0$ as in Eq. (8) (Fig. 4).

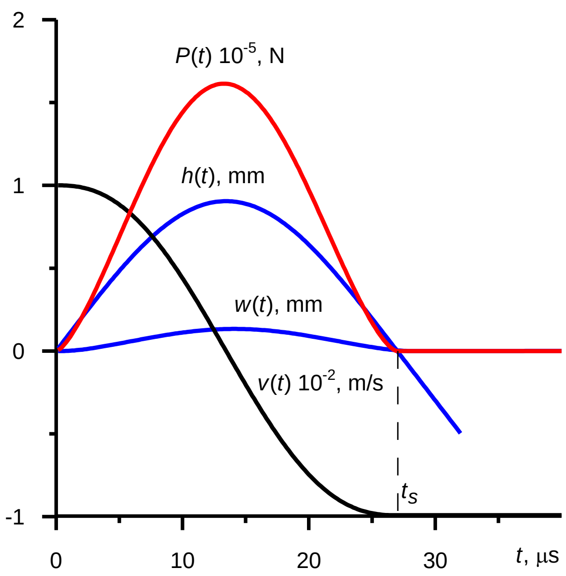

Fig. 4. Change of the force of influence on the sample P, sample displacement h, deflection of the half-space w and sample speed v over time during the Hertz impact for the collision speed V_0=100 m/s

The coefficient of restitution was marked with the letter R_f. This coefficient is the ratio of the body speed after the impact v(t_s) to the speed right before the impact V_0. In the considered ranges of speeds and dimensions of colliding bodies, $R_f = -v(t_s)/V_0 = -0.991$ (t_s = 27.0 μs, v(t_s) = –99.1 m/s). This factor hardly depends on these values.

Without considering the deflection of the elastic half-space, the problems (9) and (10) can be solved in the analytical form [11]. Maximum deflection can be written as follows:

$$\alpha_{max} = \left(\frac{5}{4}\frac{m_1 V_0^2}{K}\right)^{2/5}, \tag{45}$$

Maximum force of impact on the sample:

$$P_{max} = K\alpha_{max}^{3/2} \tag{46}$$

Collision duration t_s:

$$t_s = 2.94\frac{\alpha_{max}}{V_0} \tag{47}$$

This formula shows that the duration of the impact depends to the greatest extent on the mass of the sample m_1 and increases with it. The duration of the collision t_s is to a lesser extent influenced by the impact speed and the reduced radius of curvature of the body contact surfaces, which is within the n factor to the 1/2 rational power. As these parameters increase, the impact time is reduced. Calculation according to Eqs (46) and (47) gives P_{max} = 182,191 N and t_s = 24.6 μs. Calculation of the dimensionless coefficient $K_{max} = P_{max}/S/R_m$ = 15.97 shows that the average maximum stresses arising in the contact area are significantly higher than the tensile strength of the sample calculated under static conditions, where for copper R_m = 57 MPa and $S = \pi r_0^2$. Fig. 5 shows the K_{max} dependence of the radius r_0 ($K_{max} \sim 1/r_0^{9/5}$). Restitution coefficient is $R_f = -1$.

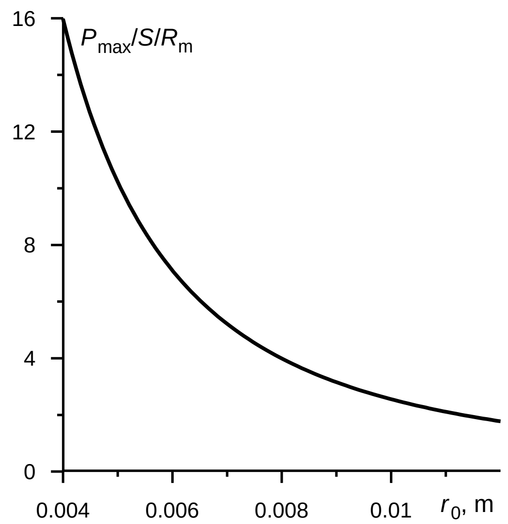

Fig. 5. The dependence of the dimensionless coefficient $K_{max} = P_{max}/S/R_m$ on r_0 radius according to Eqs (46) and (45)

It was noticed in the paper [41] that the Hertz model gives results consistent with the experiment if the duration of the collision t_s is much longer than the longest period of free oscillation T of the colliding bodies, t_s/T>10. On the other hand, according to Eq. (47), the impact duration decreases with increasing speed. Of course,

DOI 10.2478/ama-2023-0012

there is a certain upper limit for the speed $V_{0,max}$, above which the formulas obtained from Hertz's theory will lead to too considerable errors.

This consideration is often emphasised in the impact theory literature [41], but undeservedly, little attention is paid to another limitation of Hertz's theory. It is associated with the possible appearance of plastic deformations in the colliding bodies and failure to take into account the dynamic properties of strength parameters, e.g., the tensile strength parameter R_m.

If, in the post-impact conditions, the anvil was not damaged and the specimen changed shape due to plasticity (the radius of the specimen contact surface increased) but was not damaged, then the tensile strength in the specimen was not achieved. The shape of deformation and cracking in the Taylor bar impact test is the so-called mushrooming. Knowing the impact speed and the parameters of the collision bodies, we can calculate the maximum value of the force acting on the sample. This gives the opportunity to estimate the value R_m.

The dynamic yield point and the dynamic strength of the material, revealed under impact loads, assume values greater than the yield point and the material's tensile or compressive strength determined during static tests [13].

Let us note that the assumption made by Hertz about the linear elasticity of the material is not justified at sufficiently high impact velocities. Thus, Hertz's theory is probably wrong with most practical impact problems. Therefore, the work takes into account the deflection of the surface of the elastic half-space.

The performed calculations of the issue under consideration are shown in Fig. 6. We received $P_{max} = P(t_s/2) = 160{,}000$ N, $t_s = 27$ μs and $v(t_s) = -99.1$ m/s. In Fig. 5, the dimensionless factor was calculated, $K_{max} = P_{max} / S / R_m = 14.11$. Taking the deflection of the surface of the elastic half-space into account leads to an extension of the collision time and a reduction in the maximum force value P_{max} to 11.6%.

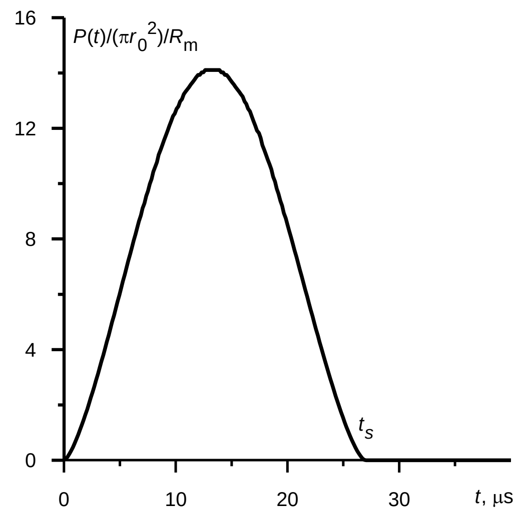

Fig. 6. Dependence of dimensionless contact stress $P(t)/(\pi r_0^2)/R_m$ arising during the collision on time for the speed of $V_0 = 100$ m/s

Analogously to Fig. 6, Fig. 7 shows the time dependencies of the component of vertical displacements $w(r, 0, t)$ to the surface at four observation points. Comparing the obtained results with the displacements of the surface points from Awrejcewicz and Pyryev [40] for the disorder $P(t)=H(t)$, we do not observe the moment of arrival of transverse S and Rayleigh R waves. For our case, the duration of the collision t_s is too high for the moments of arrival of longitudinal P, transverse S and Rayleigh R waves to be visible. The shape of the graphs repeats the shape of the interaction force, but away from the source, a slight negative deflection appears, the amplitude decreases and the width of the disturbance increases.

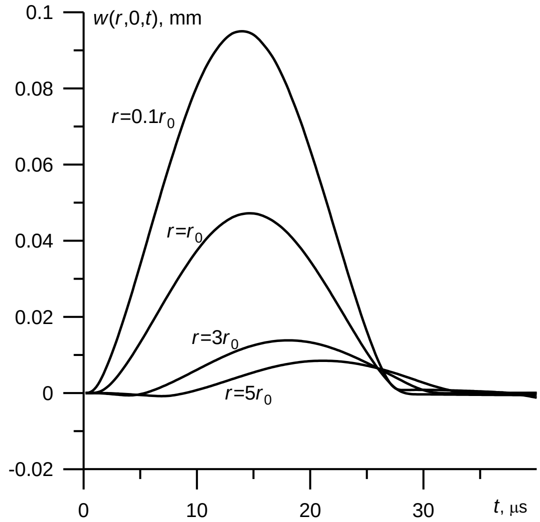

Fig. 7. Evolution of the deflection of an elastic half-space $w(r, 0, t)$ due to load $P(t)$ acting on the surface of a circle with a radius of the sample r_0 for $r = 0.1\ r_0$ (curve 1), for $r = r_0$ (curve 2), for $r = 3r_0$ (curve 3) and for $r = 5r_0$ (curve 4)

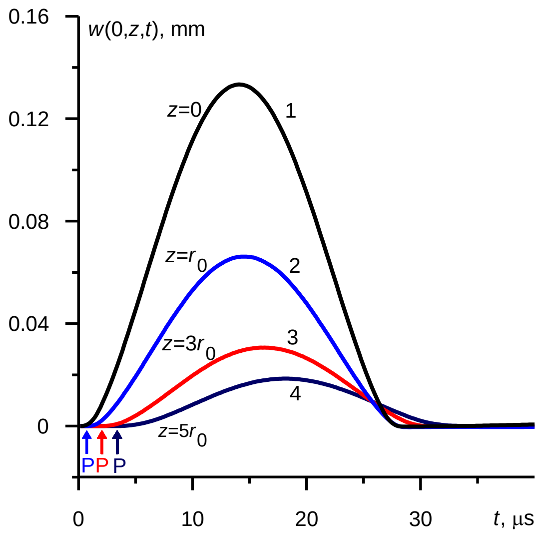

Fig. 8. Evolution of the axial displacement of an elastic half-space $w(0,z,t)$ due to load $P(t)$ acting on the surface of a circle with a radius of the sample r_0 for $z = 0$ (curve 1), for $z = r_0$ (curve 2), for $z = 3r_0$ (curve 3) and for $z = 5r_0$ (curve 4)

Fig. 8 shows the timing of the axial displacement of the elastic half-space $w(0, z, t)$ to load $P(t)$ acting on the surface of a circle with a radius of the sample r_0 for $r = 0.1\ r_0$ (curve 1), for $r = r_0$ (curve 2), for $r = 3r_0$ (curve 3) and for $r = 5r_0$ (curve 4). The shape of the graphs repeats the shape of the interaction force, but away from the source, a slight negative deflection $P(t)$ appears, the amplitude decreases and the width of the disturbance increases. In point $(0, r_0)$ at $t = r_0/c_1 = 0.67$ μs, longitudinal wave P will appear, in point $(0, 3r_0)$ at $t = r_0/c_1 = 2.0$ μs and in point $(0, 5r_0)$ at $t = 5r_0/c_1 = 3.3$ μs (see Fig. 8).

DOI 10.2478/ama-2023-0012

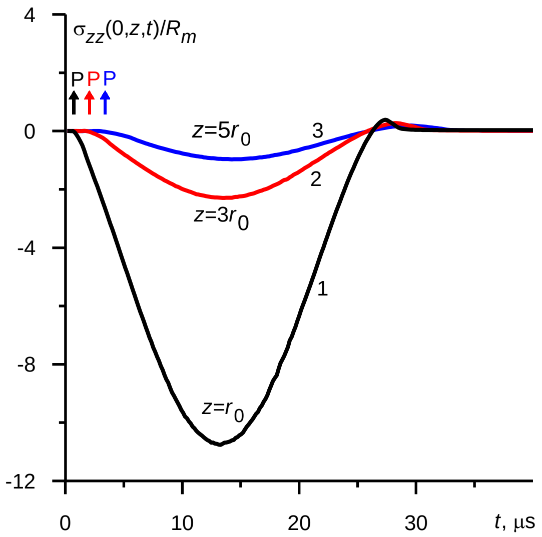

Fig. 9. Evolution of normal stress $\sigma_{zz}(0, z, t)$ on the anvil axis due to load $P(t)$ acting on the surface of a circle with a radius of the sample r_0 for $z = r_0$ (curve 1), for $z = 3r_0$ (curve 2) and for $z = 5r_0$ (curve 3)

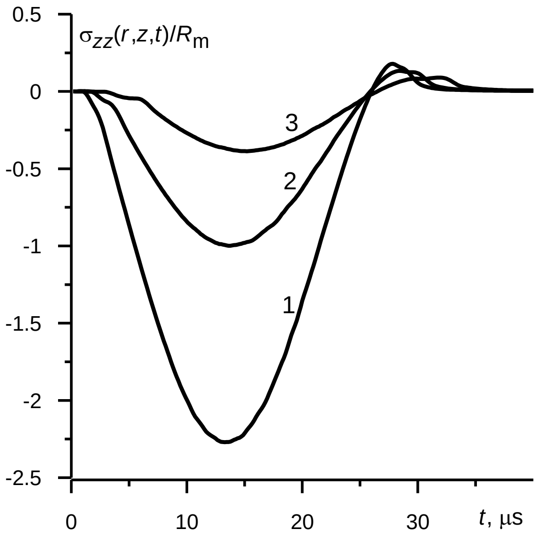

Fig. 10. Evolution of normal stress $\sigma_{zz}(r, z, t)$ in the centre of the anvil due to the load $P(t)$ acting on the surface of a circle with a radius of the sample r_0 for $z = r = 2r_0/2^{0.5}$ (curve 1), for $z = r = 3r_0/2^{0.5}$ (curve 2) and for $z = r = 5r_0/2^{0.5}$ (curve 3)

Fig. 9 shows dimensionless normal compressive stresses $\sigma_{zz}(0, z, t)/R_m$ on the anvil axis due to load $P(t)$ acting on the surface of a circle with a radius of the sample r_0 for $z = r_0$ (curve 1), for $z = 3r_0$ (curve 2) and for $z = 5r_0$ (curve 3). The amplitude of compressive stresses decreases. In point $(0, r_0)$ at $t = r_0/c_1 = 0.67$ μs, longitudinal P stress wave will appear, in point $(0, 3r_0)$ – at $t = r_0/c_1 = 2.0$ μs, and in point $(0, 5r_0)$ – at $t = 5r_0/c_1 = 3.3$ μs (see Fig. 9).

Fig. 10 shows dimensionless normal stresses $\sigma_{zz}(r, z, t)/R_m$ in the centre of the half-space on a cone at the same distances in point $(2^{0.5}r_0, 2^{0.5}r_0)$ (curve1), in point $(3r_0/2^{0.5}, 3r_0/2^{0.5})$ (curve 2) and in point $(5r_0/2^{0.5}, 5r_0/2^{0.5})$ (curve 3). The highest values of the compressive stress amplitudes decrease with increasing distance of the observation points from the disturbance site, but at the end of the stress disturbance, they change the sign into tensile stress.

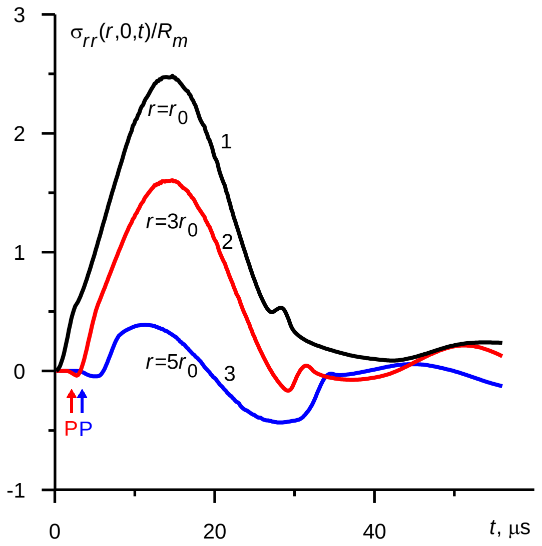

Fig. 11. Evolution of normal stress $\sigma_{rr}(r,0, t)$ on the surface of the anvil due to the load $P(t)$ acting on the surface of the circle with the radius of the sample r_0 for $r = r_0$ (curve 1), for $r = 3r_0$ (curve 2) and for $r = 5r_0$ (curve 3)

Fig. 11 shows the time dependencies of normal stress $\sigma_{rr}(r, 0, t)$ on the anvil surface due to load $P(t)$ acting on the surface of a circle with a radius of the sample r_0 for $r = r_0$ (curve 1), for $r = 3r_0$ (curve 2) and for $r = 5r_0$ (curve 3). For example, let us consider an observation point $(5r_0, 0)$ located on the anvil surface within 5 radiuses of the sample-anvil contact area. By the time $t = (5r_0 - r_0)/c_1 = 2.67$μs, there are no disturbances. At $t = 4r_0/c_1$, there will be a disturbance with the speed of the longitudinal wave c_1. The arrows on the graphs correspond to the time of arrival at the appropriate observation points of the disturbance from the centre of the contact area of the sample with the anvil.

5. CONCLUSION

A mathematical model of the dynamics of the contact system of the test sample with the anvil (semi-elastic space) during their collision was developed. The proposed method of calculations using classical Laplace and Hankel transformations allows us to solve the problem for the spatial model of the body.

The proposed analysis enables the calculation of stresses and displacements in an elastic half-space, as well as the kinematics of the tested sample.

The original elements of the paper include the proposed general approach to solving the problem of contact dynamics. The presented approach consists in determining the impact force on the sample *P(t)* during the collision as a common solution to the problem for the tested sample and the problem for an elastic semi-space under the conditions of the assumptions of Hertz's theory. The resulting force *P(t)* allows the determination of displacements and stresses.

The performed calculations showed that during a sample collision with a half-space under the conditions under consideration, the contact force *P(t)* did not have a significant effect on the formation of visible waves: transverse (S) and Rayleigh (R) waves. This is because the rate of load change is not sufficient.

The obtained solution can be used to determine the dynamic strength limit of materials. The calculations made as part of the paper showed more than threefold (1.6×10^5 N/S/R_y = 3.18) increase of the dynamic yield point for steel and more than twofold (1.6×10^5 N/S/R_m = 2.65) increase in dynamic tensile strength for steel to that determined in classical conditions. Corresponding values for a copper sample give a 14-fold (1.6×10^5 N/S/R_m = 14.0) increase of the dynamic limit of tensile strength. Considering that the sample after reflection has the shape of a mushroom with a radius r_1 = 0.006 m, we receive a sixfold (1.6×10^5 N/S_1/R_m = 6.2) increase of the dynamic tensile strength limit, where $S_1 = \pi r_1^2$.

The method proposed here can be useful for the dynamic analysis of issues such as the collision of a sample with a layered body [42].

REFERENCES

1. Taylor G. The use of flat-ended projectiles for determining dynamic yield stress. I. Theoretical considerations. Proc. R. Soc. London Ser. A. 1948;194:289–299.
2. Whiffin AC. The use of flat-ended projectiles for determining dynamic yield stress. II. Tests on various metallic materials. Proc. R. Soc. London, Ser. A. 1948;194:300–322.
3. Carrington WE, Gayler MLV. The use of flat-ended projectiles for determining dynamic yield stress. III. Changes in microstructure caused by deformation under impact at high-striking velocities. Proc. R. Soc. London, Ser. A. 1948;194:323–331.
4. Włodarczyk E, Michałowski M. Penetration of metallic half-space by a rigid bullet. Problemy Techniki Uzbrojenia. 2002;31(82):93–102.
5. Włodarczyk E, Sarzyński M. Analysis of dynamic parameters in a metal cylindrical rod striking a rigid target. Journal of Theoretical and Applied Mechanics. 2013; 51(4):847-857.
6. Włodarczyk E, Sarzynski M. Strain energy method for determining dynamic yield stress in Taylor's test. Engineering Transactions. 2017; 65(3):499-511.
7. Świerczewski M, Klasztorny M, Dziewulski P, Gotowicki P. Numerical modelling, simulation and validation of the SPS and PS systems under 6 kg TNT blast shock wave. Acta Mechanica et Automatica. 2012;6(3):77-87.
8. Kil'chevskii NA. Dynamic Contact Compression of Two Bodies. Impact [in Russian]. Kiev: Naukova Dumka; 1976.
9. Awrejcewicz J. Pyryev Yu. Nonsmooth Dynamics of Contacting Thermoelastic Bodies. New York: Springer Varlag; 2009.
10. Saint-Venant BD. Sur le choc longitudinal de deux barres élastiques. J. de Math. (Liouville) Sér. 2. 1867;12:237-276. http://portail.mathdoc.fr/JMPA/afficher_notice.php?id=JMPA_1867_2_12_A16_0
11. Hertz H. Über die Berührung fester elastischer Körper [in German]. Journal für die reine und angewandte Mathematik. 1881;92:156-171.
12. Boussinesq VJ. Application des potentiels a l'étude de l'équilibre et du movement des solides élastiques. Paris: Gauthier-Villars, Imprimeur-Libraire; 1885.
13. Johnson KL. Contact mechanics. Cambridge: Cambridge University Press; 1985.
14. Sears JE. On the longitudinal impact of metal rods with rounded ends. Proc. Cambridge Phil. Soc. 1908;14:257-286.
15. Hunter SC. Energy absorbed by elastic waves during impact. J. Mech. Phys. Solids. 1957;5:162-171.
16. Andersson M., Nilsson F. A perturbation method used for static contact and low velocity impact. Int. J. Impact Eng. 1995;16:759-775.
17. Timoshenko SP, Young DH, Weaver WJr. Vibration Problems in Engineering. New York: Wiley. 1974.
18. Popov SN. Impact of a rigid ball onto the surface of an elastic half-space. Soviet Applied Mechanics. 1990;26(3):250-256.
19. Kubenko VD. Impact of blunted bodies on a liquid or elastic medium. International Applied Mechanics. 2004;40(11):1185-1225.
20. Argatov II. Asymptotic modeling of the impact of a spherical indenter on an elastic half-space. International Journal of Solids and Structures. 2008;45:5035-5048.
21. Argatov II. Fadin YA. Excitation of the Elastic Half-Space Surface by Normal Rebounding Impact of an Indenter. Journal of Friction and Wear. 2009;30(1):1-6.
22. Argatov I, Jokinen M. Longitudinal elastic stress impulse induced by impact through a spring-dashpot system: Optimization and inverse. International Journal of Solids and Structures. 2013;50:3960-3966.
23. Goldsmith W. Impact: The Theory and Physical Behavior of Colliding Solids. London: Edward Arnold Ltd.; 1960.
24. Yang Y, Zeng Q, Wan L. Contact response analysis of vertical impact between elastic sphere and elastic half space. Shock Vib. 2018; vol. 2018: 1802174.
25. Ruta P, Szydło A. Drop-weight test based identification of elastic half-space model parameters. Journal of Sound and Vibration. 2005;282:411-427.
26. Qu A, James DL. On the impact of ground sound. Proceedings of the 22nd International Conference on Digital Audio Effects (DAFx-19), Birmingham, UK, September 2–6, 2019.2019:1-8.
27. Lamb H. On the propagation of tremors over the surface of an elastic solid. Philos. Trans. R. Soc. London. Ser. A. 1904;203:1-42.
28. Mooney HM. Some numerical solutions for Lamb's problem. Bulletin of the Seismological Society of America. 1974; 64 (2):473-491.
29. Cagniard L. Rêflextion et rêfraction des ondes sêismiques progressives, Gauthier-Villars. 1939.
30. de Hoop AT. A modification of Cagniard's method for solving seismic pulse problems. Appl. Sci. Res. 1960; B8:349-356.
31. Sánchez-Sesma FJ, Iturrarán-Viveros U, Kausel E. Garvin's generalized problem revisited. Soil Dyn. Earthq. Eng. 2013;47:4-15.
32. Pak RYS, Bai X. Analytic resolution of time-domain half-space Green's functions for internal loads by a displacement potential-Laplace-Hankel-Cagniard transform method. Proc. R. Soc. A Math. Phys. Eng. Sci. 2020;476: 20190610.
33. Pekeris CL. The seismic surface pulse. Proc. Natl. Acad. Sci. 1955; 41(7):469-480.
34. Kausel E. Fundamental Solutions in Elastodynamics: a Compendium. Cambridge University Press; 2006.
35. Kausel E. Lamb's problem at its simplest. Proceedings of the Royal Society A: Mathematical. Physical and Engineering Sciences. 2012;469:20120462.
36. Emami M, Eskandari-Ghadi M. Lamb's problem: a brief history. Mathematics and Mechanics of Solids. 2019;25(3): 108128651988367
37. Achenbach JD. Wave Propagation in Elastic Solids. New York: Elsevier. 1973.
38. Nowacki W. Thermoelasticity. 2nd edn., PWN-Polish Scientific Publishers. 1986.
39. Smetankina NV, Shupikov AN, Sotrikhin SYu, Yareshchenko VG. A Noncanonically Shape Laminated Plate Subjected to Impact Loading: Theory and Experiment. J. Appl. Mech. 2008;75(5): 051004.
40. Awrejcewicz J, Pyryev Yu. The Saint-Venant principle and an impact load acting on an elastic half-space. Journal of Sound and Vibration. 2003;264(1):245-251.
41. Panovko YaG. Introduction to the Theory of Mechanical Shock. Moscow: Nauka. 1977 [in Russian].
42. Kulczycki-Żyhajło R, Kołodziejczyk W, Rogowski G. Selected issues of theory of elasticity for layered bodies. Acta Mechanica et Automatica. 2009;3(3):32-38.

Yuriy Pyr'yev: https://orcid.org/0000-0002-9824-2846

Andrzej Penkul: https://orcid.org/0000-0001-9855-6610

Leszek Cybula: https://orcid.org/0000-0002-8897-4779

DOI 10.2478/ama-2023-0013

CuO–WATER MHD MIXED CONVECTION ANALYSIS AND ENTROPY GENERATION MINIMIZATION IN DOUBLE-LID–DRIVEN U-SHAPED ENCLOSURE WITH DISCRETE HEATING

Bouchmel MLIKI*, Rached MIRI*, Ridha DJEBALI, Mohamed A. ABBASSI***

*Research Lab, Technology Energy and Innovative Materials, Faculty of Sciences, University of Gafsa, Gafsa 2112, Tunisia
**UR22ES12: Modeling Optimization and Augmented Engineering, ISLAIB, University of Jendouba, Beja 9000, Tunisia

bouchmelmliki@hotmail.com, rachedmiri111@gmail.com, jbelii_r@hotmail.fr, abbassima@gmail.com

received 10 August 2022, revised 14 November 2022, accepted 30 November 2022

Abstract: The present study explores magnetic nanoliquid mixed convection in a double lid–driven U-shaped enclosure with discrete heating using the lattice Boltzmann method (LBM) numerical method. The nanoliquid thermal conductivity and viscosity are calculated using the Maxwell and Brinkman models respectively. Nanoliquid magnetohydrodynamics (MHD) and mixed convection are analyzed and entropy generation minimisation has been studied. The presented results for isotherms, stream isolines and entropy generation describe the interaction between the various physical phenomena inherent to the problem including the buoyancy, magnetic and shear forces. The operating parameters' ranges are: Reynolds number ($\mathrm{Re}: 1-100$), Hartman number ($\mathrm{Ha}: 0-80$), magnetic field inclination ($\gamma: 0°-90°$), nanoparticles volume fraction ($\phi: 0-0.04$) and inclination angle ($\alpha: 0°-90°$). It was found that the N_{um} and the total entropy generation augment by increasing Re, ϕ: and γ. conversely, an opposite effect was obtained by increasing Ha and α. The optimum magnetic field and cavity inclination angles to maximum heat transfer are $\gamma = 90°$ and $\alpha = 0$.

Key words: U-shaped enclosure, MHD mixed convection, nanoliquid, double lid-driven cavity, entropy generation, LBM

1. INTRODUCTION

Nanoliquid mixed convection in different geometries has elicited attention and interest from many researchers due to its availability in nature and its numerous engineering applications including in electronic equipment cooling, polymer industry, heat exchangers, automobile radiators and space technology [1–13]. Mixed convective heat transfer in enclosures has been extensively investigated during the last decades [14–17]. Mliki et al. [14] studied mixed convection in a lid-driven square cavity filled with copper–water nanofluid. They discussed the influences of volumetric fraction of nanoparticles (ϕ), Rayleigh number (Ra) and Reynolds numbers (Re) on the fluid flow, heat transfer and S_{gen}. Their results showed that the $\mathrm{Nu_m}$ and S_{gen} augment as the Rayleigh and Reynolds numbers. Also, they found that the addition of nanoparticles in pure water leads to enhancement of heat transfer rate. The results of Sheremet and Pop [15], who considered the same problem of mixed convection of nanoliquid in a lid-driven square cavity, concluded that the heat transfer was enhanced with the Richardson number. Besides, Nayak et al. [16] found that the addition of nanoparticles leads to enhancement of $\mathrm{Nu_m}$ for the mixed convection of Cu–water nanoliquid in a differentially heated cavity. Similarly, Sourtiji et al. [17] examined the mixed convection of nanoliquid in a ventilated cavity. Their results showed that the $\mathrm{Nu_m}$ augments with an increase in Reynolds number (Re), Richardson number (Ri) and nanoparticle volume fraction (ϕ). Additional papers on nanofluid mixed convection in cavities can also be found in the literature [18–21]. Aljabair et al. [20] reported a problem of mixed convection in a sinusoidal lid-driven cavity with non-uniform temperature distribution on the wall utilising nanofluid. Their results showed that heat transfer rate augments as the volumetric fraction of nanoparticles *(ϕ),* Reynolds number (Re) and Rayleigh number (Ra).

The effect of an external magnetic field on convective heat transfer in different geometries was studied by many researchers [22–25]. Aljabair et al. [22] studied the natural convection heat transfer in corrugated annuli with H_2O–Al_2O_3 nanofluid. They reported an enhancement in heat transfer by augment of the Rayleigh number and nanoparticles volume fraction. As similar finding has been observed by Mahmoudi et al. [23], who considered the magnetic field effect on natural convection in a square cavity filled with Al_2O_3–water nanoliquid and inferred that convective heat transfer was reduced by an increase in external magnetic field intensity (Ha). In another paper, Mliki et al. [24] studied the magneto-hydrodynamic (MHD) laminar convection in a linearly/sinusoidally heated cavity with a CuO–water nanoliquid using the lattice Boltzmann method (LBM). They analysed the effect of Rayleigh number (Ra), Hartmann number (Ha), heat generation or absorption coefficient (Ra) and nanoparticle volume concentration (ϕ) on the fluid flow and heat transfer. They concluded that the heat transfer rate increased when the role of Brownian motion of nanoparticles was considered. The influence of volumetric fraction of nanoparticles (ϕ), aspect ratios (AR) and Richardson number (Ri) on heat transfer and fluid movement of a hybrid H_2O–Cu–Al_2O_3 nanofluid in a multi-lid–driven concentric trapezoidal annulus has been investigated by Alesbe et al. [25]. The results indicate that the heat transfers' skin friction increases with increase in the volume fraction of nanoparticles. Additionally, the maximum stream function value increases with increase in the

sciendo
DOI 10.2478/ama-2023-0013 acta mechanica et automatica, vol.17 no.1 (2023)

aspect ratio and the volume fraction of hybrid nanofluid.

For the case of mixed convection flows, the effect of magnetic field indifferent configurations has been extensively investigated [26–29]. Hussain et al. [26] studied the mixed convection and S_{gen} in a two-dimensional double-lid–driven square cavity. They discussed the influences of volumetric fraction of nanoparticles (ϕ), Reynolds numbers (Re), Hartman number (Ha), Richardson number (Ri) and inclined magnetic field (γ) on the fluid flow, heat transfer and S_{gen}. The results indicate that the heat transfers and S_{gen} augment with the Richardson number (Ri) and Reynolds number (Re). Also, they concluded that with the increment in the solid volume fraction of nanofluids (ϕ), S_{gen} decreases. Shirvan et al. [27] numerically analysed the MHD effect on a mixed convection in a ventilated square cavity. Their results showed that the heat transfer rate augments as the Hartmann number (Ha) increases. Pordanjani and Aghakhani [28] examined the natural convection and irreversibilities between two inclined concentric cylinders in the presence of a uniform magnetic field and radiation. They observed that the thermal performance and irreversibilities have increasing pursuant to the Rayleigh number, hot pipe diameter and addition of more nanopowder. In another paper, Aghakhani et al. [29] have discussed the entropy generation and exergy analysis of Ag–MgO/water hybrid nanofluid within a circular heatsink with different numbers of outputs. They reported that an enhancement in the Re leads to a reduction in the exergy loss as well as the first and second law efficiencies.

Previous investigations have focused predominantly on investigating heat transfer by nanofluids mixed convectively with and without a magnetic field in regular geometries under uniform heating. In the present work, the nanoliquid mixed convection was considered with the associated S_{gen} in a double-lid–driven U-shaped enclosure with discrete heating under an external magnetic field. The interaction between the induced shear, buoyancy and magnetic forces was worthy of investigation, the objective being to evaluate its impact on the heat transfer and S_{gen} rates. Results are based on visualisation of the flow, thermal fields, local S_{gen}, Nu_m and total S_{gen}.

2. PROBLEM STATEMENT

The studied problem configuration was a two-dimensional double-lid–driven U-shaped enclosure with discrete heating and filled with nanoliquid, as illustrated in Fig. 1.

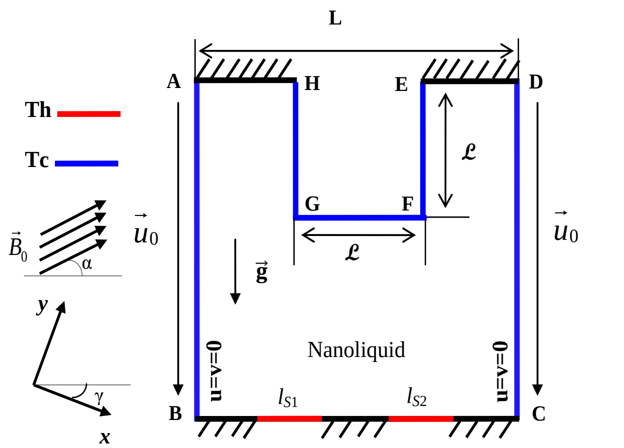

Fig. 1. Geometry of the problem

Two constant temperature heat sources of length L/5 are located at the bottom wall (Th). The walls (AB, CD, EF, FG and GH) are maintained at cold temperature Tc. The cavity aspect ratio was AR = L/L = 0.4.

The inclination of magnetic field ($\vec{B}$) and that of the cavity are γ and α, respectively. The two vertical walls (AB and DC) move downward at constant velocity Uo. Such a configuration leads to a combined and complex interaction between various effects within the cavity, including the buoyancy and shear forces and the magnetic field.

The fluid in the U-shaped enclosure is a nanoliquid (CuO–water) (Tab. 1) [30]. The density divergence in the nanoliquid was approximated by the regular Boussinesq approximation.

Tab. 1. Thermophysical properties of liquid and nanoparticles [30]

Thermophysical properties	H2O	CuO
C_p (J · kg^{-1} · K^{-1})	4,179	540
ρ (kg · m^{-3})	997.1	6,500
k (W · m^{-1} · K^{-1})	0.631	18
β × 10^{-5}(1/K)	21	0.85
σ (Ωm)$^{-1}$	0.05	2.7 · 10^{-8}

3. GOVERNING EQUATIONS

By applying a magnetic field, the governing equations for mixed convection in the two-dimensional double-lid–driven U-shaped enclosure can be obtained as follows [31]:

$$\frac{\partial U}{\partial X}+\frac{\partial V}{\partial Y}=0 \tag{1}$$

$$U\frac{\partial U}{\partial X}+V\frac{\partial U}{\partial Y}=-\frac{\partial P}{\partial X}+\frac{1}{Re}\frac{\rho_f}{\rho_{nf}}\frac{1}{(1-\varphi)^{2.5}}\left(\frac{\partial^2 U}{\partial X^2}+\frac{\partial^2 U}{\partial Y^2}\right)+ \frac{\rho_f}{\rho_{nf}}\frac{\sigma_{nf}}{\sigma_f}\frac{Ha^2}{Re}(V\sin\gamma\ \cos\gamma-U\cos^2\gamma)+ Ri\frac{\rho_f}{\rho_{nf}}\left(1-\varphi+\frac{(\rho\beta)_p}{(\rho\beta)_f}\right)\theta\ \sin\alpha \tag{2}$$

$$U\frac{\partial V}{\partial X}+V\frac{\partial V}{\partial Y}=-\frac{\partial P}{\partial X}+\frac{1}{Re}\frac{\rho_f}{\rho_{nf}}\frac{1}{(1-\varphi)^{2.5}}\left(\frac{\partial^2 V}{\partial X^2}+\frac{\partial^2 V}{\partial Y^2}\right)+ \frac{\rho_f}{\rho_{nf}}\frac{\sigma_{nf}}{\sigma_f}\frac{Ha^2}{Re}(U\sin\gamma\ \cos\gamma-V\cos^2\gamma)+ Ri\frac{\rho_f}{\rho_{nf}}\left(1-\varphi+\frac{(\rho\beta)_p}{(\rho\beta)_f}\right)\theta\ \cos\ \alpha \tag{3}$$

$$U\frac{\partial \theta}{\partial X}+V\frac{\partial \theta}{\partial Y}=\frac{\alpha_{nf}}{\alpha_f}\frac{1}{Re\ Pr}\left(\frac{\partial^2 \theta}{\partial X^2}+\frac{\partial^2 \theta}{\partial Y^2}\right) \tag{4}$$

where σ_{nf}, β, γ and α are the nanoliquid thermal diffusivity, the thermal expansion coefficient, inclined magnetic field and inclination angle of the cavity, respectively.

The dimensionless Sgen for the case of MHD nanoliquid mixed convection flow is given by [26]:

$$S_T=\frac{k_{nf}}{k_f}\left[\left(\frac{\partial\theta}{\partial X}\right)^2+\left(\frac{\partial\theta}{\partial Y}\right)^2\right]+ \chi\frac{\mu_{nf}}{\mu_f}\left[2\left(\frac{\partial U}{\partial X}\right)^2+2\left(\frac{\partial V}{\partial Y}\right)^2+\left(\frac{\partial U}{\partial Y}+\frac{\partial V}{\partial X}\right)^2\right] +\chi Ha^2\frac{\sigma_{nf}}{\sigma_f}(U\sin\gamma\ \ -V\cos\gamma)^2 \tag{5}$$

where Sgen,h, Sgen,v and Sgen,M are the Sgen due to heat

DOI 10.2478/ama-2023-0013

transport, Sgen due to fluid friction and Sgen due to application of the magnetic field, respectively. The irreversibility factor χ was expressed by:

$$\chi = \frac{\mu_f T_0}{k_f}\left(\frac{U_0}{T_h - T_c}\right)^2 \quad (6)$$

The average Sgen was calculated by:

$$S_{avr} = \frac{1}{V}\int_V S_T dV \quad (7)$$

where V was the total volume of the physical domain.

The dimensionless boundary conditions are calculated as follows: Cold walls AB, CD, EF, FG, GH: U = V = 0, θ = 0; Hot walls (0.2 ≤ IS1 ≤ 0.4) and (0.6 ≤ IS2 ≤ 0.8): θ = 1; Adiabatic walls (0 ≤ X < 0.2), (0.4 < X < 0.6) and (0.8 < X ≤ 1): $\partial T/\partial Y = 0$.

The local and integral Nu along the two heat sources (IS1, IS2) can be obtained as:

$$Nu = -\frac{k_{nf}}{k_f}\left(\frac{\partial\theta}{\partial Y}\right)\Big|_{Y=0} \quad (8)$$

$$\overline{Nu}_{I_{S_1}} = \int_{0.2}^{0.4} Nu\, dX \quad , \quad Nu_{I_{S_2}} = \int_{0.6}^{0.8} Nu\, dX \quad (9)$$

Effective density, specific heat capacity, thermal expansion coeffi-cient and thermal diffusivity of the nanoliquid are, respectively, expressed as follows [32, 33]:

$$\rho_{nf} = (1-\varphi)\rho_f + \varphi\rho_p \quad (10)$$

$$(\rho C_p)_{nf} = (1-\varphi)(\rho C_p)_f + \varphi(\rho C_p)_p \quad (11)$$

$$(\rho\beta)_{nf} = (1-\varphi)(\rho\beta)_f + \varphi(\rho\beta)_p \quad (12)$$

$$\alpha_{nf} = \frac{k_{nf}}{(\rho C_p)_{nf}} \quad (13)$$

The thermal conductivity and the electrical conductivity of the nanoliquid are, respectively, calculated as follows [34, 35]:

$$k_{static} = k_f \frac{k_P + 2k_f - 2\varphi(k_f - k_P)}{k_P + 2k_f + \varphi(k_f - k_P)} \quad (14)$$

$$\frac{\sigma_{nf}}{\sigma_f} = 1 + \frac{3\left(\frac{\sigma_s}{\sigma_f} - 1\right)\varphi}{\left(\frac{\sigma_s}{\sigma_f} + 2\right) - \left(\frac{\sigma_s}{\sigma_f} - 1\right)\varphi} \quad (15)$$

Nanoliquid effective dynamic viscosity was calculated using the Brinkman model [36]

$$\mu_{static} = \frac{\mu_f}{(1-\varphi)^{2.5}} \quad (16)$$

4. NUMERICAL METHOD

4.1. Brief introduction to LBM

The LBM was based on Ludwig Boltzmann's kinetic theory of gases. The fundamental idea is that gases/fluids can be a large number of small particles moving with random motions. The exchange of momentum and energy is achieved through particle streaming and collision.

The dimensionless equations were solved by using LBM, which employs Boltzmann's kinetic theory of gases [26]. By Bhatnagar–Gross Krook approximation, LBM was based on two distribution functions g and f of the temperature and flow fields in this study, respectively.

$$f_i(x + c_i\Delta t, t + \Delta t) = f_i(x,t) - \frac{1}{\tau_v}\left(f_i(x,t) - f_i^{eq}(x,t)\right) + \Delta t c_i F_i \quad (17)$$

$$g_i(x + c_i\Delta t, t + \Delta t) = g_i(x,t) - \frac{1}{\tau_a}\left(g_i(x,t) - g_i^{eq}(x,t)\right) \quad (18)$$

where Δt denotes the lattice time, lattice relaxation time for the flow and temperature fields, respectively. Two local equilibrium distribution functions for the temperature and flow fields g_i^{eq} and f_i^{eq} are calculated with Eqs (19) and (20) [37]:

$$f_i^{eq} = w_i r\left[1 + \frac{3(c_i.u)}{c^2} + \frac{9(c_i.u)^2}{2c^4} - \frac{3u^2}{2c^2}\right] \quad (19)$$

$$g_i^{eq} = w_i' T\left[1 + 3\frac{c_i.u}{c^2}\right] \quad (20)$$

The nine velocities (D2Q9) lattice model (Fig. 2) was used in the present study with a uniform grid size of dx = dy for simulating the steady MHD mixed convection of nanoliquid.

According to this model, the weighting factors wi and the discrete particle velocity vectors ci can be defined as follows [38]:

$$w_0 = \frac{4}{9}, w_i = \frac{1}{9} for i = 1,2,3,4 \quad and \quad w_i = \frac{1}{36} \; for \;\; i = 5,6,7,8 \quad (21)$$

$$c_i = \begin{cases} 0 & i = 0 \\ (cos[(i-1)\pi/2], sin[(i-1)\pi/2])c & i = 1,2,3,4 \\ \sqrt{2}(cos[(i-5)\pi/2 + \pi/4], sin[(i-5)\pi/2 + \pi/4])c & i = 5,6,7,8 \end{cases} \quad (22)$$

Finally, macroscopic variables (ρ, u and T) are calculated using the following equations:

$$\rho = \sum_i f_i, \qquad \rho u = \sum_i f_i \mathbf{c_i}, \qquad T = \sum_i g_i \quad (23)$$

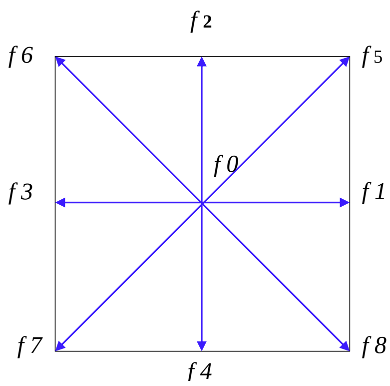

Fig. 2. Direction of streaming velocities, D2Q9

5. MESH VERIFICATION AND VALIDATION

Tab. 2 shows the calculated Num at different mesh sizes for the case: nanoliquid (Cu–water) with Re = 50; Ri = 20; ϕ = 0.04; Ha = 30; α = 45°; and γ = 0 (50 × 50, 75 × 75, 100 × 100 and 150 × 150 nodes). It was found that the variation of the Num between 100 × 100 and 150 × 150 grids was <0.005095. However, for all calculations in this numerical study, the 100 × 100 uniform grid was employed.

Tab. 2. Grid independence test for Re = 50; Ri = 20; $\phi = 4 \cdot 10^{-2}$; Ha = 30; α = 45°; and γ = 0

Grid size	$\overline{Nu}_{ls_1}$	$\overline{Nu}_{ls_2}$
50 × 50	3.910183	4.072377
75 × 75	4.232592	4.389502
100 × 100	4.418533	4.575598
150 × 150	4.510627	4.580693

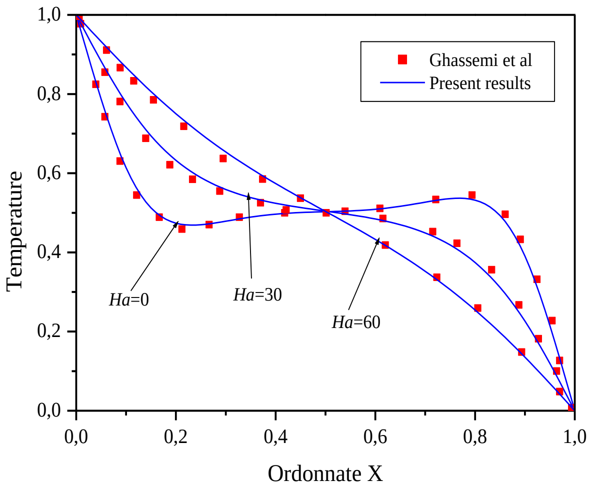

Fig. 3. Comparison of the temperature on axial midline between the present results and numerical results by Ghasemi et al. [39] (ϕ = 3 · 10–2 and Ra = 105)

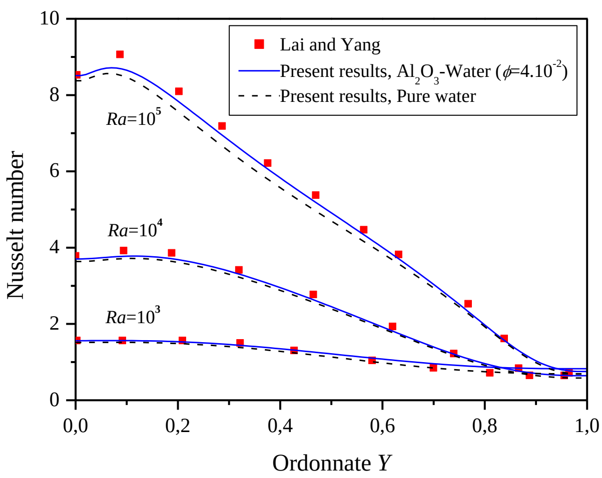

Fig. 4. Comparison of the local Nusselt number along the hot wall between the present results and numerical results by Lai and Yang [40]

For the validation of data, the present results are compared with the numerical results obtained by Ghasemi et al. [39] for the case of magnetic nanoliquid convection in a square enclosure (Fig. 3). In addition, a comparison of the local Nusselt number along the hot wall was made between the present results and the numerical results provided Lai and Yang [40] for the case of nanoliquid natural convection in a square enclosure (Fig. 4). The present numerical results have been also compared with those of Talebi et al. [41] for the case of mixed convection in a square lid-driven cavity (Fig. 5). Based on the aforementioned comparisons, the developed code was judged to be reliable for studying the MHD mixed convection of a nanoliquid confined in a double-lid–driven U-shaped enclosure with discrete heating under the effect of an external magnetic field.

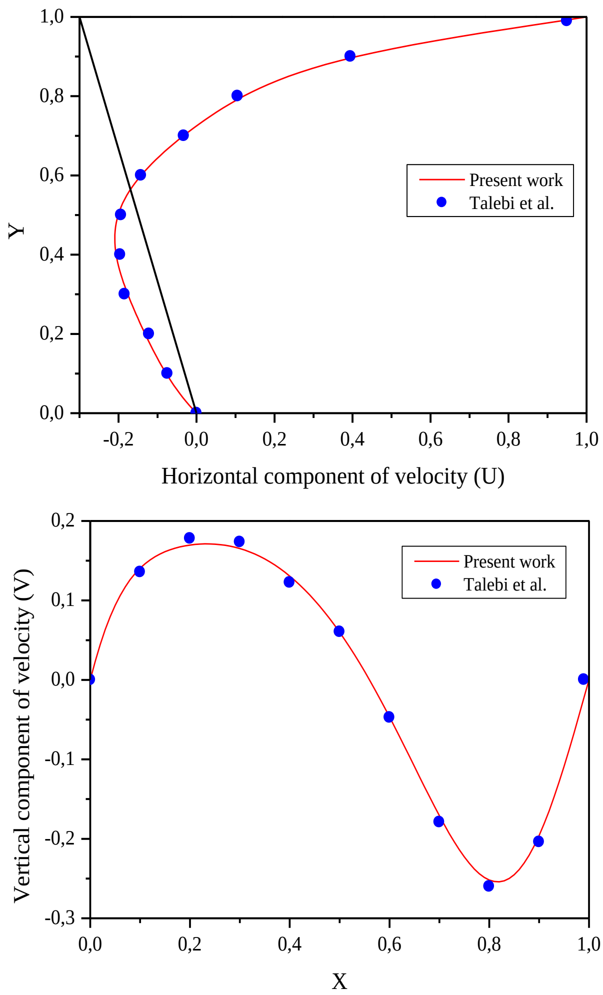

Fig. 5. Comparison of (a) horizontal component of velocity and (b) vertical component of velocity with those of de Talebi et al. [41] (Re = 100 and Ra = 1.47 · 104)

6. RESULTS AND DISCUSSION

The problem of two-dimensional MHD mixed convection in a double-lid–driven U-shaped enclosure containing a CuO–water nanoliquid was studied. The cavity aspect ratio was fixed at AR = 0.4. The effects of Reynolds number (1 ≤ Re ≤ 100), volume fraction of nanoparticles ($0 \leq \phi \leq 4 \cdot 10^{-2}$), Hartmann number (0 ≤ Ha ≤ 80), inclined magnetic field (0 ≤ γ ≤ 90°) and inclination angle of the cavity (0 ≤ α ≤ 90°) on the streamlines, local Sgen and heat transfer characteristics have been revealed.

6.1. Ifluuence of Reynolds number

Isotherms, local Sgen and streamlines of CuO–water nanoliquid for various Reynolds numbers are presented in this primary part of the numerical study for Ri = 30, γ = α = 0, Ha = 0 and ϕ = 0.04.

As can be seen from the streamlines in Fig. 6, for all Reynolds numbers, the flow structure, temperature contours and Sgen are

DOI 10.2478/ama-2023-0013

symmetrical about the vertical centerline (X = 0.5) of the heated U-shaped enclosure and are concentrated along the two heated sources (IS1 and IS2) due to enhanced fluid movement in these regions. Physically, this was true owing to the symmetrical boundary conditions about the horizontal X-axis (X = 0.5).

For low Reynolds numbers (Re = 1 and Re = 10), the fluid was well circulated in the top part of the cavity, and similarly for the density of the temperature distribution contours and local Sgen near the adiabatic walls (AH–ED). Moreover, the increase of the Reynolds number (Re = 50 and Re = 100) results in pushing the cold nanoliquid to the bottom corners (B and C), and consequently, the temperature patterns are compressed adjacently to the discrete heat sources (IS1 and IS2). This was a good reason for the increase in the value of the maximum stream function $|\psi|_{max}$ and the formation of active regions for Sgen. The cause of these changes was due to the increasing of heat transfer by the buoyancy force.

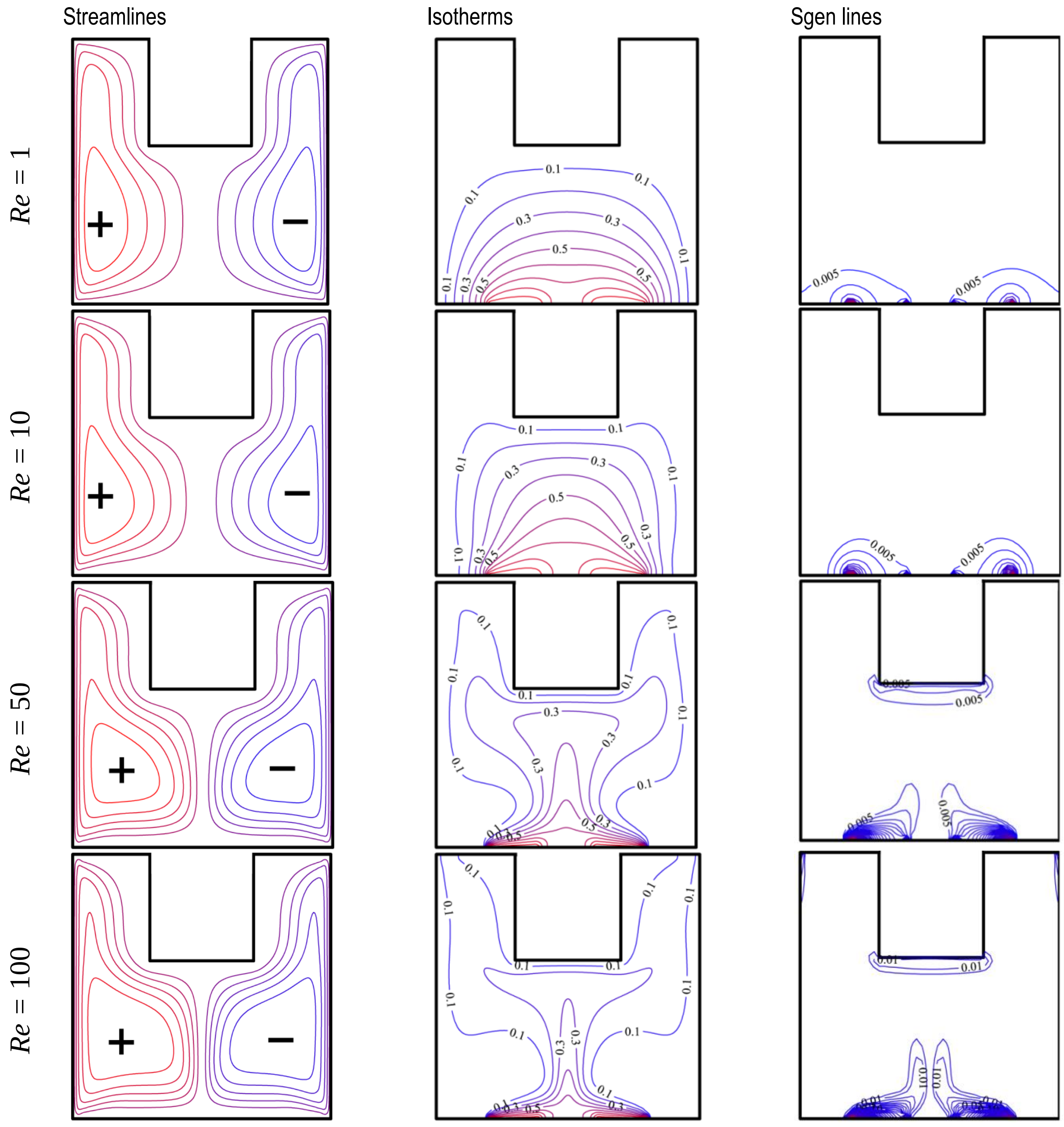

Fig. 6. Streamlines, isotherms and Sgen lines for different Re at Ri = 20, γ = α = 0, Ha = 30 and $\phi = 4 \cdot 10^{-2}$

The effect of the Reynolds number on Sgen is shown in Tab. 3. It was observed that Sgen increases with an increase in Re due to the following factors: heat transfer SHT, fluid friction SFF, magnetic field SMF and total ST increase with an increase in Re. From this table, we may observe that the effect due to fluid friction and magnetic field has been negligible in comparison with that due to the heat transfer.

Tab. 3. Reynolds number effect on SHT, SFF, SMF and S at Ri = 20, γ = α = 0, Ha = 30 and ϕ = 0.04

	Re **= 1**	***Re*** **= 10**	***Re*** **= 50**	***Re*** **= 100**
S_{HT}	2.75	3.44	9.13	12.2
S_{FF} (10^{-3})	2.91	3.06	3.31	3.77
S_{MF} (10^{-4})	4.33	4.49	5.23	5.84
S_T	2.753	3.443	9.133	12.204

Fig. 7a,b show the dependence of Num and total Sgen on the Reynolds numbers and solid concentration. By examining Eqs (14) and (21), an increase in solid concentration leads to a rise in the effective thermal conductivity. Accordingly, the maximum value of the Num and total Sgen are obtained at the maximum volumetric fraction of nanoparticles. In the case of low Reynolds numbers (Re=1 and Re=10), an increase in the solid concentration does not change the average Sgen and total Sgen. It was further observed that with the increase of the Reynolds number to Re = 50 and Re = 100, the difference between Nu (ϕ = 0) and Nu (ϕ = $4 \cdot 10^{-2}$) became faster. The variation of the total Sgen appears to be similar to the variation of Num; it was found to be increased by 11.65% when the volume fraction of nanoparticles passed from 0 to $4 \cdot 10^{-2}$ for Re = 100.

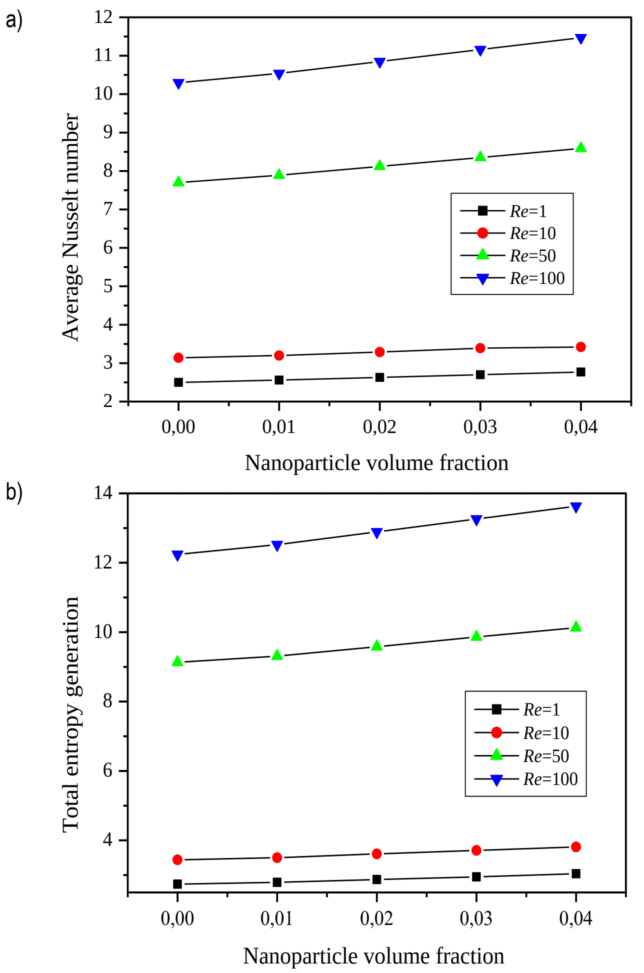

Fig. 7. Num (a) and total Sgen (b) for different values of the Reynolds numbers and volumetric fraction of nanoparticles at Ri = 20, γ = α = 0 and Ha = 30

6.2. Influence of Hartmann number

By an increase in Hartmann number (Ha), which results in a notable deterioration of the heat transfer. In fact, this can be explained by the fact that the effect of Lorentz force was opposite to the buoyancy force. It was observed that the increase in Hartmann number leads to a reduction of the flow intensity. The maximum values of the stream function equal $1.49 \cdot 10^{-1}$, $4.86 \cdot 10^{-1}$ and $2.78 \cdot 10^{-1}$ when those for Ha equal 0, 40 and 80, respectively. This can justify the observed decrease of the fluid motion and velocity. However, we note that the temperature distribution contours near the hot discrete sources are reduced as a result of the increase in the Lorentz forces. So, the presence of a magnetic field leads to substantial mixed convection flow dumping. The Ha effect on the local Sgen is displayed in Fig. 8. Increasing Hartmann number causes a reduction in the density of the local Sgen contours near the hot discrete sources. Accordingly, low Sgen values are obtained for high Ha values.

Fig. 9 (a,b) shows values of the Num and the total Sgen in the same conditions of Fig. 8 for various Hartmann numbers. The Num shown in Fig. 9(a) decreases by an increase in Hartmann number. We can explain the decrease of Num by referring to Eq. (9), which indicates that the effect of Lorentz force due to the application of an external magnetic field on heat transfer was opposite to the buoyancy force, and consequently, decreases the temperature gradients near the two heated sources (IS1 and IS2). Fig. 9(b) shows also that the behaviour of the total Sgen was similar to that of the Num.

The profiles of the dimensionless temperature in the heated U-shaped enclosure at y/L = 0.25 and y/L = 0.5 are depicted in Fig. 10(a,b). One can observe that the temperature in the U-shaped enclosure decreases by an increase in Hartmann number due to the reduction of the fluid movement and energy transferred by the discrete heat sources (IS1 and IS2). This explains the stagnation of the nanoliquid near the bottom part of the cavity for Ha = 80.

6.3. Influence of inclined magnetic field

The effects of a tilted magnetic field on the streamlines, isotherms and Sgen contours for inclination angles 0°, 30°, 60° and 90° are presented in Fig. 11. In the case of horizontal magnetic field (γ = 0), it can be seen that the streamlines contours are more clustered in the middle part of the U-shaped enclosure and are symmetrical about the vertical centreline (X = 0.5). Similarly, the temperature contours and Sgen are symmetrically distributed to the vertical centreline (X = 0.5). As γ increases to 30° and 60°, the circulation cell that was confined inside the right vertical portion of the U-shaped enclosure becomes stronger and the thermal boundary layer near the left moving walls (DE) becomes thicker. Moreover, as inclination angle α increases, the density of the Sgen distribution contours in the right part of the U-shaped enclosure grows. This is an indication of a higher heat transfer rate in this region. Finally, for γ = 90°, the flow, temperature contours and local Sgen are horizontally symmetric of the cavity and are concentrated along the two sources (IS1 and IS2). Consequently, the maximum heat flow occurs in the centre of the U-shaped enclosure.

Fig. 12 shows the impact of the inclination angle of magnetic field on Num. It was observed that at γ = 0; 90°, Num along the two heat sources (IS1, IS2) was the same. Num along the left heat source (IS1) decreases for γ ranging from 0° to 45° and then it decreases for γ = 60°–90°. On the other hand, the average heat transfer coefficient along the right heat source (IS2) increases considerably with increasing γ. This increase reaches 9.4% when γ changes from 0° to 90°. The Num maximum occurs at γ = 90°.

The effect of inclination angle of magnetic field on total Sgen is presented in Fig. 13. It was shown that the total Sgen slightly increases with the inclination angle for γ <45°. If the inclination angle was increased to 90°, the difference between ST (γ = 90°) and ST (γ = 0) becomes smaller. Consequently, a significant

DOI 10.2478/ama-2023-0013

effect of the inclination angle on the Sgen can be found for γ >45°.

6.4. Influence of inclination angle of the U-shaped enclosure

In this part, calculations are made for different inclination angles of the U-shaped enclosure α (Fig. 14). The volumetric fraction of nanoparticles was taken as $\phi = 4 \cdot 10^{-2}$, limiting the value of the validity of the Maxwell model.

For α = 0, two counter-rotating symmetric cells are formed inside the U-shaped cavity. Also, it was noticed that the temperature contours and Sgen are symmetrically distributed about the vertical centreline (X = 0.5) of the heated U-shaped enclosure. As γ increases, the circulation vortex that exists inside the left vertical portion of the cavity becomes stronger. The temperature patterns are compressed adjacently to the left moving walls (DE), and consequently, the density of the Sgen distribution grows in this region.

The effect of inclination angle of the U-shaped enclosure on the Num is depicted in Fig. 15. It was noticed that at γ = 0, the Num along the two heat sources (IS1, IS2) was the same. As α increased from 0° to 60°, the heat transfer due to left heat source S1 was enhanced. Conversely, an opposite effect associated with the Num behaviour can be found with an inclination angle of γ >60°. On the other hand, the heat transfer due to right heat source S2 decreases considerably with increasing γ. Generally, increasing α causes an increase of the Num, and consequently enhances the heat transfer process. The maximum value of the Num was 8.08 and occurs for α = 0. The variation of the total Sgen was similar to the variation of Num (Fig. 16).

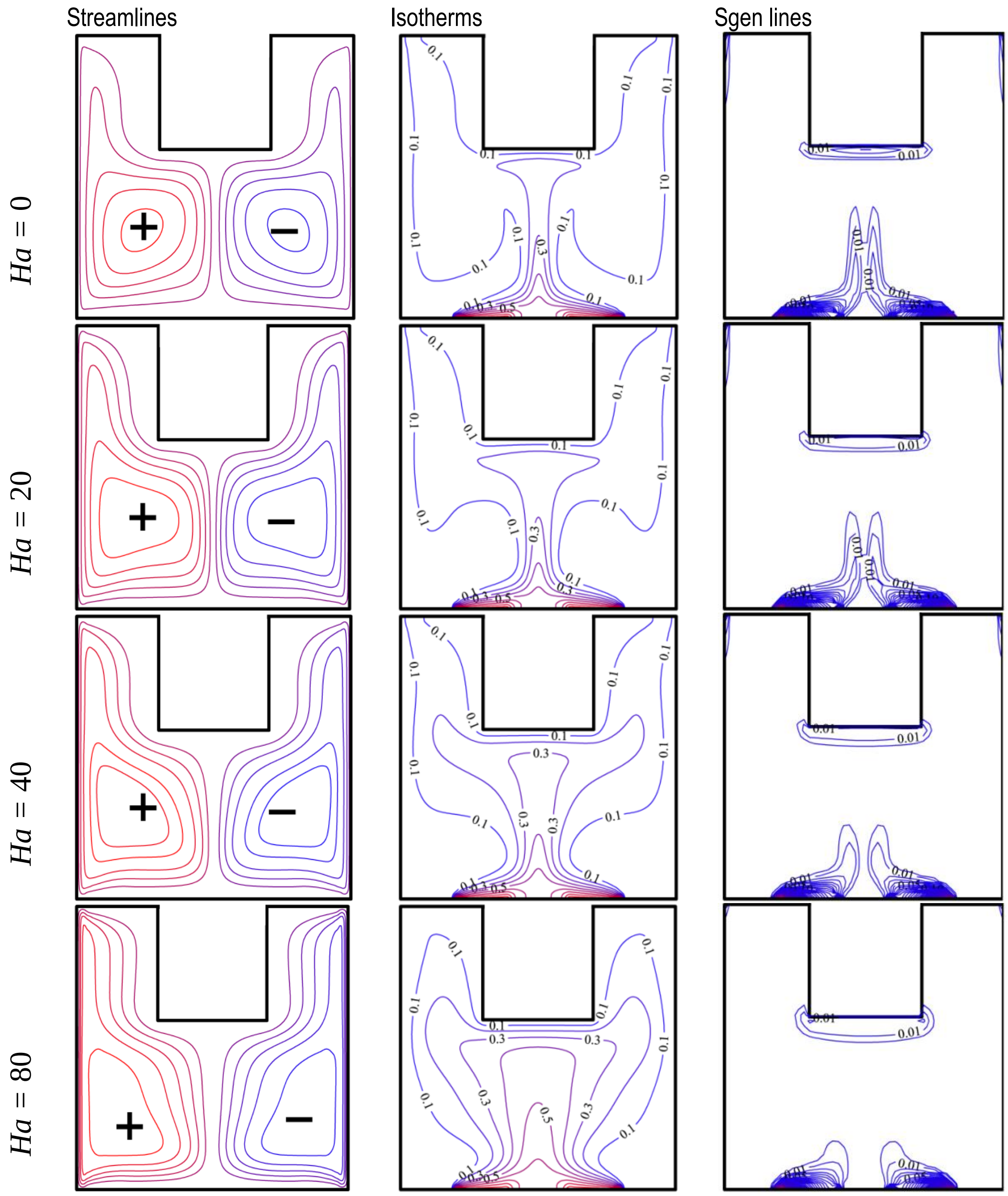

Fig. 8. Streamlines, isotherms and Sgen lines for different Ha at Re = 100, Ri = 20, γ = α = 0 and $\phi = 4 \cdot 10^{-2}$

DOI 10.2478/ama-2023-0013
acta mechanica et automatica, vol.17 no.1 (2023)

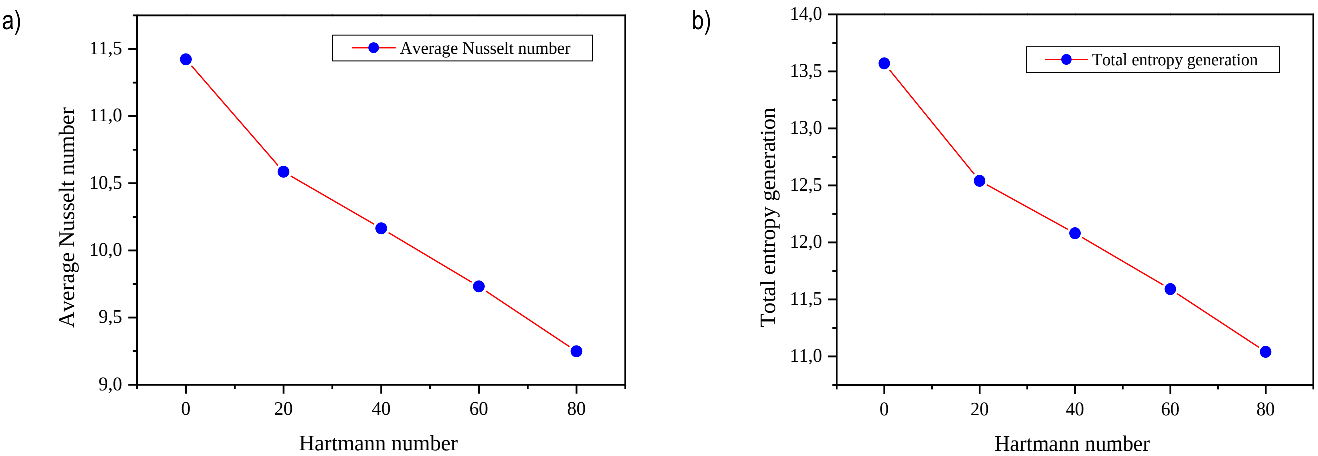

Fig. 9. Num (a) and total Sgen (b) for different values of Hartmann number at Re = 100, Ri = 20, γ = α = 0 and ϕ = 4 · 10^{-2}

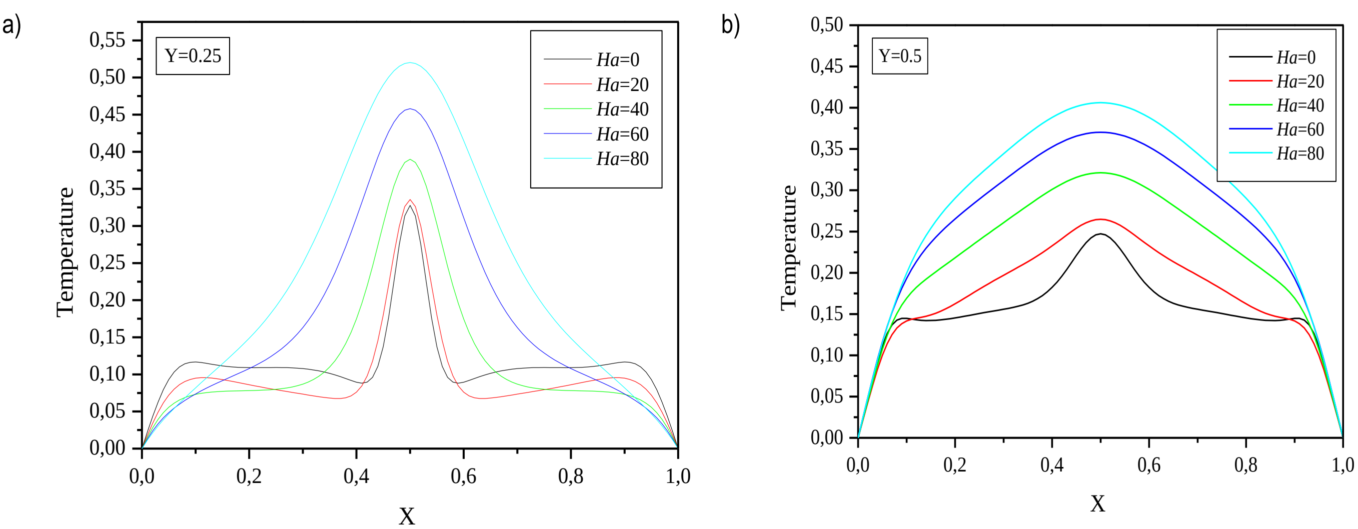

Fig. 10. Temperature variation in the middle of the cavity (a) Y = 0.25 and (b) Y = 0.5 for different values of Hartmann number at Re = 100, Ri = 20, γ = α = 0 and ϕ = 4 · 10^{-2}

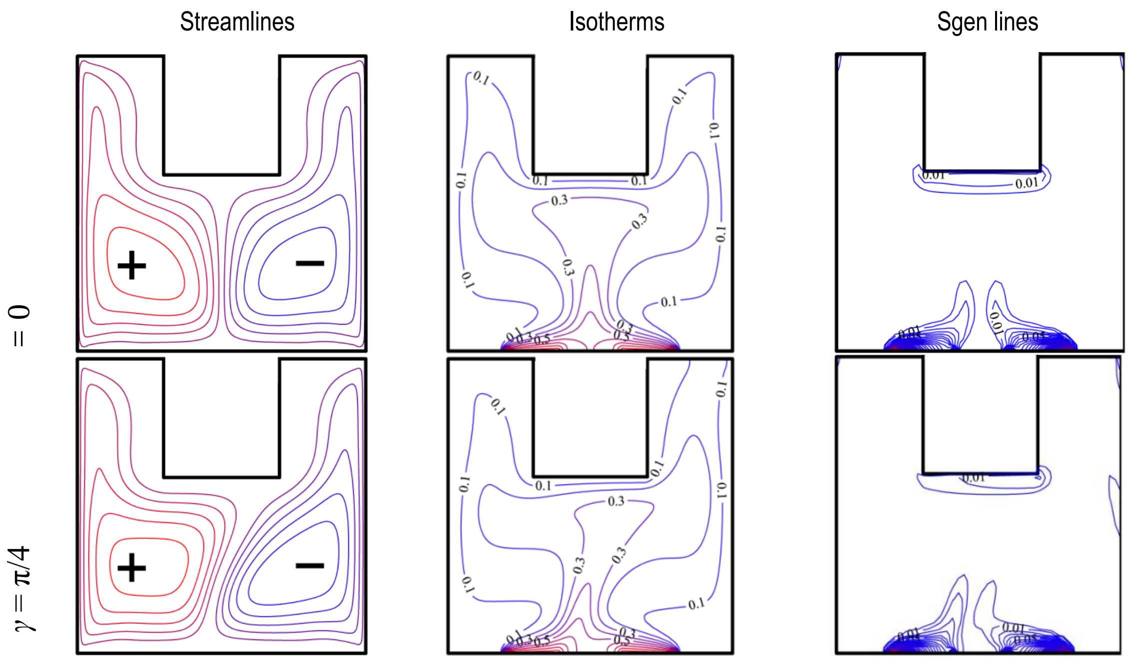

DOI 10.2478/ama-2023-0013

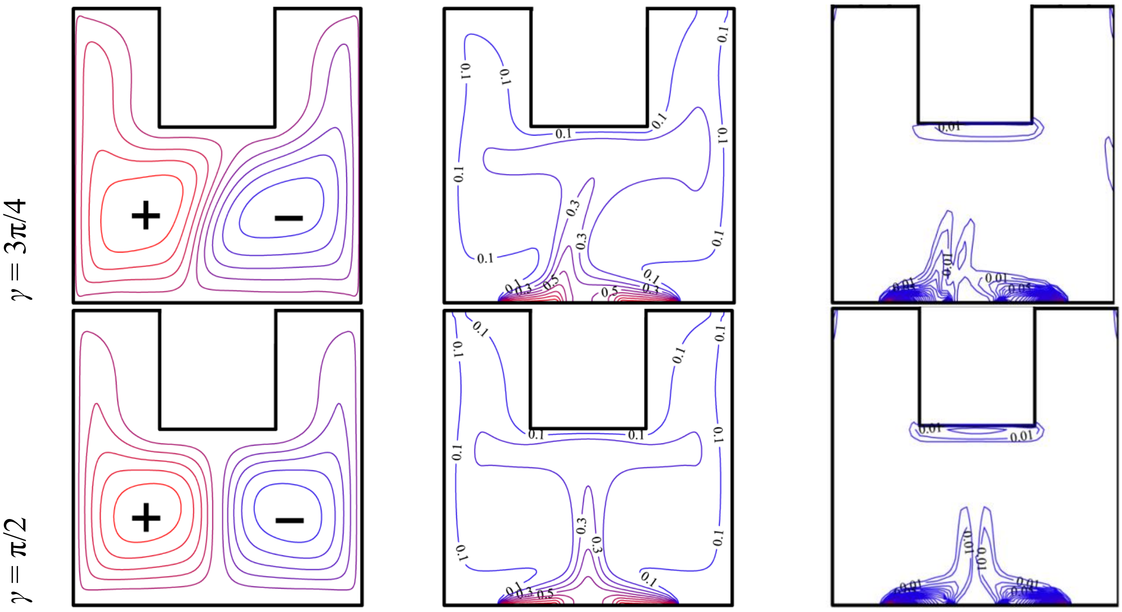

Fig. 11. Streamlines, isotherms and Sgen lines for different γ at α = 0, Re = 50, Ri = 20, Ha = 0 and $\phi = 4 \cdot 10^{-2}$

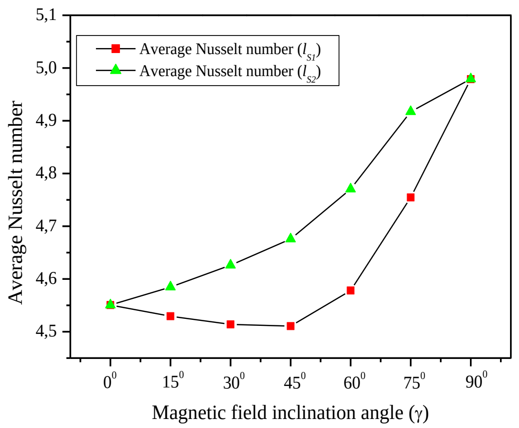

Fig. 12. Num for different γ at α = 0, Re = 50, Ri = 20, Ha = 0 and $\phi = 4 \cdot 10^{-2}$

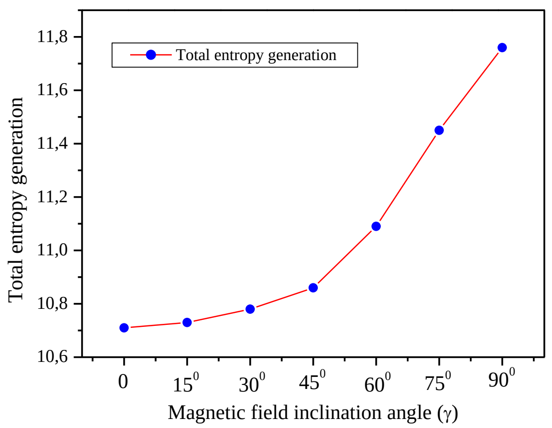

Fig. 13. Total Sgen for different γ at α = 0, Re = 50, Ri = 20, Ha = 0 and $\phi = 4 \cdot 10^{-2}$

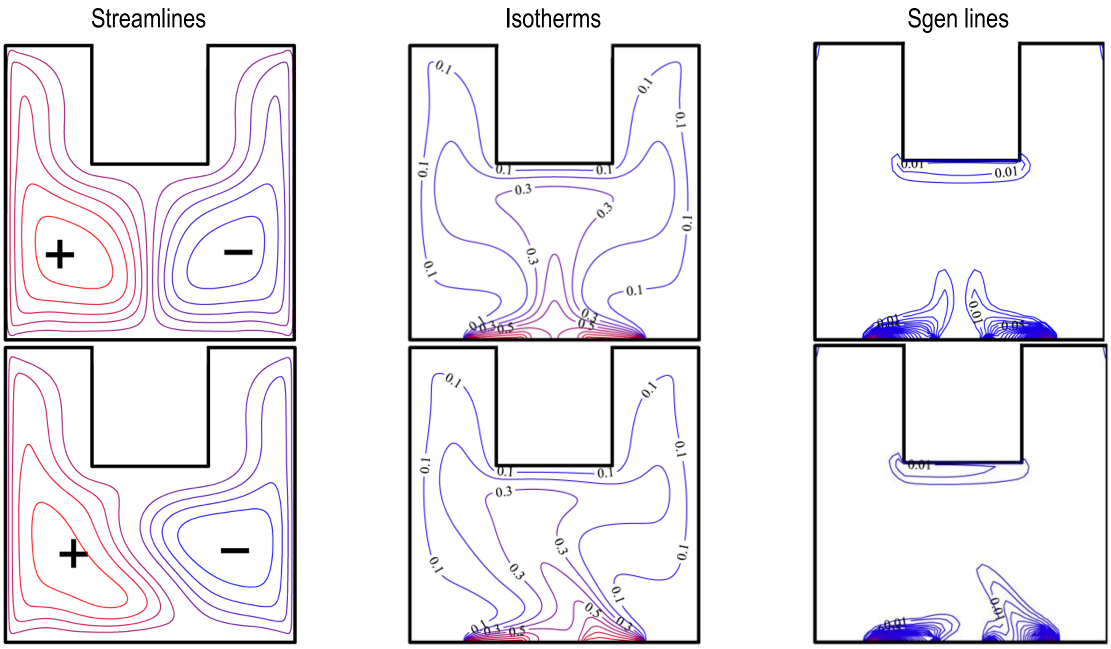

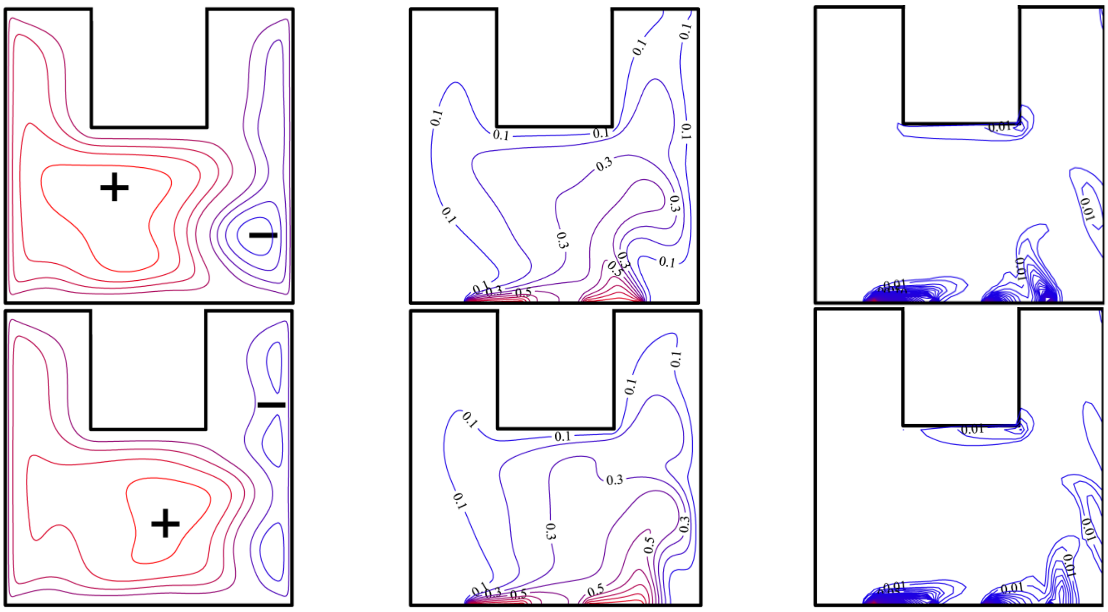

Fig. 14. Streamlines, isotherms and Sgen lines for different α at γ = 0, Re = 50, Ri = 20, Ha = 0 and $\phi = 4 \cdot 10^{-2}$

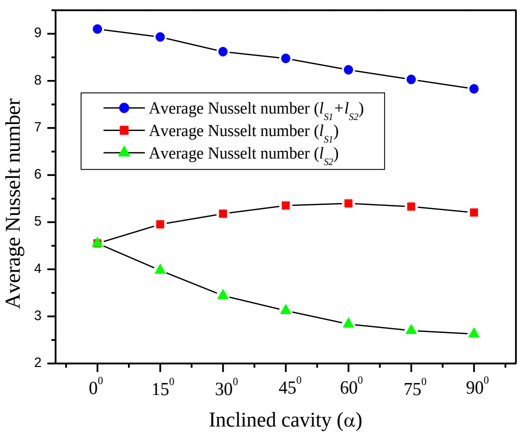

Fig. 15. Num for different α at γ = 0, Re = 50, Ri = 20, Ha = 0 and $\phi = 4 \cdot 10^{-2}$

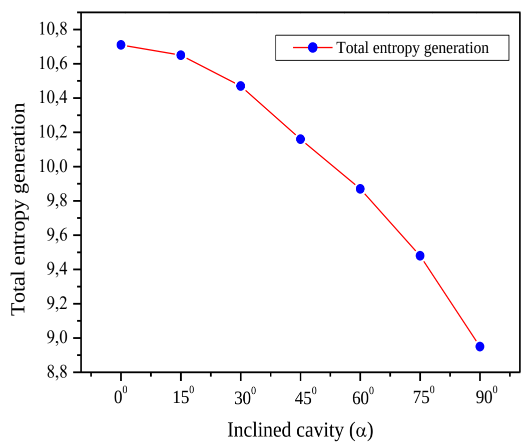

Fig. 16. Total Sgen for different α at γ = 0, Re = 50, Ri = 20, Ha = 0 and $\phi = 4 \cdot 10^{-2}$

7. CONCLUSIONS

The novelty of this research consists in the fact that it identifies, and briefly discusses, the physics parameters that have the greatest influence on MHD mixed convection heat transfer of magnetic nanoliquid (CuO/H2O) in a double-lid–driven U-shaped enclosure with discrete heating. Shortly, I will study the impact of the radiation and electric field effects on the unsteady mixed convection three-dimensional stagnation.

Key findings from this numerical study can be summarised as following:

Complex interaction between the various physical phenomena characterising this problem including the natural convection, the shear forces and the magnetic field has been observed.

The Num and the total Sgen augment with Re, ϕ and γ. On the contrary, they decrease with Ha and α.

The maximum value of |ψ|max was obtained for Re = 100.

The maximum heat flow occurs in the centre of the U-shaped enclosure.

The maximum value of |ψ|max was in an indirect relation with Hartmann number.

The optimum magnetic field and U-shaped enclosure inclination angles to maximise heat transfer are γ = 90° and α = 0.

Besides, the excellent utility and effectiveness of the LBM have been demonstrated through our experiences pertaining to its use for the investigation of several CFD and CHT problems, such as turbulent atmospheric plasma spraying jets [42–44], natural convection in confined media in regular and irregular polygons using different LBM models [45–48], MHD and porous media [49–51] and boundary layers flows [52], as well as micro flows in slip regimes [53]. Our future research works will focus on the study of pulsed and turbulent flows using the LBM method. Such problems and conditions can improve the energy efficiency of small-scale systems.

Nomenclature:

B	Magnetic field (Tesla = N/[A · m^2])
c	Lattice speed
c_s	Speed of sound

c_i	Discrete particle speed
c_p	Specific heat (J · kg^{-1} · K^{-1})
F_i	External forces (N)
Ha	Hartmann number
k	Thermal conductivity (W · m^{-1} · K^{-1})
Nu_m	Average Nusselt number
Nu	Local Nusselt number
P	Pressure (Pa)
Pr	Prandtl number
Ra	Rayleigh number
S_{gen}	Entropy generation
Re	Reynolds number
Ri	Richardson number
T	Temperature (K)
u	Horizontal component of velocity (m · s–1)
v	Vertical component of velocity (m · s–1)
x, y	Lattice coordinates (m)
L	Height of cavity (m)
	Greek letters
α	Thermal diffusivity (m2 · s–1)
β	Thermal expansion coefficient (K–1)
ϕ	Solid volume fraction
μ	Dynamic viscosity (kg · m–1 · s–1)
ρ	Fluid density (kg · m–3)
θ	Dimensionless temperature
ν	Kinematic viscosity (m2 · s–1)
σ	Electrical conductivity (Ωm)–1
ψ	Stream function (m2 · s–1)
	Subscripts
Tc	Cold temperature
Th	Hot temperature

REFERENCES

1. Khan J A, Mustafa M, Hayat T, Alsaedi A. Three-dimensional flow of nanofluid over a nonlinearly stretching sheet: An application to solar energy. Int. J. Heat Mass Transfer. 2015; 86:158-164.
2. Ganvir B, Walke V, Kriplani M. Heat transfer characteristics in nanofluid-A review. Rene. Sust. Energy Reviews. http://dx.doi.org/10.1016/j.rser.2016.11.010
3. Bigdeli MB, Fasano M, Cardellini A, Chiavazzo E, Asinari P. A review on the heat and mass transfer phenomena in nanofluid coolants with special focus on automotive applications. Rene. Sust. Energy Reviews. 2016;60:1615–1633.
4. Assel S, Shan Y, Jiyun Z, Wu J M, Leong KC. Optimization and comparison of double-layer and double-side micro-channel heat sinks with nanofluid for power electronics cooling. Applied Thermal Engineering. 2014;65:124–34.
5. Rafati M, Hamidi AA, Niaser S. Application of nanofluid in computer cooling systems (heat transfer performance of nanofluid). Applied Thermal Engineering. 2012;45:9–14.
6. Yuan LC, Chang WJ, Chieh CT. Analysis of suspension and heat transfer characteristics of Al2O3 nanofluid prepared through ultrasonic vibration. Appl Energy. 2011;88:4527–33.
7. Şahin S, Demir H. Numerical Solution Of Natural Convective Heat Transfer Under Magnetic Field Effect. Acta Mechanica et Automatica. 2019;13(1).
8. Xuan Y, Duan H, Li Q. Enhancement of solar energy absorption using a plasmonic nanofluid based on TiO2/Ag composite nanoparticles. R.S.C. Adv. 2014; 4: 16206.
9. Bhosale GH, Boiling CHF. Enhancement with Al2O3–CuO/H2O hybrid nanofluid, Int. J. Eng. Res. Technol. 2013; 2:946–50.
10. Selvakumar P, Suresh S. Use of Al2O3–Cu/water hybrid nanofluid in an electronic heat sink, IEEE Trans. Compon. Packag. Manuf. Technol. 2 (2012) 1600–7.
11. Duangthongsuk W, Wongwises S. An experimental study on the heat transfer performance and pressure drop of TiO2-water nanofluids flowing under a turbulent flow regime. Int. J. Heat Mass Transfer. 2010; 53:334–44.
12. Sundar LS, Naik MT, Sharma KV, Singh MK, Siva Reddy TC. Experimental investigation of forced convection heat transfer and friction factor in a tube with Fe3O4 magnetic nanofluid. Exp. Therm. Fluid. Sci. 2012; 37:65–71.
13. Aljabair S. Review of computational multi-phase approaches of nano-fluids filled systems. Thermal Science and Engineering Progress. 2022; 28: 101175.
14. Mliki B, Belgacem N, Abbassi M A, Kamel G, Omri A, Entropy Generation and Heat Transfer of Cu–Water Nanofluid Mixed Convection in a Cavity. Int. J. of Mech. Aero. Ind. Mecha. and Manufa. Engin. 2014; 8:2237–2143.
15. Sheremet MA, Pop I. Mixed convection in a lid-driven square cavity filled by a nanofluid: Buongiorno mathematical model. Applied Mathematics and Computation. 2015; 266: 792-808.
16. Nayak RK, Bhattacharyya S, Pop I. Numerical study on mixed convection and entropy generation of Cu–water nanofluid in a differentially heated skewed enclosure. Int. J. Heat Mass Transfer. 2015; 85: 620–634.
17. Sourtiji E, Bandpy MG, Ganji D, Hosseinizadeh S. Numerical analysis of mixed convection heat transfer of Al2O3-water nanofluid in a ventilated cavity considering different positions of the outlet port. Powder Technology. 2014; 262:71-81.
18. Toumi M, Bouzit M, Bouzit F, Mokhefi A. MHD Forced Convection Using Ferrofluid Over A Backward Facing Step Containing A Finned Cylinder. Acta Mechanica et Automatica . DOI: 10.2478/ama-2022-0009 (2021).
19. Djebali R. Mesoscopic study of mixed convection and heat transfer due to crescent shape hot source under magnetic field and Joule effect. Romanian Reports in Physics. 2021; 72: 106.
20. Ali SA , Sahira LE, Alesbe I. Mixed convection in sinusoidal lid driven cavity with non-uniform temperature distribution on the wall utilizing nanofluid. Heliyon. 2021; 7(5):06907.
21. Moumni H, Welhezi H, Djebali R, Sediki E. Accurate finite volume investigation of nanofluid mixed convection in two-sided lid driven cavity including discreteheat sources. Applied Mathematical Modelling. 2015; 39 : 4164-4179.
22. Aljabair S, Mohammed AA, Alesbe I. Natural convection heat transfer in corrugated annuli with H2O-Al2O3 nanofluid. 2020; 6(11): e05568A.
23. Mahmoudi H, Pop I, Shahi M. Efect of magnetic feld on natural convection in a triangular enclosure flled with nanofuid. Int. J. of Termal Sciences. 2012; 59 :126–140.
24. Mliki B, Abbassi M A, Omri A, Zeghmati B. Effects of nanoparticles Brownian motion in a linearly/sinusoidally heated cavity with MHD natural convection in the presence of uniform heat generation/ absorption. Powder Technology. 2016; 295: 69–83.
25. Alesbe I, Ibrahim SH, Aljabair S. Mixed convection heat transfer in multi-Lid- driven trapezoidal annulus filled with hybrid nanofluid. Journal of Physics: Conference Series. 2021; 1973:012065.
26. Hussain S, Mehmood K, Sagheer M. MHD mixed convection and entropy generation of water-alumina nanofluid flow in a double lid driven cavity with discrete heating. J of Magn. and Magn. Mater. DOI: 10.1016/j.jmmm.2016.06.006, 2016.

27. Shirvan KM, Mamourian M, Mirzakhanlari S, Moghiman M. Investigation on effect of magnetic field on mixed convection heat transfer in a ventilated square cavity, Procedia Engineering 127 (2015) 1181-1188.
28. Pordanjani AH, Aghakhani S. Numerical Investigation of Natural Convection and Irreversibilities between Two Inclined Concentric Cylinders in Presence of Uniform Magnetic Field and Radiation. Heat Transfer Engineering. 2021: 1-21.
29. Aghakhania S , Pordanjani AH, Afrand M, Farsani A K, Karimi N, Sharifpur M. Entropy generation and exergy analysis of Ag–MgO/ water hybrid nanofluid within a circular heatsink with different number of outputs. International Journal of Thermal Sciences. 2023; 184: 107891.
30. Mliki B, Abbassi MA, Omri A, Zeghmati B. Lattice Boltzmann analysis of MHD natural convection of CuO-water nanofluid in inclined C-shaped enclosures under the effect of nanoparticles Brownian motion. Powder Technology. doi: 10.1016/j.powtec.2016.11.054
31. Kumar A, Singh AK, Chandran P, Sacheti NC. Effect of perpendicular magnetic field on free convection in a rectangular cavity. Sult. Qa. Uni. J. for Sc. 2015; 20(2):149-59.
32. Mliki B, Abbassi MA, Omri A, Zeghmati B. Augmentation of natural convective heat transfer in linearly heated cavity by utilizing nanofluids in the presence of magnetic field and uniform heat generation/absorption. Powder Technology. 2015; 284:312–325.
33. Mliki B, Abbassi MA, Omri A. Lattice Boltzmann simulation of natural convection in an L-shaped enclosure in the presence of nanofluid. Eng. Sc. and Tech. an Int. J. 2015;18:503–511.
34. Mliki B, Abbassi MA, Omri A. Lattice Boltzmann Simulation of MHD Double Dispersion Natural Convection in a C-shaped Enclosure in the Presence of a Nanofluid. F. Dyn. and Mat. Proce. 2015;11(1): 87-114.
35. Mliki B, Abbassi MA, Omri A, Zeghmati B. Effectsof nanoparticles Brownian motion in a linearly/sinusoidally heated cavity with MHD natural convection in the presence of uniform heat generation/ absorption. Powder Technology. 2016; 295:69–83.
36. Brinkman HC. The viscosity of concentrated suspensions and solutions. Journal of Chemical Physics. 1952; 20 :571-581.
37. Qian YH, Humières D, Lallemand P. Lattice BGK models for Navier-Stokes equation. Europhysics Letters (Epl)). 1992; 17(6): 479.
38. Peng Y, Shu C, Chew YT. Simplified thermal lattice Boltzmann model for incompressible thermal flows. Physical Review. 2003; 68(2): 026701.
39. Ghasemi B, Aminossadati SM, Raisi A. Magnetic field effect on natural convection in a nanofluid-filled square enclosure. Int. J. Therm. Sci. 2011; 50:1748–1756.
40. Lai FH, Yang YT. Lattice Boltzmann simulation of natural convection heat transfer of Al2O3/water nanofluids in a square enclosure, Int. J. Therm. Sci. 2011; 50:1930-1941.
41. Talebi F, Mahmoudi AH, Shahi M. Numerical study of mixed convection flows in a square lid-driven cavity utilizing nanofluid. International Communications in Heat and Mass Transfer. 2010; 37 : 79–90.
42. Djebali R, Ganaoui ME, Pateyron B. A lattice Boltzmann-based investigation of powder in-flight characteristics during APS process. part I: Modelling and validation. Progress in Computational Fluid Dynamics. 2012; 12 (4):270-278.
43. Djebali R, Ganaoui ME, Pateyron B. A lattice Boltzmann based investigation of powder in-flight characteristics during APS process; part II: Effects of parameter dispersions at powder injection. Surface and Coatings Technology. 2013; 220: 157-163.
44. Djebali R, Elganaoui M, Jaouabi A, Pateyron B. Scrutiny of spray jet and impact characteristics under dispersion effects of powder injection parameters in APS process; International Journal of Thermal Sciences, 100(2016), pp. 229-239.
45. Naffouti T, Djebali R. Natural convection flow and heat transfer in square enclosure asymetrically heated from below: A lattice Boltzmann comprehensive study. Computer Modeling in Engineering and Sciences, 2012; 88 (3):211-227.
46. Abbassi MA, Djebali R, Guedri K. Effects of heater dimensions on nanofluid natural convection in a heated incinerator shaped cavity containing a heated block. Journal of Thermal Engineering. 2018; 4 (3):2018-2036.
47. Abbassi MA, Safaei MR, Djebali R, Guedri K, Zeghmati B, Alrashed AA. LBM simulation of free convection in a nanofluid filled incinerator containing a hot block. Int. Journal of Mechanical Sciences. 2018; 148:393-408.
48. Djebali R, Jaouabi A, Naffouti T, Abboudi S. Accurate LBM appraising of pin-fins heat dissipation performance and entropy generation in enclosures as application to power electronic cooling. International Journal of Numerical Methods for Heat and Fluid Flow. 2020; 30 (2):742-768.
49. Djebali R, ElGanaoui M, Naffouti T. A 2D Lattice boltzmann full analysis of MHD convective heat transfer in saturated porous square enclosure. Computer Modeling in Engineering and Sciences. 2012; 84 (6):499-527.
50. Djebali R. Numerical analysis of nanofluid cooling efficiency of hot multishaped cylinder in vertical porous channel; Romanian Journal of Physics, 65, 122 (2020).
51. Ferhi M, Djebali R, Mebarek-Oudina F, Nidal H, Abboudi S. MHD free convection through entropy generation analysis of eco-friendly nanoliquid in a divided L-shaped heat exchanger with LBM simulation. Journal of Nanofluids. 2022; 11 (1):99–112.
52. Ferhi M, Djebali R. Appraising conjugate heat transfer, heatlines visualization and entropy generation of Ag-MgO/H2O hybrid nanofluid in a partitioned medium. International Journal of Numerical Methods for Heat and Fluid Flow. 2020; 30(10):4529-4562.
53. Ferhi M, Djebali R. Heat transfer appraising and second law analysis of Cu-water nanoliquid filled microchannel: Slip flow regime. Romanian Journal of Physics. 2022; 67:605.

Acknowledgements: This work was supported by the Tunisian Ministry of Higher Education and Scientific Research under grant Project no: 20/PRD-22.

Bouchmel Mliki: https://orcid.org/0000-0002-0200-8060

Rached Miri: https://orcid.org/0000-0001-9113-5370

Ridha Djebali: https://orcid.org/0000-0002-1017-3410

Mohamed A. Abbassi: https://orcid.org/0000-0002-1915-0944

sciendo

 DOI 10.2478/ama-2023-0014

SOLUTION OF THE MODIFIED TIME FRACTIONAL COUPLED BURGERS EQUATIONS USING LAPLACE ADOMIAN DECOMPOSTION METHOD

Andrew OMAME*,, Fiazud Din ZAMAN****

*Department of Mathematics, Federal University of Technology, 1526, PMB,Owerri, Ihiagwa, Nigeria
**Abdus Salam School of Mathematical Sciences, Government College University Katchery Road, Lahore 54000, Lahore Pakistan

andrew.omame@futo.edu.ng, f.zaman@sms.edu.pk

received 25 September 2022, revised 1 November 2022, accepted 1 November 2022

Abstract: In this work, a coupled system of time-fractional modified Burgers' equations is considered. Three different fractional operators: Caputo, Caputo-Fabrizio and Atangana-Baleanu operators are implemented for the equations. Also, two different scenarios are examined for each fractional operator: when the initial conditions are $\mathrm{u}(\mathrm{x},\mathrm{y},0) = \sin(\mathrm{xy})$, $\mathrm{v}(\mathrm{x},\mathrm{y},0) = \sin(\mathrm{xy})$, and when they are $\mathrm{u}(\mathrm{x},\mathrm{y},0) = \mathrm{e}^{\{-\mathrm{kxy}\}}$, $\mathrm{v}(\mathrm{x},\mathrm{y},0) = \mathrm{e}^{\{-\mathrm{kxy}\}}$, where k,α are some positive constants. With the aid of computable Adomian polynomials, the solutions are obtained using Laplace Adomian decomposition method (LADM). The method does not need linearization, weak nonlinearity assumptions or perturbation theory. Simulations are also presented to support theoretical results, and the behaviour of the solutions under the three different fractional operators compared.

Key words: Burgers equations, Fractional derivatives, Laplace Adomian decomposition method, Semi-analytic solutions, Simulations

1. INTRODUCTION

Fractional differential equations (FDEs) are beginning to enjoy widespread application in many real life modelling problems. Fractional operators involving power-law kernel were first proposed by Riemann-Liouville and Caputo [1]. Although, these kernels are singular and constitute serious setbacks to their usage, more recent and improved operators such as Caputo-Fabrizio (CF) [2] and Atangana-Baleanu (AB) [3] operators have emerged.

The time-fractional Burgers equation is a kind of sub-diffusion convection equation. It is widely used to describe many physical problems such as unidirectional propagation of weakly nonlinear acoustic waves, shock waves in a viscous medium, flow systems, electromagnetic waves, compressible turbulence and weak shock propagation, etc [4]. Within the literature, lots of methods have been used to solve different versions of the Burgers equations, both integer order and time-fractional forms [5-10].

Agheli used the new homotopic perturbation method (NHPM) to solve a system of time fractional Burgers' equations [5]. Kaya [6] considered an explicit solution of the coupled viscous Burgers equation with the aid of the decomposition method. Majeed et al. [7] considered the solution of a one-dimensional time fractional Burgers and Fishers equations numerically with the help of the cubic B-spline approximation method. Singh et al. [8] analyzed a one-dimensional time-fractional model for damped Burgers equation involving the Caputo-Fabrizio fractional derivative. Also, the authors [9] considered the approximate analytic solution of the time-fractional damped Burgers and Cahn-Allen equations involving the Riemann-Liouville derivative using Homotopy analysis method (HAM). The existence of solutions for a coupled system of time-fractional partial differential equations (FPDEs) including continuous functions and the Caputo-Fabrizio fractional derivative was examined by Alsaedi et al. [10].

Also, several other methods have been proposed to solve non-linear fractional partial differential equations. The authors [11] numerically solved space-time fractional Burgers equations with the help of a new semi-analytical method. Safari and Sun [12] solved a fractional Rayleigh-Stokes using an improved singular boundary and dual reciprocity methods. Safari and Chen [13] solved a multi-term time-fractional mixed diffusion-wave equations with coupling of the improved singular boundary and dual reciprocity methods. In [14], Safari et al. used a meshless method to solve a variable-order fractional diffusion problems with fourth-order derivative term.

Among the available methods, the Laplace-Adomian decomposition method (LADM) has proven to be one of the most effective and straight forward method for solving non-linear FDES. This method combines both the Adomian decomposition method and Laplace transform. Also, it does not involve any predefined size declaration, discretization or linearization [15].

In this work, a modified two-dimensional system of time-fractional Burgers' equations is considered, with the help of three different fractional derivatives: Caputo, Caputo-Fabrizio and Atangana-Baleanu. The system is solved by applying LADM and the obtained results are compared. We hope this work will open up new research questions for further studies in this regard.

1.1 Preliminaries

Definition 1.1 [16] The Caputo fractional (CF) derivative of a function f of order $\theta \in R^{+}$ is defined by

$$ {}_{0}^{C}D_{t}^{\theta} f(t) = \frac{1}{\Gamma(1-\theta)} \int_{0}^{t} (t-\zeta)^{-\theta} f'(\zeta) d\zeta \quad (1) $$

Definition 1.2 [16] The Caputo Fractional integral of a function f of order $\theta \in R^+$ is defined by

$$ {}_0^C I_t^\theta f(t) = \frac{1}{\Gamma(\theta)} \int_0^t (t-\zeta)^{\theta-1} f(\zeta) d\zeta \qquad t > 0 \tag{2}$$

If $f(t) = 1$, the Caputo fractional integral is defined as

$$ {}_0^C I_t^\theta (1) = \frac{1}{\Gamma(\theta)} \int_0^t (t-\zeta)^{\theta-1} (1)(\zeta) d\zeta = \frac{t^\theta}{\Gamma(\theta+1)} \tag{3}$$

Definition 1.3 [16] For the Caputo derivative, the Laplace transform is defined by:

$$ L\{{}_0^C D_t^\theta f(t)\} = s^\theta L\{f(s)\} - s^{\theta-1} f(0), \quad 0 < \theta < 1 \tag{4}$$

Definition 1.4 [2] Let $f \in H^1(a_1, a_2),\ a_2 > a_1, \theta \in (0,1)$.The Caputo-Fabrizio fractional (CF) derivative [2] of a function f of order $\theta \in R^+$ is defined by

$$ {}_0^{CF} D_t^\theta f(t) = \frac{G(\theta)}{(1-\theta)} \int_0^t \exp\left[-\frac{\theta}{1-\theta}(t-\tau)\right] f'(\zeta) d\zeta \tag{5}$$

where $G(\theta) = (1-\theta) + \frac{\theta}{\Gamma(\theta)}$, denotes a normalization function satisfying $G(0) = G(1) = 1$.

However, if $f \notin H^1(a_1, a_2)$, then the Caputo-Fabrizio derivative is defined by

$$ {}_0^{CF} D_t^\theta f(t) = \frac{\theta G(\theta)}{(1-\theta)} \int_0^t \exp\left[-\frac{\theta}{1-\theta}(t-\tau)\right] (f(t) - f(\zeta)) d\zeta \tag{6}$$

Definition 1.5 [2] The Laplace transform of the Caputo-Fabrizio derivative is given by:

$$ L\{{}_0^{CF} D_t^\theta f(t)\} = G(\theta) \frac{sL\{f(t)\} - f(0)}{[s + \theta(1-s)]} \tag{7}$$

Definition 1.6 [3] Let $f \in H^1(a_1, a_2),\ a_2 > a_1, \theta \in (0,1)$.The Atangana-Baleanu derivative of a function f of order $\theta \in R^+$ in Caputo sense is defined by

$$ {}_0^{ABC} D_t^\theta f(t) = \frac{G(\theta)}{(1-\theta)} \int_0^t E_\theta\left[-\frac{\theta}{1-\theta}(t-\tau)\right] f'(\zeta) d\zeta \tag{8}$$

where, $E_\theta(.)$ is the Mittag-Leffler function defined by

$$ E_\theta(t) = \sum_{k=0}^\infty \frac{t^\theta}{\Gamma(\theta k + 1)}, \quad \theta > 0. \tag{9}$$

Definition 1.7 [3] The Atangana-Baleanu (AB) fractional integral in Caputo for a given function f of order $\theta \in R^+$ is defined by

$$ {}_0^{AB} I_t^\theta f(t) = \frac{1-\theta}{G(\theta)} f(t) + \frac{\theta}{G(\theta)\Gamma(\theta)} \int_0^t (t-\tau)^{\theta-1} f(\zeta) d\zeta \tag{10}$$

Definition 1.8 [3] For the AB derivative, the Laplace transform is defined as:

$$ L\{{}_0^{ABC} D_t^\theta f(t)\} = G(\theta) \frac{s^\theta L\{f(t)\} - s^{\theta-1} f(0)}{[\theta + (1-\theta)s^\theta]} \tag{11}$$

2. APPLICATIONS

Various forms of the time fractional Burgers equations have been considered by different authors. For instance, Mohammed [17] used the Conformable double Sumudu transform in solving a scalar time-fractional coupled Burgers equation. Also, the authors [18] solved a nonlinear one-dimensional fractional Burgers' equations with the aid of the Elzaki transform and homotopy perturbation method. In [19], the authors developed a modified variational iteration Laplace transform method and compared with Laplace Adomian decomposition method in solving a one-dimensional time-fractional Burgers Equations.

To the best of our knowledge, no authors have considered the coupled system of time fractional Burgers' equation using the three different fractional derivatives. In this paper, this is now solved with the aid of the Laplace Adomian Decomposition method (LADM).

2.1. The Atangana-Baleanu fractional operator

Example 2.1 Let us consider the system of modified time-fractional two-dimensional Burgers' equations

$$\frac{\partial^\theta}{\partial t^\theta} + u\frac{\partial u}{\partial x} + v\frac{\partial u}{\partial y} = \alpha\left(\frac{\partial^2 u}{\partial x^2} + \frac{\partial^2 u}{\partial y^2}\right)$$
$$\frac{\partial^\theta v}{\partial t^\theta} + u\frac{\partial v}{\partial x} + v\frac{\partial v}{\partial y} = \alpha\left(\frac{\partial^2 v}{\partial x^2} + \frac{\partial^2 v}{\partial y^2}\right), \tag{12}$$

Subject to the initial conditions:

Case 2.1 $u(x,y,0) = \sin(xy)$, $v(x,,0) = \sin(xy)$

By applying the Laplace transform of the AB derivative to the equation (12), we obtain

$$L\left[\frac{\partial^\theta}{\partial t^\theta}\right] = L\left[\alpha\left(\frac{\partial^2 u}{\partial x^2} + \frac{\partial^2 u}{\partial y^2}\right) - u\frac{\partial u}{\partial x} - v\frac{\partial u}{\partial y}\right]$$
$$L\left[\frac{\partial^\theta v}{\partial t^\theta}\right] = L\left[\alpha\left(\frac{\partial^2 v}{\partial x^2} + \frac{\partial^2 v}{\partial y^2}\right) - u\frac{\partial v}{\partial x} - v\frac{\partial v}{\partial y}\right],$$

which can be re-written as

$$L[u(x,y,t)] = \frac{u(x,y,0)}{s} + \frac{s^\theta(1-\theta)+\theta}{s^\theta G(\theta)} L\left[\alpha\left(\frac{\partial^2 u}{\partial x^2} + \frac{\partial^2 u}{\partial y^2}\right) - u\frac{\partial u}{\partial x} - v\frac{\partial u}{\partial y}\right]$$
$$L[v(x,y,t)] = \frac{v(x,y,0)}{s} + \frac{s^\theta(1-\theta)+\theta}{s^\theta G(\theta)} L\left[\alpha\left(\frac{\partial^2 v}{\partial x^2} + \frac{\partial^2 v}{\partial y^2}\right) - u\frac{\partial v}{\partial x} - v\frac{\partial v}{\partial y}\right]. \tag{13}$$

Taking inverse Laplace transform of both sides, we obtain

$$u(x,y,t) = L^{-1}\left[\frac{u(x,y,0)}{s} + \frac{s^\theta(1-\theta)+\theta}{s^\theta G(\theta)} L\left[\alpha\left(\frac{\partial^2 u}{\partial x^2} + \frac{\partial^2 u}{\partial y^2}\right) - u\frac{\partial u}{\partial x} + v\frac{\partial u}{\partial y}\right]\right]$$
$$v(x,y,t) = L^{-1}\left[\frac{v(x,y,0)}{s} + \frac{s^\theta(1-\theta)+\theta}{s^\theta G(\theta)} L\left[\alpha\left(\frac{\partial^2 v}{\partial x^2} + \frac{\partial^2 v}{\partial y^2}\right) - u\frac{\partial v}{\partial x} + v\frac{\partial v}{\partial y}\right]\right] \tag{14}$$

which is equivalent to

$$u(x,y,t) = \sin(xy) + L^{-1}\left[\frac{s^\theta(1-\theta)+\theta}{s^\theta G(\theta)} L\left[\alpha\left(\frac{\partial^2 u}{\partial x^2} + \frac{\partial^2 u}{\partial y^2}\right) - u\frac{\partial u}{\partial x} - v\frac{\partial u}{\partial y}\right]\right]$$
$$v(x,y,t) = \sin(xy) + L^{-1}\left[\frac{s^\theta(1-\theta)+\theta}{s^\theta G(\theta)} L\left[\alpha\left(\frac{\partial^2 v}{\partial x^2} + \frac{\partial^2 v}{\partial y^2}\right) - u\frac{\partial v}{\partial x} - v\frac{\partial v}{\partial y}\right]\right] \tag{15}$$

Using the ADM, we obtain

$$\sum_{j=0}^\infty u_j(x,y,t) = \sin(xy) + L^{-1}\left[\frac{s^\theta(1-\theta)+\theta}{s^\theta G(\theta)} L\left[\alpha\left(\frac{\partial^2 u}{\partial x^2} + \frac{\partial^2 u}{\partial y^2}\right) - \sum_{j=0}^\infty A_j - \sum_{j=0}^\infty B_j\right]\right]$$

$$\sum_{j=0}^{\infty} v_j(x,y,t) = \sin(xy) + L^{-1}\left[\frac{s^{\theta}(1-\theta)+\theta}{s^{\theta}G(\theta)} L\left[\alpha\left(\frac{\partial^2 v}{\partial x^2} + \frac{\partial^2 v}{\partial y^2}\right) - \sum_{j=0}^{\infty} C_j - \sum_{j=0}^{\infty} D_j\right]\right] \quad (16)$$

where, the Adomian polynomial components A_j, B_j, C_j and D_j are given as:

$$A_0 = u_0\frac{\partial u_0}{\partial x},\ A_1 = u_0\frac{\partial u_1}{\partial x} + u_1\frac{\partial u_0}{\partial x},$$
$$A_2 = u_0\frac{\partial u_2}{\partial x} + u_1\frac{\partial u_1}{\partial x} + u_2\frac{\partial u_0}{\partial x},$$
$$B_0 = v_0\frac{\partial u_0}{\partial y},\quad B_1 = v_0\frac{\partial u_1}{\partial y} + v_1\frac{\partial u_0}{\partial y},$$
$$B_2 = v_0\frac{\partial u_2}{\partial y} + v_1\frac{\partial u_2}{\partial y} + v_2\frac{\partial u_0}{\partial y},$$
$$C_0 = u_0\frac{\partial v_0}{\partial x},\ C_1 = u_0\frac{\partial v_1}{\partial x} + u_1\frac{\partial v_0}{\partial x},$$
$$C_2 = u_0\frac{\partial v_2}{\partial x} + u_1\frac{\partial v_1}{\partial x} + u_2\frac{\partial v_0}{\partial x},$$
$$D_0 = v_0\frac{\partial v_0}{\partial y},\quad D_1 = v_0\frac{\partial v_1}{\partial y} + v_1\frac{\partial v_0}{\partial y},$$
$$B_2 = v_0\frac{\partial v_2}{\partial y} + v_1\frac{\partial v_2}{\partial y} + v_2\frac{\partial v_0}{\partial y}, \quad (17)$$

For $j = 0,1,2,$

$$u_1(x,y,t) = \sin(xy) + \left[\frac{1}{G(\theta)}\left(1-\theta+\frac{\theta t^{\theta}}{\Gamma(\theta)}\right)\right]\left[\alpha\left(\frac{\partial^2 u_0}{\partial x^2} + \frac{\partial^2 u_0}{\partial y^2}\right) - u_0\frac{\partial u_0}{\partial x} - v_0\frac{\partial u_0}{\partial y}\right] = \sin(\mathrm{xy}) + \left[\frac{1}{G(\theta)}\left(1-\theta+\frac{\theta t^{\theta}}{\Gamma(\theta)}\right)\right][-\alpha(x^2+y^2)\sin(xy) - (x+y)\sin(xy)\cos(xy)]$$

$$v_1(x,y,t) = \sin(xy) + \left[\frac{1}{G(\theta)}\left(1-\theta+\frac{\theta t^{\theta}}{\Gamma(\theta)}\right)\right]\left[\alpha\left(\frac{\partial^2 v_0}{\partial x^2} + \frac{\partial^2 v_0}{\partial y^2}\right) - u_0\frac{\partial v_0}{\partial x} - v_0\frac{\partial v_0}{\partial y}\right] = \sin(xy) + \left[\frac{1}{G(\theta)}\left(1-\theta+\frac{\theta t^{\theta}}{\Gamma(\theta)}\right)\right][-\alpha(x^2+y^2)\sin(xy) - (x+y)\sin(xy)\cos(xy)]$$

$$u_2(x,y,t) = \sin(xy) + \left[\frac{1}{G(\theta)}\left(1-\theta+\frac{\theta t^{\theta}}{\Gamma(\theta)}\right)\right]\left[\alpha\left(\frac{\partial^2 u_0}{\partial x^2} + \frac{\partial^2 u_0}{\partial y^2}\right) - u_0\frac{\partial u_1}{\partial x} - u_1\frac{\partial u_0}{\partial x} - v_0\frac{\partial u_1}{\partial y} - v_1\frac{\partial u_0}{\partial y}\right] = \sin(\mathrm{xy}) + \left[\frac{1}{G(\theta)}\left(1-\theta+\frac{\theta t^{\theta}}{\Gamma(\theta)}\right)\right]\left[\alpha\left(\frac{\partial^2 u_1}{\partial x^2} + \frac{\partial^2 u_1}{\partial y^2}\right) - \sin(xy)\left(y\cos(xy) + \left[\frac{1}{G(\theta)}\left(1-\theta+\frac{\theta t^{\theta}}{\Gamma(\theta)}\right)\right][-2\alpha x\sin(xy) - \alpha y(x^2+y^2)\cos(xy) - y(x+y)[\cos^2(xy)-\sin^2(xy)] - \sin(xy)\cos(xy)]\right) - \left(\sin(xy) + \left[\frac{1}{G(\theta)}\left(1-\theta+\frac{\theta t^{\theta}}{\Gamma(\theta)}\right)\right][-\alpha(x^2+y^2)\sin(xy) - (x+y)\sin(xy)\cos(xy)]\right)y\cos(xy) - \sin(xy)\left(x\cos(xy) + \left[\frac{1}{G(\theta)}\left(1-\theta+\frac{\theta t^{\theta}}{\Gamma(\theta)}\right)\right][-2\alpha y\sin(xy) - \alpha x(x^2+y^2)\cos(xy) - y(x+y)[\cos^2(xy)-\sin^2(xy)] - \sin(xy)\cos(xy)]\right) - \left(\sin(xy) + \left[\frac{1}{G(\theta)}\left(1-\theta+\frac{\theta t^{\theta}}{\Gamma(\theta)}\right)\right][-\alpha(x^2+y^2)\sin(xy) - (x+y)\sin(xy)\cos(xy)]\right)x\cos(xy)\right]$$

$$v_2(x,y,t) = \sin(xy) + \left[\frac{1}{G(\theta)}\left(1-\theta+\frac{\theta t^{\theta}}{\Gamma(\theta)}\right)\right]\left[\alpha\left(\frac{\partial^2 v_0}{\partial x^2} + \frac{\partial^2 v_0}{\partial y^2}\right) - u_0\frac{\partial v_1}{\partial x} - u_1\frac{\partial v_0}{\partial x} - v_0\frac{\partial v_1}{\partial y} - v_1\frac{\partial v_0}{\partial y}\right] = \sin(\mathrm{xy}) + \left[\frac{1}{G(\theta)}\left(1-\theta+\frac{\theta t^{\theta}}{\Gamma(\theta)}\right)\right]\left[\alpha\left(\frac{\partial^2 u_1}{\partial x^2} + \frac{\partial^2 u_1}{\partial y^2}\right) - \sin(xy)\left(y\cos(xy) + \left[\frac{1}{G(\theta)}\left(1-\theta+\frac{\theta t^{\theta}}{\Gamma(\theta)}\right)\right][-2\alpha x\sin(xy) - \alpha y(x^2+y^2)\cos(xy) - y(x+y)[\cos^2(xy)-\sin^2(xy)] - \sin(xy)\cos(xy)]\right) - \left(\sin(xy) + \left[\frac{1}{G(\theta)}\left(1-\theta+\frac{\theta t^{\theta}}{\Gamma(\theta)}\right)\right][-\alpha(x^2+y^2)\sin(xy) - (x+y)\sin(xy)\cos(xy)]\right)y\cos(xy) - \sin(xy)\left(x\cos(xy) + \left[\frac{1}{G(\theta)}\left(1-\theta+\frac{\theta t^{\theta}}{\Gamma(\theta)}\right)\right][-2\alpha y\sin(xy) - \alpha x(x^2+y^2)\cos(xy) - y(x+y)[\cos^2(xy)-\sin^2(xy)] - \sin(xy)\cos(xy)]\right) - \left(\sin(xy) + \left[\frac{1}{G(\theta)}\left(1-\theta+\frac{\theta t^{\theta}}{\Gamma(\theta)}\right)\right][-\alpha(x^2+y^2)\sin(xy) - (x+y)\sin(xy)\cos(xy)]\right)x\cos(xy)\right]$$

Case 2.2 $u(x,y,0) = \sin(xy)$, $v(x,,0) = \sin(xy)$

$$u_1(x,y,t) = e^{-kxy} + \left[\frac{1}{G(\theta)}\left(1-\theta+\frac{\theta t^{\theta}}{\Gamma(\theta)}\right)\right][\alpha(k^2y^2e^{-kxy} + k^2x^2e^{-kxy}) + kye^{-2kxy} + kxe^{-4kxy}]$$

$$v_1(x,y,t) = e^{-kxy} + \left[\frac{1}{G(\theta)}\left(1-\theta+\frac{\theta t^{\theta}}{\Gamma(\theta)}\right)\right][\alpha(k^2y^2e^{-kxy} + k^2x^2e^{-kxy}) + kye^{-2kxy} + kxe^{-4kxy}]$$

$$u_2(x,y,t) = e^{-kxy} + \left[\frac{1}{G(\theta)}\left(1-\theta+\frac{\theta t^{\theta}}{\Gamma(\theta)}\right)\right]\left[\alpha\left(k^2y^2e^{-kxy} + k^2x^2e^{-kxy} + \left[\frac{1}{G(\theta)}\left(1-\theta+\frac{\theta t^{\theta}}{\Gamma(\theta)}\right)\right][\alpha(k^4y^4e^{-kxy} + k^4x^4e^{-kxy} + 4k^2e^{-kxy})]\right) - e^{-kxy}\left(kye^{-kxy} + \left[\frac{1}{G(\theta)}\left(1-\theta+\frac{\theta t^{\theta}}{\Gamma(\theta)}\right)\right][\alpha(-k^3y^3e^{-kxy} + 2k^2xe^{-kxy} - k^3yx^2e^{-kxy}) + 2k^2y^2e^{-2kxy} - ke^{-4kxy} + 4k^2xye^{-4kxy}]\right) - \left(e^{-kxy} + \left[\frac{1}{G(\theta)}\left(1-\theta+\frac{\theta t^{\theta}}{\Gamma(\theta)}\right)\right][\alpha(k^2y^2e^{-kxy} + k^2x^2e^{-kxy}) + kye^{-2kxy} + kxe^{-4kxy}]\right)kye^{-2kxy}\left(-kxe^{-kxy} + \left[\frac{1}{G(\theta)}\left(1-\theta+\frac{\theta t^{\theta}}{\Gamma(\theta)}\right)\right][\alpha(2k^2ye^{-kxy} - k^3xy^2e^{-kxy} - k^3x^3e^{-kxy}) - k^2e^{-2kxy} + 2k^2xye^{-2kxy} - 4k^2x^2ye^{-4kxy}]\right) - \left(e^{-kxy} + \left[\frac{1}{G(\theta)}\left(1-\theta+\frac{\theta t^{\theta}}{\Gamma(\theta)}\right)\right][\alpha(k^2y^2e^{-kxy} + k^2x^2e^{-kxy}) + kye^{-2kxy} + kxe^{-4kxy}]\right)(-kxe^{-kx})\right]$$

$$v_2(x,y,t) = e^{-kxy} + \left[\frac{1}{G(\theta)}\left(1-\theta+\frac{\theta t^{\theta}}{\Gamma(\theta)}\right)\right]\left[\alpha\left(k^2y^2e^{-kxy} + k^2x^2e^{-kxy} + \left[\frac{1}{G(\theta)}\left(1-\theta+\frac{\theta t^{\theta}}{\Gamma(\theta)}\right)\right][\alpha(k^4y^4e^{-kxy} + k^4x^4e^{-kxy} + 4k^2e^{-kxy})]\right) - e^{-kxy}\left(kye^{-kxy} + \left[\frac{1}{G(\theta)}\left(1-\theta+\frac{\theta t^{\theta}}{\Gamma(\theta)}\right)\right][\alpha(-k^3y^3e^{-kxy} + 2k^2xe^{-kxy} - k^3yx^2e^{-kxy}) + 2k^2y^2e^{-2kxy} - ke^{-4kxy} +\right.\right.$$

$4k^2xye^{-4kxy}]\Big) - \Big(e^{-kxy} + \Big[\frac{1}{G(\theta)}\Big(1-\theta+\frac{\theta t^\theta}{\Gamma(\theta)}\Big)\Big][\alpha(k^2y^2e^{-kxy} + k^2x^2e^{-kxy}) + kye^{-2kxy} + kxe^{-4kxy}]\Big)kye^{-2kxy}\Big(-kxe^{-kxy} + \Big[\frac{1}{G(\theta)}\Big(1-\theta+\frac{\theta t^\theta}{\Gamma(\theta)}\Big)\Big][\alpha(2k^2ye^{-kxy} - k^3xy^2e^{-kxy} - k^3x^3e^{-kxy}) - k^2e^{-2kxy} + 2k^2xye^{-2kxy} - 4k^2x^2ye^{-4kxy}]\Big) - \Big(e^{-kxy} + \Big[\frac{1}{G(\theta)}\Big(1-\theta+\frac{\theta t^\theta}{\Gamma(\theta)}\Big)\Big][\alpha(k^2y^2e^{-kxy} + k^2x^2e^{-kxy}) + kye^{-2kxy} + kxe^{-4kxy}]\Big)(-kxe^{-kx})\Big]$

2.2. The Caputo fractional operator

Applying the Laplace transform to system (12) and solving via the Caputo fractional derivative, we have using the initial conditions:

Case 2.3 $u(x,y,0) = \sin(xy)\,,\ v(x,y,0) = \sin(xy)$

$u_2(x,y,t) = \sin(xy) + \Big[\frac{t^\theta}{\Gamma(\theta+1)}\Big]\Big[\alpha\Big(\frac{\partial^2u_0}{\partial x^2}+\frac{\partial^2u_0}{\partial y^2}\Big) - u_0\frac{\partial u_1}{\partial x} - u_1\frac{\partial u_0}{\partial x} - v_0\frac{\partial u_1}{\partial y} - v_1\frac{\partial u_0}{\partial y}\Big] = \sin(\mathrm{xy}) + \Big[\frac{t^\theta}{\Gamma(\theta+1)}\Big]\Big[\alpha\Big(\frac{\partial^2u_1}{\partial x^2}+\frac{\partial^2u_1}{\partial y^2}\Big) - \sin(xy)\Big(y\cos(xy) + \Big[\frac{t^\theta}{\Gamma(\theta+1)}\Big][-2\alpha x\sin(xy) - \alpha y(x^2+y^2)\cos(xy) - y(x+y)[\cos^2(xy)-\sin^2(xy)] - \sin(xy)\cos(xy)]\Big) - \Big(\sin(xy) + \Big[\frac{t^\theta}{\Gamma(\theta+1)}\Big][-\alpha(x^2+y^2)\sin(xy) - (x+y)\sin(xy)\cos(xy)]\Big)y\cos(xy) - \sin(xy)\Big(x\cos(xy) + \Big[\frac{t^\theta}{\Gamma(\theta+1)}\Big][-2\alpha y\sin(xy) - \alpha x(x^2+y^2)\cos(xy) - y(x+y)[\cos^2(xy)-\sin^2(xy)] - \sin(xy)\cos(xy)]\Big) - \Big(\sin(xy) + \Big[\frac{t^\theta}{\Gamma(\theta+1)}\Big][-\alpha(x^2+y^2)\sin(xy) - (x+y)\sin(xy)\cos(xy)]\Big)x\cos(xy)\Big]$ $v_2(x,y,t) = \sin(xy) + \Big[\frac{t^\theta}{\Gamma(\theta+1)}\Big]\Big[\alpha\Big(\frac{\partial^2v_0}{\partial x^2}+\frac{\partial^2v_0}{\partial y^2}\Big) - u_0\frac{\partial v_1}{\partial x} - u_1\frac{\partial v_0}{\partial x} - v_0\frac{\partial v_1}{\partial y} - v_1\frac{\partial v_0}{\partial y}\Big] = \sin(\mathrm{xy}) + \Big[\frac{t^\theta}{\Gamma(\theta+1)}\Big]\Big[\alpha\Big(\frac{\partial^2u_1}{\partial x^2}+\frac{\partial^2u_1}{\partial y^2}\Big) - \sin(xy)\Big(y\cos(xy) + \Big[\frac{t^\theta}{\Gamma(\theta+1)}\Big][-2\alpha x\sin(xy) - \alpha y(x^2+y^2)\cos(xy) - y(x+y)[\cos^2(xy)-\sin^2(xy)] - \sin(xy)\cos(xy)]\Big) - \Big(\sin(xy) + \Big[\frac{t^\theta}{\Gamma(\theta+1)}\Big][-\alpha(x^2+y^2)\sin(xy) - (x+y)\sin(xy)\cos(xy)]\Big)y\cos(xy) - \sin(xy)\Big(x\cos(xy) + \Big[\frac{t^\theta}{\Gamma(\theta+1)}\Big][-2\alpha y\sin(xy) - \alpha x(x^2+y^2)\cos(xy) - y(x+y)[\cos^2(xy)-\sin^2(xy)] - \sin(xy)\cos(xy)]\Big) - \Big(\sin(xy) + \Big[\frac{t^\theta}{\Gamma(\theta+1)}\Big][-\alpha(x^2+y^2)\sin(xy) - (x+y)\sin(xy)\cos(xy)]\Big)x\cos(xy)\Big]$

Case 2.4 $u(x,y,0) = e^{-kxy},\ v(x,,0) = e^{-kxy}$

$u_2(x,y,t) = e^{-kxy} + \Big[\frac{t^\theta}{\Gamma(\theta+1)}\Big]\Big[\alpha\Big(k^2y^2e^{-kxy} + k^2x^2e^{-kxy} + \Big[\frac{t^\theta}{\Gamma(\theta+1)}\Big][\alpha(k^4y^4e^{-kxy} + k^4x^4e^{-kxy} + 4k^2e^{-kxy})]\Big) - e^{-kxy}\Big(kye^{-kxy} + \Big[\frac{t^\theta}{\Gamma(\theta+1)}\Big][\alpha(-k^3y^3e^{-kxy} + 2k^2xe^{-kxy} - k^3yx^2e^{-kxy}) + 2k^2y^2e^{-2kxy} - ke^{-4kxy} + 4k^2xye^{-4kxy}]\Big) - \Big(e^{-kxy} + \Big[\frac{t^\theta}{\Gamma(\theta+1)}\Big][\alpha(k^2y^2e^{-kxy} + k^2x^2e^{-kxy}) + kye^{-2kxy} + kxe^{-4kxy}]\Big)kye^{-2kxy}\Big(-kxe^{-kxy} + \Big[\frac{t^\theta}{\Gamma(\theta+1)}\Big][\alpha(2k^2ye^{-kxy} - k^3xy^2e^{-kxy} - k^3x^3e^{-kxy}) - k^2e^{-2kxy} + 2k^2xye^{-2kxy} - 4k^2x^2ye^{-4kxy}]\Big) - \Big(e^{-kxy} + \Big[\frac{t^\theta}{\Gamma(\theta+1)}\Big][\alpha(k^2y^2e^{-kxy} + k^2x^2e^{-kxy}) + kye^{-2kxy} + kxe^{-4kxy}]\Big)(-kxe^{-kx})\Big]$

$v_2(x,y,t) = e^{-kxy} + \Big[\frac{t^\theta}{\Gamma(\theta+1)}\Big]\Big[\alpha\Big(k^2y^2e^{-kxy} + k^2x^2e^{-kxy} + \Big[\frac{t^\theta}{\Gamma(\theta+1)}\Big][\alpha(k^4y^4e^{-kxy} + k^4x^4e^{-kxy} + 4k^2e^{-kxy})]\Big) - e^{-kxy}\Big(kye^{-kxy} + \Big[\frac{t^\theta}{\Gamma(\theta+1)}\Big][\alpha(-k^3y^3e^{-kxy} + 2k^2xe^{-kxy} - k^3yx^2e^{-kxy}) + 2k^2y^2e^{-2kxy} - ke^{-4kxy} + 4k^2xye^{-4kxy}]\Big) - \Big(e^{-kxy} + \Big[\frac{t^\theta}{\Gamma(\theta+1)}\Big][\alpha(k^2y^2e^{-kxy} + k^2x^2e^{-kxy}) + kye^{-2kxy} + kxe^{-4kxy}]\Big)kye^{-2kxy}\Big(-kxe^{-kxy} + \Big[\frac{t^\theta}{\Gamma(\theta+1)}\Big][\alpha(2k^2ye^{-kxy} - k^3xy^2e^{-kxy} - k^3x^3e^{-kxy}) - k^2e^{-2kxy} + 2k^2xye^{-2kxy} - 4k^2x^2ye^{-4kxy}]\Big) - \Big(e^{-kxy} + \Big[\frac{t^\theta}{\Gamma(\theta+1)}\Big][\alpha(k^2y^2e^{-kxy} + k^2x^2e^{-kxy}) + kye^{-2kxy} + kxe^{-4kxy}]\Big)(-kxe^{-kx})\Big]$

2.3. The Caputo-Fabrizio fractional operator

Applying the Laplace transform to system (12) and solving via the Caputo-Fabrizio fractional derivative, we have, using the initial conditions:

Case 2.5 $u(x,y,0) = e^{-kxy},\ v(x,,0) = e^{-kxy}$

$u_2(x,y,t) = \sin(xy) + [1+\theta(t-1)]\Big[\alpha\Big(\frac{\partial^2u_0}{\partial x^2}+\frac{\partial^2u_0}{\partial y^2}\Big) - u_0\frac{\partial u_1}{\partial x} - u_1\frac{\partial u_0}{\partial x} - v_0\frac{\partial u_1}{\partial y} - v_1\frac{\partial u_0}{\partial y}\Big] = \sin(\mathrm{xy}) + [1+\theta(t-1)]\Big[\alpha\Big(\frac{\partial^2u_1}{\partial x^2}+\frac{\partial^2u_1}{\partial y^2}\Big) - \sin(xy)(y\cos(xy) + [1+\theta(t-1)][-2\alpha x\sin(xy) - \alpha y(x^2+y^2)\cos(xy) - y(x+y)[\cos^2(xy)-\sin^2(xy)] - \sin(xy)\cos(xy)]) - (\sin(xy) + [1+\theta(t-1)][-\alpha(x^2+y^2)\sin(xy) - (x+y)\sin(xy)\cos(xy)])y\cos(xy) - \sin(xy)\,(x\cos(xy) + [1+\theta(t-1)][-2\alpha y\sin(xy) - \alpha x(x^2+y^2)\cos(xy) - y(x+y)[\cos^2(xy)-\sin^2(xy)] - \sin(xy)\cos(xy)]) - (\sin(xy) + [1+\theta(t-1)][-\alpha(x^2+y^2)\sin(xy) - (x+y)\sin(xy)\cos(xy)])x\cos(xy)\Big]$

$v_2(x,y,t) = \sin(xy) + [1+\theta(t-1)]\Big[\alpha\Big(\frac{\partial^2v_0}{\partial x^2}+\frac{\partial^2v_0}{\partial y^2}\Big) - u_0\frac{\partial v_1}{\partial x} - u_1\frac{\partial v_0}{\partial x} - v_0\frac{\partial v_1}{\partial y} - v_1\frac{\partial v_0}{\partial y}\Big] = \sin(\mathrm{xy}) + [1+\theta(t-$

DOI 10.2478/ama-2023-0014

$1)]\Big[\alpha\left(\frac{\partial^2 u_1}{\partial x^2}+\frac{\partial^2 u_1}{\partial y^2}\right)-\sin(xy)(ycos(xy)+[1+\theta(t-1)][-2\alpha xsin(xy)-\alpha y(x^2+y^2)\cos(xy)-y(x+y)[\cos^2(xy)-\sin^2(xy)]-\sin(xy)\cos(xy)])-(\sin(xy)+[1+\theta(t-1)][-\alpha(x^2+y^2)sin(xy)-(x+y)\sin(xy)\cos(xy)])ycos(xy)-\sin(xy)\,(xcos(xy)+[1+\theta(t-1)][-2\alpha ysin(xy)-\alpha x(x^2+y^2)\cos(xy)-y(x+y)[\cos^2(xy)-\sin^2(xy)]-\sin(xy)\cos(xy)])-(\sin(xy)+[1+\theta(t-1)][-\alpha(x^2+y^2)\sin(xy)-(x+y)sin(xy)\cos(xy)])xcos(xy)\Big]$

Case 2.6 $u(x,y,0)=e^{-kxy},\ v(x,,0)=e^{-kxy}$

$u_2(x,y,t)=e^{-kxy}+\left[\frac{t^\theta}{\Gamma(\theta+1)}\right]\Big[\alpha\Big(k^2y^2e^{-kxy}+k^2x^2e^{-kxy}+\left[\frac{t^\theta}{\Gamma(\theta+1)}\right][\alpha(k^4y^4e^{-kxy}+k^4x^4e^{-kxy}+4k^2e^{-kxy})]\Big)-e^{-kxy}\Big(kye^{-kxy}+\left[\frac{t^\theta}{\Gamma(\theta+1)}\right][\alpha(-k^3y^3e^{-kxy}+2k^2xe^{-kxy}-k^3yx^2e^{-kxy})+2k^2y^2e^{-2kxy}-ke^{-4kxy}+4k^2xye^{-4kxy}]\Big)-\Big(e^{-kxy}+\left[\frac{t^\theta}{\Gamma(\theta+1)}\right][\alpha(k^2y^2e^{-kxy}+k^2x^2e^{-kxy})+kye^{-2kxy}+kxe^{-4kxy}]\Big)kye^{-2kxy}(-kxe^{-kxy}+1+\theta(t-1)[\alpha(2k^2ye^{-kxy}-k^3xy^2e^{-kxy}-k^3x^3e^{-kxy})-k^2e^{-2kxy}+2k^2xye^{-2kxy}-4k^2x^2ye^{-4kxy}])-(e^{-kxy}+[1+\theta(t-1)][\alpha(k^2y^2e^{-kxy}+k^2x^2e^{-kxy})+kye^{-2kxy}+kxe^{-4kxy}])(-kxe^{-kx})\Big]$

$v_2(x,y,t)=e^{-kxy}+[1+\theta(t-1)][\alpha(k^2y^2e^{-kxy}+k^2x^26+1+\theta(t-1)[\alpha(k^4y^4e^{-kxy}+k^4x^4e^{-kxy}+4k^2e^{-kxy})])-e^{-kxy}(kye^{-kxy}+[1+\theta(t-1)][\alpha(-k^3y^3e^{-kxy}+2k^2xe^{-kxy}-k^3yx^2e^{-kxy})+2k^2y^2e^{-2kxy}-ke^{-4kxy}+4k^2xye^{-4kxy}])-(e^{-kxy}+[1+\theta(t-1)][\alpha(k^2y^2e^{-kxy}+k^2x^2e^{-kxy})+kye^{-2kxy}+kxe^{-4kxy}])kye^{-2kxy}(-kxe^{-kxy}+[1+\theta(t-1)][\alpha(2k^2ye^{-kxy}-k^3xy^2e^{-kxy}-k^3x^3e^{-kxy})-k^2e^{-2kxy}+2k^2xye^{-2kxy}-4k^2x^2ye^{-4kxy}])-(e^{-kxy}+[1+\theta(t-1)][\alpha(k^2y^2e^{-kxy}+k^2x^2e^{-kxy})+kye^{-2kxy}+kxe^{-4kxy}])(-kxe^{-kx})]$

2.4. Numerical simulations

In this section, we present some numerical results to justify the theoretical analysis and computations. It is imperative to state that the MATLAB R2020a version was used to run all the simulations in this section. The solution profiles for u at initial time $t=0$ when the fluid viscosity is 1.0, using the three different fractional operators are presented in Figs.1(a)-(b).

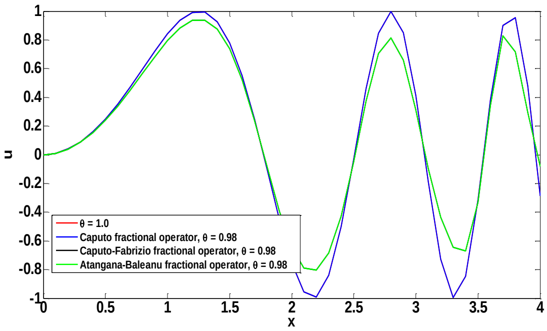

Fig. 1(a). Case 1: Solution profile for u when $t=0,\alpha=1.0$

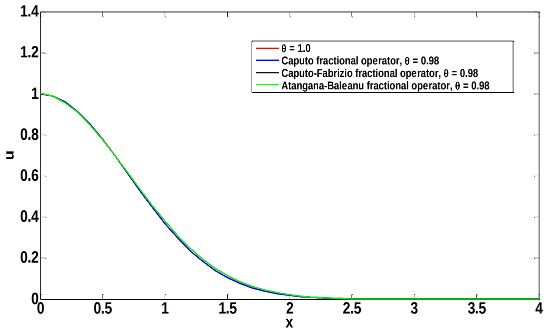

Fig. 1(b). Case 2: Solution profile for u when $t=0,\alpha=1.0$

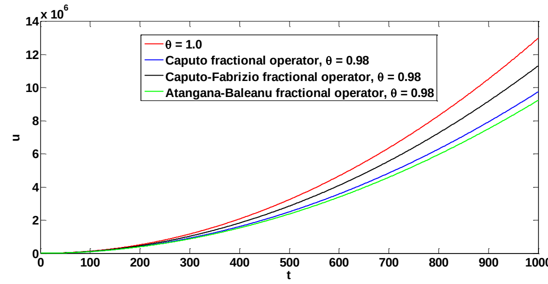

Fig. 2(a). Case 2: Solution profile for u when $x=y=1,\alpha=1.0$

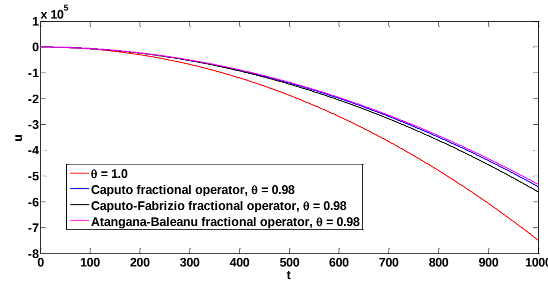

Fig. 2(b). Case 2: Solution profile for u when $x=y=1,\alpha=1.0$

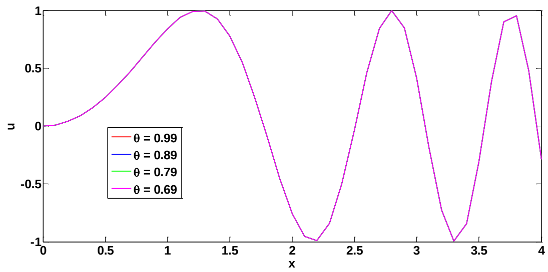

Fig. 3(a). Case 1: Solution profile for u when $t=0,\alpha=1.0$

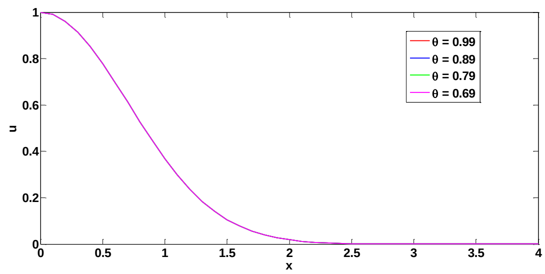

Fig. 3(b). Case 2: Solution profile for u when $t=0,\alpha=1.0$

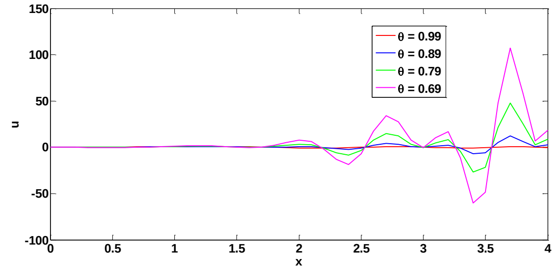

Fig. 4(a). Case 1: Solution profile for u when $t = 0, \alpha = 1.0$

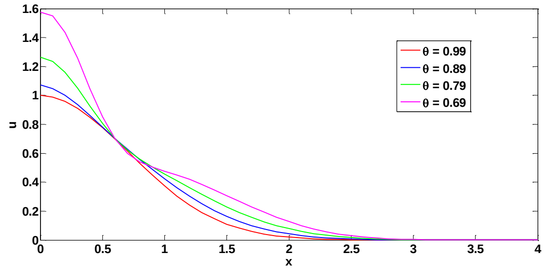

Fig. 4(b). Case 2: Solution profile for u when $t = 0, \alpha = 1.0$

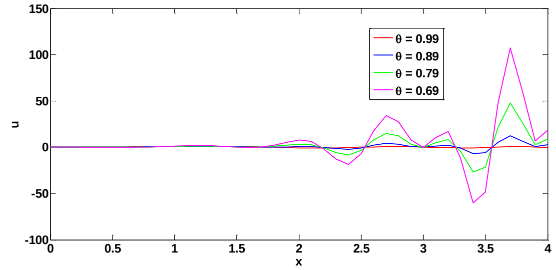

Fig. 5(a). Case 1: Solution profile for u when $t = 0, \alpha = 1.0$

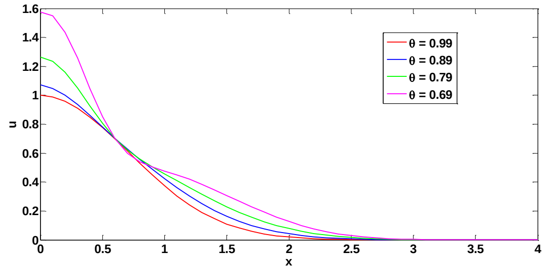

Fig. 5(b). Case 2: Solution profile for u when $t = 0, \alpha = 1.0$

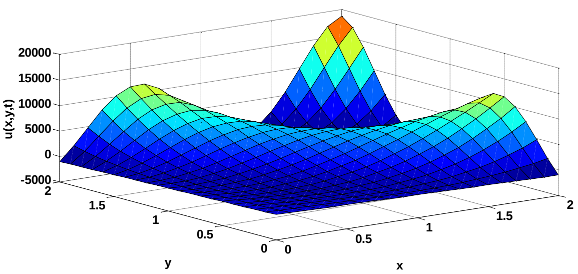

Fig. 6(a). Case 1: Solution profile for u when $\alpha = 1.0,\ \theta = 0.95, t = 20$

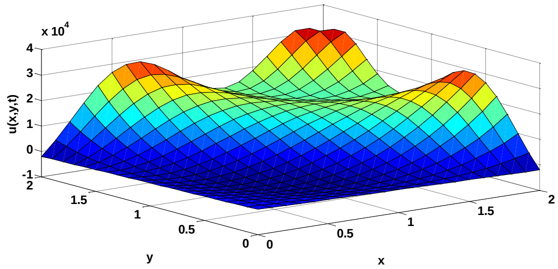

Fig. 6(b). Case 2: Solution profile for u when $\alpha = 2.0,\ \theta = 0.95, t = 20$

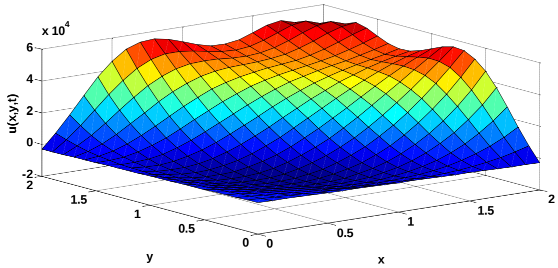

Fig. 6(c). Case 1: Solution profile for u when $\alpha = 3.0,\ \theta = 0.95, t = 20$

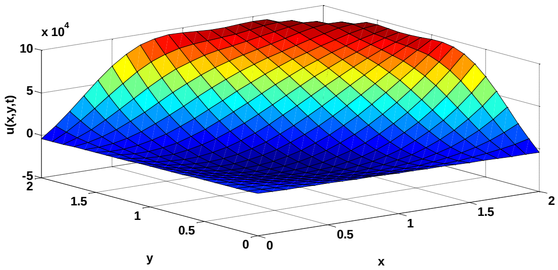

Fig. 6(d). Case 1: Solution profile for u when $\alpha = 4.0,\ \theta = 0.95, t = 20$

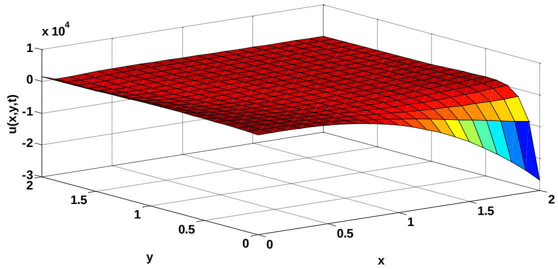

Fig. 7(a). Case 2: Solution profile for u when $\alpha = 1.0,\ \theta = 0.95, t = 20$

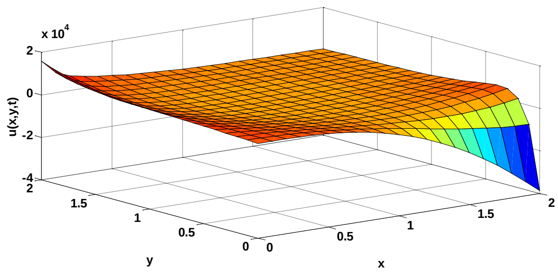

Fig. 7(b). Case 2: Solution profile for u when $\alpha = 2.0,\ \theta = 0.95, t = 20$

DOI 10.2478/ama-2023-0014

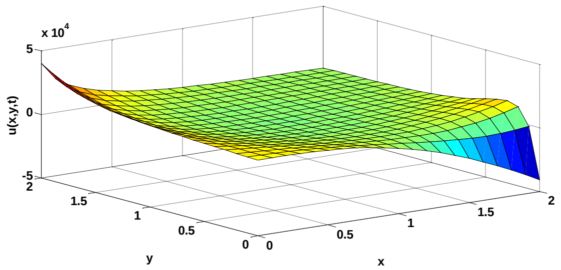

Fig. 7(c). Case 2: Solution profile for u when $\alpha = 3.0,\ \theta = 0.95, t = 20$

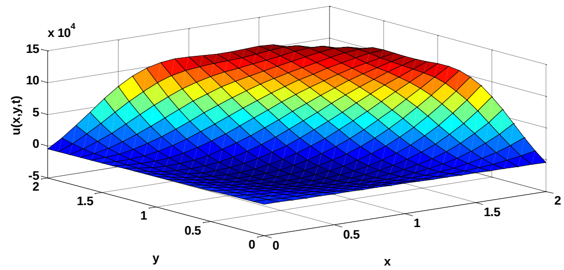

Fig. 8(d). Case 1: Solution profile for u when $\alpha = 4.0,\ \theta = 0.95, t = 20$

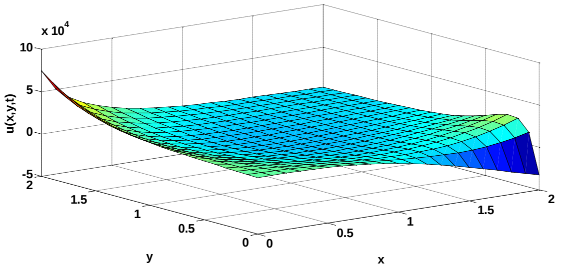

Fig. 7(d). Case 2: Solution profile for u when $\alpha = 4.0,\ \theta = 0.95, t = 20$

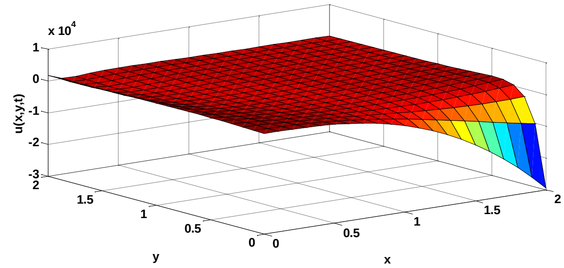

Fig. 9(a). Case 2: Solution profile for u when $\alpha = 1.0,\ \theta = 0.95, t = 20$

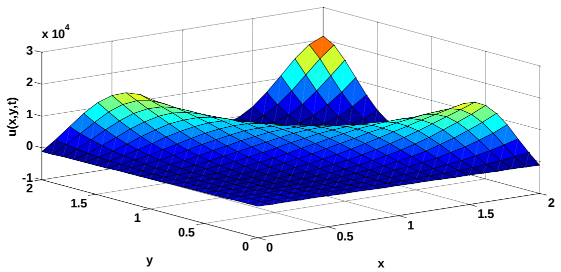

Fig. 8(a). Case 1: Solution profile for u when $\alpha = 1.0,\ \theta = 0.95, t = 20$

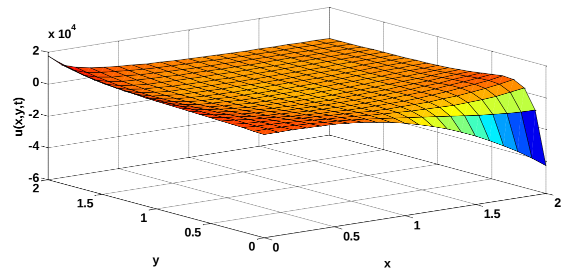

Fig. 9(b). Case 2: Solution profile for u when $\alpha = 2.0,\ \theta = 0.95, t = 20$

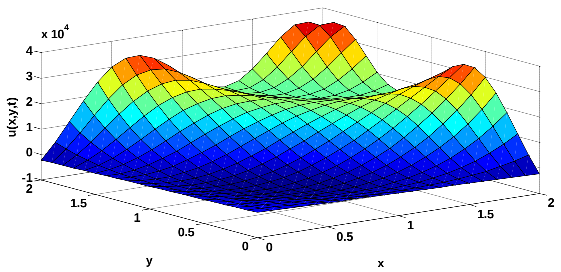

Fig. 8(b). Case 1: Solution profile for u when $\alpha = 2.0,\ \theta = 0.95, t = 20$

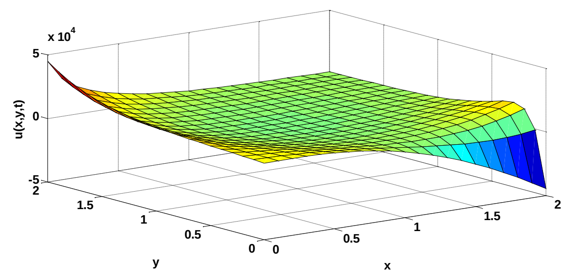

Fig. 9(c). Case 2: Solution profile for u when $\alpha = 3.0,\ \theta = 0.95, t = 20$

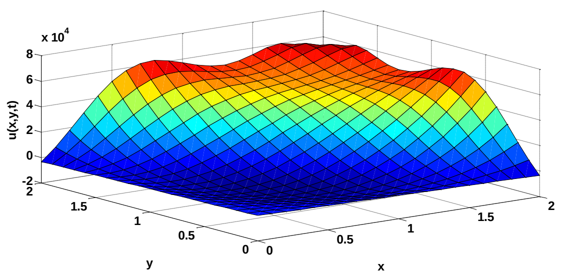

Fig. 8(c). Case 1: Solution profile for u when $\alpha = 3.0,\ \theta = 0.95, t = 20$

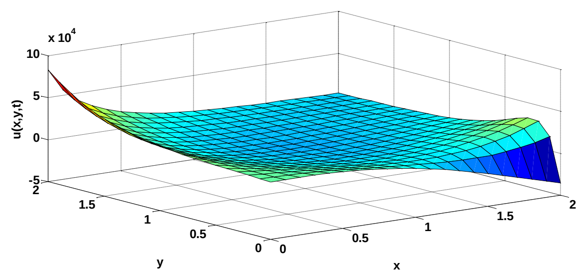

Fig. 9(d). Case 2: Solution profile for u when $\alpha = 4.0,\ \theta = 0.95, t = 20$

DOI 10.2478/ama-2023-0014

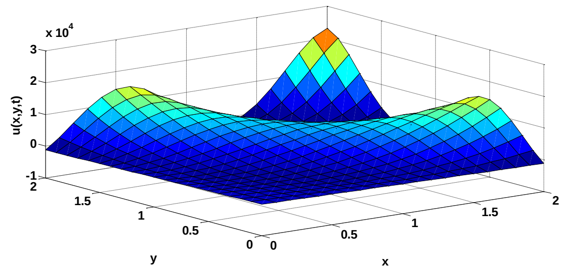

Fig. 10(a). Case 1: Solution profile for u
when $\alpha = 1.0,\ \theta = 0.95, t = 20$

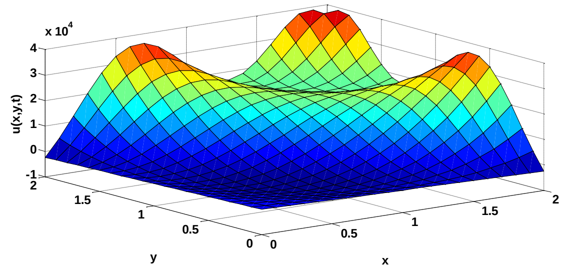

Fig. 10(b). Case 1: Solution profile for u
when $\alpha = 2.0,\ \theta = 0.95, t = 20$

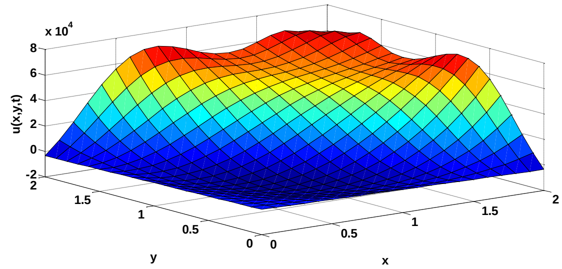

Fig. 10(c). Case 1: Solution profile for u
when $\alpha = 3.0,\ \theta = 0.95, t = 20$

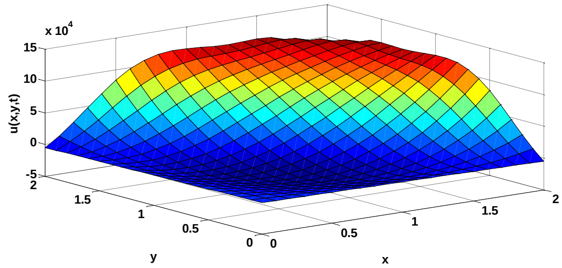

Fig. 10(d). Case 1: Solution profile for u
when $\alpha = 4.0,\ \theta = 0.95, t = 20$

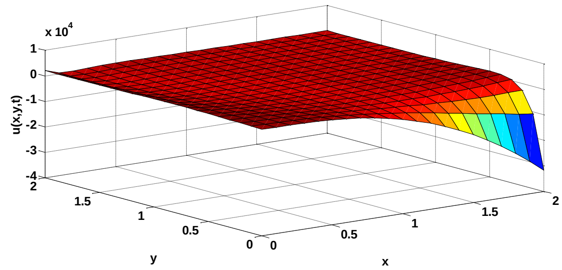

Fig. 11(a). Case 2: Solution profile for u
when $\alpha = 1.0,\ \theta = 0.95, t = 20$

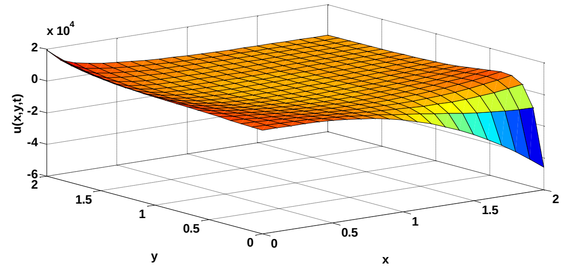

Fig. 11(b). Case 2: Solution profile for u
when $\alpha = 2.0,\ \theta = 0.95, t = 20$

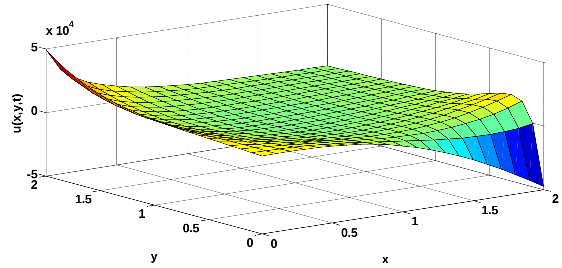

Fig. 11(c). Case 2: Solution profile for u
when $\alpha = 3.0,\ \theta = 0.95, t = 20$

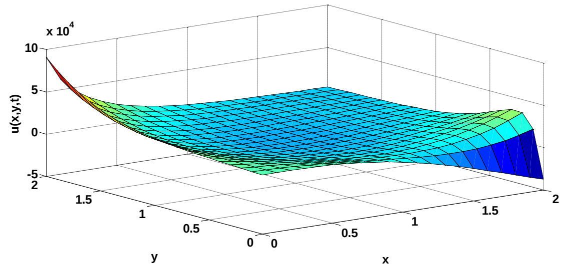

Fig. 11(d). Case 2: Solution profile for u
when $\alpha = 4.0,\ \theta = 0.95, t = 20$

The solution profiles for u over time when $\mathrm{x} = \mathrm{y} = 1$ and when the fluid viscosity is 1.0, using the three different fractional operators are presented in Figs.2(a)-(b).The solution profiles for u at initial time $\mathrm{t} = 0$ when the fluid viscosity is 1.0, using the Caputo fractional operator are presented in Figs.3(a)-(b). The solution profiles for u at initial time $\mathrm{t} = 0$ when the fluid viscosity is 1.0, using the Caputo-Fabrizio fractional operator are presented in Figs.4(a)-(b).The solution profiles for u at initial time $\mathrm{t} = 0$ when the fluid viscosity is 1.0, using the Atangana-Baleanu fractional operator are presented in Figs.5(a)-(b).The solution profiles for u at initial conditions $\mathrm{u}(\mathrm{x},\mathrm{y},0) = \sin(\mathrm{xy}), \mathrm{v}(\mathrm{x},\mathrm{y},0) = \sin(\mathrm{xy})$, over time, when the fluid viscosity α is varied from 1.0 to 4.0, and the fractional order $\theta = 0.95$, using the Atangana-Baleanu fractional operator are presented in Figs. 6(a)-(d). It is observed that as the viscosity is increased, the fluid velocity is stabilized.The solution profiles for u at initial conditions $\mathrm{u}(\mathrm{x},\mathrm{y},0) = \mathrm{e}^{-\mathrm{kxy}},\ \mathrm{v}(\mathrm{x},\mathrm{y},0) = \mathrm{e}^{-\mathrm{kxy}}$, over time, when the fluid viscosity α is varied from 1.0 to 4.0, and the fractional order $\theta = 0.95$, using the Atangana-Baleanu fractional operator are presented in Fig.ure 7(a)-(d).The solution profiles for u at initial conditions $\mathrm{u}(\mathrm{x},\mathrm{y},0) = \sin(\mathrm{xy}),\ \mathrm{v}(\mathrm{x},\mathrm{y},0) = \sin(\mathrm{xy})$, over time, when the fluid viscosity α is varied from 1.0 to 4.0, and the fractional order $\theta = 0.95$, using the Caputo fractional operator are presented in Figs. 8(a)-(d).The solution profiles foru at initial conditions $\mathrm{u}(\mathrm{x},\mathrm{y},0) = \mathrm{e}^{-\mathrm{kxy}},\ \mathrm{v}(\mathrm{x},\mathrm{y},0) = \mathrm{e}^{-\mathrm{kxy}}$, over time,

DOI 10.2478/ama-2023-0014

when the fluid viscosity α is varied from 1.0 to 4.0, and the fractional order $\theta = 0.95$, using the Caputo fractional operator are presented in Figs. 9(a)-(d).The solution profiles for u at initial conditions $u(x,y,0) = \sin(xy)$, $v(x,y,0) = \sin(xy)$, over time, when the fluid viscosity α is varied from 1.0 to 4.0, and the fractional order $\theta = 0.95$, using the Caputo-Fabrizio fractional operator are presented in Fig.ure 10(a)-(d).The solution profiles for u at initial conditions $u(x,y,0) = e^{-kxy}$, $v(x,y,0) = e^{-kxy}$, over time, when the fluid viscosity α is varied from 1.0 to 4.0, and the fractional order $\theta = 0.95$, using the Caputo-Fabrizio fractional operator are presented in Figs. 11(a)-(d). It is observed from the figures that as the viscosity is increased, the fluid velocity is stabilized.

It is also worth stating that the CPU time using the Caputo fractional operator was 0.863006 seconds. Using the Caputo-Fabrizio operator, the CPU time was 0.954948 seconds while with the AB fractional operator the CPU time was 0.860035 seconds.

3. CONCLUSION

In this work, a coupled system of time-fractional modified Burgers' equations with appropriate initial values is solved using the Laplace Adomian decomposition method. Three different fractional operators: Caputo, Caputo-Fabrizio and Atangana-Baleanu operators are considered for the equations. Also, two different scenarios are examined for each fractional operator: when the initial conditions are $u(x,y,0) = \sin(xy)$, $v(x,y,0) = \sin(xy)$, and when they are $u(x,y,0) = e^{-kxy}$, $v(x,y,0) = e^{-kxy}$, where k, α are some positive constants. With the aid of computable Adomian polynomials, the solutions are obtained. The method does not need linearization, weak nonlinearity assumptions or perturbation theory. Simulations are also presented to support theoretical results, and the behaviour of the solutions under the three different fractional operators compared.

Future work shall consider other numerical schemes such as singular boundary and dual reciprocity methods on the current coupled system. We shall also consider modified Burgers equations with higher order dissipation term.

REFERENCES

1. Caputo M. Linear models of dissipation whose Q is almost frequency independent, Annals of Geophysics 196;19(4):383-393.
2. Caputo M, Fabrizio M. A new definition of fractional derivative without singular kernel, Progress in Fractional Differentiation and Applications 2015;1(2):1-3.
3. Atangana A, Baleanu D. New fractional derivatives with nonlocal and non-singular kernel: theory and applications to heat transfer model, Therm Sci. 2016;20(2):763-769.
4. Li L, Li D. Exact solutions and numerical study of time fractional Burgersequations,Applied Mathematics Letters, 2020;100:106011 https://doi.org/10.1016/j.aml.2019.106011.
5. Agheli B, Darzi R. Analysis of solution for system of nonlinear fractional Burger differential equations based on multiple fractional power series, Alexandria Engineering Journal, 2017;56(2):271-276, https://doi.org/10.1016/j.aej.2016.12.021.
6. Kaya D. An explicit solution of coupled viscous Burgers equation by the decomposition method, International Journal of Mathematics and Mathematical Sciences, 2001;27:802356. https://doi.org/10.1155/S0161171201010249
7. Majeed A, Kamran M, Iqbal MK. Baleanu D. Solving time fractional Burgers and Fisher's equations using cubic B-spline approximation method. Adv Differ Equ 2020;175. https://doi.org/10.1186/s13662-020-02619-8
8. Singh J, Kumar D, Qurashi MA, Baleanu D. Analysis of a New Fractional Model for Damped Bergers' Equation, Open Physics, 2017;15(1):35-41. https://doi.org/10.1515/phys-2017-0005
9. Esen A, Yagmurlu NM, Tasbozan O. Approximate Analytical Solution to Time- Fractional Damped Burger and Cahn- AllenEquations, Appl. Math. Inf. Sci., 2013;7(5):1951-1956.
10. Alsaedi A, Baleanu D, Etemad S, Rezapour S. On coupled systems of time-fractional differential problems by using a newfractional derivative, Journal of Function Spaces, 2016:4626940, https://doi.org/10.1155/2016/4626940.
11. Safari F, Chen W. Numerical approximations for space-time fractional Burgers equations via a new semi-analytical method, Comput Math Appl, 2021;96:55-66, https://doi.org/10.1016/j.camwa.2021.03.026.
12. Safari F, Sun H. Improved singular boundary method and dual reciprocity method for fractional derivative Rayleigh-Stokes problem. Engrg Comput 2021;37:3151-3166 . https://doi.org/10.1007/s00366-020-00991-3
13. Safari F, Chen W. Coupling of the improved singular boundary method and dual reciprocity method for multi-term time-fractional mixed diffusion-wave equations, Comp Math Appl, 2019;78(5):1594-1607, https://doi.org/10.1016/j.camwa.2019.02.001.
14. Safari F, Jing L, Lu J, Chen W. A meshless method to solve the variable-order fractional diffusion problems with fourth-order derivative term, Engrg Anal Bound Elem, 2022;143:677-686, https://doi.org/10.1016/j.enganabound.2022.07.012.
15. Jafari H, Khalique CM, Nazari M. Application of the Laplace decomposition method for solving linearand nonlinear fractional diffusion-wave equations. Appl. Math. Lett. 2011;24:1799-1805.
16. Carpinteri A, Mainardi F. Fractals and Fractional Calculus in continuum mechanics, Springer-Verlag Wien GmbH, 1997.
17. Mohamed ZM, Hamza AE, Sedeeg AKH. Conformable double Sumudu transformations an efficient approximation solutions to the fractional coupled Burgers equation, Ain Shams Engineering Journal, 2022:101879,https://doi.org/10.1016/j.asej.2022.101879.
18. Mohamed ZM, Yousif M, Hamza AE. Solving Nonlinear Fractional Partial Differential Equations Using the Elzaki Transform Method and the Homotopy Perturbation Method, Abstract and Applied Analysis, 2022:4743234, https://doi.org/10.1155/2022/4743234
19. Mohamed ZM, Elzaki TM, Algolam MS, Abd Elmohmoud EM, Hamza AE. New Modified Variational Iteration Laplace Transform Method Compares Laplace Adomian Decomposition Method for Solution Time-Partial Fractional Differential Equations, J. Appl. Math, 2021:6662645, https://doi.org/10.1155/2021/6662645

Acknowledgments: Authors are most thankful to the handling editor and reviewers for their constructive suggestions and queries which has greatly helped in improving the quality of the manuscript.

Andrew Omame: https://orcid.org/0000-0002-1252-1650

Fiazud Din Zaman: https://orcid.org/0000-0002-6498-0664

sciendo
DOI 10.2478/ama-2023-0015
acta mechanica et automatica, vol.17 no.1 (2023
Special Issue "Computational Technologies in Engineering TKI2022"

FAILURE ANALYSIS OF BEAM COMPOSITE ELEMENTS SUBJECTED TO THREE-POINT BENDING USING ADVANCED NUMERICAL DAMAGE MODELS

Patryk RÓŻYŁO*

*Faculty of Mechanical Engineering, Department of Machine Design and Mechatronics, Lublin University of Technology, ul. Nadbystrzycka 36, 20-618 Lublin, Poland

p.rozylo@pollub.pl

received 11 November 2022, revised 4 December 2022, accepted 4 December 2022

Abstract: This paper deals with the experimental and numerical analysis of three-point bending phenomenon on beam composite profiles. Flat rectangular test specimens made of carbon–epoxy composite, characterised by symmetric [0/90/0/90]s laminate ply lay-up, were used in this study. Experimental testing was carried out with a COMETECH universal testing machine, using special three-point bending heads. In addition, macroscopic evaluation was performed experimentally using a KEYENCE Digital Microscope with a mobile head recording real-time images. Parallel to the experimental studies, numerical simulations were performed using the finite element method in ABAQUS software. The application of the above-mentioned interdisciplinary research techniques allowed for a thorough analysis of the phenomenon of failure of the composite material subjected to bending. The obtained research results provided a better understanding of the failure mechanism of the composite material.

Key words: three-point bending, carbon–epoxy laminate, numerical simulation, experimental tests, finite element method, failure

1. INTRODUCTION

Beam composite structures are commonly used for stiffening elements in the aerospace, construction and automotive industries. These types of structures are primarily subjected to compression and bending. In the case of compression of beam structures, many additional phenomena occur, such as loss of stability and complex failure mechanism, as described in detail by the authors of many research papers [1–3]. The prediction of the maximum load of composite structure is still very desirable. The composite materials are still expansive group of materials which are characterised by the occurrence of multiple complex forms of damage, thus requiring in-depth research. Besides a series of already known behaviours of beam composite structures that occur in axial [4], or eccentric compression [5–9], it is also important to know the behaviour of the structure, in bending [10–14]. The cognitive value of the behaviour of beam structures made of composite materials is still very important, and despite the many studies conducted in this area, the behaviour of the structure subjected to bending taking into account the complex failure mechanism is not yet clearly defined.

Beam composite structures, regardless of the loading conditions to which they are subjected, are currently an area of interest for many researchers [15–18]. In the case of the bending behaviour of a structure, it is necessary to be able to correctly analyse the damage forms occurring as a result of the loading process on the structure. It is essential, above all, to estimate the loads that cause the limit states of the bending structure, as well as to register the damage forms that appear during the failure tests. Consequently, it is important to understand how to identify the damage phases that occur during testing. The above demands a comprehensive analysis, both on the basis of experimental studies and numerical simulations, using the finite element method (FEM), which enables to characterise the complex phenomenon of composite material failure, including the phenomena directly accompanying the failure [19–27]. The main theory that allows assessment of the damage initiation phenomenon in the case of composite materials–laminates is the first ply failure (FPF) theory [28]. This theory assumes that composite failure occurs when the first layer of the composite is damaged. The damage initiation can be determined by many factors, such as damage to the fibres or matrix of the composite material. Besides damage initiation, there are other phenomena that contribute to the failure of the composite material, such as delamination. It is important to evaluate the phenomena contributing to the degradation of the composite material structure.

The evaluation of the failure phenomenon is slightly different for experimental studies and numerical simulations using FEM. In the case of experimental research, usually the testing instruments such as universal testing machine (UTM) [19], acoustic emission method equipment [29] and others are used to evaluate the failure phenomenon of beam composite materials. As part of the experimental study, it is possible to estimate both loads and register damage forms of beam structures made of laminates [19, 27]. On the other hand, numerical simulations allow for a thorough estimation of any phenomena which directly contribute to the loss of load-carrying capacity of composite structures. Within the framework of numerical simulations using FEM, it is possible, among other things, to accurately determine the damage initiation phenomenon of a composite material using special damage models.

The widely used method of damage initiation assessment is based on the Hashin's criterion [30]. Based on the Hashin criterion, it can be evaluated whether the damage occurred due to failure of the fibres or matrix of the composite material, through compression or tension. This criterion allows assessment of damage initiation; however, after further consideration of the energy criterion, it is also possible to assess the damage evolution. Generally, the damage model allowing for damage initiation based on the Hashin criterion and damage evolution based on the energy criterion is called progressive failure analysis (PFA) [31–33]. The fundamentals of the described issues are based on the continuum damage mechanics (CDM) [34, 35], where the beginnings of the damage mechanisms description were presented in the paper [36], and the first model taking into account especially the damage initiation phenomenon within the framework of numerical simulations in the ABAQUS program was presented in the paper [37]. Many contemporary researchers have dealt with the analysis of the failure phenomenon of beam composite materials based on PFA, beginning with the paper [38] to more recent papers [39, 40]. Moreover, other very advanced damage models are available, which allow the simulation of delamination – a method based on the cohesive zone model (CZM). The above model provides an assessment of composite material damage as a result of simulation of permanent rupture of the connection between the constituent layers of the composite (both in the damage initiation – usually based on the criterion of maximum nominal stress (MAXS) and damage evolution, based on the energy criterion) [41–43]. The above-mentioned damage model is based on the traction-separation law (which describes the relationship between traction-stress in the material interface and adequate displacement peak, between two parts of a material being separated) [44, 45], where a graphical representation of this law is shown in the paper [46]. The phenomenon of delamination-induced damage has been thoroughly demonstrated in many research papers [47–52]. Furthermore, a commonly used damage model is the eXtended finite element method (XFEM), which allows the simulation of material cracking (fracture) [53–56]. The above-mentioned model offers the ability to reproduce the entire crack geometry independently of the adopted mesh, so that no sophisticated mesh is needed to model the crack growth. The methods described above allow evaluation of the complex failure mechanism of the composite material.

The scope of the study was primarily to conduct experimental tests and numerical simulations (using FEM) [57] of three-point bending of a beam composite structure. The experimental tests were carried out using a UTM and a digital microscope with a mobile head that allows recording the damage state of the composite material. In the case of numerical simulations, nonlinear analysis was carried out, taking into account two advanced damage models: a CZM allowing simulation of the delamination phenomenon (CZM) and a model allowing simulation of material crack initiation and propagation (XFEM). The use of independent numerical damage models allows a comprehensive assessment of the damage phenomenon [58, 59], which was verified experimentally [19, 20, 60]. It is necessary to employ interdisciplinary and independent research methods allowing for description of composite failure [61–66]. The primary objective of this study was to develop complex numerical models that allow for a comprehensive evaluation of the failure phenomenon enabling a better understanding of the experimental results.

2. METHODOLOGY OF THE STUDY

The test specimens were made of carbon–epoxy composite using autoclave technique. Ultimately, six specimens were prepared for experimental testing. The geometry of the specimens was selected so as to perform three-point bending tests over the full load range. The above-mentioned method of manufacturing of beam multilayer composite materials enabled to obtain a material structure with high structural properties, as well as the proportion of fibres relative to the whole structure in the range of 55%–60%, which is described in more detail in the papers [67, 68]. The use of the mentioned technique allows the production of composite profiles with high quality of material structure [67]. The columns under consideration were made by autoclaving technique using a vacuum package made on a special mould reproducing the shape and dimensions of the manufactured beams. The prepared hermetic package ensuring the maintenance of a vacuum of value of about −0.1 MPa was subjected to the polymerisation process in a laboratory autoclave, ensuring the required pressure by creating an additional overpressure in the autoclave of 0.4 MPa. In the case of the carbon–epoxy composite, a material heating temperature of 135°C for about 2 h was used to ensure completion of the pre-preg polymerisation process (Fig. 1.). In order to eliminate unfavourable phenomena that can occur during the manufacturing process (excessive increase of thermal stresses in the material and limitation of proper relaxation of primary and thermal stresses), precise control of the heating and cooling rate of 0.033 K/s was applied.

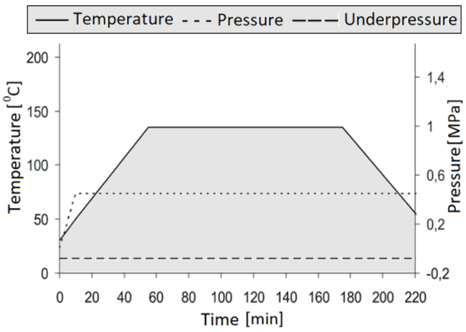

Fig. 1. Process of composite manufacturing

The manufactured composite specimens were characterised by a symmetrical stacking sequence of laminate layers [0/90/0/90]s which may be otherwise represented as [0/90/0/90/90/0/90/0]. The specimens consisted of eight layers, where the length and width of the specimens were 135 mm and 15 mm, respectively, and the thickness of each individual layer was 0.131 mm. A graphical representation of the test specimen is presented in Fig. 2.

The material properties of test specimens (six samples) were determined based on static tensile PN-EN ISO 527-5, compression PN-EN ISO 14126 as well as shear test PN-EN ISO 14129. The determined material properties were determined using the UTM – Tab. 1 [4, 19–21, 49, 64, 67, 69].

The experimental investigations were conducted primarily using a UTM COMETECH model QC-508 (type M2F). The machine was equipped with an NTS load cell with a maximum capacity of 2.5 kN. The machine had a special module for performing three-point bending tests. All the test parameters such as force and

DOI 10.2478/ama-2023-0015
acta mechanica et automatica, vol.17 no.1 (2023
Special Issue "Computational Technologies in Engineering TKI2022"

displacement were registered using the Amis-Plus 1.5.6 software. The experimental tests were carried out at room temperature with a constant crosshead speed of 2 mm/min [70]. Moreover, a modern digital microscope from KEYENCE (model VHX 970F) was used in the experimental studies. The microscope had a special module containing a mobile (portable) measuring head, which was extremely useful in the framework of the conducted experimental tests of three-point bending. The mobile (portable) microscope head allowed for image capture with a maximum zoom of 200×, while in the present study a zoom of 30× was used, covering the most important area of damage to the laminate during the conducted tests. In addition, a special mechanical articulated arm having an attachment to a mobile (portable) digital microscope head was also used in the experimental study. The use of this arm made it possible to properly mount the microscope head in such a way as to be able to record the image associated with the area of damage to the composite structure. The test stand accessories are shown in Fig. 3.

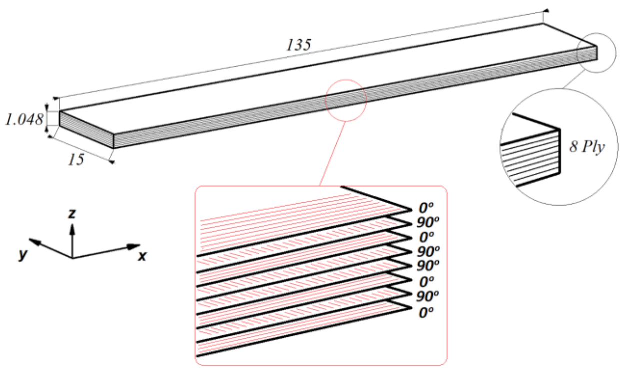

Fig. 2. Graphical representation of test specimens

Tab. 1. Mechanical properties of the composite material [19, 67, 68]

Mechanical Properties		Strength Properties	
Young' Modulus E_1 [MPa]	130710	Tensile Strength (0°) F_{T1} [MPa]	1867
Young' Modulus E_2 [MPa]	6360	Compressive Strength (0°) F_{C1} [MPa]	1531
Poisson's Ratio v_{12} [-]	0.32	Tensile Strength (90°) F_{T2} [MPa]	26
Kirchhoff modulus G_{12} [MPa]	4180	Compressive Strength (90°) F_{C2} [MPa]	214
		Shear Strength F_{12} [MPa]	100

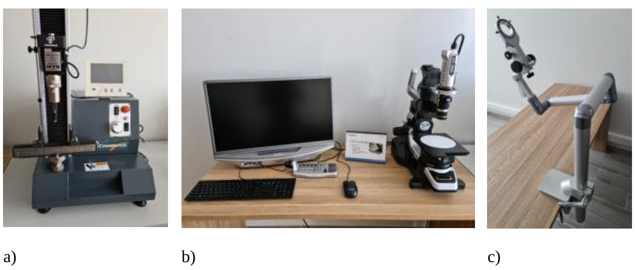

Fig. 3. Test stand: (a) UTM with three-point bending head, (b) digital microscope with mobile head and (c) articulated arm for microscope head

Experimental tests were carried out using the testing devices presented above, which made it possible to realise the process of three-point bending with simultaneous recording of test parameters, such as the force–displacement relationship, as well as recording of laminate failure forms. The tests were conducted in such a way that, in addition to recording the loading force and the displacement of the crosshead, the damage forms of the composite specimens were also registered, using a mobile microscope head mounted on an articulated arm, at a distance that allowed the correct recording of the images in digital form. The test stand during the experimental trials conducted is shown in Fig. 4.

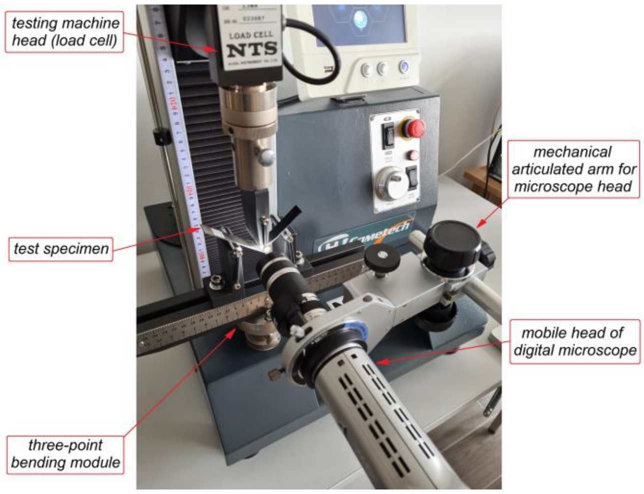

Fig. 4. Test stand during three-point bending test

During the experimental tests, loads corresponding to the loss of load-carrying capacity of the structure were registered, where complex phases of laminate failure such as fibre failure and delamination were observed, which was the direct cause of the decrease in load carried by the structure. The failure of the structure was observed both in the Amis-Plus 1.5.6 software, which was used to generate force–displacement characteristics, as well as within complex failure forms captured using a digital microscope head.

Numerical simulations using the FEM were conducted in ABAQUS. This advanced computational software made it possible to perform a comprehensive nonlinear analysis, including composite material failure (using static analysis). In the framework of numerical simulations, the author's numerical model was prepared in order to precisely represent the actual process of three-point bending realised on beam composite structures. The prepared finite element analysis (FEA) model had a material model with parameters compatible with the material properties shown in Tab. 1 (using Engineering Constants approach). The numerical model was developed to ensure full reproduction of the boundary conditions that actually occurred in the experimental studies. The numerical calculations were realised based on the Newton–Raphson incremental-iterative method, which is presented in detail in the paper [71]. The finite element (FE) models generated in ABAQUS program are usually nonlinear (and can involve from a few to thousands of variables). Regarding the above, the equilibrium equations obtained by discretising the virtual work equation can be represented using the equation:

$$F^N(u^M) = 0 \tag{1}$$

DOI 10.2478/ama-2023-0015

where F^N denotes the force component conjugate to the N^{th} variable in the problem and u^M constitutes the value of the M^{th} variable.

Numerical calculations generally use Newton's method (as a numerical method for solving the nonlinear equilibrium equations). The motivation for this choice is the convergence rate obtained by using the above-mentioned method compared with the modified Newton or quasi-Newton methods. Assume that, after an iteration i, an approximation uiM to the solution has been reached. Moreover, let ci+1M be the difference between this solution and the exact solution to the discrete equilibrium presented within the framework of Eq. (1). Regarding the above:

$$F^N(u_i^M + c_{i+1}^M) = 0 \tag{2}$$

By expanding the left-hand side of this equation (Taylor series) to an approximate solution, one obtains:

$$F^N(u_i^M) + \frac{\partial F^N}{\partial u^P}(u_i^M)c_{i+1}^P + \frac{\partial^2 F^N}{\partial u^P \partial u^Q}(u_i^M)c_{i+1}^P c_{i+1}^Q + .. = 0 \tag{3}$$

When u_i^M is a close approximation to the solution, the magnitude of any c_{i+1}^M will be small, so all of the above conditions except the first two can be neglected, giving a linear form of equations:

$$K_i^{NP} c_{i+1}^P = -F_i^N, \;\; K_i^{NP} = \frac{\partial F^N}{\partial u^P}(u_i^M), \;\; F_i^N = F^N(u_i^M) \tag{4}$$

A further approximation of the solution is:

$$u_{i+1}^M = u_i^M + c_{i+1}^M \tag{5}$$

and the iteration continues. The above relations describe the procedure of the method used to solve the nonlinear problem.

One of two damage models that was used to simulate the failure phenomenon was the CZM [19, 72]. The CZM allowed for the evaluation of the regions affected by delamination in the bending composite profiles. The above-mentioned damage model was based on a delamination technique using a cohesive surfaces approach. Numerical simulations were performed using the delamination technique based on the traction-separation law. The mechanical behaviour (in the elastic range) of the cohesive layer is characterised by nominal traction stress vector Eq. (6) [46, 73]:

$$t = \begin{Bmatrix} t_n \\ t_s \\ t_t \end{Bmatrix} = \begin{bmatrix} K_{nn} & K_{ns} & K_{nt} \\ K_{ns} & K_{ss} & K_{st} \\ K_{nt} & K_{st} & K_{tt} \end{bmatrix} \begin{Bmatrix} \delta_n \\ \delta_s \\ \delta_t \end{Bmatrix} = K\delta. \tag{6}$$

where t, t_n, t_s and t_t are tractions in the cohesive layer; K, K_{nn}, K_{ss} and K_{tt} represent the cohesive layer stiffness and δ, δ_n, δ_s and δ_t are separation displacement of the cohesive layer (in global, normal, shear and transverse shear directions).

The damage initiation within the CZM for the numerical model adopted for the study was based on the MAXS criterion – MAXS. Damage initiation occurs when the relationship describing the damage initiation achieves a value of 1 [46, 73]:

$$\max\left\{\frac{\langle t_n \rangle}{t_n^0}, \frac{t_s}{t_s^0}, \frac{t_t}{t_t^0}\right\} = 1. \tag{7}$$

where t_n^0, t_s^0 and t_t^0 are peak values of the contact stress (when the separation is either purely normal, shear or transverse shear direction to the interface of material) and ⟨ ⟩ denotes Macaulay bracket (purely compressive stresses/strains do not cause damage initiation).

When the damage initiation is fulfilled, further loading of the composite structure causes damage evolution phenomenon. The damage evolution law describes the rate at which the cohesive stiffness is degraded once the corresponding damage initiation criterion is reached. In the case of damage evolution, the damage parameter D has been defined. A scalar damage parameter (monotonically evolves from 0 to 1), defines the overall damage directly at the contact point in the composite material. The contact stress components, in terms of the traction-separation law, are defined by appropriate conditions and expressed by the following relationships [46, 73]:

$$t_n = \begin{cases} (1-D)\bar{t_n}, & \bar{t_n} \geq 0 \\ \bar{t_n}, & \text{otherwise} \end{cases} \tag{8}$$

$$t_s = (1-D)\bar{t_s}, \tag{9}$$

$$t_t = (1-D)\bar{t_t}, \tag{10}$$

where $\bar{t_n}$, $\bar{t_s}$ and $\bar{t_t}$ represent the stress components which were determined on the basis of the elastic traction-separation behaviour for the current separations (without material damage).

In order to describe the damage evolution under a combination of normal as well as shear separations (across the interface), it is useful to introduce an effective separation [72, 73]:

$$\delta_m = \sqrt{\langle \delta_n \rangle^2 + \delta_s^2 + \delta_t^2} \tag{11}$$

In the present study, the energy criterion was used to describe the damage evolution (using fracture energy parameters). Damage evolution phenomenon was defined using the Benzeggagh–Kenane (B–K) energy criterion [41]. Regarding the adopted damage evolution criterion, it is necessary to define the parameters: G_n^C, G_s^C as well as η. Regarding the above-mentioned criterion, $G_s^C = G_t^C$. The above-mentioned criterion is represented by the following relationships [46, 73]:

$$G^C = G_n^C + (G_s^C - G_n^C)\left\{\frac{G_S}{G_T}\right\}^\eta, \tag{12a}$$

$$G_S = G_s + G_t, \;\; G_T = G_n + G_s + G_t, \tag{12b}$$

where G_n, G_s and G_t denote parameters (fracture energies) which constitute the work done by the tractions and their conjugate relative displacement (in the normal, first and second shear directions); G^C denotes (mixed-mode) critical fracture energy; G_n^C, G_s^C and G_t^C are the parameters of critical fracture energies causing failure (in the normal, first and second shear directions); G_S represents the amount of total work done by the shear traction and the corresponding relative displacement components; G_T is the total work done by the normal and shear traction based on energies; and η represents the cohesive property parameter.

For the linear approach under damage evolution, in the framework of numerical simulations, the damage parameter is presented as [46, 73]:

$$D = \frac{\delta_m^f(\delta_m^{max} - \delta_m^0)}{\delta_m^{max}(\delta_m^f - \delta_m^0)} \tag{13}$$

where δ_m^f, δ_m^0 and δ_m^{max} represent the parameters of effective separation at complete failure ($\delta_m^f = 2G^C/T^0_{eff}$, and T^0_{eff} denotes the effective traction at damage initiation), at damage initiation, as well as at the maximum measured value during loading history.

In order to better represent the CZM, Fig. 5 shows the constitutive traction-separation law – CZM [46].

DOI 10.2478/ama-2023-0015

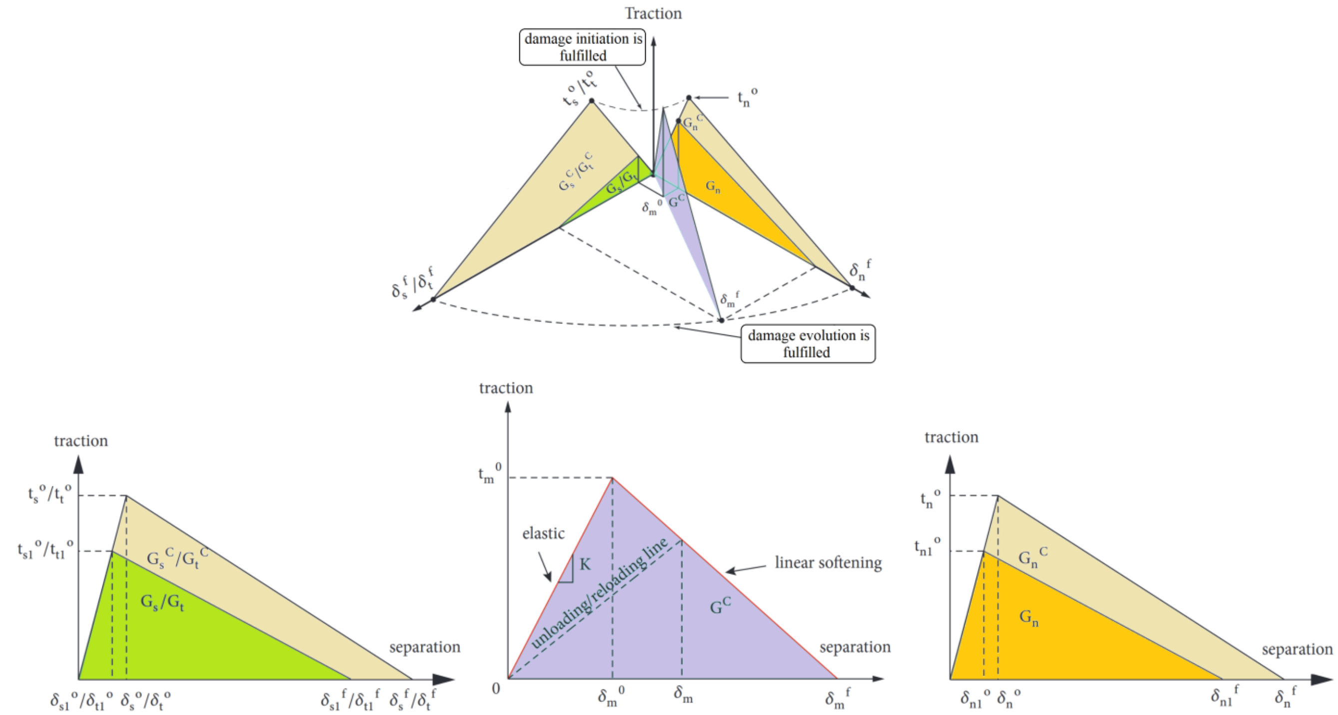

Fig. 5. Constitutive traction-separation law – CZM

The second damage model that was used in the study was the XFEM model. The MAXS criterion was used to determine the beginning of crack initiation phenomenon. Modelling discontinuities (crack) with the conventional FEM demands that the mesh conforms to the geometric discontinuities. Consequently, the XFEM was introduced (alleviates the need to create a conforming mesh). The present method was initially introduced in the framework of paper [74], which was a further extension of the method based on the concept of partition of unity [75] that allows local enrichment functions to be easily incorporated using FE approximation. The presence of (eventually) discontinuities is ensured using the enriched functions in conjunction (with additional degrees of freedom). The above-mentioned model is very attractive to simulate initiation as well as propagation of a discrete crack process. The XFEM method alleviates some deficiencies closely associated with meshing crack surfaces [74]. The damage simulation method described above enables simulating the propagation of discontinuities independently of the original FE mesh. The propagation of discontinuities (cracking) is represented by a displacement approximation function which was expressed as follows [73, 76, 77]:

$$u = \sum_{i=1}^{N} N_i(x)\left[u_i + H(x)a_i + \sum_{\alpha=1}^{4} F_\alpha(x) b_i^\alpha\right] \tag{14}$$

where $N_i(x)$ constitutes the usual nodal (displacement) shape functions; u_i represents the usual nodal displacement vector which was closely associated with the continuous part of the FE solution; a_i is additional degree of freedom of the element node penetrated by the crack tip; $H(x)$ denotes the discontinuous jump function – across the crack surfaces; b_i^α is vector of enriched nodes degree of freedom; and $F_\alpha(x)$ denotes the elastic asymptotic crack-tip functions (approximate expression of displacement field function at the crack tip).

The discontinuous jump function $H(x)$ is given the form [76, 77]:

$$H(x) = \begin{cases} +1, & if\ (x - x^*) \cdot n \geq 0 \\ -1, & otherwise \end{cases} \tag{15}$$

where x defines a Gaussian integration point; x^* denotes the point on the crack closest to x; n is the normal vector outside the crack at x^*; and $H(x)$ indicates the element penetrated by the crack surface (which is 1 on the positive, and −1 on the negative side of the crack).

In addition, the crack tip local coordinate system [73, 76] is presented in Fig. 6 for better understanding of the issues described.

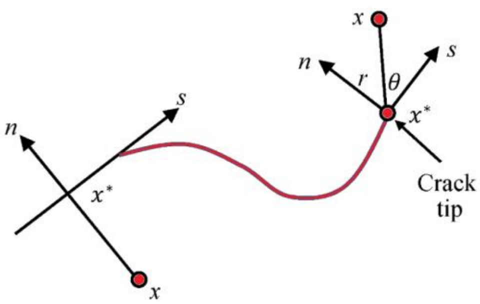

Fig. 6. Crack tip local coordinate system

The asymptotic crack tip functions in elastic material (approximate expression of displacement field function at the crack tip) $F_\alpha(x)$, is presented as [76, 77]:

$$F_\alpha(x) = \left[\sqrt{r} \cdot sin\frac{\theta}{2}, \sqrt{r} \cdot cos\frac{\theta}{2}, \sqrt{r} \cdot sin\theta \cdot sin\frac{\theta}{2}, \sqrt{r} \cdot sin\theta \cdot cos\frac{\theta}{2}\right] \tag{16}$$

where (r, θ) denote a local polar coordinate system defined and the crack tip (with its origin at the crack tip) θ=0 is tangent to the

DOI 10.2478/ama-2023-0015

crack at the tip.

In the case of simulation of crack growth (using the XFEM technique), it is necessary to define both damage initiation (fracture initiation) as well as damage evolution criterion of the materials. Crack initiation (damage initiation) refers to the beginning of degradation of the cohesive response directly at an enriched element. Moreover, the degradation process begins when the stresses (or the strains) satisfy the specified damage initiation criteria. In the case of this study, the MAXS criterion was used (corresponding to the damage initiation criterion for the CZM, as described earlier). The above-mentioned criterion can be represented as [73, 77]:

$$f = max\left\{\frac{\langle t_n \rangle}{t_n^0}, \frac{t_s}{t_s^0}, \frac{t_t}{t_t^0}\right\}. \quad (17)$$

where t_n, t_s, t_t are the normal and two shear component to the likely cracked surface; t_n^0, t_s^0, t_t^0 – are the peak values of the nominal stress; $\langle\ \rangle$ denotes Macaulay bracket (used to signify that a purely compressive stress state does not cause (initiate) damage; and damage is assumed to initiate when the MAXS ratio reaches a value of 1).

Similarly to the previous description concerning the CZM, when the damage initiation is satisfied, further loading of the composite structure causes damage evolution phenomenon (based on the energy criterion). When damage initiation criterion is achieved, a linear energy-based softening controlled by the B–K-Law is applied [41, 77], as was in the case with the previously described CZM damage model. Numerical simulations (using FEM) were carried out based on the prepared numerical model which considered previously described damage simulation techniques (CZM and XFEM). In the numerical simulations, the aforementioned two damage models were applied simultaneously within the numerical model in order to allow for both delamination (CZM) and material fracture (XFEM) damage phenomena of the composite material. In this study, the material model of Lamina type (elastic parameters with fail stress) was used. The composite material had orthotropic properties (where basic material data are shown in Tab. 1). Regarding the use of two advanced damage models, the parameters of the CZM as well as XFEM [78] were applied, as presented in Tab. 2.

Tab. 2. CZM and XFEM parameters

Damage initiation stress in normal direction t_n [N/mm^2]	Damage initiation stress in normal direction t_s, t_t [N/mm^2]	Fracture energy in normal direction G_n^C [N/mm]	Fracture energy in first and second shear direction G_s^C, G_t^C [N/mm]
18	14	0.32	0.68

During the preparation of the numerical model, each of the eight composite layers (the thickness of each layer was 0.131 mm) was modelled separately. The composite structures are usually modelled using the method of modelling the laminate as a multilayer composite, modelled using the Conventional or Continuum Shell method [19, 67]. The above approach in modelling of the composite structure allowed the simulation of complex failure phenomena, including delamination and material cracking. The composite structure was prepared using *3D Stress* technique – based on regular hexagonal mesh, using solid FEs *C3D8R* (where each of the FE is characterised by having 8-nodes, 3 degrees of freedom in each node of the FE, linear shape function and reduced integration). In addition, three identical non-deformable objects used to support the deformable composite structure were modelled in the numerical simulations. The non-deformable cylindrical objects were modelled using *R3D4* FEs (each of the FE is characterised by having four nodes and three translational degrees of freedom in each node of the FE). The discrete model consisted of a total of 19,272 FEs (16,200 linear hexahedral elements of type C3D8R and 3,072 linear quadrilateral elements of type R3D4) and 37,984 computational nodes. The cohesive surfaces (considering cohesive behaviour with stiffness parameters), normal and tangential behaviour (without friction), as well as damage with damage initiation and evolution parameters) were implemented between all laminate layers (a total of seven cohesive surfaces). In addition, each layer was assigned the possibility of a cracking phenomenon, depending on the material strength according to the XFEM model which allows the simulation of the fracture phenomenon. Moreover, the contact interactions (in normal and tangential direction) between the non-deformable objects and the composite structure, with the friction 0.1 were also defined. The boundary conditions were applied at specially generated reference points, which were coupled to non-deformable cylindrical objects. The top non-deformable object was assigned boundary conditions under which it was allowed to move only in the direction of the composite specimen relative to the *Z*-axis. The bottom non-deformable objects had all degrees of freedom locked. This approach made it possible to simulate the three-point bending phenomenon of the composite specimen. The boundary conditions and discrete model are presented in Fig. 7.

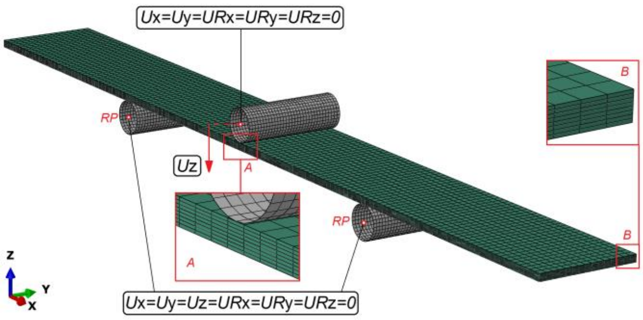

Fig. 7. Discrete model of composite profile with boundary conditions

3. RESULTS

In this section, both the results of the three-point bending as well as damage initiation and evolution of the failure mechanism will be presented in detail. The results of failure will be presented on the basis of experimental investigations using UTM and digital microscope as well as non-linear numerical simulations using two independent damage models (CZM and XFEM). In the case of experimental tests, curves describing the course of the load versus displacement, registered directly with the load cell – Fig. 8.

In the course of the conducted three-point bending tests, during the movement (displacement in the direction of the composite specimen) of the test head, the force acting on the composite structure was registered. Consequently, experimental curves (load–displacement) were determined for all six actual specimens.

Fig. 8. Test stand prepared for three-point bending tests

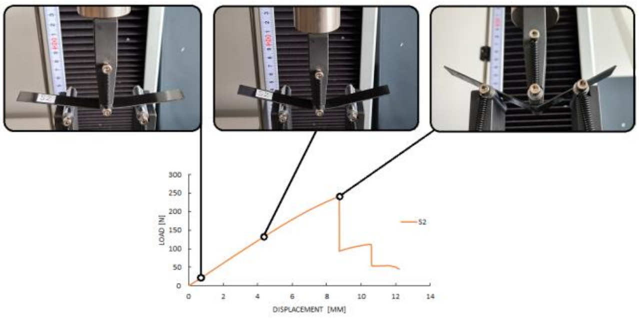

Fig. 9. Determination of load–displacement curves

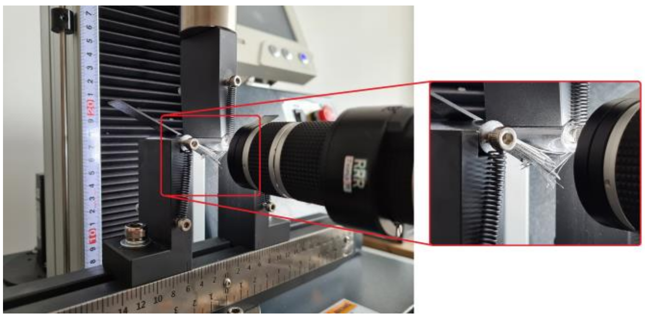

Fig. 10. Recording of composite material failure form

Fig. 9 shows the stages of loading the structure until it collapses. The structure worked elastically until a rapid loss of load-carrying capacity (displacement slightly exceeding 8.5 mm), followed by a complex phase of failure. Experimental investigations allowed both the determination of load–displacement curves for each test specimen and the evaluation of the form of structural failure of the composite material using a mobile head of the digital microscope. The above-mentioned mobile microscope head made it possible to record complex forms of failure, for all test specimens, using a 30× zoom (Fig. 10.).

The recorded forms of failure were then stored in the memory of the computer controlling the digital microscope. This approach allowed comparison of the obtained forms of failure of the composite material structure for all test specimens, with further possibility of comparison with the result of numerical simulation. In the case of the numerical simulations, the actual boundary conditions were fully reproduced, and the additional consideration of the previously described independent failure models enabled a comprehensive evaluation of the failure phenomenon during the three-point bending test. Within the framework of numerical simulations, the curve describing the course of the load versus displacement was determined, which allowed comparison with the experimental results.

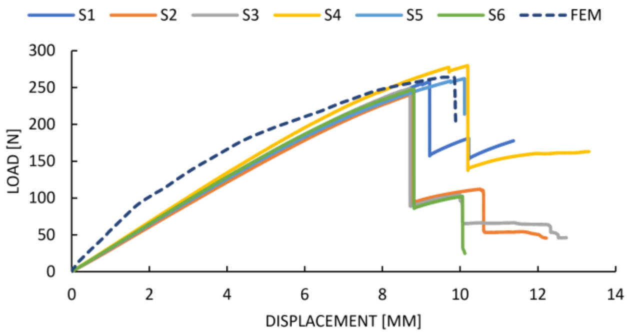

Fig. 11. Comparison of experimental load–displacement curves with FEM simulation result

On the basis of the conducted tests, very good agreement was observed in the qualitative aspect of the results, both between the individual experimental tests and the numerical simulation result. The highest value of load corresponding to loss of load-carrying capacity was observed for the specimen designated S4, for which the failure force was about 279.79 N. The lowest failure force was 240.75 N and related to specimen S2. The maximum discrepancy between the failure load results in the context of the experimental study was about 14%. The experimental specimen, designated as S4, shows a significantly higher ultimate load value than the other five specimens, which significantly affects the maximum discrepancy of the results of the loads corresponding to the loss of load-carrying capacity. If only the values of all the experimental specimens except S4 were compared, the maximum discrepancy would decrease significantly. Regarding the numerical simulation, it was observed that the maximum value of the failure force was 264.05 N. The discrepancy between the average value of failure force of the experimental study and the FEM simulation result was 3%. The above indicates a very precise preparation of the numerical model in terms of quantitative evaluation of research results. Tab. 3 shows the values of the failure loads.

The measurable effect of experimental studies and numerical simulations was the qualitative evaluation of the obtained forms of failure. For the experimental tests, complex failure forms were registered for each test specimen, which was finally compared with the FEA results. The forms of failure observed during the experimental tests conducted are shown in Fig. 12.

DOI 10.2478/ama-2023-0015

Tab. 3. Limit load values

Experimental study [N]	Average value of experimental study [N]	Numerical study [N]
S1 – 258.39	256.33	264.05
S2 – 240.75		
S3 – 248.93		
S4 – 279.79		
S5 – 262.17		
S6 – 247.92		

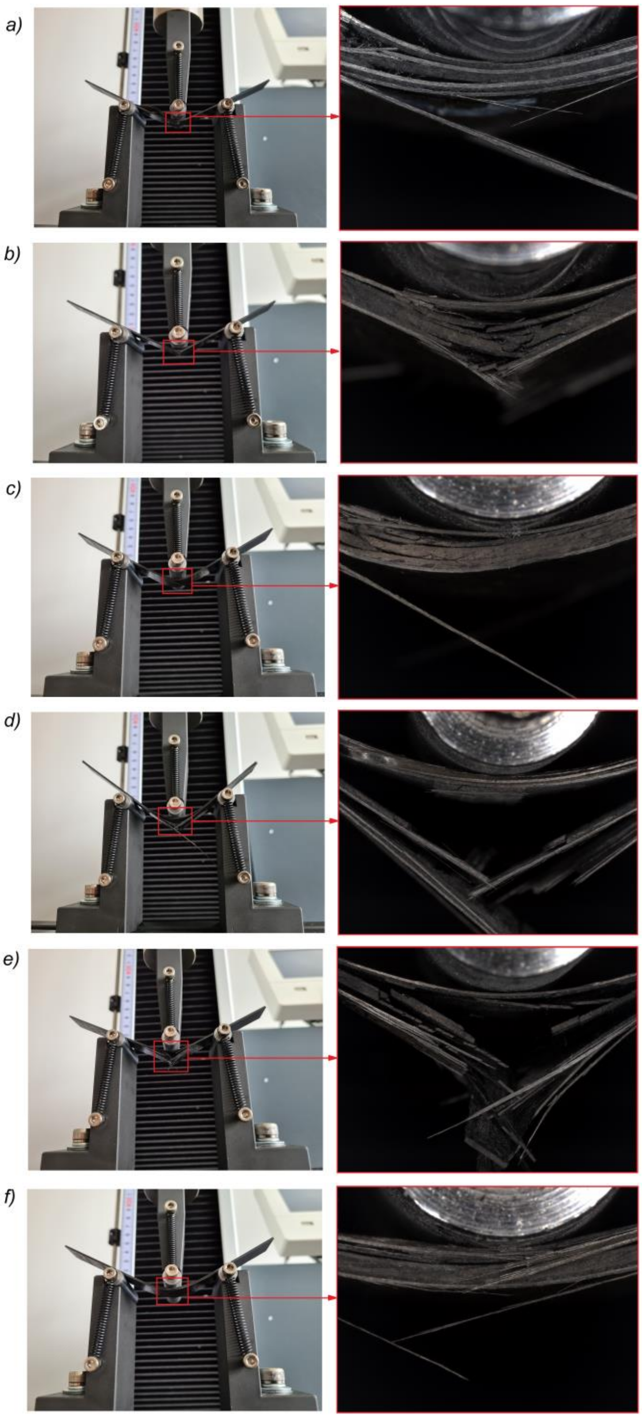

Fig. 12. Experimentally determined failure forms for individual specimens: (a) S1, (b) S2, (c) S3, (d) S4, (e) S5 and (f) S6

In each of the analysed cases, a complex failure mechanism of the composite material was observed. It was observed that delamination, fibre cracking (due to fibre bending) and matrix crushing occurred. Although all of the experimental specimens had the same composite lay-up, the failure forms (or rather, the propagation of these forms) were slightly different. However, this had no significant effect on the discrepancy of the limit loads presented previously. The dominant failure form occurred in the central part of the test specimen, in the area at which the load from the testing machine head was generated. The use of a mobile head of digital microscope allowed for precise recording of the failure forms. Simultaneously conducted numerical simulations made it possible to compare the test results in the context of qualitative assessment. Fig. 13 shows a complex form of structural failure of a composite material using overall scalar stiffness degradation (SDEG) parameter.

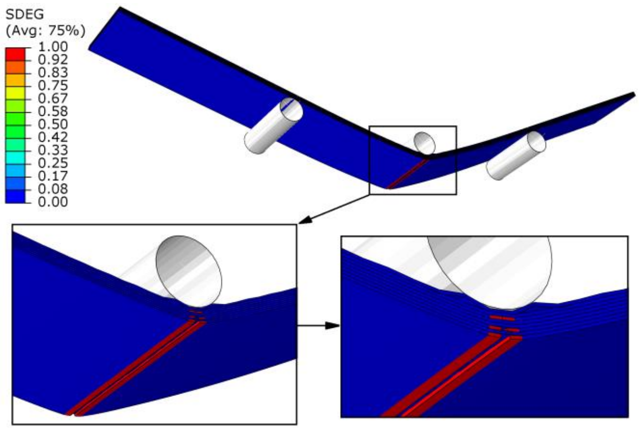

Fig. 13. Loss of load-carrying capacity of composite structure – numerical simulation result

A complex state of failure of the material structure was observed, both through the occurrence of material cracking (using the XFEM model) and delamination (using the CZM technique). Achieving a value of 1 within SDEG parameter indicates a total loss of stiffness (stiffness degradation) in a specific area. Moreover, the numerical simulation showed the damage evolution phenomenon, where initially cracking of the composite material was observed, followed by delamination phenomenon – Fig. 14.

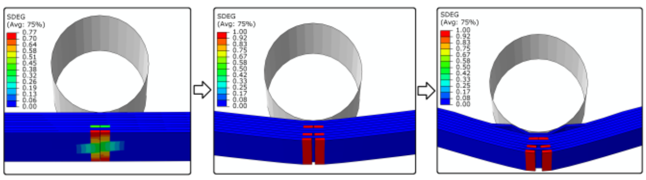

Fig. 14. Evolution of composite material failure phenomenon – simulation result

Within the framework of the conducted tests, very high agreement in terms of quality was observed between the result of the experimental tests and the numerical simulation – which is confirmed in Fig. 15.

DOI 10.2478/ama-2023-0015
acta mechanica et automatica, vol.17 no.1 (2023
Special Issue "Computational Technologies in Engineering TKI2022"

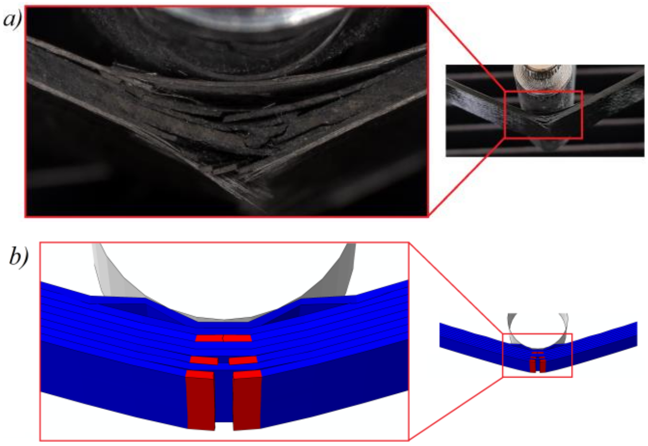

Fig. 15. Comparison of failure modes: (a) experimental tests (specimen S2) and (b) numerical simulation

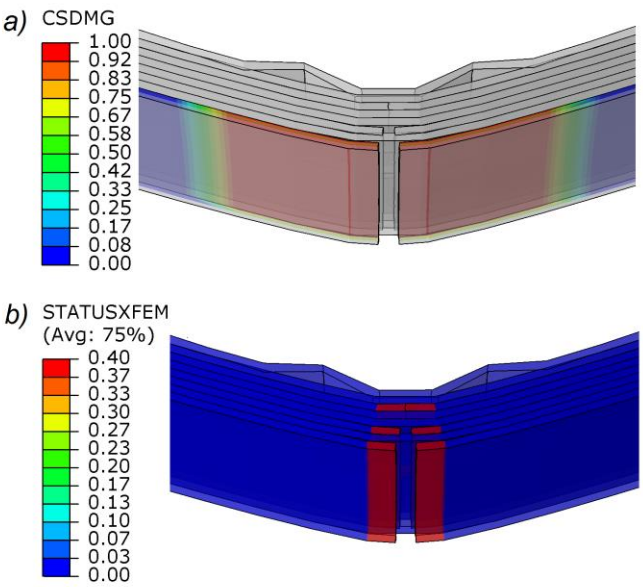

Fig. 16. Failure of composite structure: (a) CSDMG (between the two outer layers) and (b) XFEM

In the case of numerical simulations, using the two previously mentioned advanced techniques to simulate the failure phenomenon of the composite material, a complex failure mechanism adequate for the experimental studies was obtained. The results of numerical calculations provided the necessary information on the complex course of failure of the composite material. In the initial stage of damage in FEM simulations the cracking of composite material layers was observed (Fig. 14), after which, during further loading of the structure in the framework of the three-point bending test, the phenomenon of layer cracking deepened along with the occurrence of the delamination phenomenon (Fig. 15b). The layer cracking phenomenon mainly affected those layers in which the fibres of the composite material were aligned along the length of the test specimen (layers 1, 3, 6 and 8). Moreover, the results of the failure phenomenon based on the CSDMG parameter – which determines the damage evolution of the cohesive zone – and XFEM – which represents the failure due to material cracking – are presented in the numerical simulation – Fig. 16. Obviously, the delamination-induced damage occurred between all the constituent layers of the composite material; however, Fig. 16a shows an example of the result between the bottom two outer layers of the composite material.

Any permanent forms of damage that appeared, such as delamination, or the complete rupture of the layers, took place at the time of loss of load-carrying capacity – or immediately afterwards, as evidenced by the curves from the tests in Fig. 11. The numerical simulation techniques used in the study of the phenomenon of the complex mechanism of failure of the composite material, confirmed experimentally obtained forms of failure, especially in the context of qualitative assessment (quantitative agreement is shown in Fig. 11 and Tab. 3). The numerical simulation provided a virtual representation of the failure phenomenon of the composite material, including the phenomena directly contributing to the failure. Fig. 17 presents in detail the obtained form of failure during numerical simulations using FEM.

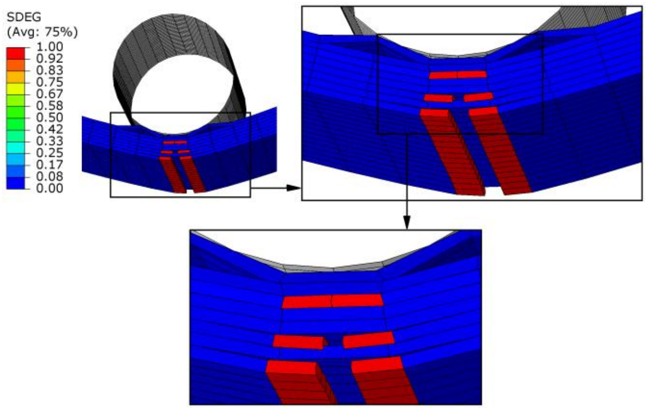

Fig. 17. Failure in terms of numerical simulation

4. CONCLUSION

The limit states of a three-point bending composite structure were determined from the tests. Based on the investigations, the following general conclusions were formulated:

- It is possible to evaluate the failure analysis, especially with regard to the delamination and crack propagation phenomena (directly preceding the loss of load-carrying capacity) of beam composite structures, using experimental investigations (UTM and digital microscope) as well as numerical simulations using FEM (especially using CZM and XFEM);
- The evaluation of limit loads (critical, damage initiation, delamination and loss of load-carrying capacity loads) allows assessment of the complex failure mechanism;
- Simultaneous use of several independent numerical damage models allows for faithful representation of the actual damage phenomenon;
- The use of a mobile digital microscope head allows recording of the complex mechanism of failure, which in turn allows comparison of failure forms with FEA.

In the context of the quantitative evaluation, it was estimated that the discrepancy of the results corresponding to the failure load between all experimental tests does not exceed 14%. This discrepancy would be even lower (<10%) if not for one of the specimens designated as S4. Moreover, the discrepancy of the average result of the failure load from the experimental tests in relation to the result from the FEM simulation was about 3%, which proves the high quality of the prepared numerical model. In the study, a complex failure mechanism of the composite material was observed, within which both material cracking and delamination occurred – as demonstrated by the experimental studies and FEM simulations. The main failure area occurring in the central part of the composite profile (opposite to the applied load), resulting from the specific nature of the tests conducted, is an ideal example of the progressive failure of the composite material structure, in which advanced forms of damage could be observed.

Future research plans include the use of the acoustic emission method to estimate the initiation and evolution of damage to the composite material during experimental tests. This will allow, first of all, to compare the results in the context of phenomena directly affecting the loss of load-carrying capacity and to compare them with the damage initiation and evolution criteria realised within FEM.

The research presented in the paper provides the basis for the research conducted under the project No. 2021/41/B/ST8/00148 (in terms of presenting interdisciplinary research methods on composite materials), financed by the National Science Centre, Poland – on composite profiles with closed sections. The research techniques presented in this paper will be used to carry out research within the framework of the aforementioned scientific project.

REFERENCES

1. Fascetti A, Feo L, Nistic N, Penna R. Web-flange behavior of pultruded GFRP I beams: a lattice model for the interpretation of experimental results. Composites Part B Eng, 2016;100:257-269.
2. Berardi VP, Perrella M, Feo L, Cricrì G. Creep behavior of GFRP laminates and their phases: experimental investigation and analytical modeling. Composites Part B Eng, 2017;122:136-144.
3. Kubiak T, Kolakowski Z, Swiniarski J, Urbaniak M, Gliszczynski A. Local buckling and post-buckling of composite channel-section beams – numerical and experimental investigations. Composites Part B Eng, 2016;91:176-188.
4. Rozylo P. Experimental-numerical study into the stability and failure of compressed thin-walled composite profiles using progressive failure analysis and cohesive zone model. Composite Structures, 2021;257:113303.
5. Debski H, Rozylo P, Teter A. Buckling and limit states of thin-walled composite columns under eccentric load. Thin-Walled Structures, 2020;149:106627.
6. Debski H, Rozylo P, Wysmulski P. Stability and load-carrying capacity of short open-section composite columns under eccentric compression loading. Composite Structures, 2020;252:112716.
7. Rozylo P, Debski H. Stability and load-carrying capacity of short composite Z-profiles under eccentric compression. Thin-Walled Structures, 2020;157:107019.
8. Debski H, Samborski S, Rozylo P, Wysmulski P. Stability and Load-Carrying Capacity of Thin-Walled FRP Composite Z-Profiles under Eccentric Compression. Materials, 2020;13:2956.
9. Rozylo P, Debski H. Effect of eccentric loading on the stability and load-carrying capacity of thin-walled composite profiles with top-hat section. Composite Structures, 2020;245:112388.
10. Gliszczynski A, Czechowski L. Collapse of channel section composite profile subjected to bending, Part I: Numerical investigations. Compos Struct, 2017;178:383–394.
11. Jakubczak P, Gliszczynski A. Bienias J, Majerski K. Kubiak T. Collapse of channel section composite profile subjected to bending Part II: Failure analysis. Compos Struct, 2017;179:1–20.
12. Kazmierczyk F, Urbaniak M, Swiniarski J, Kubiak T. Influence of boundary conditions on the behaviour of composite channel section subjected to pure bending – Experimental study. Compos Struct, 2022;279:114727.
13. Gliszczynski A, Kubiak T. Load-carrying capacity of thin-walled composite beams subjected to pure bending. Thin-Walled Struct, 2017;115:76–85.
14. Czechowski L, Gliszczynski A, Bienias J, Jakubczak P, Majerski K. Composites Part B, 2017;111:112-123.
15. Banat D, Mania RJ. Failure assessment of thin-walled FML profiles during buckling and postbuckling response. Compos Part B Eng 2017;112:278-289.
16. Madukauwa-David ID, Drissi-Habti M. Numerical simulation of the mechanical behavior of a large smart composite platform under static loads. Composites Part B Eng 2016;88:19-25.
17. Feo L, Latour M, Penna R, Rizzano G. Pilot study on the experimental behavior of GFRP-steel slip-critical connections. Composites Part B Eng 2017;115:209-222.
18. Chroscielewski J, Miskiewicz M, Pyrzowski Ł, Sobczyk B, Wilde K. A novel sandwich footbridge - Practical application of laminated composites in bridge design and in situ measurements of static response. Composites Part B Eng 2017;126:153-161.
19. Rozylo P. Stability and failure of compressed thin-walled composite columns using experimental tests and advanced numerical damage models. Int J Numer Methods Eng. 2021;122:5076-5099.
20. Rozylo P, Wysmulski P. Failure analysis of thin-walled composite profiles subjected to axial compression using progressive failure analysis (PFA) and cohesive zone model (CZM). Composite Structures, 2021;262:113597.
21. Rozylo P, Debski H, Wysmulski P, Falkowicz K. Numerical and experimental failure analysis of thin-walled composite columns with a top-hat cross section under axial compression. Composite Structures 2018;204:207-216.
22. Paszkiewicz M, Kubiak T. Selected problems concerning determination of the buckling load of channel section beams and columns. Thin-Walled Structures 2015;93:112-121.
23. Ascione F. Influence of initial geometric imperfections in the lateral buckling problem of thin walled pultruded GFRP I-profiles. Composite Structures 2014;112:85–99.
24. Sohn MS, Hu XZ, Kim JK, Walker L. Impact damage characterisation of carbon fibre/epoxy composites with multi-layer reinforcement. Composites Part B: Engineering 2000;31:681-691.
25. Batra RC, Gopinath G, Zheng JQ. Damage and failure in low energy impact of fiber-reinforced polymeric composite laminates. Composite Structures 2012;94:540-547.
26. Rozylo P, Ferdynus M, Debski H, Samborski S. Progressive Failure Analysis of Thin-Walled Composite Structures Verified Experimentally. Materials, 2020;13:1138.
27. Debski H, Rozylo P, Gliszczynski A, Kubiak T. Numerical models for buckling, postbuckling and failure analysis of predamaged thin-walled composite struts subjected to uniform compression. Thin-Walled Structures, 2019;139:53-65.
28. Reddy JN, Pandey AK. A first-ply failure analysis of composite laminates. Comput Struct, 1987;25:371–393.
29. Kubiak T, Samborski S, Teter A. Experimental investigation of failure process in compressed channel-section GFRP laminate columns assisted with the acoustic emission method. Compos Struct, 2015; 133:921-929.
30. Hashin Z, Rotem A. A fatigue failure criterion for fibre reinforced materials. J. Compos. Mater, 1973;7:448–464.
31. Camanho PP, Maimí P, Dávila CG. Prediction of size effects in notched laminates using continuum damage mechanics. Compos. Sci. Technol, 2017;67:2715–2727.
32. Camanho PP, Matthews FL. A progressive damage model for mechanically fastened joints in composite laminates. J. Comp. Mater, 1999;33:2248–2280.

33. Barbero EJ, Cosso FA. Determination of material parameters for discrete damage mechanics analysis of carbon epoxy laminates. Compos. Part B Eng, 2014;56:638–646.
34. Lemaitre J, Plumtree A. Application of damage concepts to predict creep fatigue failures. J. Eng. Mater. Technol, 1979;101:284–292.
35. Ribeiro ML, Vandepitte D, Tita V. Damage model and progressive failure analyses for filament wound composite laminates. Appl. Compos. Mater, 2013;20:975–992.
36. Kachanov LM. Time of the rupture process under creep conditions, Izv. AN SSSR. Otd. Tekh. Nauk, 1958;8:26–31.
37. Matzenmiller A, Lubliner J, Taylor LR. A constitutive model for anisotropic damage in fiber composites. Mech. Mater, 1995;20:125–152.
38. Lapczyk I, Hurtado JA. Progressive damage modeling in fiber-reinforced materials. Compos. Part A Appl. Sci. Manuf, 2007;38: 2333–2341.
39. Bisagni C, Di Pietro, G, Fraschini L, Terletti D. Progressive crushing of fiber reinforced composite structural components of a Formula One racing car. Compos. Struct, 2005;68:491–503.
40. Li W, Cai H, Li C, Wang K, Fang L. Progressive failure of laminated composites with a hole under compressive loading based on micro-mechanics. Adv. Compos. Mater, 2014;23:477–490.
41. Benzeggagh ML, Kenane M. Measurement of Mixed-Mode Delamination Fracture Toughness of Unidirectional Glass/Epoxy Composites with Mixed-Mode Bending Apparatus. Composites Science and Technology, 1996;56:439–449.
42. Dugdale DS. Yielding of steel sheets containing slit, Journal of the Mechanics and Physics of Solids, 1960;8(2):100-104.
43. Barenblatt GI. The mathematical theory of equilibrium cracks in brittle fracture. Advances in Applied Mechanics, 1962;7:55-129.
44. Turon A, Camanho PP, Costa J, Dávila CG. A damage model for the simulation of delamination in advanced composites under variable-mode loading, Mechanics of Materials, 2006;38(11):1072-1089.
45. Camanho PP, Davila CG, de Moura MF. Numerical simulation of mixed-mode progressive delamination in the composite materials, Journal of Composite Materials, 2003;37(16):1415-1438.
46. Hu H, Niu F, Dou T, Zhang H. Rehabilitation Effect Evaluation of CFRP-Lined Prestressed Concrete Cylinder Pipe under Combined Loads Using Numerical Simulation. Mathematical Problems in Engineering, 2018;2018:3268962.
47. Borg R, Nilsson L, Simonsson K. Simulating DCB, ENF and MMB experiments using shell elements and a cohesive zone model, Composites Science and Technology, 2004;64:269-278.
48. Zhao L, Gong Y, Zhang J, Chen Y, Fei B. Simulation of delamination growth in multidirectional laminates under mode I and mixed mode I/II loadings using cohesive elements, Composite Structures, 2014; 116:509-522.
49. Rozylo P. Failure analysis of thin-walled composite structures using independent advanced damage models. Composite Structures, 2021;262:113598.
50. Li ZM, Qiao P. Buckling and postbuckling behavior of shear deformable anisotropic laminated beams with initial geometric imperfections subjected to axial compression. Engineering Structures, 2015;85:277–292.
51. Bouhala L, Makradi A, Belouettar S, Younes A, Natarajan S. An XFEM/CZM based inverse method for identification of composite failure parameters. Comput. Struct, 2015;153:91-97.
52. Paneretti E, Fanteria D, Danzi F. Delaminations growth in compression after impact test simulations: Influence of cohesive elements parameters on numerical results. Compos. Struct, 2016;137:140-147.
53. Moes N, Dolbow J, Belytschko T. A finite element method for crack growth without remeshing. Int J Numer Methods Eng, 1999;46(1):131–50.
54. Moës N, Belytschko T. Extended finite element method for cohesive crack growth. Eng Fracture Mech, 2002;69(7):813–33.
55. Dolbow J, Moës N, Belytschko T. An extended finite element method for modeling crack growth with frictional contact. Comput Methods Appl Mech Eng, 2001;190(51-52):6825–46.
56. Melenk J, Babuska I. The partition of unity ˙nite element method: Basic theory and applications. computer methods. Appl. Mech Eng, 1996;39:289–314.
57. Zienkiewicz OC, Taylor RL. Finite Element Method—Solid Mechanics, 5th ed.; Elsevier: Barcelona, Spain, 2000.
58. Parlapalli MR, Soh KC, Shu DW, Ma G. Experimental investigation of delamination buckling of stitched composite laminates. Composites: Part A, 2007;38:2024–2033.
59. Turvey GJ, Zhang Y. A computational and experimental analysis of the buckling, postbuckling and initial failure of pultruded GRP columns. Composite Structures, 2006;84:1527–1537.
60. Bohse J. et al. Damage analysis of Polymer Matrix Composites by Acoustic Emission Testing. DGZfP-Proceedings BB 90-CD:339-348.
61. Riccio A, Saputo S, Sellitto A, Di Caprio F, Di Palma L. A numerical-experimental assessment on a composite fuselage barrel vertical drop test: Induced damage onset and evolution. Composite Structures, 2020;248:112519.
62. Gliszczynski A, Kubiak T. Progressive failure analysis of thin-walled composite columns subjected to uniaxial compression. Composite Structures, 2017;169:52-61.
63. Aveiga D, Ribeiro ML. A Delamination Propagation Model for Fiber Reinforced Laminated Composite Materials. Mathematical Problems in Engineering, 2018;2018:1861268.
64. Rozylo P, Debski H, Falkowicz K, Wysmulski P, Pasnik J, Kral J. Experimental-Numerical Failure Analysis of Thin-Walled Composite Columns Using Advanced Damage Models. Materials, 2021;14(6): 1506.
65. Banat D, Mania RJ, Degenhardt R. Stress state failure analysis of thin-walled GLARE composite members subjected to axial loading in the post-buckling range. Composite Structures, 2022;289:115468.
66. Banat D, Mania RJ. Damage analysis of thin-walled GLARE members under axial compression – Numerical and experiment investigations. Compos. Struct, 2020;241:112102.
67. Debski H. Experimental investigation of post-buckling behavior of composite column with top-hat cross-section. Eksploat. Niezawodn, 2013;15:106–110.
68. Debski H. Badania numeryczne i doświadczalne stateczności i nośności kompozytowych słupów cienkościennych poddanych ściskaniu. Zeszyty naukowe nr 1161, Wydawnictwo Politechniki Łódzkiej, ISSN 0137-4834, Łódź, 2013.
69. Rozylo P. Comparison of Failure for Thin-Walled Composite Columns. Materials, 2022;15:167.
70. Debski H, Rozylo P, Wysmulski P, Falkowicz K, Ferdynus M. Experimental study on the effect of eccentric compressive load on the stability and load-carrying capacity of thin-walled composite profiles. Composites Part B, 2021;226:109346.
71. Li Z, Cen S, Wu CJ, Shang Y, Li CF. High-performance geometric nonlinear analysis with the unsymmetric 4-node, 8-DOF plane element US-ATFQ4. Int J Numer Methods Eng, 2018;114:931–954.
72. Camanho PP, Davila CG. Mixed-mode decohesion finite elements for the simulation of delamination in composite materials. NASA/TM-2002–211737, 2002:1–37.
73. Dassault Systemes Simulia Corp. Abaqus 2020 Documentation. Providence, RI, USA, 2020.
74. Belytschko T, Black T. Elastic Crack Growth in Finite Elements with Minimal Remeshing. International Journal for Numerical Methods in Engineering, 1999;45:601–620.
75. Melenk J, Babuska I. The Partition of Unity Finite Element Method: Basic Theory and Applications. Computer Methods in Applied Mechanics and Engineering, 1996;39:289–314.
76. Yu Z, Zhang J, Shen J, Chen H. Simulation of crack propagation behavior of nuclear graphite by using XFEM, VCCT and CZM methods. Nuclear Materials and Energy, 2021;29:101063.

77. Heidari-Rarani M, Sayedain M. Finite element modeling strategies for 2D and 3D delamination propagation in composite DCB specimens using VCCT, CZM and XFEM approaches. Composites Part C: Open Access, 2020;2:100014.
78. Kolanu NR, Raju G, Ramji M. A unified numerical approach for the simulation of intra and inter laminar damage evolution in stiffened CFRP panels under compression. Composites Part B, 2020;190: 107931.

Acknowledgments: The research was conducted under project No. 2021/41/B/ST8/00148, financed by the National Science Centre, Poland.

Patryk Różyło: https://orcid.org/0000-0003-1997-3235